

Strategies for stabilization and activation of Mn- and Co-based catalysts for the oxygen evolution reaction

vorgelegt von:

M. Sc.

Javier Francisco Villalobos Porras

ORCID: 0000-0002-8032-6574

an der Fakultät II – Mathematik und Naturwissenschaften
der Technischen Universität Berlin
zur Erlangung des akademischen Grades

Doktor der Naturwissenschaften

Dr. rer. nat.

genehmigte Dissertation

Promotionsausschuss:

Vorsitzender: Prof. Dr. Arne Thomas (Technische Universität Berlin)

Gutachter: Prof. Dr. Roel van de Krol (Technische Universität Berlin)

Gutachter: Prof. Dr. Jan Philipp Hofmann (Technische Universität Darmstadt)

Gutachter: Dr. Marcel Risch (Helmholtz-Zentrum Berlin)

Tag der wissenschaftlichen Aussprache: 29. September 2022

Berlin 2022

Abstract

The complex kinetics of the oxygen evolution reaction (OER) makes this reaction one of the most considerable challenges for implementing water splitting as a solution to efficiently storage renewable energy, like sunlight. The sluggish kinetics of OER catalysis make high catalytic activity and stability under harsh conditions fundamental requirements for the overall efficiency of the process. While many studies are focused on the inherent activity of the electrocatalysts, a better understanding of the material transformations relating to degradation, stabilization, restructuring and activation is highly desirable, both from a scientific perspective and for applications.

Na-containing Co- and Mn-based oxides were electrodeposited by a new electrodeposition method in alkaline media. Tartrate is included in the electrodeposition electrolyte to complex and stabilized the metallic (Co and Mn) ions, preventing their spontaneous precipitation. The CoO_x films showed higher catalytic activity than the MnO_x films, but both had a current drop over cycling. By an applying a 30-minute open circuit break, the CoO_x current fully recovered, whereas the MnO_x recovered partially, suggesting that some changes are irreversible. The Tafel slope of both films were 120 mV dec^{-1} or higher and increased over cycling, indicating a chemical rate-limiting step or poor conductivity of the films. The changes in the catalytic current were related to a partial oxidation at the near-surface region of MnO_x (and CoO_x), proved by X-ray absorption spectroscopy (XAS).

By introducing 30 % of MnO_x into CoO_x , a new material, $(\text{Co}_{0.7}\text{Mn}_{0.3})\text{O}_x$, was formed. The $(\text{Co}_{0.7}\text{Mn}_{0.3})\text{O}_x$ films proved to be more stable than the single oxides under similar conditions (no current drop was observed at catalytic potentials). The catalytic activity of $(\text{Co}_{0.7}\text{Mn}_{0.3})\text{O}_x$ was not significantly different than CoO_x , in terms of overpotential ($\eta \approx 500 \text{ mV}$ at 10 mA) and current density ($j \approx 12 \text{ mAcm}^{-2}$ at 1.74 V vs. RHE). The increase of the stability (without affecting the catalytic activity significantly) was assigned to various factors, namely, prevention of MnO_4^- ions dissolution, a higher conductivity and an optimization of the metal oxygen binding energy.

To understand how to use the structural changes beneficially, the electrochemical restructuring of Ery (a synthesized crystalline mineral: $\text{Co}_3(\text{AsO}_4)_2 \cdot 8\text{H}_2\text{O}$) was studied in different electrolytes (with same pH and concentration). The restructuring to a Co-based amorphous oxide was deconvoluted in three processes: amorphization, anionic exchange and redox activity change, using X-ray diffraction (XRD), energy dispersive X-ray spectroscopy (EDX) and the electrochemical redox-charge (ERC), respectively. The rate of these processes and the

structural order of the final material (proved by EXAFS) were directly affected by the electrolyte's nature. The slowest amorphization was observed in carbonate electrolyte, where the ERC increased the most. Interestingly, the current was only significantly activated (100 % of the initial value) in carbonate electrolyte, demonstrating that the electrochemical restructuring and the current activation are two different processes, where activation has further requirements, namely, an adequate cluster size, a high Co oxidation state and high redox activity.

Developing strategies to extend the lifetime and increase the efficiency of OER electrocatalysts is essential for their future bigger-scale application in energy storage. Stability, activation and reactivation are desirable features when coupling OER electrocatalysts to renewable sources for sustainable energy production.

Kurzfassung

Die komplexe Kinetik der Sauerstoffentwicklungsreaktion (OER) macht diese Reaktion zu einer der größten Herausforderungen bei der Umsetzung der Wasserspaltung als Lösung für die effiziente Speicherung erneuerbarer Energien wie zum Beispiel Sonnenlicht. Die träge Kinetik der OER Katalyse macht eine hohe katalytische Aktivität und Stabilität unter erschwerten Bedingungen zu grundlegenden Anforderungen für die Gesamteffizienz des Prozesses. Während sich viele Studien auf die intrinsische Aktivität der Elektrokatalysatoren konzentrieren, ist ein besseres Verständnis der Materialumwandlungen im Zusammenhang mit Abbau, Stabilisierung, Umstrukturierung und Aktivierung sowohl aus wissenschaftlicher Sicht als auch für praktische Anwendungen äußerst wünschenswert.

Na-haltige Oxide auf Co- und Mn-Basis wurden mit einer neuen Elektroabscheidungsmethode in alkalischen Medien abgeschieden. Der Elektrolyt enthält Tartrate, der die metallischen Ionen (Co und Mn) komplexiert, stabilisiert und ihre spontane Ausfällung verhindert. Die CoO_x -Filme wiesen eine höhere katalytische Aktivität auf als die MnO_x -Filme, jedoch hatten beide einen Stromabfall während des Zyklus. Nach einer 30-minütigen Unterbrechung des Stromkreises erholte sich der CoO_x -Strom vollständig, während sich der MnO_x -Strom nur teilweise erholte, was darauf hindeutet, dass einige Veränderungen irreversibel sind. Die Tafelsteigung beider Filme lag bei 120 mV pro Dekade oder höher und nahm im Laufe der Zyklen zu, was auf einen chemischen geschwindigkeitsbegrenzenden Schritt oder eine schlechte Leitfähigkeit der Filme hinweist. Durch die Einführung von 30 % MnO_x in CoO_x wurde ein neues Material, $(\text{Co}_{0.7}\text{Mn}_{0.3})\text{O}_x$, gebildet. Die Veränderungen des katalytischen Stroms standen im Zusammenhang mit einer teilweisen Oxidation im oberflächennahen Bereich von MnO_x (und CoO_x), was durch Röntgenabsorptionsspektroskopie (XAS) nachgewiesen wurde.

Die $(\text{Co}_{0.7}\text{Mn}_{0.3})\text{O}_x$ -Filme erwiesen sich unter ähnlichen Bedingungen als stabiler als die einzelnen Oxide (bei katalytischen Potentialen wurde kein Stromabfall beobachtet). Die katalytische Aktivität von $(\text{Co}_{0.7}\text{Mn}_{0.3})\text{O}_x$ unterschied sich nicht signifikant von der von CoO_x , was die Überspannung ($\eta \approx 500$ mV bei 10 mA) und die Stromdichte ($j \approx 12$ mA cm⁻² bei 1.74 V vs. RHE) betrifft. Die Erhöhung der Stabilität (ohne signifikante Beeinträchtigung der katalytischen Aktivität) wurde verschiedenen Faktoren zugeschrieben, nämlich der Verhinderung der Auflösung von MnO_4^- Ionen, einer höheren Leitfähigkeit und einer Optimierung der Metallsauerstoff-Bindungsenergie.

Um zu verstehen, wie die strukturellen Veränderungen vorteilhaft genutzt werden können, wurde die elektrochemische Umstrukturierung von Ery (Erythrin, einem synthetisierten kristallinen Mineral: $\text{Co}_3(\text{AsO}_4)_2 \cdot 8\text{H}_2\text{O}$) in verschiedenen Elektrolyten (mit gleichem pH-Wert und gleicher Konzentration) untersucht. Die Umstrukturierung zu einem amorphen Oxid auf Co-Basis wurde in drei Prozesse unterteilt: Amorphisierung, Anionenaustausch und Änderung der Redoxaktivität, wobei Röntgenbeugung (XRD), energiedispersive Röntgenspektroskopie (EDX) bzw. die elektrochemische Redoxladung (ERC) verwendet wurden. Die Geschwindigkeit dieser Prozesse wurde direkt von der Art des Elektrolyten beeinflusst. Die langsamste Amorphisierung wurde in Karbonatelektrolyten beobachtet, wo die ERC am stärksten anstieg. Interessanterweise wurde der Strom nur in Karbonatelektrolyten signifikant aktiviert (100 % des ursprünglichen Wertes), was zeigt, dass die elektrochemische Umstrukturierung und die Stromaktivierung zwei unterschiedliche Prozesse sind. Für diese Aktivierung gelten weitere Voraussetzungen, nämlich eine angemessene Clustergröße, ein hoher Co-Oxidationszustand und eine hohe Redoxaktivität.

Die Entwicklung von Strategien zur Verlängerung der Lebensdauer und Steigerung der Effizienz von OER-Elektrokatalysatoren ist für ihre künftige Anwendung in größerem Maßstab bei der Energiespeicherung von entscheidender Bedeutung. Stabilität, Aktivierung und Reaktivierung sind wünschenswerte Merkmale bei der Kopplung von OER-Elektrokatalysatoren mit erneuerbaren Quellen zur nachhaltigen Energieerzeugung.

Acknowledgments

There is plenty of people who supported me during the years, either academically, with scientific contributions, discussions, equipment, or emotionally, offering me advice, a friendship, companion. I am grateful to all these people and I would like express my gratitude and appreciation. Thanks to:

Firstly, Dr. Marcel Risch, who gave the opportunity to start next to him the research group as his first PhD student in his group in Helmholtz-Zentrum Berlin (HZB). I appreciate very much all the scientific support that he gave me during this time, discussions, advice, and direction. I would like to thank him for being supportive, responsive and understanding.

Prof. Dr. Roel van de Krol, for being part of my committee, not only in this thesis but also in HZB. I thank him for following my progress and for the fruitful discussions we had.

Prof. Dr. Jan Philipp Hofmann for kindly agreeing to be the external examiner of this work.

Prof. Dr. Holger Dau, who has been part of my academic growth even before I started my doctoral studies. I appreciate all the productive discussions we had.

CE-NOME group. To each of the members and students of CE-NOME in HZB I am greatly thankful. To Dr. Dulce Morales-Hernández, who helped me so much whenever I had questions about electrochemistry, especially impedance. To Mr. Joaquín Morales-Santelices, for sharing with me the toughness of the in-situ experiments and bringing rhythm to the group. To Mr. Denis Antipin, who was with me in the group almost from the very beginning and has helped me understanding kinetics. Even though we had tough times due to the pandemic, they always brought joy to my life (even during beamtimes).

The second part of the group, located in Göttingen, Dr. Max Baumung and Frederik Stender, for all discussions and support.

Students in the group and to those, who have already left the group for their support, Sepideh, Kristian, Patricia, Ben.

Dr. Michael Tovar and Dr. Daniel Abou-Ras for their trainings and advice in microscopy and diffraction techniques.

Beamlines scientists. Dr. Ivo Zizak, Dr. Michael Haumann, Dr. Götz Schuck, Dr. Jie Xiao and Dr. Ronny Golnak, for all their support during beamtimes.

My collaborators in Costa Rica. I thank Dr. Diego González, Dr. Mavis Montero and Dr. Roberto Urcuyo for their support and useful discussions on part of this work.

Paul Pitzinger. for being so supportive during this time. I thank him for listening to me, cheering me up and for cooking when I had beamtime. He definitely made this time more enjoyable.

My friends in Berlin. During these years I have met amazing people who has helped me in one way or another. Laura, Mark, Alex, Peter, Ivo, Paul, Cor, Fran, Jose, Mau, Matthias, Pablo, Gaby, Michael, Melissa. I particularly want to thank Laura and Alex for the nice “chisme” times and for cheering me up in HZB.

My beloved family. Even though being more than ten thousand kilometers away, their support was incredible. To my parents, Xinia and Martin, to my sister, Amelia, and to my abuela, Aracelly, thanks.

My friends in Costa Rica. Plenty of friends that I have left back in Costa Rica. Vini, Diana, JuanPa, Marta, Jose, Elias, Christian, Paola, Jessica, Joselyn, Rodolfo, Isaac, Cami, Diego, Gaby, Melissa, Sergio, Rey, Ethel. And to other friends with a costarican heart, but now living closer to me (in Europe), Tati, Naty, Fer. Thanks!

The European Research Council (ERC). This project has received funding from ERC under the European Union’s Horizon 2020 research and innovation programme under grant agreement No 804092.

List of publications

This thesis is based on the following three publications:

Paper 1:

Reversible and irreversible processes during cyclic voltammetry of an electrodeposited manganese oxide as catalyst for the oxygen evolution reaction

Javier Villalobos, Ronny Golnak, Lifei Xi, Götz Schuck and Marcel Risch

J. Phys. Energy, 2020, **2**, 034009

This is the Accepted Manuscript version of an article accepted for publication in Journal of Physics Energy. IOP Publishing Ltd is not responsible for any errors or omissions in this version of the manuscript or any version derived from it. The Version of Record is available online at <https://doi.org/10.1088/2515-7655/ab9fe2>.

Paper 2:

Stabilization of a Mn-Co oxide during oxygen evolution in alkaline media

Javier Villalobos, Dulce M. Morales, Denis Antipin, Götz Schuck, Ronny Golnak, Jie Xiao and Marcel Risch

ChemElectroChem, 2022, **9**, e20220048

This is the published version of the following article: *ChemElectroChem*, 2022, **9**, e20220048, which has been published in final form at <https://doi.org/10.1002/celec.202200482>.

Paper 3:

Requirements for Beneficial Electrochemical Restructuring: A Model Study on a Cobalt Oxide in Selected Electrolytes

Javier Villalobos, Diego González-Flores, Roberto Urcuyo, Mavis L. Montero, Götz Schuck, Paul Beyer, and Marcel Risch

Adv. Energy Mater., 2021, **11**, 2101737

This is the published version of the following article: *Adv. Energy Mater.*, 2021, **11**, 2101737, which has been published in final form at <https://doi.org/10.1002/aenm.202101737>.

Declaration of authors' contributions

The contribution of the co-authors in each of the publications relevant to this thesis is specified below. The first author (underlined name) and the corresponding author (with an asterisk, *) validate this information.

Javier Villalobos, Ronny Golnak, Lifei Xi, Götz Schuck, Marcel Risch,* Reversible and irreversible processes during cyclic voltammetry of an electrodeposited manganese oxide as catalyst for the oxygen evolution reaction. J. Phys. Energy, 2020, 2, 034009.

JV: design and performance of the experiments, data collection, data analysis, figures design, writing, conceptualization, visualization, literature curation, draft manuscript preparation, RG: data discussion, beamline support, help in data collection, LX: beamline support, beamline support, help in data collection, GS: data discussion, help in data collection, MR: conceptualization, data/literature curation, funding acquisition, project administration, resources, supervision, writing, final version approval.

Javier Villalobos, Diego González-Flores, Roberto Urcuyo, Mavis L Montero, Götz Schuck, Paul Beyer, Marcel Risch,* Requirements for Beneficial Electrochemical Restructuring: A Model Study on a Cobalt Oxide in Selected Electrolytes. Adv. Energy Mater., 2021, 11, 2101737

JV: design and performance of the experiments, data collection, data analysis, figures design, writing, conceptualization, visualization, literature curation, draft manuscript preparation, DGF: design and performance of the experiments, data collection, conceptualization, resources, funding acquisition, supervision, RU: data collection, data analysis, MLM: data discussion, conceptualization, GS: beamline support, PB: beamline support, help in data collection, data analysis, MR: conceptualization, data/literature curation, funding acquisition, project administration, resources, supervision, writing, final version approval.

Javier Villalobos, Dulce M Morales, Denis Antipin, Götz Schuck, Ronny Golnak, Jie Xiao, Marcel Risch,* Stabilization of a MnCo Oxide During Oxygen Evolution in Alkaline Media. ChemElectroChem, 2022, 9, e20220048

JV: design and performance of the experiments, data collection, data analysis, figures design, writing, conceptualization, visualization, literature curation, draft manuscript preparation, DMM: help in data collection, data analysis, results discussion, DA: help in data collection, results discussion, GS: beamline support help in data collection, JX: beamline support, help in data collection, data analysis, RG: beamline support, help in data collection, data analysis, MR: conceptualization, data/literature curation, funding acquisition, project administration, resources, supervision, writing, final version approval.

Contents

Abstract	ii
Kurzfassung	iv
Acknowledgments	vi
List of publications	viii
Declaration of authors' contributions	v
Chapter 1. Introduction and motivation	5
Clean energy for all.....	5
Renewable sources and energy storage.....	5
Chapter 2. Scientific context	7
Electrocatalytic oxygen evolution.....	7
Activity, stability, and selectivity	8
Deactivation	10
Stabilization	10
Activation.....	11
Electrochemical restructuring	11
Transition metal oxides for oxygen evolution	12
Mn-based oxides	13
Co-based oxides	15
Scope and organization of this thesis.....	18
References.....	20
Chapter 3. Methods	27
Fundamentals of electrocatalysis	27
Nernst equation	27
Butler-Volmer equation	28
Tafel equation	29
Rotating-ring disk electrode.....	30
X-ray absorption spectroscopy	32
Treatment of the data	34
Estimation of the oxidation state.....	37
EXAFS.....	39
Data simulation	41
Chapter 4. Reversible and irreversible processes during cyclic voltammetry of an electrodeposited manganese oxide as catalyst for the oxygen evolution reaction	43
Abstract.....	43
Introduction.....	44
Methods.....	45

Materials	45
Electrodeposition of MnOx films	45
Electrochemical measurements.....	45
X-ray absorption spectroscopy (XAS).....	46
Results and discussion	47
Electrodeposition of films on glassy carbon.....	47
Electrocatalytic investigations	48
Local structure and valence changes due to cycling.....	51
Conclusions.....	54
Acknowledgments.....	55
References.....	55
Supplementary material	59
Chapter 5. Stabilization of a Mn-Co oxide during oxygen evolution in alkaline media .	70
Results and discussion	71
Conclusion	77
Experimental Section.....	77
Materials	77
Films electrodeposition.....	77
Electrochemical measurements.....	77
Scanning electron microscopy (SEM) and energy dispersive X-ray spectroscopy (EDX)	77
X-ray absorption spectroscopy (XAS).....	77
Acknowledgements.....	78
References.....	78
Supplementary material	81
Chapter 6. Requirements for Beneficial Electrochemical Restructuring: A Model Study on a Cobalt Oxide in Selected Electrolytes	96
Introduction.....	96
Results and Discussion	97
Summary and Conclusion.....	103
Experimental Section.....	103
Acknowledgements.....	104
Data Availability Statement.....	104
Keywords	104
Supporting Information.....	106
Chapter 7: Conclusions and outlook	124

List of abbreviations

UN	United Nations
OER	Oxygen evolution reaction
HER	Hydrogen evolution reaction
NHE	Normal hydrogen electrode
SHE	Standard hydrogen electrode
RHE	Reversible hydrogen electrode
SCE	Saturated calomel reference electrode
E_a	Activation energy
ΔG	Gibb's energy difference
η	Overpotential
CV	Cyclic voltammetry
CA	Chronoamperometry
ATMO	Amorphous transition metal oxides
FTO	Fluorine-doped tin oxide
ITO	Indium-doped tin oxide
ATO	Antimony-doped tin oxide
GC	Glassy carbon
GF	Graphite foil
GR	Graphite rod
(R)RDE	(Rotating-)ring disk electrode
TOF	Turnover frequency
BSFC	$\text{Ba}_{0.5}\text{Sr}_{0.5}\text{Co}_{0.8}\text{Fe}_{0.2}\text{O}_{3-\delta}$
PBCO	$\text{PrBaCo}_2\text{O}_{5-\delta}$
Pi	0.1 M phosphate buffer pH 7
OER-PSII	Oxygen evolution complex – photosystem II
XAS	X-ray absorption spectroscopy
XANES	X-ray absorption near edge structure
EXAFS	Extended X-ray absorption fine structure
EQCM	Electrochemical quartz crystal microbalance
ICP-MS	Inductively coupled plasma mass spectrometry
OCP/OCV	Open-circuit potential/voltage
SEM	Scanning electronic microscopy
EIS	Electrochemical impedance spectroscopy
EDX	Energy dispersive X-ray spectroscopy

TEY	Total electron yield
FT	Fourier transform
i	Current
j	Current density
j_{\max}	Maximum current density
$E-iR/E-iR_u$	Potential corrected by the uncompensated resistance
R	Interatomic (atomic – backscatter) distance
N	Coordination (neighboring atoms) number
σ	Debye-Waller factor
HZB	Helmholtz-Zentrum Berlin
ERC	Electrode redox charge
Ery	Erythrite ($\text{Co}_3(\text{AsO}_4)_2 \cdot 8\text{H}_2\text{O}$)
$I_{\text{Ery}(020)}$	Integration of the Ery(020) reflection
CPR	Cobalt peak ration
XRD	X-ray diffraction
α	Charge transfer coefficient

Chapter 1. Introduction and motivation

Clean energy for all

The risks of climate change, such as extreme weather and the threat to human health and ecosystems worldwide, remain in the societal community's focus, and their consequences are scientifically well-documented.¹⁻³ One of the major links between climate change and the economy is energy production and consumption, including industrial manufacturing,⁴ transportation,⁵ and electricity production.⁶ The industrial and economic growth in the last century has had a significant impact on general energy consumption, which tends to increase over the years.⁷ Since energy (including electricity and transportation) is conventionally produced by burning fossil fuels, tremendous amounts of CO₂ are emitted daily to the atmosphere, enlarging climate change.⁷

In 2015, the General Assembly of the United Nations (UN) defined sustainable energy as the seventh of the 17 goals for "Transforming our world: the 2030 Agenda for Sustainable Development", namely "ensure access to affordable, reliable, sustainable and modern energy for all", which must be accomplished by 2030.⁸ One of the biggest challenges to achieving this goal is shifting the way energy is produced, from conventional to renewable sources. Solar-, wind-, and hydropower are typical sources for sustainable electricity production. For instance, approximately 100 000 TW of solar energy reaches the Earth's surface, meaning that one hour of solar energy is enough to supply the global human's energy needs for approximately one year.⁹ Big amounts of electricity can also be produced from other renewable sources, hydro or wind power. Even though large amounts of electricity can be generated from renewable sources, their fluctuating nature limits their use.

Renewable sources and energy storage

Unlike electricity produced from fossil fuels, renewable sources are vulnerable or dependent on weather conditions, year seasons, day-night and unpredictable factors, which results in fluctuating electricity production.¹⁰ Unfortunately, the maximum production peak of a specific source does not necessarily overlap the maximum consumption peak in electricity (rush hour). For instance, in Figure 1.1a, the graph compares the energy consumption in Germany with the

solar energy production in 2018. Whereas electricity consumption is the highest during winter (due to the poor natural light and the need for heating systems), solar energy production is the lowest of the year. A similar effect occurs within a day. Figure 1.1b shows the daily average electricity consumption and solar energy production during July 2018. Certainly, the highest solar energy production occurs during the day, like the highest electricity consumption. Yet, during the night, the electricity consumption continues, while the solar energy production drops to zero.

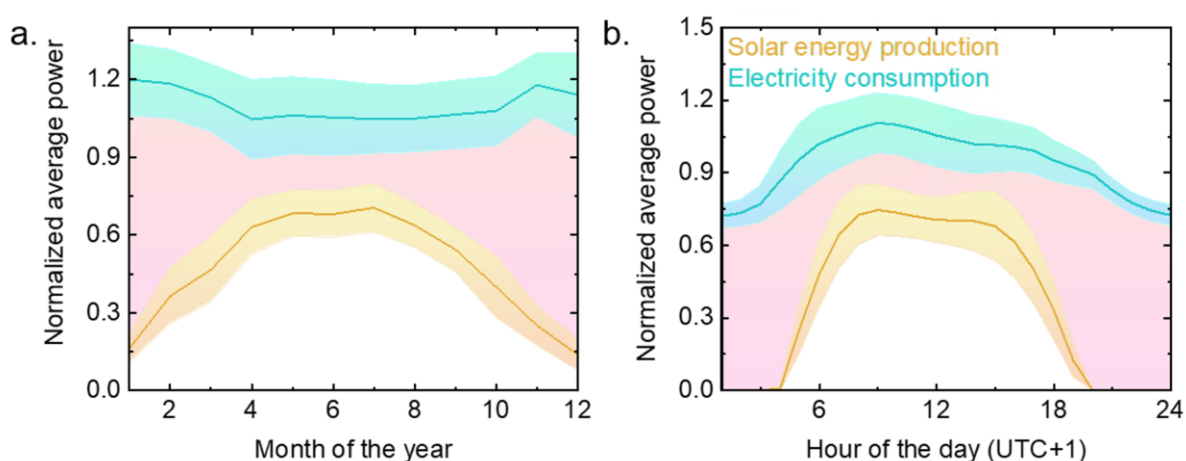


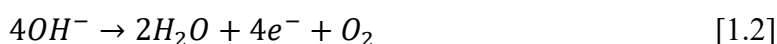
Figure 1.1. The normalized average power of solar energy production (yellow) and electricity consumption (green) of 2018 as a function of: **a.** Month of the year and **b.** Hour of the day. The average power was normalized by the average value between 1980–2018. The red area represents the consumed power that is not covered by solar energy and must be supplied by other sources. The light-colored areas represent the error. Data were obtained from reference.¹⁰

The fluctuating nature of renewable energies requires long-term energy storage methods. Therefore, the electricity excess of peak production can be stored to be eventually used when it is required. One of the most promising solutions is storing energy as chemical products of high energetic value. Thus, the excess energy can be stored in chemical bonds by producing chemical fuels, such as hydrogen or liquid hydrocarbons like methanol.⁹ Such fuels can be electrochemically produced by water splitting, which could, in principle, be CO₂-emissions free. However, a critical bottleneck in the overall process is the electrocatalytic water splitting itself, conformed by two half-reactions the hydrogen evolution reaction (HER) in cathode and the oxygen evolution reaction (OER) in the anode, where the latter is the most energetically demanding.¹¹

Chapter 2. Scientific context

Electrocatalytic oxygen evolution

The OER has significantly received major attention as a kinetically more sluggish process determining the overall performance of the reaction. The OER has a standard potential of 1.23 V vs. NHE (at pH 7, 25 °C and 1 atm) and produces oxygen, electrons, and either proton ions or water molecules, depending on the pH of the electrolyte, acid, near-neutral (equation 1.1) or alkaline (equation 1.2).¹²



The difference between the standard potential and the actual potential required to overtake the energy barrier of the OER is called overpotential (η) and it is dependent on the material used as an anode.¹³ Despite the apparent simplicity of the OER (equations 1 and 2), it is a complex multistep reaction of four electrons, implying slow kinetics. Therefore, η values are usually high, requiring large amounts of energy for the reaction to happen and making essential the use of an (electro)catalyst.

A catalyst is used to modify the reaction's kinetics, reducing the activation energy (E_a) by creating intermediate states (Figure 1.2a). The activation energy of the different steps depends on the used catalysts. In the case of an electrocatalyst, it biases the η of an electrochemical reaction; a catalyst with a lower overpotential requires less energy for the electrocatalytic reaction to happen (Figure 1.2b). Moreover, other factors like scaling relationships through intermediates¹⁴ and the η of electrochemical kinetics¹⁵ (described by the Butler Volmer equation, discussed in the next chapter) enhance the offset between the theoretical and experimental OER potentials. This offset is represented by the difference between the blue and orange line in Figure 1.2b.

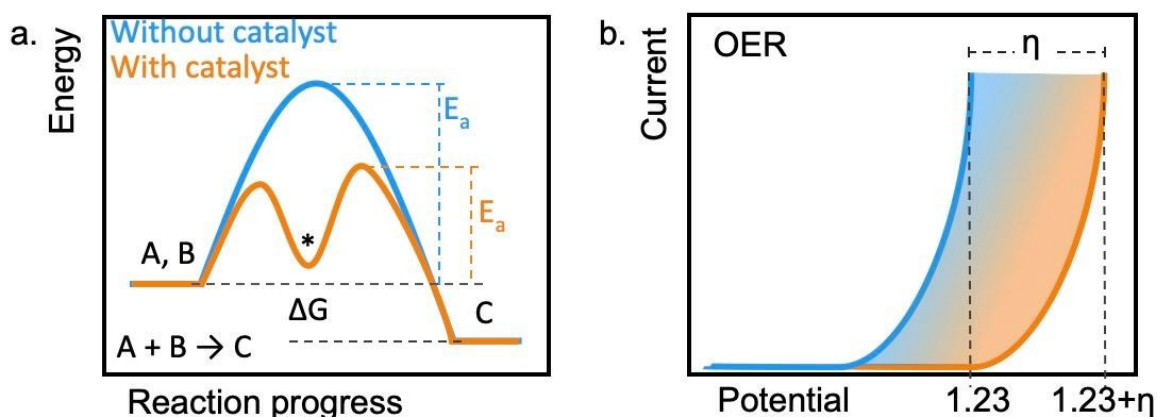


Figure 1.2. **a.** Diagram of energy as a function of reaction progress of a given chemical reaction ($A+B \rightarrow C$), which shows the difference between the reaction with (orange) and without (blue) catalyst. The asterisk (*) represents the formation of an intermediate. E_a represents the activation energy and ΔG the Gibbs energy difference, **b.** Diagram of current as a function of potential, which shows the difference between the reaction standard potential and potential with an electrocatalyst.

Catalytic reactions are conveniently studied as catalytic cycles, where the catalysts must remain unchanged before and after the catalytic reaction. Even though the catalyst can suffer changes during the catalytic cycle, the initial and final state must be the same, being this the concept itself of catalysis. In other words, the catalyst should remain unaffected after the catalytic reaction.¹⁶

Nevertheless, the final application of the OER includes the use of catalysts in electrolyzers and fuel cells, which are expected to operate under harsh conditions for long periods of time, leading to electrocatalysts aging, e.g., catalyst degradation (either superficially or bulky).

Activity, stability, and selectivity

The definition of good catalysis is not trivial, yet three pillars constitute the foundation of an (electro)catalyst,^{17,18} namely:

- Activity: efficient conversion rate from reactants to products.
- Stability: lack of change in activity over time.
- Selectivity: reaction direction to yield a particular product.

Whereas the focus of most of the research in the last two decades has been on discovering highly active materials or improving the catalytic activity of the already known electrocatalysts, stability and selectivity have been left as parameters of secondary importance.¹⁸ Stability is an essential parameter in the development of applications.¹⁶ Catalytic stability is herein defined as the absence of corrosion, erosion, or active sites blockage, and it can be electrochemically tracked over time using cyclic voltammetry (CV)¹⁹ or chronoamperometry (CA)²⁰ as changes in the produced current.²¹ The stability issues are commonly related to changes in the catalyst, such as degradation, corrosion, blockage of the active sites.^{16,21,22} It is important to note that mechanical issues, such as catalyst's detachment or erosion, would directly affect the catalytic current as well, yet the mechanical stability is not the scope of this thesis. Some of these changes can destabilize the produced current permanently by modifying the chemical structure of the catalyst (irreversible changes), yet some of these changes affect the catalyst's structure reversibly (reversible changes). The identification and deconvolution of the reversible changes from those irreversible are essential to gain insights into the stability requirements.²¹ For such a purpose, complementary techniques must be coupled to the electrochemical experiments to study possible changes occurring in the catalysts under catalytic conditions. Some of the complementary techniques include spectroscopy,^{23,24} microscopy,^{25,26} and diffraction-based techniques.^{27,28} Yet, many phases (like some oxides) lack crystallinity, which is a requirement for diffraction-based techniques, limiting their use.

The catalyst's structural changes previously mentioned can affect the catalytic current, which can be electrochemically tracked by cyclic voltammetry or chronoamperometry at a meaningfully applied potential. Besides the catalytic current, other parameters can be used to track the stability of a material, i.e., Tafel slope or turnover frequency (TOF).

The Tafel slope can be estimated as the overpotential as the function of the logarithmic current ($b = \partial E / \partial \log i$), thus its units are mV dec^{-1} . This parameter associates the kinetic current scaling with overpotential, in other words, the large increase in current due to a small increment in overpotential. Thanks to mechanistic consideration and kinetics studies, different Tafel slope values can be correlated with rate-limiting steps and surface intermediate coverage.^{29,30} For instance, the value of 60 mV dec^{-1} is associated with a chemical rate-limiting step with an electrochemical pre-equilibrium, whereas a value of 120 mV dec^{-1} is related to an electrochemical rate-limiting step. Values higher than 120 mV dec^{-1} are associated with a chemical limiting step or poor material conductivity.

The TOF is used to estimate the amount of product (oxygen molecules in the case of OER) per active site per time, thus its unit is s^{-1} . In OER, it is commonly reported as the number of

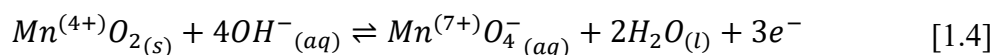
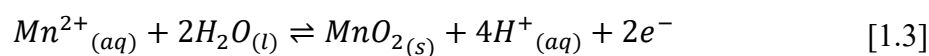
molecules of oxygen per active site per second. TOF values can be used to compare the catalytic performance of different catalysts at the same overpotential.

Deactivation

The instability of the catalytic material during oxygen evolution conditions is frequently labeled as degradation or deactivation.^{31,32} The material changes include the dissolution of anions or cations,^{22,33,34} morphological changes,^{35–37} and structural changes.^{38,39}

Thermodynamic considerations have shown that materials with a high content of oxygen atoms in the lattice (like oxides) are prone to degradation due to the instability of the oxygen anions, which results in the dissolution of anions and cations into the electrolyte.⁴⁰ Such anionic and cationic exchange have been observed during OER conditions in crystalline⁴¹ and amorphous materials.²³ The dissolution or exchange of ions from the catalyst into the electrolyte during OER has been associated with structural changes in the material, for instance, the oxidation of Mn in LiMn₂O₄ towards Mn⁴⁺ by losing of Li⁺ ions.³⁸

The deactivation of a material can be electrochemically detected by tracking the current density and overpotential, yet, identifying and understanding the material's changes require additional techniques. A clear example is the deactivation of Mn-based oxides, which has been related to the dissolution of Mn ions into the electrolyte. A convenient complementary technique is using an RRDE station to track the dissolution of Mn ions. The dissolution of Mn likely leads to the formation of permanganate as described by the equations 1.3 and 1.4 (where equation 1.3 is unlikely in alkaline media), these permanganate ions can be reduced at the ring with an applied potential of 1.2 V vs. RHE. Thus, the current collection in the ring is proportional to the amount of reduced permanganate.



Understanding the degradation mechanism is fundamental to design new catalysts or develop strategies to prevent deactivating structural changes.

Stabilization

Even though amorphous Co oxides are promising candidates as catalysts for OER in terms of their high catalytic activity, their current tends to destabilize over time. The destabilization has

been related to limitations in material conductivity.^{42,43} Mohammadi and collaborators⁴⁴ explored the limits of the self-healing properties in an amorphous Co oxide in near-neutral pH and concluded that even when the material is re-electrodeposited after its dissolution, the catalytic properties change over time, namely, a decrease in the TOF and an increase in the Tafel slope.

An approach recently used to tune the catalytic stability²⁰ of single oxides is the introduction of a second metal into the oxide structure. Such effect has been associated with an enrichment of the oxygen defects in the material structure and changes in the charge transfer resistance of the material.^{20,45} For instance, Li and collaborators²⁰ introduced Mn into the spinel structure of Co_3O_4 , obtaining Co_2MnO_4 , and compared the catalytic activity in acid media (pH 1 H_2SO_4) of both materials. Interestingly, the stabilization of the current was extended from 5 h in Co_3O_4 to 300 h in Co_2MnO_4 , which did not affect the current significantly or the chemical structure of the material, probed by XAS. However, the introduction of Mn into Co-based oxides might also affect the η by increasing it in some cases¹⁹ or decreasing it in other.^{46–48}

The development of new strategies for the stabilization of catalyst materials and insight into the origin of stabilization are essential for the durability of the OER electrocatalysts.

Activation

Besides the stabilization of catalysts under OER conditions, a step beyond is the activation of the catalytic current. In this case, the material is expected to suffer structural changes, which eventually have a beneficial impact on the catalytic activity, e.g., an η decrease or a current increase. Catalytic activation can happen either by enhancing the catalytic activity of each of the active sites or by increasing the number of accessible active sites.

Catalytic activation can occur by different methods, such as the formation of a new phase,³⁵ introduction⁴¹ or removal²⁷ of ions from the catalyst, or the formation of new material.⁴⁹ When this process occurs during an electrochemical process (typically catalysis itself), it may be called electrochemical restructuring.

Electrochemical restructuring

Whereas the electrochemical restructuring is frequently conceptualized as having a negative impact on the OER, numerous reports in the last years have shown an overall increase of the current after restructuring.^{41,49,50}

The degradation and the activation of materials may occur due to the electrochemical restructuring, meaning under oxygen evolution conditions. The restructuring of the catalyst can be tracked during the electrochemical experiment, e.g., series of CVs or CA. A constant increase in the cathodic area of the cycle is a clear indicator of structural changes in the catalyst. An example is the electrochemical restructuring of $\text{Ba}_{0.5}\text{Sr}_{0.5}\text{Co}_{0.8}\text{Fe}_{0.2}\text{O}_{3-\delta}$ (BSCF) during cyclic voltammetry, where the formation of a Co-based oxide was confirmed by XAS.⁵¹

Another possible indicator of electrochemical restructuring during oxygen evolution conditions is the variation of current density over time. For instance, the current density of Pak ($\text{Co}_3(\text{PO}_4)_2 \cdot 8\text{H}_2\text{O}$) increased during an applied potential ($E=1.76$ V vs. RHE) for 10 h.⁴⁹ The increase in the current was assigned to the amorphization of the material into a Co-based oxide (Figure 1.3), which owned a higher number of accessible active sites.

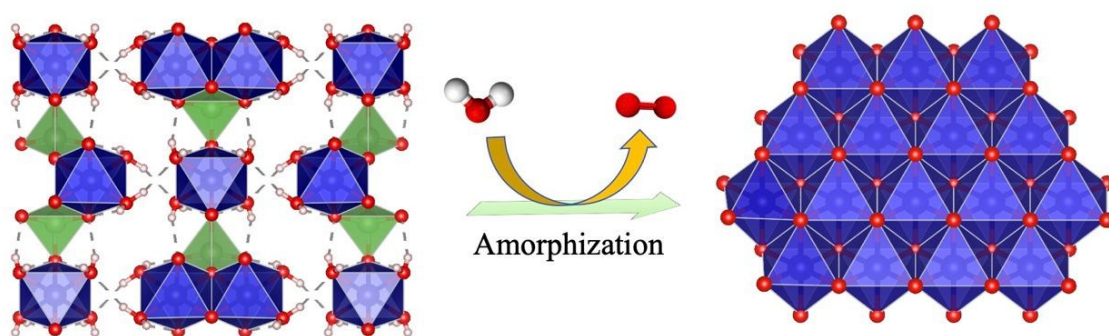


Figure 1.3. Diagram of the amorphization of Pak to an amorphous Co-based oxide during the oxygen evolution reaction.

Transition metal oxides for oxygen evolution

Amorphous transition metal oxides (ATMO) have received much attention in the last decades as electrocatalysts for OER. They own particularly high catalytic activity and are mostly stable in electrolytes with a pH above the near-neutral.⁵² They possess many advantages over the benchmark Ir- or Ru-based oxides in alkaline media, like their high activity, high stability, and low cost.⁵³

Mn-based oxides

Much attention has been focused on Mn-based oxides due to their low toxicity and great abundance on the Earth's crust. Mn oxides are commonly reported as bioinspired materials since the active site cluster in photosystem II consists of CaMn_4O_5 , which makes this kind of material scientifically interesting.^{54–56}

Mn owns rich redox chemistry, which allows different oxidation states to be stable in solid materials, from Mn^{2+} to Mn^{7+} . Thus, a wide range of different Mn-based oxides phases can be found depending on the pH and potential, as is shown by the Pourbaix diagram in Figure 1.4.

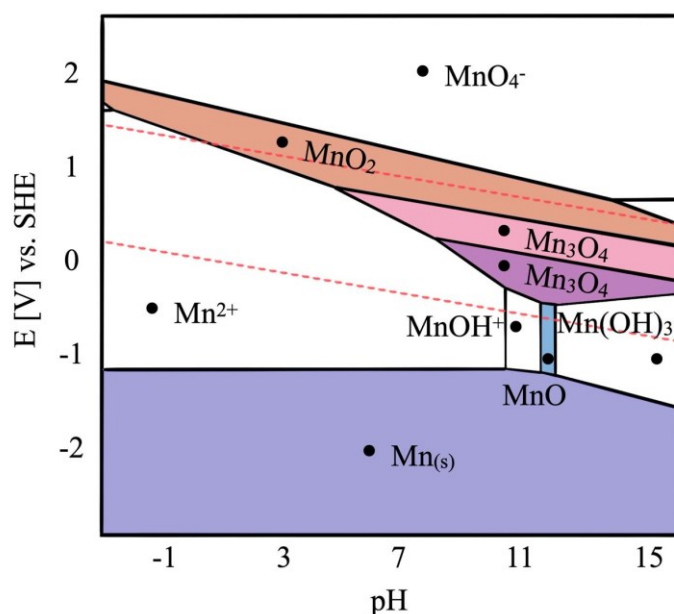


Figure 1.4. Pourbaix diagram, E vs. SHE as a function of pH, of a solution 1 mM Mn. The colored areas represent solid species whereas the white areas represent the aqueous ions. The dashed red lines show the stability limits of water in the system. The figure was adapted from The Materials Project.⁵⁷

As expected, in pH values under neutral, the Mn^{2+} ions are commonly found in solution. Yet, towards higher pH or potential values solid phases like Mn_2O_3 , MnO_2 and Mn_3O_4 are generated. Such variation of Mn-based oxide phases makes challenging the study of single-phase OER catalyst; minor changes in pH or potential can lead to the formation of a different phase. The OER catalytic activity of many single Mn-based oxides has been studied in the past years, yet the knowledge about degradation, stabilization, and activation processes in these materials is still limited and insufficient.

Numerous Mn-based materials can be found naturally, e.g., minerals, yet a common technique to obtain oxides used for OER catalysis is electrodeposition.⁵⁴ Some conditions of the electrodeposition method might vary, such as the substrate, the electrolyte, or the electrodeposition technique. Commonly used substrates are fluorine-doped/tin(IV)-alloyed indium(III) oxides (FTO/ITO)-covered glasses,^{58–61} which are useful for in-situ or postmortem spectroscopic techniques since they are semiconducting and transparent to most visible light. Carbon-based surfaces are also used as support material for the electrodeposited oxides, including glassy carbon (GC), graphite foil (GF), and graphite rods (GR), which are thermally stable⁵⁴ and can be used in rotating-ring disk electrode (RRDE) stations.^{27,62} Parameters, such as pH and dissolved ions, play an important role in the electrodeposition electrolyte. For instance, the pH-dependency was studied in electrolytes containing NO_3^- and PO_4^{3-} ions.⁶³ The results showed significant differences in the Tafel slope of the electrodeposited oxides, whereas in acid media (pH 2) the Tafel slope was quasi-infinite, in alkaline media (pH 12), it was about 60 mV dec^{-1} . Moreover, it was been shown that the presence of different anions in the electrodeposition electrolyte, including borate, phosphate, acetate, and sulfate, results in the formation of Mn-based oxides with different currents (at $\eta = 480 \text{ mV}$), where phosphate showed the highest current and sulfate the lowest.⁵⁴ Additionally, Mn-based electrodeposited in alkaline media and in KOH- or NaOH-based electrolytes have shown higher stability than those deposited in near-neutral pH or lower.^{63–65} Presumably, the high stability is due to the high redox stability (OH^- derives from water), high ionic strength, and high reactivity with protons.⁵⁴ Lastly, the formation of a more active Mn oxide was enhanced by the use of CV as the electrodeposition method in comparison to the potentiostatic electrodeposition that produced an inactive material.⁶⁶

As discussed previously, the electrolyte pH has an essential role in the stability study of Mn-based oxides, not only because of the phase chemical stability but also because of the species proportionation. A study of CV and UV-vis spectroscopy suggested that in neutral and acid pH values (pH 4–8) Mn^{3+} species present in the catalyst tend to disproportionate into Mn^{2+} and Mn^{4+} , whereas in alkaline pH (≥ 9) the comproportionation of Mn^{2+} and Mn^{4+} into Mn^{3+} is likely to happen.^{58,67} The discussion about the species responsible for the major OER catalytic activity is still under debate, some of the reports for different Mn-based oxides are summarized in the next paragraph.

Mn^{3+} -containing oxides have been reported with high catalytic activity in phases like $\alpha\text{-Mn}_2\text{O}_3$,⁶⁸ Mn_3O_4 ,⁶⁹ amorphous MnOx .⁶⁹ In alkaline media, $\alpha\text{-Mn}_2\text{O}_3$ was stable for at least

2 h, when the corrosion potential (1.7 V vs. RHE) was not exceeded. Even though the predominant oxidation state is Mn^{3+} , the catalytic activity was attributed to Mn^{4+} , which was formed reversibly at catalytic potentials.⁶⁸ Moreover, the Mn^{3+} sites have been reported to be the major catalytic contributors, having the disadvantage of not being highly stable, especially in near-neutral pH values.^{58,67} The high catalytic activity of the Mn^{3+} sites agrees with the activity descriptor proposed by Suntivich et al.,⁷⁰ in which a transition metal site with an e_g orbital occupancy close to the unit should present the highest catalytic activity. Octahedral Mn^{4+} -containing oxides have been reported as highly active but only in the presence of Mn^{3+} .^{71–74} In contrast, the material is rather inactive in the predominantly Mn^{4+} phases.⁵⁵ Lastly, the role of the tetrahedral Mn^{2+} sites (for instance in Mn_3O_4) is still not well understood, yet its dissolution is likely.⁶⁴ Systematic studies of the Mn oxidation state in oxides have shown that the lowest overpotential is obtained with an average oxidation state between 3.5+ and 3.7+,^{27,75–77} whereas the partial oxidation of the surface towards Mn^{4+} has been associated with deactivation processes,^{64,68} promoting the destabilization of the current.

Co-based oxides

Co-based oxides a promising candidate for OER catalysis since they own low overpotentials in a wide range of pH values from near-neutral media (overpotential around 400–490 mV)^{78–80} to alkaline media (overpotential around 320–450 mV).^{81–84} As in Mn-based oxides, numerous phases of Co-based oxide can be found depending on the pH and the potential, as it can be observed in Figure 1.5.

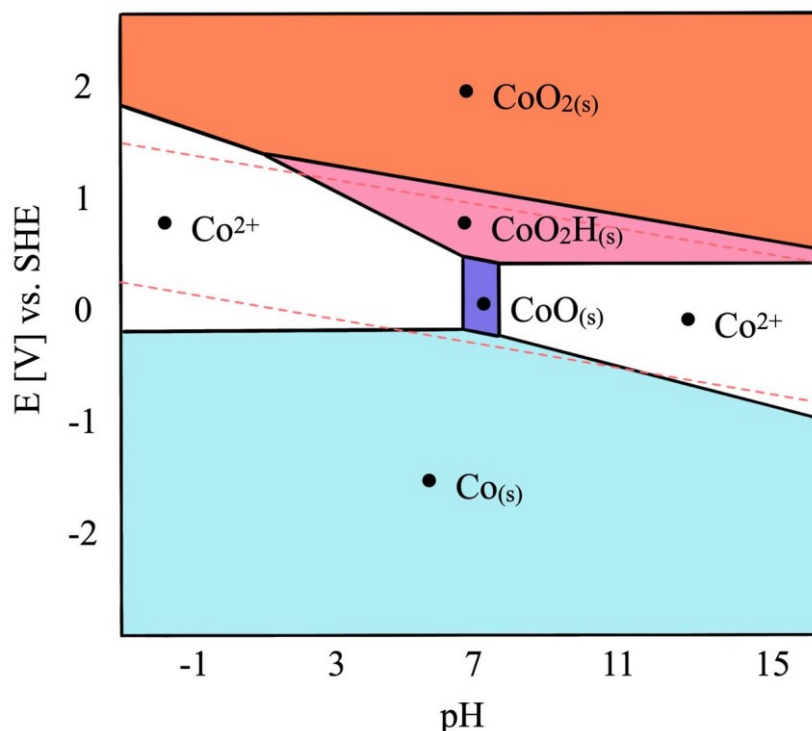


Figure 1.5. Pourbaix diagram, E vs. SHE as a function of pH, of a solution 1 mM Co. The colored areas represent solid species whereas the white areas represent the aqueous ions. The dashed red lines show the stability limits of water in the system. The figure was adapted from The Materials Project.⁵⁷

Among the Co-based oxides, the amorphous layered oxides own outstanding properties in near-neutral media, such as self-healing,^{85,86} and structural flexibility in terms of various oxidation states.^{87,88} Thus, the structural properties, as well as catalytic activity of the amorphous Co-based oxides, have been extensively studied in the last years. Consequently, electrochemical parameters such as Tafel slope, TOF and η are reported.^{23,49,78,82,84}

Generally, the Co-based oxides have shown a Co oxidation state between 2⁺ and 3⁺ at the resting state.^{89,90} Yet, the transition to higher oxidation states has been observed during cyclic voltammetry. The Co²⁺/Co³⁺ transition has been identified around 1.4 V vs. RHE, and the transition Co³⁺/Co⁴⁺ around 1.6 V vs. RHE.⁹¹ The transition of Co²⁺ to higher oxidation states at non-OER potentials suggests the 2⁺ oxidation state as not relevant for OER.⁹¹ On the other hand, Co³⁺ has been typically detected, not only at resting state but also at higher potentials, including OER potentials.^{91–93} Likewise, Co⁴⁺ has been observed at OER potentials, suggesting the need of Co⁴⁺ (and Co³⁺) for OER.^{91–96} However, the evidence correlating the Co⁴⁺ oxidation state with the evolution of oxygen is still scarce.

TOF of transition metal oxides

The stability and activity of Mn-based and Co-based oxides was previously described, yet the comparison between different catalysts is not trivial. As mentioned above, TOF is useful parameter to compare the catalytic performance of different materials at a selected potential. In other to compare the herein discussed materials with other OER typical catalysts (for instance, Ru-based oxides or photosystem II), TOF values of common OER catalysts are summarized as an example in Figure 1.6. Variations in the electrodeposition methods provoke a larger range of TOF values for the electrodeposited oxides. An interesting observation is the significantly higher TOF values of the mixed MnCo oxide in comparison to the single Co- or Mn-based oxides, indicating a beneficial effect in the kinetics of OER.

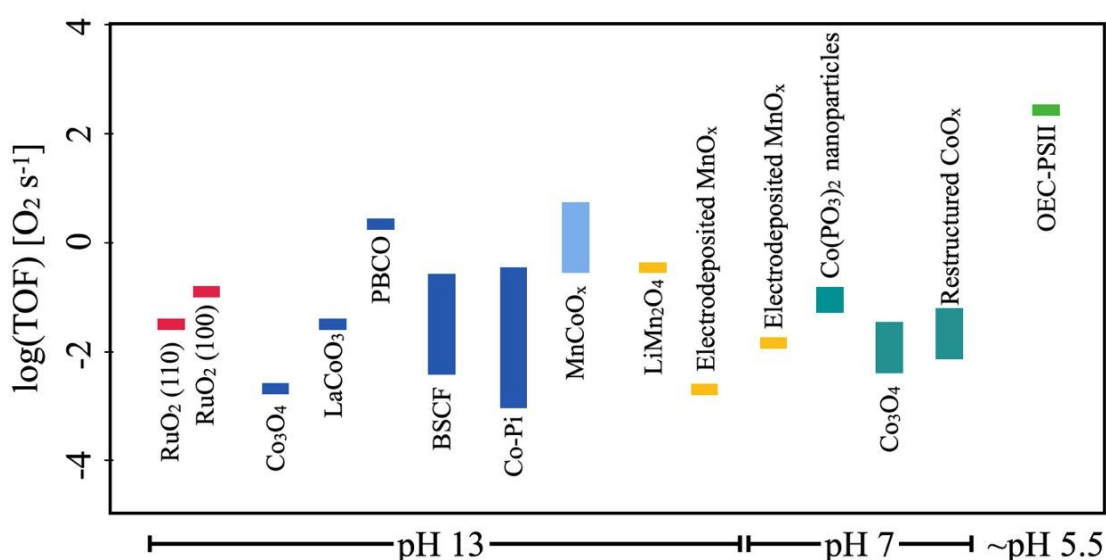


Figure 1.6. Turnover frequencies (TOF) of select oxides: thin-film surfaces of rutile RuO₂ (grown on MgO for the (110) and SrTiO₃ for the (100)).⁹⁷ Commercial Co₃O₄ powder,⁹⁸ LaCoO₃ (001) thin film (grown on Nb:SrTiO₃), PrBaCo₂O_{5+δ} powder (PBCO),⁸¹ Ba_{0.5}Sr_{0.5}Co_{0.8}Fe_{0.2}O_{3-δ} (BSCF, grown on La_{0.8}Sr_{0.2}MnO_{3-δ} on SrTiO₃),⁸³ electrodeposited cobalt hydroxide ("Co-Pi" or "CoCat"),^{82,99} layered hydroxide MnCoO_x (Mn:Co::1:1) was formed in pH 10 and drop-casted on GC,¹⁰⁰ the commercial LiMn₂O₄ was ink-casted on GC,²⁹ the MnO_x studied in KOH was electrodeposited in near-neutral pH on FTO glass,¹⁰¹ the MnO_x studied in neutral pH was electrodeposited in pH 6 on ITO glass,⁶⁶ the Co(PO₃)₂ was synthesized thermally at more than 350 °C and deposited on Ni foam,⁷⁹ the Co₃O₄ studied in pH 7 was synthesized by thermal methods at 165 °C and drop-casted on GC,⁸⁰ the

restructuringd CoOx was obtained by the amorphization of a Co-based crystalline material during CV in pH 7,⁴⁹ and the TOF of Mn₄Ca oxygen evolution complex of photosystem II (OEC-PS II) was calculated at 0.3 V overpotential and for membrane particles (pH ~5.5 in the lumen).¹⁰² All TOF values were estimated with an overpotential of about 300 mV. This figure was modified from reference with permissions of Royal Society of Chemistry.¹⁰³

As in Mn oxides, the Co oxides can be (electro-)deposited on different substrates depending on the necessity, such as FTO,^{23,78} ITO,^{49,90} GC.^{91,104} Yet, Co-based oxides are commonly obtained by electrodeposition in a pH-neutral Co²⁺-rich electrolyte (usually using Co(NO₃)₂ as a precursor).^{89,90} The electrodeposited oxide is conformed of Co-based oxide cluster with several Co atoms, the extension of the layers (number of Co atoms per cluster) depends on the electrodeposition conditions, e.g., the anions in the electrolyte.⁸⁸ A less common method to obtain amorphous Co oxides (and other ATMO) is from the electrochemical restructuring of a Co-based crystalline material.^{49,105} In the process, the original crystalline material is amorphized during the OER catalysis until an amorphous Co-based oxide is obtained. The properties of the final material depend on the initial crystalline material and the electrolyte where the restructuring process occurs.²³

Scope and organization of this thesis

The main scope of this thesis is to contribute to the field of the oxygen evolution reaction with Mn-based and Co-based catalysts, focusing on understanding the possible changes that the materials suffer after catalysis, increasing the stability of the materials, and using beneficially the material's restructuring. The topics herein are addressed with the aim of understanding better the degradation, stabilization, and activation processes of ATMO catalysis, thus with the desire of providing new insights for the future design of highly active and stable OER catalysts. To achieve this aim, three hypotheses are stated:

- The observed current decrease can be deconvoluted into reversible and irreversible changes in the catalyst.
- The stability of a Co-based electrocatalyst can be increased by the introduction of second metallic oxide into the oxide structure.
- The electrochemical restructuring during oxygen evolution conditions can be beneficially used to increase the current of a Co-based electrocatalyst.

The motivation of this work, the state-the-art, and the organization of this thesis are defined in this introduction (**Chapter 1 and 2**). The fundamentals of the techniques herein used are described in **Chapter 3**, including electrochemistry, X-ray absorption spectroscopy as well as data treatment. This description may facilitate the reader the understanding of the results obtained in the following chapters.

A new electrodeposition method in alkaline media for amorphous Mn oxides is reported in **Chapter 4**. The Mn oxide films were used to investigate catalytic current changes during cycling due to structural changes. The drop in the catalytic current was related to the oxidation of the near-surface region towards Mn^{4+} , probed by XAS. Yet, the catalytic current was partially recovered after a 30-minute OCP break, which indicates that some of the changes affecting the catalytic current are reversible.

The electrodeposition method was successfully extended to amorphous Co oxide and mixed CoMn oxide films in **Chapter 5**. As observed in the Mn oxide, the catalytic current of the Co oxide films decreased during cycling by about 30 %. After cycling, oxidation of the near-surface region towards Co^{3+} was observed by XAS. With the aim of stabilizing the catalytic current, Mn oxide was introduced into the Co oxide, forming $\text{Co}_{0.7}\text{Mn}_{0.3}\text{O}_x$. The initial catalytic current was lower in $\text{Co}_{0.7}\text{Mn}_{0.3}\text{O}_x$ than in CoO_x , yet it was stable during 100 cycles. The introduction of Mn oxide into the Co oxide stabilized the catalytic current during cyclic voltammetry. As expected, no significant structural changes were observed after catalysis. The stabilization was understood in terms of an increase in the conductivity and an optimization of the metal-oxygen binding energy.

The two first chapters are focused on gaining insights into degradation and stabilization by studying structural changes in the catalysts. In **Chapter 6**, the structural changes during catalysis are beneficially used to activate the current. For such purpose, a Co-based crystalline material (Ery) was synthesized and used as a model for the electrochemical investigation. The structural changes in Ery were tracked during 800 cycles in four different electrolytes (with same pH and same concentration). Ery was electrochemically restructuringd into an amorphous Co oxide, yet different restructuring rates were observed depending on the electrolyte. Interestingly, only in carbonate electrolyte, the current was activated (around 100 % in comparison to the initial state). This model indicated that three requirements are needed to obtain a beneficial electrochemical restructuring: high Co oxidation state, adequate cluster size, and a high number of Co redox sites.

Finally, the main conclusions and scientific insights of each of chapters 3-5 are summarized in **Chapter 7** in order to propose a main conclusion and the importance of these results. The still open questions are also mentioned to suggest the outlook of this research field.

References

- 1 Y. Dafermos, M. Nikolaidi and G. Galanis, *Ecol. Econ.*, 2018, **152**, 219–234.
- 2 R. C. Hale, M. E. Seeley, M. J. La Guardia, L. Mai and E. Y. Zeng, *J. Geophys. Res. Ocean.*, 2020, **125**, 1–40.
- 3 D. Kirikkaleli, H. Güngör and T. S. Adebayo, *Bus. Strateg. Environ.*, 2021, 1–15.
- 4 G. R. Mitchell, *Procedia Manuf.*, 2017, **12**, 298–306.
- 5 L. E. Erickson and M. Jennings, *AIMS Public Heal.*, 2017, **4**, 47–61.
- 6 J. Goldemberg, J. Martinez-Gomez, A. Sagar and K. R. Smith, *Environ. Res. Lett.*, 2018, **13**, 030201.
- 7 T. Ahmad and D. Zhang, *Energy Reports*, 2020, **6**, 1973–1991.
- 8 United Nations, 17 Goals to Transform Our World,
https://www.un.org/en/development/desa/population/migration/generalassembly/docs/globalcompact/A_RES_70_1_E.pdf.
- 9 Q. Schiermeier, J. Tollefson, T. Scully, A. Witze and O. Morton, *Nature*, 2008, **454**, 816–823.
- 10 D. Tong, D. J. Farnham, L. Duan, Q. Zhang, N. S. Lewis, K. Caldeira and S. J. Davis, *Nat. Commun.*, 2021, **12**, 1–12.
- 11 M. Risch, *Nat. Energy*, 2021, **6**, 576–577.
- 12 L. Gao, X. Cui, C. D. Sewell, J. Li and Z. Lin, *Chem. Soc. Rev.*, 2021, **50**, 8428–8469.
- 13 A. J. Bard and L. R. Faulkner, *Electrochemical methods and applications*, Wiley-Interscience, New York, London, 2nd ed., 2000.
- 14 I. C. Man, H. Y. Su, F. Calle-Vallejo, H. A. Hansen, J. I. Martínez, N. G. Inoglu, J. Kitchin, T. F. Jaramillo, J. K. Nørskov and J. Rossmeisl, *ChemCatChem*, 2011, **3**, 1159–1165.
- 15 D. A. García-Osorio, R. Jaimes, J. Vazquez-Arenas, R. H. Lara and J. Alvarez-Ramirez, *J. Electrochem. Soc.*, 2017, **164**, E3321–E3328.
- 16 F. Hess, B. M. Smarsly and H. Over, *Acc. Chem. Res.*, 2020, **53**, 380–389.
- 17 Y. Wang, X. Zheng and D. Wang, *Nano Res.*, 2022, **15**, 1730–1752.
- 18 J. Masa, C. Andronescu and W. Schuhmann, *Angew. Chemie - Int. Ed.*, 2020, **59**,

- 15298–15312.
- 19 I. Abidat, N. Bouchenafa-Saib, A. Habrioux, C. Comminges, C. Canaff, J. Rousseau, T. W. Napporn, D. Dambournet, O. Borkiewicz and K. B. Kokoh, *J. Mater. Chem. A*, 2015, **3**, 17433–17444.
 - 20 A. Li, S. Kong, C. Guo, H. Ooka, K. Adachi, D. Hashizume, Q. Jiang, H. Han, J. Xiao and R. Nakamura, *Nat. Catal.*, , DOI:10.1038/s41929-021-00732-9.
 - 21 S. Geiger, O. Kasian, A. M. Mingers, S. S. Nicley, K. Haenen, K. J. J. Mayrhofer and S. Cherevko, *ChemSusChem*, 2017, **10**, 4140–4143.
 - 22 S. Geiger, O. Kasian, M. Ledendecker, E. Pizzutilo, A. M. Mingers, W. T. Fu, O. Diaz-Morales, Z. Li, T. Oellers, L. Fruchter, A. Ludwig, K. J. J. Mayrhofer, M. T. M. Koper and S. Cherevko, *Nat. Catal.*, 2018, **1**, 508–515.
 - 23 J. Villalobos, D. González-Flores, K. Klingan, P. Chernev, P. Kubella, R. Urcuyo, C. Pasquini, M. R. Mohammadi, R. D. L. Smith, M. L. Montero and H. Dau, *Phys. Chem. Chem. Phys.*, 2019, **21**, 12485–12493.
 - 24 M. V. Abrashev, P. Chernev, P. Kubella, M. R. Mohammadi, C. Pasquini, H. Dau and I. Zaharieva, *J. Mater. Chem. A*, 2019, **7**, 17022–17036.
 - 25 G. Lole, V. Roddatis, U. Ross, M. Risch, T. Meyer, L. Rump, J. Geppert, G. Wartner, P. Blöchl and C. Jooss, *Commun. Mater.*, 2020, **1**, 68.
 - 26 J. Scholz, M. Risch, G. Wartner, C. Luderer, V. Roddatis and C. Jooss, *Catalysts*, 2017, **7**, 15–19.
 - 27 M. Baumung, F. Schönewald, T. Erichsen, C. A. Volkert and M. Risch, *Sustain. Energy Fuels*, 2019, **3**, 2218–2226.
 - 28 D. M. Morales, M. A. Kazakova, S. Dieckhöfer, A. G. Selyutin, G. V. Golubtsov, W. Schuhmann and J. Masa, *Adv. Funct. Mater.*, 2020, **30**, 1–12.
 - 29 L. Köhler, M. Ebrahimizadeh Abrishami, V. Roddatis, J. Geppert and M. Risch, *ChemSusChem*, 2017, **10**, 4479–4490.
 - 30 D. Antipin and M. Risch, *ChemRxiv. Cambridge Cambridge Open Engag.* 2021, , DOI:10.26434/chemrxiv-2021-hgbq6.
 - 31 C. Spöri, J. T. H. Kwan, A. Bonakdarpour, D. P. Wilkinson and P. Strasser, *Angew. Chemie - Int. Ed.*, 2017, **56**, 5994–6021.
 - 32 O. Kasian, S. Geiger, T. Li, J. P. Grote, K. Schweinar, S. Zhang, C. Scheu, D. Raabe, S. Cherevko, B. Gault and K. J. J. Mayrhofer, *Energy Environ. Sci.*, 2019, **12**, 3548–3555.
 - 33 I. Spanos, A. A. Auer, S. Neugebauer, X. Deng, H. Tüysüz and R. Schlögl, *ACS*

- Catal.*, 2017, **7**, 3768–3778.
- 34 S. Polani, K. E. Macarthur, M. Klingenhof, X. Wang, P. Paciok, L. Pan, Q. Feng, A. Kormányos, S. Cherevko, M. Heggen and P. Strasser, *ACS Catal.*, 2021, 11407–11415.
 - 35 A. Bergmann, E. Martinez-Moreno, D. Teschner, P. Chernev, M. Gliech, J. F. De Araújo, T. Reier, H. Dau and P. Strasser, *Nat. Commun.*, 2015, **6**, 8625.
 - 36 D. Chinnadurai, R. Rajendiran, O. L. Li and K. Prabakar, *Appl. Catal. B Environ.*, 2021, **292**, 120202.
 - 37 C. L. I. Flores and M. D. L. Balela, *J. Solid State Electrochem.*, 2020, **24**, 891–904.
 - 38 M. Baumung, L. Kollenbach, L. Xi and M. Risch, *ChemPhysChem*, 2019, **20**, 1–9.
 - 39 M. Görlin, M. Gliech, J. F. De Araújo, S. Dresch, A. Bergmann and P. Strasser, *Catal. Today*, 2016, **262**, 65–73.
 - 40 T. Binninger, R. Mohamed, K. Waltar, E. Fabbri, P. Levecque, R. Kötz and T. J. Schmidt, *Sci. Rep.*, 2015, **5**, 1–7.
 - 41 J. Wang, S. J. Kim, J. Liu, Y. Gao, S. Choi, J. Han, H. Shin, S. Jo, J. Kim, F. Ciucci, H. Kim, Q. Li, W. Yang, X. Long, S. Yang, S. P. Cho, K. H. Chae, M. G. Kim, H. Kim and J. Lim, *Nat. Catal.*, 2021, **4**, 212–222.
 - 42 H. Jin, J. Wang, D. Su, Z. Wei, Z. Pang and Y. Wang, *J. Am. Chem. Soc.*, 2015, **137**, 2688–2694.
 - 43 X. Li, Y. Sun, Q. Wu, H. Liu, W. Gu, X. Wang, Z. Cheng, Z. Fu and Y. Lu, *J. Am. Chem. Soc.*, 2019, **141**, 3121–3128.
 - 44 M. R. Mohammadi, S. Loos, P. Chernev, C. Pasquini, I. Zaharieva, D. González-Flores, P. Kubella, K. Klingan, R. D. L. Smith and H. Dau, *ACS Catal.*, 2020, **10**, 7990–7999.
 - 45 N. I. Kim, Y. J. Sa, T. S. Yoo, S. R. Choi, R. A. Afzal, T. Choi, Y. S. Seo, K. S. Lee, J. Y. Hwang, W. S. Choi, S. H. Joo and J. Y. Park, *Sci. Adv.*, 2018, **4**, eaap9360.
 - 46 T. Priamushko, R. Guillet-Nicolas, M. Yu, M. Doyle, C. Weidenthaler, H. Tuysüz and F. Kleitz, *ACS Appl. Energy Mater.*, 2020, **3**, 5597–5609.
 - 47 Y. Hu, H. Chen, X. Zhang, W. Wen, Q. He and C. He, *J. Phys. Chem. C*, 2019, **123**, 22130–22138.
 - 48 T. Maiyalagan, K. A. Jarvis, S. Therese, P. J. Ferreira and A. Manthiram, *Nat. Commun.*, 2014, **5**, 1–8.
 - 49 D. González-Flores, I. Sánchez, I. Zaharieva, K. Klingan, J. Heidkamp, P. Chernev, P. W. Menezes, M. Driess, H. Dau and M. L. Montero, *Angew. Chemie - Int. Ed.*, 2015,

- 54**, 2472–2476.
- 50 A. Indra, P. W. Menezes, N. R. Sahraie, A. Bergmann, C. Das, M. Tallarida, D. Schmeißer, P. Strasser and M. Driess, *J. Am. Chem. Soc.*, 2014, **136**, 17530–17536.
 - 51 M. Risch, A. Grimaud, K. J. May, K. A. Stoerzinger, T. J. Chen, A. N. Mansour and Y. Shao-Horn, *J. Phys. Chem. C*, 2013, **117**, 8628–8635.
 - 52 L. Zhang, Q. Fan, K. Li, S. Zhang and X. Ma, *Sustain. Energy Fuels*, 2020, **4**, 5417–5432.
 - 53 D. Zhou, P. Li, W. Xu, S. Jawaid, J. Mohammed-Ibrahim, W. Liu, Y. Kuang and X. Sun, *ChemNanoMat*, 2020, **6**, 336–355.
 - 54 J. Melder, P. Bogdanoff, I. Zaharieva, S. Fiechter, H. Dau and P. Kurz, *Z. Phys. Chem.*, 2020, **234**, 925–978.
 - 55 I. Zaharieva, D. González-Flores, B. Asfari, C. Pasquini, M. R. Mohammadi, K. Klingan, I. Zizak, S. Loos, P. Chernev and H. Dau, *Energy Environ. Sci.*, 2016, **9**, 2433–2443.
 - 56 M. M. Najafpour, S. Heidari, S. E. Balaghi, M. Hołyńska, M. H. Sadr, B. Soltani, M. Khatamian, A. W. Larkum and S. I. Allakhverdiev, *Biochim. Biophys. Acta - Bioenerg.*, 2017, **1858**, 156–174.
 - 57 A. Jain, S. P. Ong, G. Hautier, W. Chen, W. D. Richards, S. Dacek, S. Cholia, D. Gunter, D. Skinner, G. Ceder and K. A. Persson, *APL Mater.*, , DOI:10.1063/1.4812323.
 - 58 T. Takashima, K. Hashimoto and R. Nakamura, *J. Am. Chem. Soc.*, 2012, **134**, 1519–1527.
 - 59 Z. N. Zahran, E. A. Mohamed, T. Ohta and Y. Naruta, *ChemCatChem*, 2016, **8**, 532–535.
 - 60 F. Zhou, A. Izgorodin, R. K. Hocking, V. Armel, L. Spiccia and D. R. MacFarlane, *ChemSusChem*, 2013, **6**, 643–651.
 - 61 T. Takashima, K. Hashimoto and R. Nakamura, *J. Am. Chem. Soc.*, 2012, **134**, 18153–18156.
 - 62 J. Scholz, M. Risch, K. A. Stoerzinger, G. Wartner, Y. Shao-Horn and C. Jooss, *J. Phys. Chem. C*, 2016, **120**, 27746–27756.
 - 63 M. Huynh, D. K. Bediako and D. G. Nocera, *J. Am. Chem. Soc.*, 2014, **136**, 6002–6010.
 - 64 M. Rabe, C. Toparli, Y. H. Chen, O. Kasian, K. J. J. Mayrhofer and A. Erbe, *Phys. Chem. Chem. Phys.*, 2019, **21**, 10457–10469.

- 65 J. Melder, S. Mebs, P. A. Heizmann, R. Lang, H. Dau and P. Kurz, *J. Mater. Chem. A*, 2019, **7**, 25333–25346.
- 66 I. Zaharieva, P. Chernev, M. Risch, K. Klingan, M. Kohlhoff, A. Fischer and H. Dau, *Energy Environ. Sci.*, 2012, **5**, 7081–7089.
- 67 H. Ooka, T. Takashima, A. Yamaguchi, T. Hayashi and R. Nakamura, *Chem. Commun.*, 2017, **53**, 7149–7161.
- 68 M. Kölbach, S. Fiechter, R. van de Krol and P. Bogdanoff, *Catal. Today*, 2017, **290**, 2–9.
- 69 A. Ramírez, P. Hillebrand, D. Stellmach, M. M. May, P. Bogdanoff and S. Fiechter, *J. Phys. Chem. C*, 2014, **118**, 14073–14081.
- 70 J. Suntivich, K. J. May, H. A. Gasteiger, J. B. Goodenough and Y. Shao-horn, *Science*, 2011, **334**, 2010–2012.
- 71 Z. M. Chan, D. A. Kitchaev, J. N. Weker, C. Schnedermann, K. Lim, G. Ceder, W. Tumas, M. F. Toney and D. G. Nocera, *Proc. Natl. Acad. Sci. U. S. A.*, 2018, **115**, E5261–E5268.
- 72 Y. Surendranath, D. A. Lutterman, Y. Liu and D. G. Nocera, *J. Am. Chem. Soc.*, 2012, **134**, 6326–6336.
- 73 M. Khan, E. Suljoti, A. Singh, S. A. Bonke, T. Brandenburg, K. Atak, R. Golnak, L. Spiccia and E. F. Aziz, *J. Mater. Chem. A*, 2014, **2**, 18199–18203.
- 74 S. Raabe, D. Mierwaldt, J. Ciston, M. Uijtewaald, H. Stein, J. Hoffmann, Y. Zhu, P. Blöchl and C. Jooss, *Adv. Funct. Mater.*, 2012, **22**, 3378–3388.
- 75 M. Risch, K. A. Stoerzinger, B. Han, T. Z. Regier, D. Peak, S. Y. Sayed, C. Wei, Z. Xu and Y. Shao-Horn, *J. Phys. Chem. C*, 2017, **121**, 17682–17692.
- 76 M. F. Tesch, S. A. Bonke, T. E. Jones, M. N. Shaker, J. Xiao, K. Skorupska, R. Mom, J. Melder, P. Kurz, A. Knop-Gericke, R. Schlögl, R. K. Hocking and A. N. Simonov, *Angew. Chemie - Int. Ed.*, 2019, **58**, 3426–3432.
- 77 L. Xi, C. Schwanke, J. Xiao, F. F. Abdi, I. Zaharieva and K. M. Lange, *J. Phys. Chem. C*, 2017, **121**, 12003–12009.
- 78 Y. Surendranath, M. W. Kanan and D. G. Nocera, *J. Am. Chem. Soc.*, 2010, **132**, 16501–16509.
- 79 H. S. Ahn and T. D. Tilley, *Adv. Funct. Mater.*, 2013, **23**, 227–233.
- 80 L. Ma, S. F. Hung, L. Zhang, W. Cai, H. Bin Yang, H. M. Chen and B. Liu, *Ind. Eng. Chem. Res.*, 2018, **57**, 1441–1445.
- 81 A. Grimaud, K. J. May, C. E. Carlton, Y. L. Lee, M. Risch, W. T. Hong, J. Zhou and

- Y. Shao-Horn, *Nat. Commun.*, 2013, **4**, 1–7.
- 82 S. W. Lee, C. Carlton, M. Risch, Y. Surendranath, S. Chen, S. Furutsuki, A. Yamada, D. G. Nocera and Y. Shao-Horn, *J. Am. Chem. Soc.*, 2012, **134**, 16959–16962.
- 83 M. Risch, K. A. Stoerzinger, S. Maruyama, W. T. Hong, I. Takeuchi and Y. Shao-Horn, *J. Am. Chem. Soc.*, 2014, **136**, 5229–5232.
- 84 M. S. Burke, S. Zou, L. J. Enman, J. E. Kellon, C. A. Gabor, E. Pledger and S. W. Boettcher, *J. Phys. Chem. Lett.*, 2015, **6**, 3737–3742.
- 85 C. Costentin and D. G. Nocera, *Proc. Natl. Acad. Sci. U. S. A.*, 2017, **114**, 13380–13384.
- 86 D. A. Lutterman, Y. Surendranath and D. G. Nocera, 2009, 3838–3839.
- 87 P. W. Menezes, A. Indra, N. R. Sahraie, A. Bergmann, P. Strasser and M. Driess, *ChemSusChem*, 2015, **8**, 164–167.
- 88 M. Risch, K. Klingan, F. Ringleb, P. Chernev, I. Zaharieva, A. Fischer and H. Dau, *ChemSusChem*, 2012, **5**, 542–549.
- 89 M. Risch, V. Khare, I. Zaharleva, L. Gerencser, P. Chernev and H. Dau, *J. Am. Chem. Soc.*, 2009, **131**, 6936–6937.
- 90 M. W. Kanan, Y. Surendranath and D. G. Nocera, *Chem. Soc. Rev.*, 2009, **38**, 109–114.
- 91 M. Risch, F. Ringleb, M. Kohlhoff, P. Bogdanoff, P. Chernev, I. Zaharieva and H. Dau, *Energy Environ. Sci.*, 2015, **8**, 661–674.
- 92 H. Y. Wang, S. F. Hung, Y. Y. Hsu, L. Zhang, J. Miao, T. S. Chan, Q. Xiong and B. Liu, *J. Phys. Chem. Lett.*, 2016, **7**, 4847–4853.
- 93 J. Zhou, Y. Wang, X. Su, S. Gu, R. Liu, Y. Huang, S. Yan, J. Li and S. Zhang, *Energy Environ. Sci.*, 2019, **12**, 739–746.
- 94 E. C. M. Tse, T. T. H. Hoang, J. A. Varnell and A. A. Gewirth, *ACS Catal.*, 2016, **6**, 5706–5714.
- 95 M. W. Kanan, J. Yano, Y. Surendranath, M. Dincă, V. K. Yachandra and D. G. Nocera, *J. Am. Chem. Soc.*, 2010, **132**, 13692–13701.
- 96 J. G. McAlpin, Y. Surendranath, M. Dincă, T. A. Stich, S. A. Stoian, W. H. Casey, D. G. Nocera and R. D. Britt, *J. Am. Chem. Soc.*, 2010, **132**, 6882–6883.
- 97 K. A. Stoerzinger, L. Qiao, M. D. Biegalski and Y. Shao-Horn, *J. Phys. Chem. Lett.*, 2014, **5**, 1636–1641.
- 98 A. Grimaud, C. E. Carlton, M. Risch, W. T. Hong, K. J. May and Y. Shao-Horn, *J. Phys. Chem. C*, 2013, **117**, 25926–25932.

- 99 M. W. Kanan and D. G. Nocera, *Science*, 2008, **321**, 1072–1075.
- 100 F. Song and X. Hu, *J. Am. Chem. Soc.*, 2014, **136**, 16481–16484.
- 101 C. G. Morales-Guio, L. Liardet and X. Hu, *J. Am. Chem. Soc.*, 2016, **138**, 8946–8957.
- 102 H. Dau, C. Limberg, T. Reier, M. Risch, S. Roggan and P. Strasser, *ChemCatChem*, 2010, **2**, 724–761.
- 103 W. T. Hong, M. Risch, K. A. Stoerzinger, A. Grimaud, J. Suntivich and Y. Shao-Horn, *Energy Environ. Sci.*, 2015, **8**, 1404–1427.
- 104 A. Bergmann, T. E. Jones, E. Martinez Moreno, D. Teschner, P. Chernev, M. Gliech, T. Reier, H. Dau and P. Strasser, *Nat. Catal.*, 2018, **1**, 711–719.
- 105 M. Risch, A. Grimaud, K. J. May, K. A. Stoerzinger, T. J. Chen, A. N. Mansour and Y. Shao-Horn, *J. Phys. Chem. C*, 2013, **117**, 8628–8635.
- 106 S. Licht, *Anal. Chem.*, 1985, **57**, 514–519.
- 107 R. L. Doyle, I. J. Godwin, M. P. Brandon and M. E. G. Lyons, *Phys. Chem. Chem. Phys.*, 2013, **15**, 13737–13783.
- 108 F. Dalton, *Electrochem. Soc. Interface*, 2016, **25**, 50–59.
- 109 S. Veszteg, N. Barankai, P. Broekmann and H. Siegenthaler, *Electrochem. Comm.*, 2016, **68**, 54–58.
- 110 J. G. Vos and M. T. M. Koper, *J. Electroanal. Chem.*, 2019, **850**, 113363.
- 111 J. Scholz, M. Risch, K. A. Stoerzinger, G. Wartner, Y. Shao-Horn and C. Jooss, *J. Phys. Chem. C*, 2016, **120**, 27746–27756.
- 112 M. Newville, *Rev. Mineral. Geochemistry*, 2014, **78**, 33–74.
- 113 S. Calvin, *XAFS for Everyone*, 2013.
- 114 J. J. Rehr and R. C. Albers, *Rev. Mod. Phys.*, 2000, **72**, 621–654.
- 115 H. Dau, P. Liebisch and M. Haumann, *Anal. Bioanal. Chem.*, 2003, **376**, 562–583.
- 116 A. C. Thompson and D. Vaughan, *X-ray Data Booklet*, Lawrence Berkeley National Laboratory, Berkeley, 2nd editio., 2001.

Chapter 3. Methods

The purpose of this section is to familiarize the reader with most of the experimental techniques used to obtain the results herein exposed. Since the focus of this thesis is the OER, the techniques are described in terms and with examples of oxygen evolution. This chapter is organized into two main parts, one dedicated to the electrochemical techniques, where the catalytic properties of the materials are explored, and a second part dedicated to the characterization of the material, in which structural changes can be tracked. The details of the experimental conditions are specified in the experimental section of each of the results chapters.

Fundaments of electrocatalysis

The fundaments of electrocatalysis herein mentioned and explained are based on the textbook “Electrochemical methods and application” by A. Bard & L- Faulkner.¹³

Nernst equation

The potential of an electrochemical reaction strongly depends on the concentration of the redox pairs. This effect is given by the Nernst equation (equation 2.1).

$$E = E^0 + \frac{RT}{zF} \ln(Q) \quad [2.1]$$

Where, E represents the reduction potential, E^0 the standard potential, R the universal gas constant, T absolute temperature, z the ion charge (transferred electrons), F the Faraday constant and Q the reaction quotient. In an redox couple electrochemical reaction, Q is defined as the ratio between the chemical activities of the reduced (a_{red}) by the oxidized species (a_{ox}). The Nernst equation can be rewritten at room temperature (T=298 K), equation 2.2.

$$E = E^0 + \frac{0.059}{z} \log\left(\frac{a_{red}}{a_{ox}}\right) \quad [2.2]$$

This equation can be rewritten in terms of the OER (equation 1.1) to obtain equation 2.3. By aqueous and liquid species, the activity is considered, whereas by gases the pressure must be used. The species variables (activity or pressure) must be raised to the power of the coefficients. For instance, in equation 1.1, two molecules of water are used to produce four protons. Thus, in equation 2.3 the concentration of water and hydronium are elevated to the power of six and

four, respectively. Moreover, z is substituted by four, the numbers of electrons involved in the reaction.

$$E_{OER} = E^0 + \frac{0.059}{4} \log \left(\frac{(a_{H_3O^+})^4 p_{O_2}}{(a_{H_2O})^2} \right) \quad [2.3]$$

In an aqueous solution, as there is an excess of water, the activity is one by definition.¹⁰⁶ Likewise, the pressure of oxygen at ambient pressure can be assumed as $p(O_2)=1$ (if the pressure of oxygen differs, the term should be considered), resulting in equation 2.4.

$$E_{OER} = 1.23 + \frac{0.059}{4} \log((c_{H_3O^+})^4) \quad [2.4]$$

And since the concentration of protons is directly related to the pH ($pH = -\log(c_{H^+})$), the equation can be rewritten as equation 2.5.

$$E_{OER} = 1.23 - 0.059 \cdot pH \quad [2.5]$$

Thus, the potential of the oxygen evolution is thermodynamically dependent on the pH of the electrolyte (using the normal hydrogen electrode, NHE). Yet, other factors affect the kinetics of the reaction.

Butler-Volmer equation

The kinetics of reaction occurring on the electrode's surface strongly depends of the applied potential for all faradaic processes. Thus, the potential difference at the interface can be used to control reactivity.

As described in the previous chapter, the energy of reactants and products of a chemical reaction can be visualized as function of the reaction coordinate (Figure 1.2). Similarly, it occurs in electrochemical reactions. Yet, the energy of the surface and the electrode potential have an important effect, which disturbs the equilibrium of the electrochemical reaction, resulting in the electrochemical kinetics (where $\Delta G \neq 0$). The Butler-Volmer equation (equation 2.6) conveniently describes the dependency of the electrode current on the potential difference between the electrode and the bulk of the electrolyte (considering that both, the cathodic and anodic reactions occur on a single electrode).

$$j = j_0 \cdot \left\{ \exp \left[\frac{\alpha_a z F \eta}{RT} \right] - \exp \left[-\frac{\alpha_c z F \eta}{RT} \right] \right\} \quad [2.6]$$

Where, j represents the electrode current density, j_0 the exchange current density, T absolute temperature, z the numbers of electrons involved, F the Faraday constant, R the universal gas constant, η the activation overpotential (difference between electrode potential and equilibrium potential, $E - E_{eq}$), α_a and α_c the anodic and cathodic charge transfer coefficient, respectively.

Moreover, j_0 is defined as $j_0 = Fk^0C$, where F represents the Faraday constant, k^0 the reaction standard rate constant and C the reactant's bulk concentration (for a first reaction order).

There are two limiting cases of the Butler-Volmer equation. The first is at low overpotentials, so-called polarization resistance, where the equation is oversimplified since $E \approx E_{eq}$. The second case is at very high overpotentials (where $E \approx E_{eq} \gg 0$ or $E \approx E_{eq} \ll 0$, $|\eta| > 0.1$ V), and the equation is simplified to the Tafel equation.

Tafel equation

For large values of η , either positive or negative, one of the terms in equation 2.6 becomes negligible. For instance, at a very negative overpotential: $\exp\left[-\frac{\alpha_c z F \eta}{RT}\right] \ll \exp\left[\frac{\alpha_a z F \eta}{RT}\right]$, and the Butler-Volmer equation becomes equation 2.7, which can be rewritten as equation 2.8.

$$j = j_0 \cdot e^{\frac{-\alpha z F \eta}{RT}} \quad [2.7]$$

$$\eta = \frac{RT}{\alpha z F} \ln(j_0) - \frac{RT}{\alpha z F} \ln(j) \quad [2.8]$$

Yet, the simplification is applicable only if the counter reaction's (anodic reaction in reduction process, or cathodic reaction in an oxidation process) is negligible (less than 1 %). If this is not the case, the system will approach the mass-transfer limited current by the time the overpotential is established. Thus, Tafel relationships cannot be observed since they require the absence of mass-transfer effects on the current. In contrary, when the electrode kinetics are sluggish and significantly higher overpotentials are required (like in OER), good Tafel relationships can be observed.

Consequently, a Tafel plot can be constructed if logarithm of j is plotted as a function of η . The slope of the linear fit of this plot can be represented as $\frac{-\alpha z F}{2.3 RT}$. However, the linearity behavior sharply deviates as η approaches zero since counter reactions cannot be neglected.

In terms of an electrocatalyst, the Tafel slope does not depend on the amount of catalytic material or the number of active sites, thus it is a useful parameter to compare different electrocatalysts or conditions of the same reaction. A vast number of Tafel slope values can be found in literature for different materials, reactions and conditions. For instance, in OER a value of 60 mV dec⁻¹ is assigned to a chemical rate-limiting step with an electrochemical pre-equilibrium. Whereas a value of 120 mV dec⁻¹ is associated with an electrochemical rate-limiting step, and a value much greater than 120 mV dec⁻¹ is related to a chemical limiting step or poor material conductivity.¹⁰⁷

Rotating-ring disk electrode

The rotating-ring disk electrode (RRDE) is a useful technique for the study of two electrochemical reactions occurring simultaneously; one reaction is carried on at the disk and another at the ring, while the setup rotates. This technique is based on the principle of forced convection of the electrolyte in the electrochemical cell, thus mass (such as ions or molecules) is transported through the solution from the first reaction spot to the second.¹⁰⁸

A common experimental setup is CV series occurring at the disk and CA occurring at the ring. Thus, the ions or molecules produced during the CV can be transported to the ring to be detected as an electrochemical response. It is important to note that the convection of ions (or molecules) has a direct impact on the electrochemical response, therefore, it is influenced by the local concentration of these species. A meaningful example is the detection of oxygen at the ring produced from an OER occurring at the disk (Figure 2.1). The setup is conformed of a glassy carbon rod as the disk and a Pt ring, both are separated by a Teflon sleeve. The glassy carbon was coated with catalyst and series of CV are applied. The Pt ring performs a CA, in which the applied potential can reduced the O_2 molecules produced by the disk,¹⁰⁹ where oxygen detection is limited by diffusion. The rotation of the setup causes a laminar flow of the electrolyte and thus, a continuous mass transport.

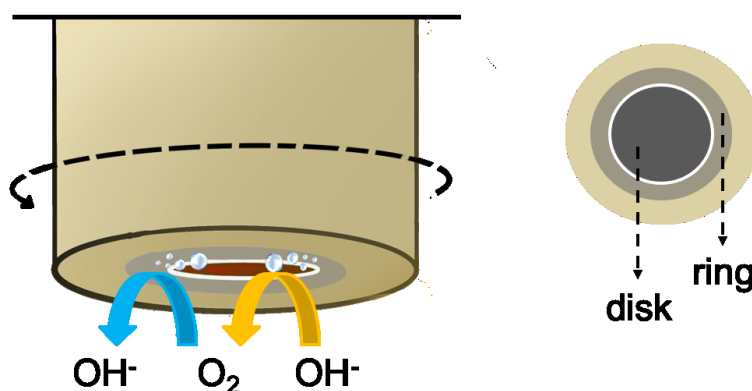


Figure 2.1. Diagram of the mass transport in an RRDE of the O_2 product of OER reaction in alkaline media. The disk evolves oxygen molecules which are transported, assisted by the laminar flow, to the ring to be reduced. A transversal view of the RRDE is shown on the right side, indicating the disk and ring layout.

An advantage of the RRDE setup is that the oxygen evolved by the disk can be quantitatively detected as an electrochemical signal in the ring. Nonetheless, only one portion of the products

generated by the disk can be collected by the ring. This fraction is called collection efficiency and it is estimated as the ratio between the limiting current at the ring and the limiting current of the disk.¹¹⁰ Yet, this estimation requires a collection efficiency factor, which depends on the geometry of the disk and ring electrodes, and on the roughness of the catalytic film. In the case of OER, the produced oxygen owns a low solubility in water, generating oxygen bubbles easily. The formation of bubbles leads to troubles at the ring since the bubbles tend to escape from the electrolyte and cannot be detected.

Besides the oxygen evolution, other reactions might occur at the disk, such as competitive reactions or redox reactions in the catalysts, which complicate an exact approximation of the onset of the OER in three-electrode electrochemical cells. Yet, another helpful advantage of RRDE is that an estimation of the onset potential of the OER can be obtained as the current at the ring starts to increase.¹¹¹ This rough estimation can be defined as current density that significantly differs from the noise of the measurement. A typical electrochemical setting for a RRDE experiment is shown in Figure 2.2a, where the potential is swept in a range while a single potential step is applied at the ring. The signal obtained for an actual experiment of oxygen detection is shown in Figure 2.2b, where both, ring and disk, currents increase as oxygen evolved. The disk shows the oxidation of OH^- ions to O_2 , whereas the ring shows the reduction of O_2 to OH^- ions.

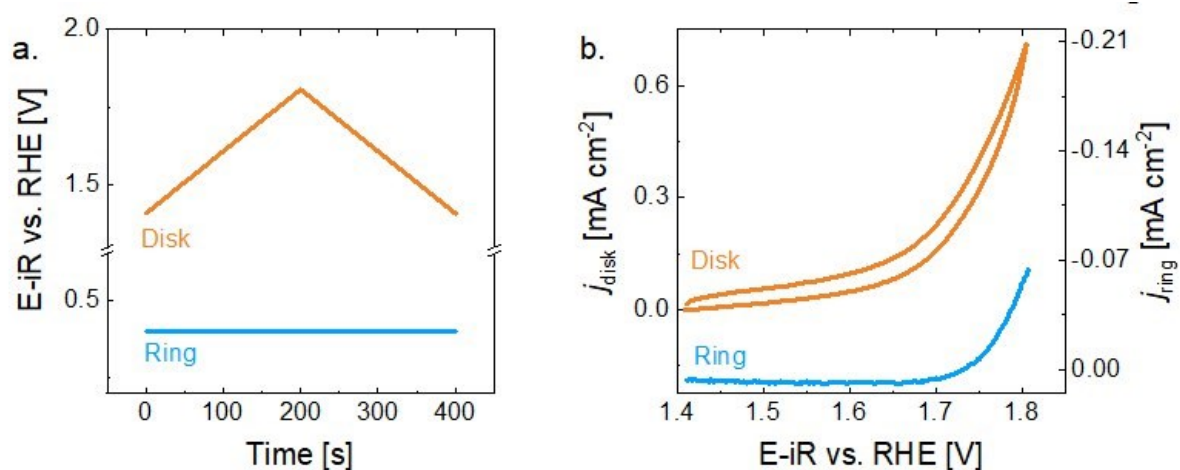


Figure 2.2. **a.** Applied potential at the disk and the ring as a function of time for one cycle in a CV experiment, **b.** CV experiment at the disk collected on an Mn oxide-covered glassy carbon rod and CA experiment at the Pt ring, in a 0.1 M NaOH Ar-purged solution with 1600 rpm of rotation.

X-ray absorption spectroscopy

The descriptions and explanations of x-ray absorption spectroscopy are based on reference materials.^{112–115}

The absorption of X-rays occurs when X-ray radiation of equal or higher energy to the binding energy of a core electron hits a given atom. The quantized nature of such transition results in a sharp absorption as a function of energy, which is called edge. The edge of an atom is given according to the principal quantum number ($n=1,2,3\dots$). For instance, the K-edge is related to the transitions of the 1s orbital, whereas the L-edge to 2s and 2p (Figure 2.3). A dipole forbidden transition results in a small feature at lower energy than the edge, such feature is called pre-edge. The pre-edge is useful to obtain information about the symmetry of the studied atom.

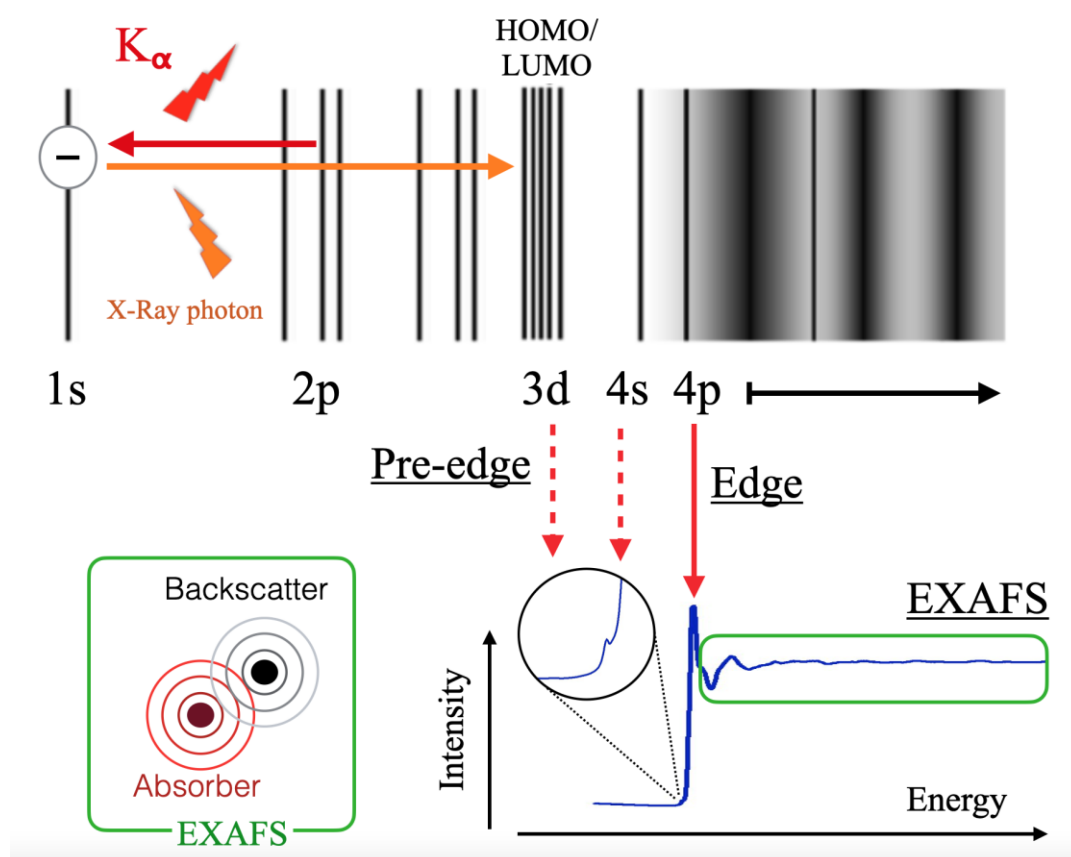


Figure 2.3. Diagram of the X-Ray absorption K edge of a transition metal. K_{α} represents the emitted fluorescence resulting from the relaxation of a 2p electron into a core-hole effect. The dotted red arrows represent the dipole and parity forbidden transitions ($1s \rightarrow 3d$), which conforms the pre-edge. The solid red arrow represents the transition $1s \rightarrow 4p$, forming the edge. At high enough energy the photoelectron may leave the atom and be backscattered by the

surrounding atoms, generating the EXAFS effect. The EXAFS phenomenon is highlighted in green boxes.

The pre-edge, the edge, and about 20 eV further constitute the X-ray near edge structure (XANES), which contains vast information about the oxidation state, coordination sphere, and structure of the scattering atom. All this information is encoded in the position and shape of the XANES spectrum. Usually, the experimentally measured spectra are compared to reference measured spectra of samples with well-known chemical structures, oxidation state, and coordination sphere.

The energy of the incidence X-rays can be further increased after the edge and the 1s electrons can be expelled from the scatter atom, generating a photoelectron. The emitted wave is subsequently scattered by the surrounding atoms, resulting in constructive and destructive interference between the emitted and the scattered waves. The amplitude of such interference is modulated depending on how the scanning energy affects the wavelength of the scattered photoelectron. Thus, the scattering effect depends not only on the absorber atom but also on the nature of the surrounding (scattering) atoms. As a result of the scanned energy after the edge, an oscillatory pattern is obtained, which is called extended X-ray absorption fine structure (EXAFS). The obtained spectrum provides useful information about neighboring atoms around the main scatter atoms, such as the identity of the atoms, distance to the absorber atom, and the number of them.

An EXAFS pattern must be modeled to obtain this information, in which the contribution from different scatters at certain distances are added as shells. In this way, each shell contributes to the whole spectrum by adding scattering events. The modeling of these events is described by the EXAFS equation (Equation 2).

$$\chi(k) = S_0^2 \cdot \sum_i^{n_{shell}} A(R_i, k)_i \cdot N_i \cdot e^{-2\sigma_i^2 \cdot k^2} \cdot \sin(2k \cdot R_i + \phi_i) \quad [3.9]$$

where, S_0^2 represents the amplitude reduction factor, $A(R_i, k)_i$ the scattering amplitude for the i -shell, k the photoelectron wave-vector, N_i the coordination number or degeneracy, σ_i the Debye-Waller parameter, R_i the half path length or distance between absorber and scatter and ϕ_i the phase shift.

The scattering function depends on the distance R between the scatterer and the absorber and the photoelectron energy. When the photoelectron is scattered, it suffers a phase shift due to

the direction change and the interaction with potential fields from other atoms. The degeneracy, N , relates to the number of scatters at a specific distance. The distance to a given scatterer differs slightly among the different atoms due (among others) to a structural component and thermal effects, resulting in a distribution of similar distances. This distribution is represented by the Debye-Waller factor. Commonly, the variable is associated with the disorder of the material.

The structural information from the EXAFS spectra can be more easily visualized if the data is converted from the energy to the space domain by a Fourier transform. In this way, the neighboring atoms are observed as peaks in the space domain. Each peak contains the information about the identity of the neighboring atom, the distance with the absorber atom, the number of them and the distribution of similar distances.

Treatment of the data

The data treatment differs slightly depending on the beamline station and on the needs of specific sets of data. Herein, the data treatment is described based on fluorescence files obtained from the beamline station KMC-3 in BESSY II.

The measurements contain information from four ionization chambers, namely: I_{00} , I_0 , I_1 , and I_2 . The arrangement of these ionization chambers can be observed in Figure 2.4. In the case of I_{00} , it is a set-up before the other chambers, used by the beamline to control the intensity and calibration of the beam. The fluorescence signal is recorded by a detector with 13 elements, meaning 13 spectra per measurement. The in-coming rate (ICR) corresponds to all fluorescence counts collected by each of the elements, whereas the fluorescence signal (commonly abbreviated as Fluo) corresponds to a selected window of Ka emissions, corresponding to the metal of interest (Figure 2.5a).

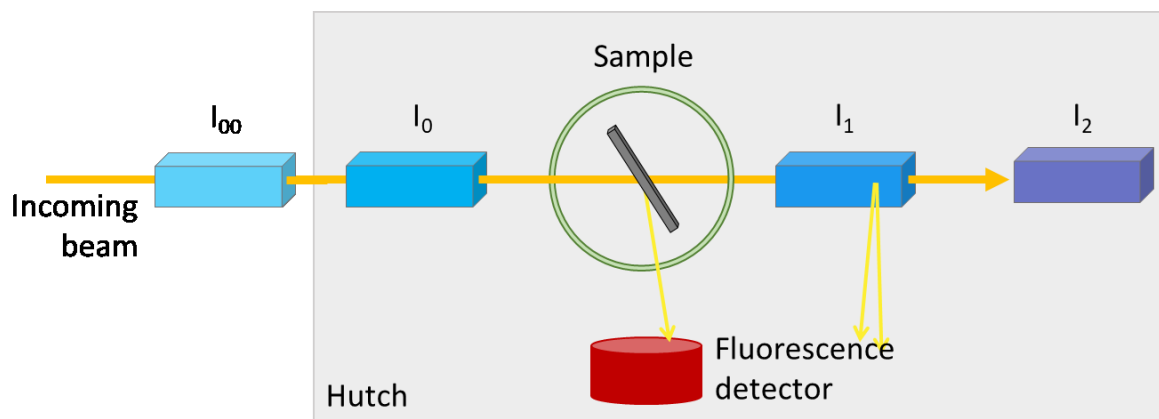


Figure 2.4. Diagram of the basic setup for XAS measurements collection. The ionization chambers are represented as I_{00} , I_0 , I_1 , and I_2 . The sample is placed in the sample holder in a 45° position. The gray background represents the hutch.

After collection the spectra at the beamline station, the data must be treated with a series of steps to facilitate its analysis. The treatment depends on the quality and type of data collected, yet, some typical applied treatments are dead time correction, calibration of the absorption, energy calibration, background subtraction and post-edge normalization.

Dead time correction. Energy resolving detectors collect photons to be analyzed. Thus, there is a dynamic range. This range can be oversaturated when too many photons reach the detector and cannot be analyzed, leading to a nonlinear behavior between the fluorescence and the ICR. The effect in the photocounts can be corrected by the non-detected photons due to the dead time of the detector. The out-coming range (OCR) is corrected using an exponential fit from the ICR values (equation 2.10), thus a calibration curve is obtained by measuring time scans at a fixed energy for the corresponding shaping time of the 13-element detector.

$$OCR = A \cdot (1 - e^{-k \cdot ICR}) \quad [2.10]$$

Calibration of the absorption. Using the Beer-Lambert law, the absorbance of an absorbing layer, e.g., sample, can be estimated by the beam intensity (BI) passing by position zero and one. The Beer-Lambert law postulates the linear relationship between the absorbance of monochromatic light and the concentration of an absorbing layer (equation 1.11). Therefore, the fluorescence counts intensity can be converted to absorbance by the equation 2.12, using the intensity of the ion chamber zero and one. The fluorescence signal must be normalized by I_0 , to remove possible variations or abnormalities in the incoming beam (Figure 2.7a).

$$A = \log \left(\frac{BI_0}{BI_1} \right) \quad [2.12]$$

$$A_1 = -\log \left(\frac{I_1}{I_0} \right) \quad [2.12]$$

Energy calibration. the change in the settings of the beamline can cause variation in the radiation calibration, thus it is recommended to perform energy calibration as frequent as reasonable not no later than after changing the edge. For such a purpose, the spectrum of a standard metallic foil (of the metal of interest) must be collected. Then, the derivative of A_2 , A_2' , must be calculated and plotted. The first peak (coming from the first inflection point) of A_2' is fitted, e.g., with a Gaussian function. The maximum of the peak represents the energy value of the edge, which must be compared and shifted with values reported in the literature¹¹⁶ (Figure 2.5d). Finally, all experimental data must be shifted in the energy axis as the reference.

Background subtraction. The region before the edge rising must be subtracted to remove the background signal (Figure 2.5b). Commonly, a constant or a linear function creates a good fit. A good fit should not affect the oscillations of the spectrum after the edge and the slope of the fit should be similar to the one of the data after the edge. After this step, the files of a sample can be averaged into a single spectrum.

Post-edge normalization. Once the background has been subtracted, a normalization to 1 must be perform after the edge rising (Figure 2.6c), as a division by an equation. Polynomial equation of order 1, 2 or 3 can be used depending on the quality of the data. A common approach is to use the lowest order possible. A good fit should not affect the oscillations of the spectrum and it is expected that the slopes of the fit and the background are similar. After this step, this data can be used to estimate the edge energy and the XANES spectra can be compared.

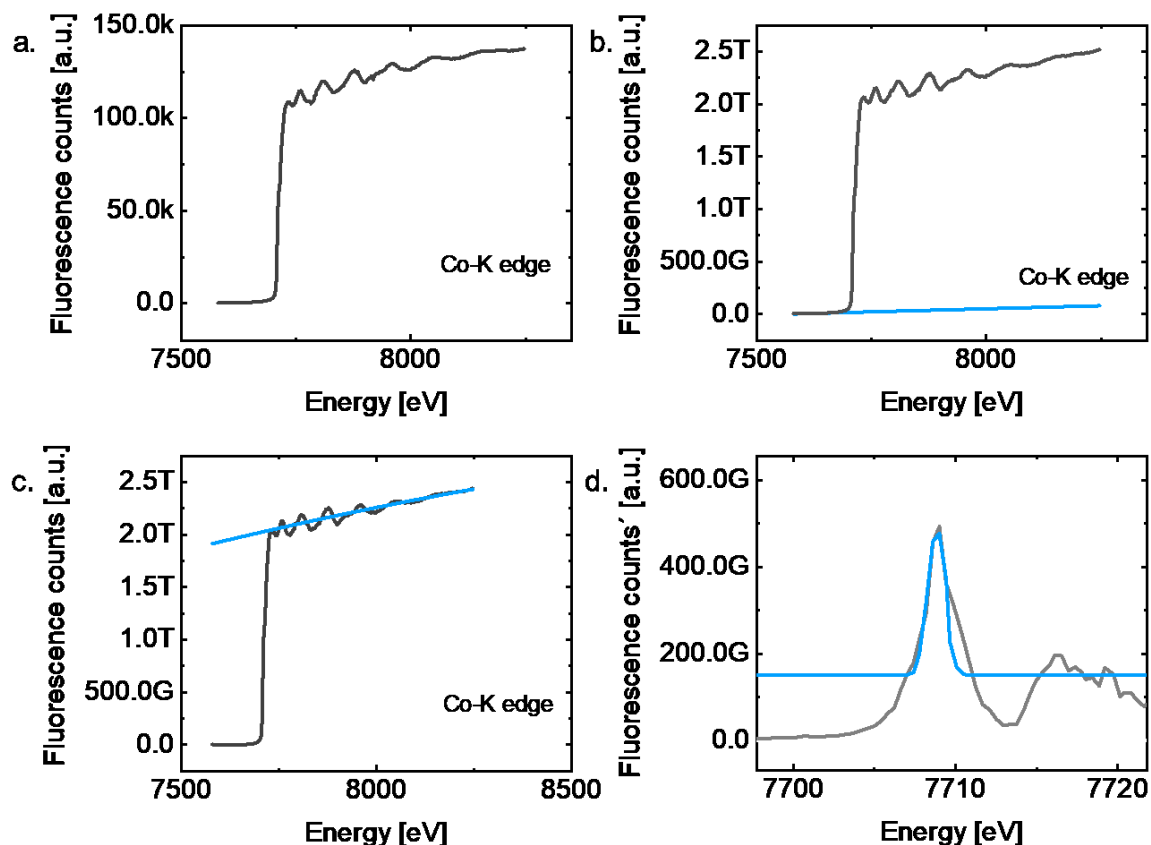


Figure 2.5. **a.** Untreated Co-K edge fluorescence spectrum collected on a metallic Co foil, **b.** Background subtraction of the Co-K edge spectrum with a straight line (blue line) in the region before the edge rising, **c.** Normalization of the Co-K edge spectrum to 1 by a polynomial equation of first order, **d.** Definition of the edge energy of the Co foil for energy calibration by the derivative of the absorption spectrum.

Estimation of the oxidation state

A typical approach is using XANES spectra to estimate the oxidation state of the metal in a material. Specifically, the edge energy can be used since it depends on the oxidation state of the metal and the nature of the ligands. For such a purpose, a calibration curve must be constructed using reference compounds with a similar coordination sphere, e.g., ligands and geometry. An example of this approach is shown in Figure 2.5, where a group of Co-based oxides is used to build a calibration curve. The average oxidation state of the absorber atom (Co) is obtained from the XANES spectra (Figure 2.5a). Once the energy has been calibrated (see below) and the data has been normalized, the edge position can be estimated. The accuracy of the oxidation state will depend on the quality and purity of the references used. The integral

method can be used, in which a step integral function (equation 4) estimates the energy position of the edge.

$$E^{edge} = E_1 + \frac{1}{\mu_2 - \mu_1} \int_{E_1}^{E_2} \mu_2 - \tilde{\mu}(E) dE \quad [2.13]$$

where, $\tilde{\mu}(E) = \begin{cases} \mu_1 & \text{for } \mu(E) < \mu \\ \mu_2 & \text{for } \mu(E) > \mu_1 \\ \mu(E) & \text{else} \end{cases}$, by setting the limits as $\mu_1=0.15$ and $\mu_2=1.0$, The first

value is chosen to prevent an effect of the pre-edge feature in the estimation of E^{edge} . The second value is chosen to ensure that the E^{edge} is not strongly affected by the amplitude of the “edge-peak”. The integral step is illustrated in Figure 2.6.

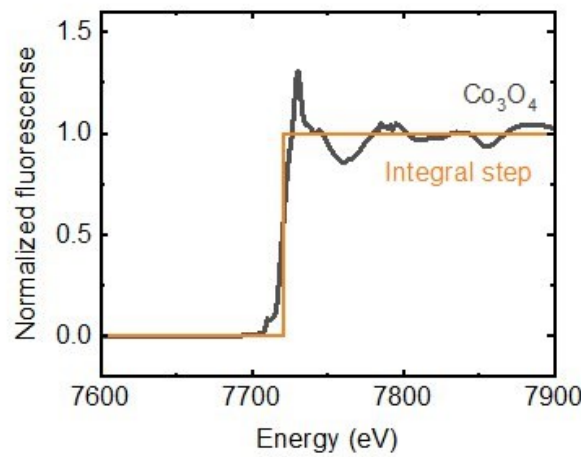


Figure 2.6. Illustration of the step function used to determine the edge position in a Co_3O_4 powder, used as a reference.

The edge position of the measured experimental spectra must be compared to a set of measured reference spectra. At least, three well-known reference samples with different oxidation states should be measured to build a calibration curve (Figure 2.7a), in which the measured samples can be interpolated. The calibration curve of the Co K-edge is presented as an example (Figure 2.7b), where $\text{Co}^{(2+)}\text{O}$, $\text{Co}_3^{(2.7+)}\text{O}_4$ and $\text{LiCo}^{(3+)}\text{O}_2$ are used as references. In this case, the calibration curve includes Co average oxidation states from 2+ to 3+, therefore, Co-based oxide samples can be interpolated to estimate the oxidation state. The accuracy of the results depends on the linear fitting of the calibration curve and it can be estimated using the root mean square of the difference between the input references oxidation states and the estimated ones.

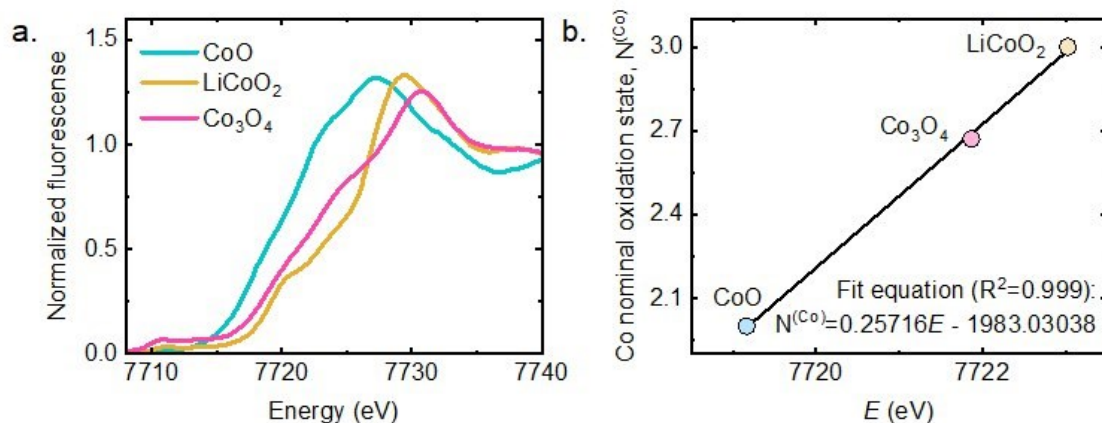


Figure 2.7. a. XANES spectra of the Co-K edge collected on Co⁽²⁺⁾O, Co₃^(2.7+)O₄ and LiCo⁽³⁺⁾O₂, used as references, **b.** Nominal Co oxidation state of references as a function of the energy of the Co-K edge denoted by E. The fit equation is shown in the graph. The energy of the edge was estimated by the integral method.

EXAFS

The data in the EXAFS region is fitted with a spline function (with number of knots between 3 and 7 depending on the sample) going through the middle of the oscillations of the data (Figure 2.8a). The spline function is set as the zero and it is adjustable and smooth function. Thus, oscillations with positive and negative values are found depending if they are above or below the spline. The energy scale (E) is modified E-E₀, where E₀ is the first inflection point (for Co 7709 eV, and for Mn 6539 eV) (Figure 2.8b). Then, the x axis (energy) is changed to an axis of the magnitude of the photo-electron wave vector as described in equation 2.9 (Figure 2.8c).

Typically, the spectrum is weighted by k³ (or k²) to compensate for the oscillations damping towards high k values. The k³-weighted spectrum is used to perform the simulations. Subsequently, a Fourier transform is performed to the k³-weighted spectrum and the energy axis is converted to a space axis (so-called reduced distance), thus the structural data can be more practically analyzed. The peaks in the Fourier transformed data correspond to different neighboring scattering atoms located at a certain distance from the absorbing atom (Figure 2.8d). At higher k values the phase shift is less pronounced causing an effect that simulates a shorter distance when the Fourier transform is applied, resulting in peaks at lower distances than the real distance. This effect occurs due to the dependence of the phase shift with k. Therefore, the data must be corrected by a theoretical or experimental standard. This is usually

performed using the FEFF program, which calculates the corresponding phase functions with theoretical models. The magnitude of the Fourier transform is finally plotted, as observed in Figure 2.8d.

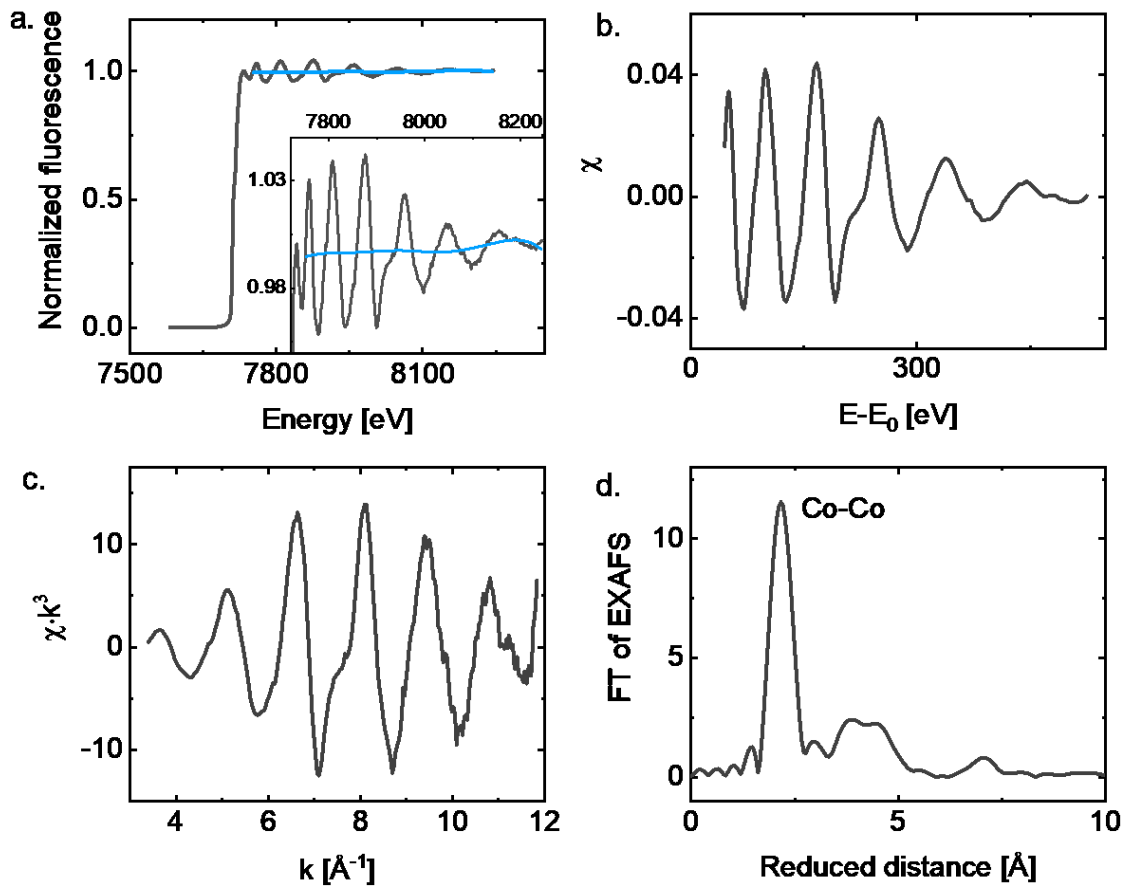


Figure 2.8. **a.** Normalized fluorescence spectrum of Co-K edge collected on a metallic Co foil and the spline function (blue). The inset shows a zoom-in section of the data, **b.** Cut-out of the EXAFS oscillations, so-called χ spectrum. The energy axis becomes the energy offset $E-E_0$, **c.** The χ spectrum is k^3 weighted and the energy offset becomes the photo-electron wave vector, **d.** Fourier transform of the EXAFS spectrum. The x axis is called reduced distance, representing the reduced interatomic distances.

The Fourier transform must be applied over a finite range of k since the data available is also finite. Yet, it may be not obvious which energy values are present in that data range. Thus, the k range inputted to analyze the data has an impact on the result, e.g., if the range does not contain a whole number of oscillations in a periodic function. Consequently, a window function

must be applied ($W(k)$, equation 2.14), in which the $\chi(E)$ smoothly reduces to zero or an enough small value to prevent sharp discontinuities and a strong k range dependence.

$$W(k) = \begin{cases} \left[0.5 \left(1 - \cos\left(\pi \frac{k - k_0}{a}\right)\right)\right]^p, & \text{when } k_0 \leq k < k_0 + a \\ \left[0.5 \left(1 - \cos\left(\pi \frac{k_n - k}{b}\right)\right)\right]^p, & \text{when } k_n - b < k \leq k_n \\ 1, & \text{when } k_0 + a \leq k \leq k_n - b \end{cases} \quad [2.14]$$

where p is the cosine exponent, k_0 and k_n are the starting and ending k -values and a and b are the starting and ending regions over which, the cosine is applied (equations 2.15 and 2.16).

$$a = (k_n - k_0)L \quad [2.15]$$

$$b = (k_n - k_0)R \quad [2.16]$$

Possible values for L and R are between 0 (no dampening) and 0.5 (strong dampening; $L=R=0.5$, $p=1$ is the Hann window). L and R values of 0.1 are typical values, meaning that the starting 10% and the ending 10% of the weighted EXAFS oscillations are dampened by the cosine function.

Data simulation

The spectra are simulated using the SimX Lite software (in-house software). Three relevant parameters can be obtained from the EXAFS simulations: N , which is related to the number of neighboring atoms around the absorber atom, R , related to the averaged interatomic distance between the absorber atom and the scatter, and σ (Debye-Waller factor), associated with the distance distribution in a material. The phase functions are calculated using the FEFF8-Lite program (version 8.5.3, self-consistent field option activated). The atomic coordinates of the FEFF input files were generated from reported chemical structures. An amplitude reduction factor (S_0^2) of 0.7 was used. The EXAFS simulations were optimized by the minimization of the error sum obtained by summation of the squared deviations between measured and simulated values (least-squares fit, equation 2.17). The fit was performed using the Levenberg-Marquardt method with numerical derivatives.

$$\delta = \sum_i^n (m_i - e_i)^2 \quad [2.17]$$

Where m_i represents the data point of the simulated EXAFS spectrum and e_i represents the data point of the experimental EXAFS spectrum.

For the quantification of the goodness of the fit parameters in the EXAFS simulations, the equation 2.18 is used. The obtained numerical value corresponds to the relative difference between the experimental and the simulated spectra after Fourier-filtering.

$$R_f = 100 \frac{\sum |m_i^{ff} - e_i^{ff}|}{\sum |e_i^{ff}|} \quad [2.18]$$

Where, m^{ff} and e^{ff} represents the Fourier-filtered model and experimental k-weighted EXAFS curves, respectively. The sums consider all points in the fit region and spectra displayed.

Chapter 4. Reversible and irreversible processes during cyclic voltammetry of an electrodeposited manganese oxide as catalyst for the oxygen evolution reaction

Journal of Physics: Energy

Reversible and irreversible processes during cyclic voltammetry of an electrodeposited manganese oxide as catalyst for the oxygen evolution reaction

Javier Villalobos¹, Ronny Golnak², Lifei Xi¹, Götz Schuck³ and Marcel Risch^{5,1,4}

Author e-mails

marcel.risch@helmholtz-berlin.de

Author affiliations

¹ Nachwuchsgruppe Gestaltung des Sauerstoffentwicklungsmechanismus, Helmholtz-Zentrum Berlin für Materialien und Energie GmbH, Hahn-Meitner Platz 1, 14109, Berlin, Germany

² Department of Highly Sensitive X-ray Spectroscopy, Helmholtz-Zentrum Berlin für Materialien und Energie, GmbH, Berlin 12489, Germany

³ Department of Structure and Dynamics of Energy Materials, Helmholtz-Zentrum Berlin für Materialien und Energie, GmbH, Berlin 14109, Germany

⁴ Institut für Materialphysik, Georg-August-Universität Göttingen, Friedrich-Hund-Platz 1, 37077, Göttingen, Germany

Abstract

Manganese oxides have received much attention over the years among the wide range of electrocatalysts for the oxygen evolution reaction (OER) due to their low toxicity, high abundance and rich redox chemistry. While many previous studies focused on the activity of these materials, a better understanding of the material transformations relating to activation or degradation is highly desirable, both from a scientific perspective and for applications. We electrodeposited Na-containing MnO_x without long-range order from an alkaline solution to investigate these aspects by cyclic voltammetry, scanning electron microscopy and x-ray absorption spectroscopy at the Mn-K and Mn-L edges. The pristine film was assigned to a layered edge-sharing Mn^{3+/4+} oxide with Mn-O bond lengths of mainly 1.87 Å and some at 2.30 Å as well as Mn-Mn bond lengths of 2.87 Å based on fits to the extended x-ray fine structure. The decrease of the currents at voltages before the onset of the OER followed power laws with three different exponents depending on the number of cycles and the Tafel slope decreases from 186 ± 48 to 114 ± 18 mV dec⁻¹ after 100 cycles, which we interpret in the context of

surface coverage with unreacted intermediates. Post-mortem microscopy and bulk spectroscopy at the Mn-K edge showed no change of the microstructure, bulk local structure or bulk Mn valence. Yet, the surface region of MnO_x oxidized toward Mn^{4+} , which explains the reduction of the currents in agreement with literature. Surprisingly, we find that MnO_x reactivates after 30 min at open-circuit (OC), where the currents and also the Tafel slope increase. Reactivation processes during OC are crucial because OC is unavoidable when coupling the electrocatalysts to intermittent power sources such as solar energy for sustainable energy production.

Introduction

Among the wide range of transition metal oxides used for the oxygen evolution reaction (OER), manganese oxides have received much attention over the years because their low toxicity and their high abundance (10th in Earth crust). Furthermore, photosystem II has an active site consisting of CaMn_4O_5 , which makes manganese oxides scientifically interesting as biomimetic catalysts [1–6]. In the past years, the attention was mainly focused on simple manganese oxides [3–13], such as Mn_3O_4 , Mn_2O_3 , MnO_2 and variants with non-binding, redox-inactive cations, e.g. $\delta\text{-AMnO}_2$ (A is group I/II cation) [14–16]. The activation and degradation processes of Mn oxides are less understood than the activity of these catalysts. Usually, degradation is associated with changes of the surface and bulk oxide composition, long range order (i.e. crystallinity) and/or microstructure, but it can also be caused by detachment, particle agglomeration, or blocking by oxygen bubbles [17–21]. These material modifications due to activation and degradation can be electrochemically observed as changes in overpotential at fixed current or changes in current at fixed overpotential [17, 22–24]. Cyclic voltammetry (CV) is the other common electrochemical test of these processes and frequently used as an activation procedure [25–28]. This activation procedure is also known as pretreatment or conditioning, and it is usually carried out as several cycles in a limited range of voltage. The promotion of the catalytic properties after an activation process has been studied for oxides such as Ir- [26, 28], Co- [27, 29] and also Mn-based oxides [25, 30]. Common sweep speeds for these studies are in the range of 10 to 200 mV s^{-1} , while they are slower for studies with the focus on activity. Typically, the activation is performed for 20 to 50 cycles, but in some cases, the final activated material does not form until the 200th cycle [31].

Understanding the processes of activation and degradation of oxides in alkaline media requires measurements complementary to electrochemical methods. Frydendal *et al* [32] argue that the stability degradation of electrodeposited Mn oxides cannot be determined based on electrochemical experiments alone, which is supported by gravimetric experiments using an electrochemical quartz crystal microbalance (EQCM) and inductively coupled plasma mass spectrometry (ICP-MS). Geiger *et al* [33] recently proposed the S-number as a metric of catalyst degradation which requires the determination of the material loss, e.g. by ICP-MS measurements. Köhler *et al* [1] and Baumung *et al* [34] studied the activation of LiMn_2O_4 particles during CV using a rotating ring-disk electrode (RRDE) where the ring was set to a voltage sensitive to dissolved Mn.

Valuable insight into the mechanism of catalysis, activation and degradation of manganese oxides has been obtained in the last decade from spectroscopy including x-ray absorption spectroscopy (XAS) [35–43], UV–Vis spectroscopy [44–46] and Raman spectroscopy [46]. We focus on alkaline electrolytes herein. The distinction between acidic, neutral and alkaline conditions is important because Mn^{3+} ions disproportionate to Mn^{2+} and Mn^{4+} in acidic and neutral electrolytes, while Mn^{2+} and Mn^{4+} ions comproportionate to Mn^{3+} in alkaline

electrolytes [44, 45]. Nakamura and coworkers [44, 45] discuss that more Mn^{3+} ions lead to higher activity, which is in line with the e_g orbital descriptor proposed by Suntivich *et al* [47]. In their catalytic model, comproportionation of Mn^{4+} serves as a secondary supply of the catalytically active Mn^{3+} , which may explain that the lowest overpotential in systematic studies of the OER on simple manganese oxides is usually found for mixed $\text{Mn}^{3+/4+}$ oxides [3, 4, 38–40, 42]. Therefore, it is critical to control the distribution of Mn cations in Mn-based electrocatalysts for the OER to understand their activity and potential degradation. Jaramillo and coworkers showed precious support materials (e.g. Au) induce Mn oxidation after the OER to such a mixed $\text{Mn}^{3+/4+}$ oxide [41, 43]. Moreover, the voltage range in CV can have drastic influence on the observed redox features and thus the nature of the Mn oxide [46, 48]. Post-mortem and *in situ* experiments on many Mn oxides show clear valence changes during electrocatalytic experiments in alkaline media [37–40], often accompanied by structural changes [35, 36]. Interestingly, studies including low voltages in addition to those supporting the OER often show the formation of Mn_3O_4 ($\text{Mn}^{2+}\text{Mn}^{3+}_2\text{O}_4$), which was not present in the pristine material [35, 38, 46]. The exact role of tetrahedral Mn^{2+} in Mn_3O_4 is unknown but Rabe *et al* [46] show that it hinders Mn dissolution using a combination of *in situ* Raman spectroscopy and ICP-MS.

In this study, we electrodeposited Na-containing MnO_x films without long-range order directly in an alkaline electrolyte using a complexing agent, while most other manganese oxide catalysts are deposited at lower pH (e.g. [12]). By this approach, we avoid complications due to ion exchange and focus on the changes of the Mn valence to identify activation and degradation processes during cyclic voltammetry and open-circuit conditions at pH 13. Electrochemical changes were observed and correlated with post-mortem XAS. Unexpectedly, we found that our MnO_x films reactivate after open-circuit.

Methods

Materials

$\text{Mn}(\text{NO}_3)_2 \cdot 4\text{H}_2\text{O}$ ($\geq 99.99\%$), MnO_2 ($\geq 99\%$), Mn_3O_4 ($\geq 97\%$), Mn_2O_3 ($\geq 99.9\%$), L-(+)-Tartaric acid ($\geq 99.5\%$) and (2 M and 0.1 M) NaOH solutions were ordered from Sigma-Aldrich. Graphite foil ($\geq 99.8\%$) with a thickness of 0.254 mm ordered from VWR, deionized water ($>18\text{M}\Omega\text{ cm}$). All reactants were used as received, without any further treatment.

Electrodeposition of MnO_x films

0.6 mmol of $\text{Mn}(\text{NO}_3)_2 \cdot 4\text{H}_2\text{O}$ and 6 mmol of L-(+)-tartaric acid were dissolved in a small volume of deionized water (approx. 1 ml). 120 ml of Ar-purged 2 M NaOH solution were added slowly with stirring to the previous solution, changing from colorless to beige. Electrodeposition was carried out using a Gamry 600+ potentiostat and a three-electrode cell made from a three-neck round-bottom flask. The separation between the necks and thus electrodes was less than 1 cm. The working electrodes were either a glassy carbon disk (4 mm diameter; HTW Sigradur G) in a rotating disk electrode (RDE) or graphite paper (Alfa Aesar). The unrotated RDE was mounted onto a commercial rotator (ALS RRDE-3 A Ver 2.0). We used a saturated calomel reference electrode (SCE; ALS RE-2BP) and a graphite rod (redox.me, HP-III, High Pure Graphite) as the counter electrode. The galvanostatic deposition was performed at $150\ \mu\text{A}/\text{cm}^2$ until a charge density of $40\ \text{mC cm}^{-2}$ was reached.

Electrochemical measurements

The detailed protocol for electrocatalytic investigations is documented in table S1 (available online at stacks.iop.org/JPENERGY/02/034009/mmedia) for glassy carbon electrodes and in

table S2 for graphite foil. The measurements on glassy carbon electrodes were carried out using two Gamry 600+ potentiostats connected as a bipotentiostat in a single-compartment three-electrode electrochemical cell made of polymethyl pentene (ALS) filled with about 60 ml solution of 0.1 M NaOH (pH 13). A commercial rotator (ALS RRDE3-A Ver 2.0) was used with commercial rotating ring-disk electrodes with exchangeable disks of 4 mm diameter and a Pt ring with inner ring diameter of 5 mm and outer diameter of 7 mm. The graphite foil was clamped in the same cell as the RRDE. A coiled platinum wire was used as a counter electrode and a SCE (ALS RE-2BP) as a reference electrode, which was calibrated daily against a commercial reversible hydrogen electrode (RHE; Gaskatel HydroFlex) as detailed in figure S1. The electrochemical experiments were performed at constant controlled temperature of 25.0 °C. The ring was set to detect oxygen at 0.4 V vs. RHE as calibrated previously [34]. Before any experiment, the electrolyte was purged with Ar for at least 30 min. Typical electrolyte resistances of $R = 40 \pm 9 \Omega$ were determined by electrochemical impedance spectroscopy (EIS) (representative data in figure S2 a). The ohmic drop (also called iR drop) was corrected during post-processing by subtraction of iR from the measured voltages, where i and R are the measured current and resistance (figure S2b). All voltages are given relative to the reversible hydrogen electrode (RHE).

The instantaneous Tafel slope was calculated by the first derivative of the iR -corrected voltage as function of the logarithm of the current density. The Tafel slope was also obtained by linear regression of the iR -corrected voltage ($E-iR$) against $\log_{10}(i)$, using the cathodic half-cycle of the cyclic voltammetry of iR -corrected data in the range between 1.71 and 1.77 V vs. RHE. The electrodes were swept at 100 mV s^{-1} and rotated at 1600 rpm. The error represents the standard deviation of three independently prepared electrodes.

Scanning electron microscopy (SEM) and energy dispersive x-ray spectroscopy (EDX)

The sample morphology was determined using a Zeiss LEO Gemini 1530 scanning electron microscope, acceleration voltage of 3 keV and in high vacuum (around 10^{-9} bar) and using a secondary electron inLens detector. The images were taken in different regions of the sample to get representative data. EDX measurements were performed using a Thermo Fischer detector with an acceleration voltage of 12 keV.

X-ray absorption spectroscopy (XAS)

All XAS data were collected at an average nominal ring current of 300 mA in top-up and multi-bunch mode at the BESSY II synchrotron operated by Helmholtz-Zentrum Berlin. Soft XAS measurements at the Mn-L edges were conducted using the LiXEdrom experimental station at the UE56/2 PGM-2 beamline [49]. Reference samples were measured as finely dispersed powders attached to carbon tape and electrodeposited samples were measured on graphite foil (Alfa Aesar). All samples were measured at room temperature and in total electron yield (TEY) mode and with horizontally linear polarization of the beam. The TEY measurements were carried out by collecting the drain current from the sample. The sample holder was connected to an ammeter (Keithley 6514). In order to avoid radiation damage, the incoming photon flux was adjusted to get a TEY current from the sample of around 10 pA. In addition, the sample was kept as thin as possible. XAS spectra for each sample were collected at a few locations to ensure representativity of the data and to further minimize radiation damage as well as local heating. The energy axis was calibrated using a Mn-L edge spectrum of MnSO_4 as a standard where the maximum of the L_3 -edge was calibrated to 641 eV (figure S3). This reference was calibrated against molecular oxygen as described elsewhere [38, 50]. All spectra were normalized by the subtraction of a straight line

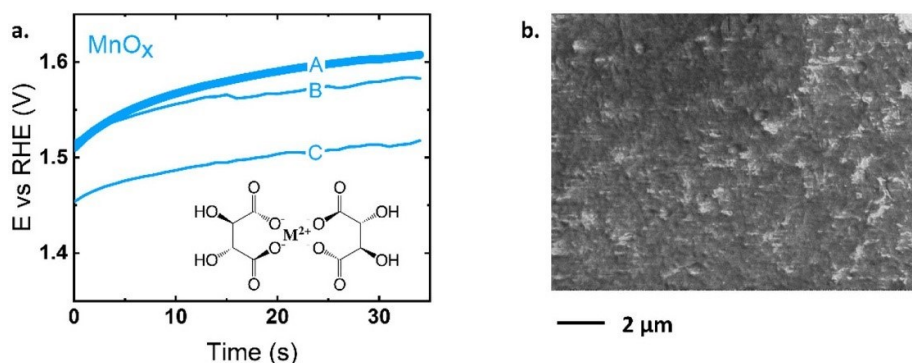


Figure 1. (a) Chronoamperometry during electrodeposition of MnO_x films on glassy carbon, samples A (thick line), B and C (thin lines). The inset shows the coordination complex of divalent metal (M^{2+}) due to the presence of tartrate ions. (b) SEM image of sample A.

obtained by fitting the data before the L_3 edge and division by a polynomial function obtained by fitting the data after the L_2 edge (figure S4).

Hard XAS at Mn-K edge was performed at the KMC-2 beamline [51]. The general used setup was organized as it follows: I_0 ionization chamber, sample, I_1 ionization chamber or FY detector, energy reference and I_2 ionization chamber. The used double monochromator consisted of two Ge-graded Si(111) crystal substrates[52] and the polarization of the beam was linear horizontal. Reference samples were prepared by dispersing a thin and homogenous layer of the powder on Kapton tape, after removing excess of powder, the tape was folded several times to get 2 cm x 1 cm windows. Reference samples were measured in transmission mode between two ion chamber detectors at room temperature. Electrodeposited samples were measured on graphite foil in fluorescence mode with a Bruker X-Flash 6/60 detector. Energy calibration of the x-ray absorption near edge structure (XANES) was made with the corresponding metal foil, setting the inflection point for Mn at 6539 eV. All spectra were normalized by the subtraction of a straight line obtained by fitting the data before the K edge and division by a polynomial function obtained by fitting the data after the K edge (figure S5). The Fourier transform (FT) of the extended x-ray absorption fine structure (EXAFS) was calculated between 40 and 440 eV (3.2 to 10.7 \AA^{-1}) above the Mn-K edge ($E_0 = 6539 \text{ eV}$). A cosine window covering 10% on the left side and 10% on the right side of the EXAFS spectra was used to suppress the side lobes in the FTs.

EXAFS simulations were performed using the software SimX Lite. After calculation of the phase functions with the FEFF8-Lite [53] program (version 8.5.3, self-consistent field option activated). Atomic coordinates of the FEFF input files were generated from the structure of $\text{MnOOH} \cdot x\text{H}_2\text{O}$ (birnessite) [54]; the EXAFS phase functions did not depend strongly on the details of the used model. An amplitude reduction factor (S_0^2) of 0.7 was used. The data range used in the simulation was 44 to 420 eV (3.4 to 10.5 \AA^{-1}) above the Mn-K edge ($E_0 = 6539 \text{ eV}$). The EXAFS simulations were optimized by the minimization of the error sum obtained by summation of the squared deviations between measured and simulated values (least-squares fit). The fit was performed using the Levenberg–Marquardt method with numerical derivatives.

Results and discussion

Electrodeposition of films on glassy carbon

An electrodeposition protocol was developed to produce Mn oxides at alkaline pH. In these electrolytes, manganese might deposit in a numerous of stable oxide forms, commonly Mn_3O_4 (Mn^{2+} , Mn^{3+}), Mn_2O_3 (Mn^{3+}) or MnO_2 (Mn^{4+}) [55]. Conventionally, solvated Mn^{2+} cations would spontaneously precipitate as oxides or hydroxides at $\text{pH} > 8$. Therefore, we

stabilized them using tartrate as a complexing agent to control their deposition in NaOH (inset of figure 1(a)). Furthermore, electrolyte anions may exchange with the deposited films, e.g. [31], which is prevented when the electrolyte composition does not change significantly during deposition and catalytic investigation.

Manganese oxides were deposited on glassy carbon electrodes for electrocatalytic investigations and on graphite paper for x-ray absorption spectroscopy (XAS). We first focus on the discussion of the samples deposited on glassy carbon disks. The deposition setup consisted of a commercial rotator for RDEs and a three-electrode cell (figure S6). The films were deposited at constant current density of $150 \mu\text{A}/\text{cm}^2$ (figure 1(a)), which allows to control the deposited charge by stopping the experiment after a certain time. The deposition profiles of MnO_x showed increasing voltage after short times and reached a steady-state after about 20 s. The steady-state voltage of the samples was $1.66 \pm 0.04 \text{ V}$ vs. RHE and the final deposited charge density after 34 s was 40 mC cm^{-2} .

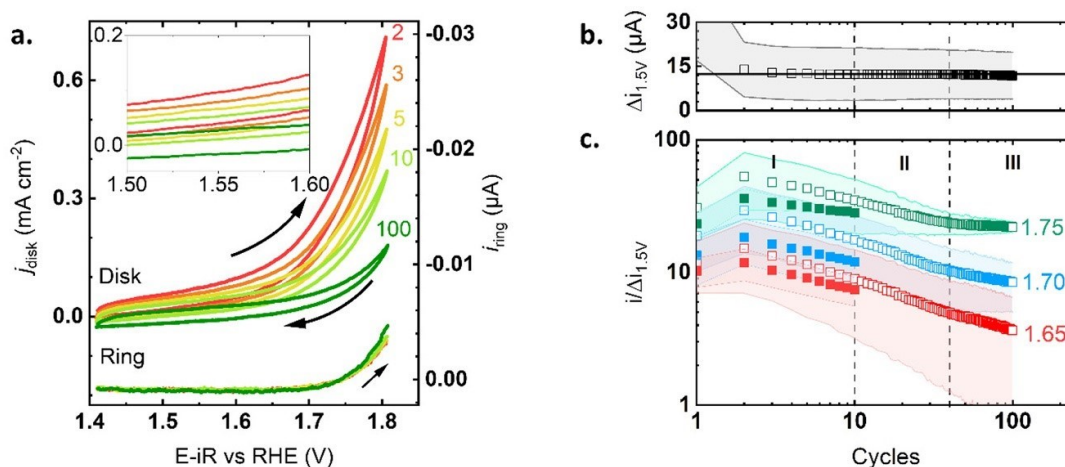


Figure 2. (a) CV performed on a MnO_x -covered disk (sample A) with a scan rate of 100 mV s^{-1} in 0.1 M NaOH with rotation 1600 rpm and constant voltage of 0.4 V vs. RHE at the ring. (b) Average $\Delta i_{1.5\text{V}}$ of all samples as function of cycles for the first 100 cycles (calculation detailed in the text). (c) Average current ratio $i/\Delta i_{1.5\text{V}}$ of all samples as function of cycling at selected voltages. The data was evaluated during the first 100 cycles (open squares) and 10 cycles after 30 min of OCV (solid squares). The dashed lines delimit three different regions, labeled as I, II and III. The light-colored areas represent the standard deviation of three samples.

The film corresponding to MnO_x sample A in figure 1(a) was subsequently characterized by SEM and EDX to check the coverage and homogeneity of the film. As it can be seen in figure 1(b), MnO_x covered the whole surface of the glassy carbon substrate with texture on the micrometer scale. EDX elemental mapping showed a homogeneous distribution of the electrodeposited Mn and O atoms (figure S8), thus corroborating the formation of MnO_x anywhere on the substrate. Our films also contained Na (figure S8b), likely between layers of MnO_x . The crystallinity of the film was too low to be resolved by x-ray diffraction (XRD). In summary, the developed alkaline electrodeposition protocol ensured producing homogeneously covered films of Na-containing MnO_x without long-range order.

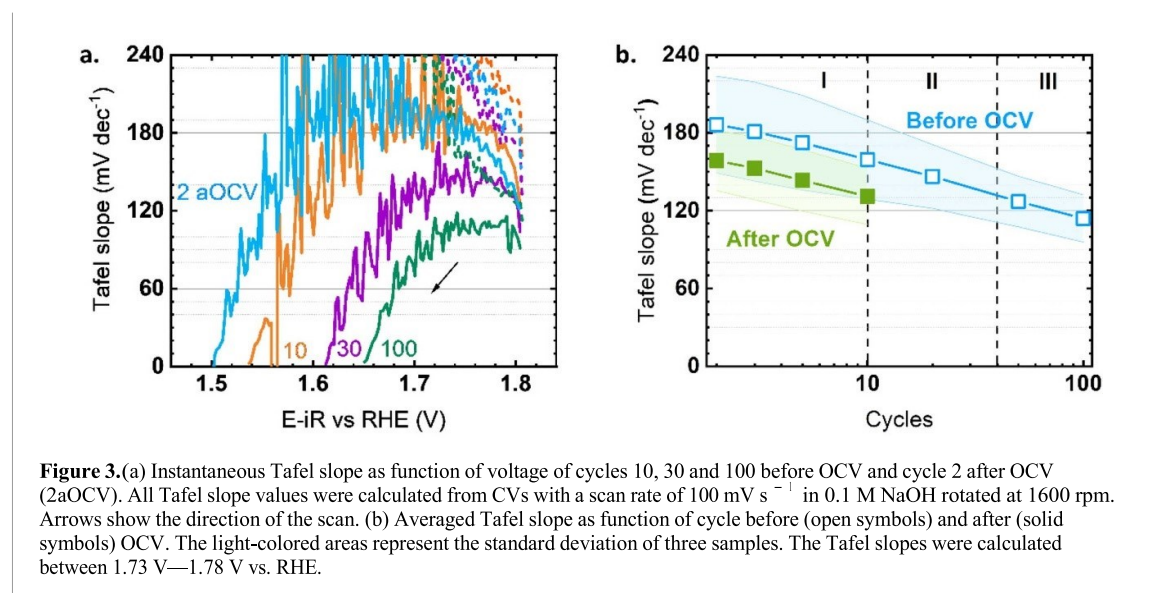
Electrocatalytic investigations

In order to evaluate the catalytic activity, activation and possible degradation of the films on glassy carbon disks, series of CV were performed in a RRDE station (representative data of MnO_x sample A in figure 2 and all data in figure S7). The sweep speed was 100 mV s^{-1} , which is typical for activation studies, while cycling is a typical method for activation studies [30, 56–58]. The CVs of the MnO_x disks show an exponential increase of the current density

at about 1.65 V vs. RHE for the 2nd cycle and 1.70 V vs. RHE for the 100th cycle. Additionally, about half the maximum current density was lost during 100 cycles. There were no additional redox peaks in the CV. The MnO_x film disks showed hysteresis, i.e. capacitive currents, which reduced with cycling (insets of figure 2). Furthermore, the current offset reduced with cycling. The offset could be eliminated by selecting a wider scan range to more negative voltages (figure S9). The presence of the shifts in figure 2 may thus indicate an incomplete reduction process that is continued over many cycles.

The onset of the OER was determined using the anodic ring currents, which we assign to oxygen detection by reduction [34]. The cathodic ring scan is not shown as it shows hysteresis due to delayed oxygen release. The traces of the anodic ring currents were more similar than those of the disk currents. The onset of the OER on MnO_x was consistently at 1.70 V vs. RHE independent of the cycle number as determined by the rise of the currents above the noise level. The differences in the trends between the disk and ring currents suggest that MnO_x changes electrochemically with cycling without affecting the oxygen detected at the ring.

The trends of the disk currents during cycling were also evaluated at selected voltages with and without oxygen evolution (figures 2(b), (c)). The currents were corrected for capacitance by averaging the anodic and cathodic scans [59]. To account for differences in surface area for the different films with the same composition, all currents were divided by the difference between the anodic and cathodic currents at 1.50 V vs. RHE ($\Delta i_{1.5 \text{ V}}$). After 5 cycles, $\Delta i_{1.5 \text{ V}}$ becomes steady with average values of $12 \pm 1 \mu\text{A}$ (figure 2(b)). The differential capacity is defined as $C = dQ/dE \approx \Delta i / (\Delta E / \Delta t)$ where $\Delta E / \Delta t$ is the sweep speed (here: 100 mV s^{-1}). This is a rough approximation as the capacitance is commonly obtained by systematic experiments at several sweep speeds [60]. Yet, it allows tracking the changes of surface area with cycling using the regular CV method. SEM showed no significant morphology changes after 100 cycles for the three MnO_x samples (figure S10).



The current ratios $i/\Delta i_{1.5 \text{ V}}$ of MnO_x followed a power law with different exponents depending number of cycles and whether oxygen is evolved (figure 2(c); open symbols). A large negative exponent means fast decay of the current with cycle number, while a large positive exponent means a fast increase of the currents with cycling. The exponent was about $-1/3$ for the initial 10 cycles (region I), about $-1/4$ for intermediate cycles (10 to 40; region II) and

depended on the applied voltage for the later cycles, i.e. after about 40 cycles (region III). The exponent was similar to the initial value of $-1/3$ before the onset of the OER (1.65 V vs. RHE); it was about $-1/5$ at the onset (1.70 V) and close to zero for oxygen evolution (1.75 V vs. RHE). The spread of the currents (light colored area) was smallest for the steady-state (zero exponent) at this voltage.

In summary, the currents decreased with cycling for MnO_x and reached a steady-state only at the voltage which support oxygen evolution (1.75 V vs. RHE). These trends can be explained by (1) change in coverage with intermediates (hydroxylation or O_2 coverage) [1, 61], (2) material dissolution [17], modifications of the catalyst material such (3) change in structure [19] or (4) transition metal valence [18]. The transient changes of point (1) can only be investigated *in situ*, while the irreversible changes of points (2)-(4) are expected to persist in a post-mortem experiment. Other explanations may be possible, but we deem these points the most likely ones and thus we address these possible explanations of the trends point by point below.

To distinguish irreversible surface changes and transient changes, we let the films rest at open-circuit voltage (OCV) for 30 min and then performed an additional 10 cycles. This simple test was recently introduced by El-Sayed *et al* [62] for galvanostatic measurements using RDEs of iridium on ATO (antimony-doped tin oxide). The authors attribute the unexpected recovery of currents after OCV to the removal of nano and micro bubbles of oxygen within the catalyst layer, i.e. a change of (product) coverage. Here, we extend it to electrocatalyst tests using CV (figure 2(b); solid symbols).

The exponents of the current ratio differed depending on the previously applied voltage after the OCV period for all films, suggesting partially reversible processes. The exponent was identical ($-1/3$) below the onset of the OER and less negative at the onset ($-1/4$) and above ($-3/20$). Furthermore, the current ratios were offset to lower values, i.e. the prefactor of the power law was lower. We interpret these observations as follows: the reduced prefactor indicates irreversible changes due to a reduction of active sites, either by material dissolution or deactivation of the active sites. Note that we normalized by a quantity proportional to the surface area so that we can exclude it as the source of the lower prefactor and hence currents. We cannot exclude dissolution of specific cations that leads to a different surface composition as observed, e.g. for the perovskite $\text{La}_{0.6}\text{Sr}_{0.4}\text{MnO}_3$ [63]. We attribute the changes in the exponent to a combination of transient changes of species adsorbed on the surface and the irreversible changes listed above.

The Tafel slope ($b = \partial \log i / \partial E$) in chemical equilibrium depends on the surface coverage where usually limiting cases of the adsorption isotherms are discussed [1, 61, 64, 65]. Since these values do not depend on the amount of compound or active sites, they are usually associated with mechanisms of specific reactions and vast reported values can be found for a wide range of materials in OER catalysis. The Tafel slope is very large (approaching infinity) if an early chemical step limits the reaction without any pre-equilibria [61]. In particular, very large Tafel slopes are also expected if the intermediate that reacts chemically during the rate-limiting step approaches full surface coverage in the Langmuir adsorption model [61]. A Tafel slope of 120 mV dec^{-1} is predicted (at 25°C) if an electrochemical step limits the kinetics, if the electrochemically reacting intermediate reaches full coverage in the Langmuir model or if the chemically reacting intermediate reaches full coverage in the Temkin model [61]. A Tafel slope of 60 mV dec^{-1} (at 25°C) indicates a chemical rate-limiting step with an electrochemical pre-equilibrium for low coverage of the reacting intermediate (in the Langmuir model) [1, 61]. Values between 60 and 120 mV dec^{-1} are not predicted by common kinetic models. Thus, the Tafel slope does depend on the surface coverage but not uniquely.

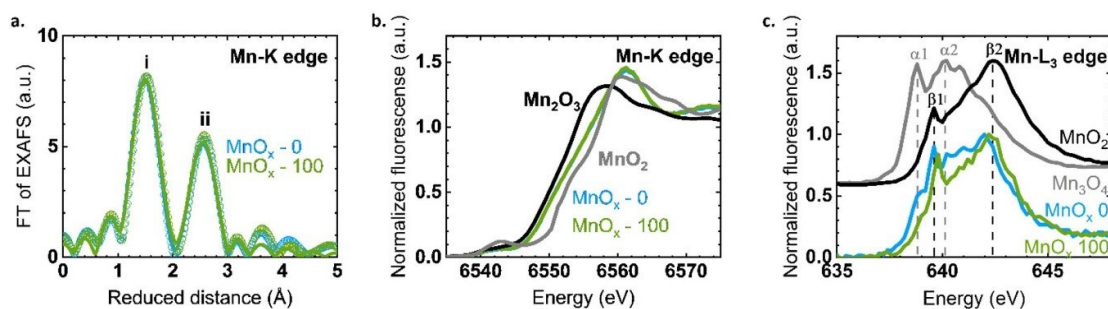


Figure 4. (a) Fourier-transform EXAFS spectra for Mn K-edge collected on pristine MnO_x (blue symbols) and after 100 cycles of OER catalysis (green symbols). The corresponding lines are results from EXAFS simulations (see table 1 for parameters). The reduced distance is by about 0.3 Å shorter than the precise distance obtained by EXAFS simulations. (b) XANES spectra for Mn-K edge collected on MnO_x after 0 cycles and 100 cycles. The Mn-K edge spectra of Mn₂O₃ and MnO₂ were added as references. (c) Mn-L₃ edge spectra for pristine MnO_x (MnO_x - 0) and MnO_x after 100 cycles (MnO_x - 100); and MnO₂ and Mn₃O₄, which were used as references.

We analyzed the Tafel slope during selected cycles of a representative sample (figure 3, all samples in figure S11). The Tafel slopes during the anodic scans in figure 3(a) were larger as compared to those of the cathodic scans. Clearly a sweep speed of 100 mV s⁻¹ was too fast to establish a chemical equilibrium. If an electrochemical equilibrium plays a mechanistic role, then the produced intermediates were biased toward the oxidative site of the equilibrium (e.g. M^{III}OH → M^{IV}O) during the cathodic scan, due to the voltages above the equilibrium voltage. During the 10th scan, the Tafel slope of MnO_x was 180 mV dec⁻¹ at the onset of the OER and below it (1.7 to 1.6 V vs. RHE). Note that previously electrochemically produced intermediates can react chemically below the onset of the OER (as determined by the ring during the anodic scan). After 100 cycles, the Tafel slope decreased to 110 mV dec⁻¹ between 1.8 and 1.7 V vs. RHE. In fact, the Tafel slopes decreased exponentially before and after the OCV (figures 3(b) and S12). After the OCV (2aOCV), the trace of the Tafel slope and its constant value of 180 mV dec⁻¹ matched that of the 10th cycle before the OCV (figure 3(a)). In summary, the region of constant Tafel slope (or minimum) shifted to lower voltages with cycling for both materials. The Tafel slope decreased for MnO_x with cycling. After OCV, the voltage dependence and value (within error) of the Tafel slope matched those observed initially. We interpret these trends as a reversible formation of an active state (with certain intermediate coverage) on MnO_x.

Local structure and valence changes due to cycling

We used XAS to study the irreversible changes due to cycling. XAS experiments were necessary due to its fine chemical sensitivity and the absence of crystallinity required for diffraction techniques. Changes in the local structure of the oxides were identified using the EXAFS at the Mn-K edge [66–68]. The XANES was used to discuss changes of the metal valence where we analyzed the bulk-sensitive K edge and more surface-sensitive L edge of Mn.

The sample for the XAS investigations were prepared on graphite foil by the same procedure as discussed above (table S2). The deposition of the same charge density on the larger graphite foil also resulted in a steady-state after about 20 s but at lower voltages of 1.37 ± 0.03 V vs. RHE (figure S7). The systematic shift by about + 300 mV did not affect the observed electrocatalytic behavior with cycling (figure S14). While there may have been minor variations of the film composition, valence and roughness due to the different steady-state voltages, the identical cycling trends strongly suggest that the trends in the XAS data can be used to rationalize the cycling trends of films deposited on both graphite foil and glassy carbon.

The R-factor used Fourier filtered data between 1 and 3 Å and was calculated by using the formula $R_f = 100 \Sigma(m_l^{ff} - e_l^{ff})^2 / \Sigma(e_l^{ff})^2$, where m_l^{ff} represents the Fourier-filtered model and e_l^{ff} represents the experimental k-weighted EXAFS curve.

The Fourier transform of the EXAFS of MnO_x showed the expected features of layered hydroxides (figure 4(a)), namely two peaks at about 1.5 and 2.5 Å reduced distance labeled i and ii, respectively. The FT of the EXAFS did not change with cycling for these peaks. We simulated peaks i and ii using MnOOH · xH₂O (birnessite) [54] (figure 4(a)). The fit results corroborate the assignment to a layered hydroxide as the R-factors were below 2% [68] (table 1). There were no drastic changes with cycling in the local structure of the bulk but we cannot exclude surface changes (additional discussion below). The metal-oxygen bond length is 1.87 Å (peak i), which is typical for Mn^{3+/4+}O₆ cations [54, 69]. Yet, there is another Mn-O bond length of around 2.30 Å, which significantly improves the fit. This bond length is similar to the one in Mn²⁺O and may indicate a minor impurity phase [54]. The Mn-Mn distances were 2.87 Å in MnO_x. These distances have been widely reported for amorphous electrodeposited oxides where they correspond to hexacoordinated Mn-O and di-μ-oxo bridged metals, i.e. edge-sharing octahedra [3, 70]. The absence of clear FT peaks at higher reduced distance implies a lack of long-range order.

Table 1. EXAFS absorber–backscatter distance (R), coordination numbers (N) and Debye–Waller factor (σ) as determined by simulation of the k^3 -weighted EXAFS spectra at the Mn-K edge for pristine MnO_x (MnO_x-0) and after 100 cycles (MnO_x-100). Shells were simulated using phase functions from a previously reported birnessite structure [54].

Sample	Parameter	Mn–O1	Mn–O2	Mn–Mn	R— factor
MnO _x -0	N	5.0	1.0	4.3	0.59%
	R (Å)	1.87	2.30	2.86	
	σ (Å)	0.05	0.05 ^a	0.08	
	N	5.2	1.5	4.2	
MnO _x -100	R (Å)	1.87	2.30	2.86	0.85%
	σ (Å)	0.05	0.05 ^a	0.08	

^aindicates fixed values (not simulated).

A qualitative estimation of the average bulk metal valence can be achieved by comparison of the XANES spectra of the films and suitable reference materials (figure 4(b)). The Mn-K edge spectra of MnO_x were compared with the two references Mn³⁺₂O₃ and β -Mn⁴⁺O₂. The edge rise of our films falls between that of the references, which indicates that the average Mn valence is between + 3 and + 4 in the film. The spectra of MnO_x showed negligible changes.

As catalysis is a surface process, we turned our attention to soft x-ray spectroscopy accessed by the electron yield mode. The escape depth of the electrons is 2.6 ± 0.3 nm at the Mn-L edge of a comparable oxide [71], so that we probe the near surface regions of the samples. In contrast to the K edge XANES, we found clear changes with cycling near the surface at the L₃ edge (figure 4(c)). The main peaks of the references Mn^{2.6+}₃O₄ and β -Mn⁴⁺O₂ were labeled α 1- α 2 and β 1- β 2, respectively. Peak α 1 can be assigned to Mn²⁺ in tetrahedral coordination [38]. The Mn-L₃ spectrum of pristine MnO_x was broad and contained features of both references. We found a clear reduction of the normalized spectral intensity at the energies assigned to peaks α 1 and α 2 after 100 cycles (figure 4(b)). The spectrum of MnO_x after 100 cycles closely resembled that of the MnO₂ reference but a slight shoulder at the energy of α 1 remained.

We conclude that the MnO_x films were deposited as layers of edge-sharing octahedra with low long-range order. The local bulk structure was preserved upon cycling. There were no changes in the bulk, while the surface region of MnO_x oxidizes toward Mn⁴⁺ and Mn₃O₄ or another phase that contained tetrahedral Mn²⁺ was consumed but did not vanish completely. Having uncovered the local structure and surface valence changes on MnO_x, we can now interpret the trends during electrocatalytic cycling in this context. Irreversible catalyst changes lead to a decrease of the current ratio at all voltages below the onset of the OER. The current ratio at low overpotential achieved steady-state after 50 cycles, which did not persist after OCV. This irreversible decrease in current ratio could either be explained by loss of tetrahedral Mn²⁺, possibly as Mn₃O₄, at the surface or surface oxidation toward Mn⁴⁺. While the role of the former is not well understood, there is a broad consensus on the role of Mn⁴⁺ as discussed in the next paragraphs.

The most commonly studied oxide with tetrahedral Mn²⁺ is Mn₃O₄, which consists of tetrahedral Mn²⁺ and octahedral Mn³⁺ cations. Some studies state that (bulk) Mn₃O₄ is an active electrocatalyst [12, 72–74], while it is the least active catalyst in comparative studies [11, 25]. Thus, it is unclear if bulk Mn₃O₄ is an electrocatalyst as its electric conductivity is low [35] and other Mn oxide phases are found at the surface of bulk Mn₃O₄ such as amorphous Mn^{3+/4+}-oxide [75] or birnessite-type MnO_x [11, 76], both of which are formed at

voltages below the onset of the OER [77, 78]. Huynh *et al* [79] identified Mn_3O_4 as a precursor to an active birnessite-like phase. Finally, Wei *et al* [80] propose that only the octahedral Mn site is active for the OER in spinel oxides. In summary, tetrahedral Mn^{2+} is likely not directly relevant during the OER but may be important for the formation of the active phase and as a passivating phase that prevents Mn leaching [46]. The role of (octahedral) Mn^{4+} for the OER is better understood. Mn^{4+} forms at voltages below the onset of the OER [38, 46]. While many of the more active Mn-based electrocatalysts contain Mn^{4+} in addition to Mn^{3+} [10, 39, 40, 81–84], those with predominately Mn^{4+} are inactive [3]. Recently, Baumung *et al* [18] showed that (bulk) oxidation of $\text{LiMn}^{3.5+}_2\text{O}_4$ toward Mn^{4+} increases the overpotential of the OER. This can be rationalized qualitatively using the occupancy of the e_g orbitals as proposed by Suntivich *et al* [47] where the lowest overpotential is predicted for an e_g occupancy of about one (Mn^{3+}) and both higher or lower e_g occupancy (i.e. Mn^{2+} and Mn^{4+}) leads to an increase in overpotential. Yet, small amounts of Mn^{2+} and Mn^{4+} are beneficial if Mn comproportionation of these ions to Mn^{3+} is possible on the surface of the Mn oxide [44, 45]. Thus, the lowest overpotential in systematic studies of the OER on manganese oxides is usually found between $\text{Mn}^{3.5+}$ and $\text{Mn}^{3.7+}$ [3, 4, 38–40, 42], rather than Mn^{3+} . Nonetheless, materials with mainly Mn^{4+} perform significantly worse than those with sizable amount of Mn^{3+} , e.g. Köhlbach *et al* [85] attributed the formation of Mn^{4+} on the surface to deactivation of $\alpha\text{-Mn}_2\text{O}_3$ films and Rabe *et al* [46] identified the highest rate of Mn dissolution on MnO_2 during CV. Therefore, we conclude that the Mn^{4+} on the surface of our MnO_x films is responsible for the observed decrease in the current. Future studies should address the optimal amount of Mn^{4+} at the surface during the oxidizing conditions of the OER to maximize activity and to simultaneously prevent deactivation processes during catalyst conditioning or operation.

In addition to the previously reported irreversible change of manganese oxides, we also found that the film could be partially reactivated after 30 min at OCV (figures 2(b) and 3). The OCV was 0.97 V or lower and reached a steady-state for one sample at 0.88 V vs. RHE (figure S16). At these voltages, reduction of Mn^{4+} to Mn^{3+} is expected as shown by an *in situ* soft XAS study [38] and chemical reactions such as oxygen evolution by reduction of Mn^{4+} may occur [3]. We interpreted the increase of the measured current and of the Tafel slope as the reversible formation of an active state with a certain, still unknown, high coverage of catalytic intermediates, which could be associated with a valence change of the MnO_x surface. The elucidation of possible valence changes and thus the active state requires specialized *in situ* experiments which are beyond the scope of this report. We note that the identical exponents initially and after OCV suggest that Mn^{4+} is produced at the same rate after reactivation. The reactivation after OCV is significant for catalysis on manganese oxides and their activation protocol. Degradation tests based purely on electrochemical methods such as CV or voltage/current holding may suggest an irreversible material degradation while an optimized measurement protocol could recover some activity.

Conclusions

We deposited a Na-containing layered oxide of $\text{Mn}^{3+/4+}$ without long-range order in NaOH solution with a complexing agent added. The onset of the OER was at 1.7 V vs. RHE as determined by oxygen detection at the ring of an RRDE. We tracked the currents by CV during 100 cycles where 3 regions with different trends could be identified: 1–10 cycles, 10–40 cycles and 40–100 cycles. At voltages below the onset of the OER, the currents decrease with cycling but the OER currents at 1.75 V vs. RHE reached a steady-state in the 3rd region. Thus, an activation protocol at 100 mV s^{-1} should at least be performed for 40 cycles on our

MnO_x. The bulk of the cycled MnO_x film was not changed but its surface was oxidized toward Mn⁴⁺. It agrees with previous reports that the oxidized MnO_x surface hinders the OER. Interestingly, the currents during CV could be partially recovered after 30 min of OCV, which was not observed previously. We attribute the underlying process to high coverage with unreacted intermediates as supported by the high Tafel slopes. The reactivation after OCV is significant as some manganese oxides or Mn-containing oxides may be more robust as estimated based on continuous cycling. A measurement protocol without continuous cycling may prevent some but not all activity-reducing processes. Coupling of electrocatalysts to intermittent sources such as solar energy naturally leads to OCV conditions during operation. Therefore, it is important how an electrocatalyst for sustainable fuel production reacts to OCV, which is understudied.

Acknowledgments

We acknowledge Denis Antipin, Max Baumung, Florian Schönewald, Dr. Daowei Gao and Dr. Laura Pardo for helping in data collection. Frederik Stender is thanked for writing the electrochemistry analysis script and Dr. Petko Chernev for permission to use his software SimXLite. We thank Helmholtz-Zentrum Berlin (HZB) for the allocation of synchrotron radiation beamtime and acknowledge the HZB CoreLab CCMS (Correlative Microscopy and Spectroscopy) for training and advising in SEM. This project has received funding from the European Research Council (ERC) under the European Union's Horizon 2020 research and innovation programme under grant agreement No 804092.

Conflict of interest

The authors declare no conflict of interest.

ORCID iDs

Javier Villalobos <https://orcid.org/0000-0002-8032-6574>

Marcel Risch <https://orcid.org/0000-0003-2820-7006>

References

- [1] Köhler L, Ebrahimizadeh Abrishami M, Roddatis V, Geppert J and Risch M 2017 Mechanistic parameters of electrocatalytic water oxidation on LiMn₂O₄ in comparison to natural photosynthesis *ChemSusChem* **10** 4479–90
- [2] Najafpour M M, Heidari S, Balaghi S E, Hołynska M, Sadr M H, Soltani B, Khatamian M, Larkum A W and Allakhverdiev S I 2017 Proposed mechanisms for water oxidation by Photosystem II and nanosized manganese oxides *Biochim. Biophys. Acta – Bioenerg.* **1858** 156–74
- [3] Zaharieva I, Gonz'alez-Flores D, Asfari B, Pasquini C, Mohammadi M R, Klingan K, Zizak I, Loos S, Chernev P and Dau H 2016 Water oxidation catalysis – role of redox and structural dynamics in biological photosynthesis and inorganic manganese oxides *Energy Environ. Sci.* **9** 2433–43
- [4] Melder J, Bogdanoff P, Zaharieva I, Fiechter S, Dau H and Kurz P 2020 Water-oxidation electrocatalysis by manganese oxides: syntheses, electrode preparations, electrolytes and two fundamental questions *Zeitschrift Fur Phys. Chemie* **234** 925–78
- [5] Najafpour M M, Renger G, Hołynska M, Moghaddam A N, Aro E-M, Carpentier R, Nishihara H, Eaton-Rye J J, Shen J-R and Allakhverdiev S I 2016 Manganese compounds as water-oxidizing catalysts: from the natural water-oxidizing complex to nanosized manganese oxide structures *Chem. Rev.* **116** 2886–936
- [6] Wiechen M, Najafpour M M, Allakhverdiev S I and Spiccia L 2014 Water oxidation catalysis by manganese oxides: learning from evolution *Energy Environ. Sci.* **7** 2203–12
- [7] Gao Q, Ranjan C, Pavlovic Z, Blume R and Schlögl R 2015 Enhancement of stability and activity of MnO_x/Au electrocatalysts for oxygen evolution through adequate electrolyte composition *ACS Catal.* **5** 7265–75
- [8] Kurz P 2016 Biomimetic water-oxidation catalysts: manganese oxides *Solar Energy for Fuels* (Berlin: Springer) pp 49–72
- [9] Kumbhar V S, Lee H, Lee J and Lee K 2019 Recent advances in water-splitting electrocatalysts based on manganese oxide *Carbon Resour. Convers.* **2** 242–55

- [10] Smith P F *et al* 2016 Coordination geometry and oxidation state requirements of corner sharing MnO₆ octahedra for water oxidation catalysis: an investigation of manganite (γ -MnOOH) *X ACS Catal.* **6** 2089–99
- [11] Ramírez A, Hillebrand P, Stellmach D, May M M, Bogdanoff P and Fiechter S 2014 Evaluation of MnO_x, Mn₂O₃, and Mn₃O₄ electrodeposited films for the oxygen evolution reaction of water *J. Phys. Chem. C* **118** 14073–81
- [12] Gorlin Y and Jaramillo T F 2010 A bifunctional nonprecious metal catalyst for oxygen reduction and water oxidation *J. Am. Chem. Soc.* **132** 13612–4
- [13] Zaharieva I, Chernev P, Risch M, Klingan K, Kohlhoff M, Fischer A and Dau H 2012 Electrosynthesis, functional, and structural characterization of a water-oxidizing manganese oxide *Energy Environ. Sci.* **5** 7081–9
- [14] Frey C E, Wiechen M and Kurz P 2014 Water-oxidation catalysis by synthetic manganese oxides-systematic variations of the calcium birnessite theme *Dalt. Trans.* **43** 4370–9
- [15] Heese-Gärtlein J, Morales D, Rabe A, Bredow T, Schuhmann W and Behrens M 2020 Factors governing the activity of α -MnO₂ catalysts in the oxygen evolution reaction: conductivity vs. exposed surface area of cryptomelane *Chem. – A Eur. J.* (submitted) (<https://doi.org/10.1002/chem.201905090>)
- [16] Song L, Duan Y, Liu J and Pang H 2020 Transformation between nanosheets and nanowires structure in MnO₂ upon providing Co²⁺ ions and applications for microwave absorption *Nano Res.* **13** 95–104
- [17] Geiger S, Kasian O, Mingers A M, Nicley S S, Haenen K, Mayrhofer K J J and Cherevko S 2017 Catalyst stability benchmarking for the oxygen evolution reaction: the importance of backing electrode material and dissolution in accelerated aging studies *ChemSusChem* **10** 4140–3
- [18] Baumung M, Kollenbach L, Xi L and Risch M 2019 Undesired bulk oxidation of LiMn₂O₄ increases overpotential of electrocatalytic water oxidation in lithium hydroxide electrolytes *ChemPhysChem* **20** 2981–8
- [19] Risch M, Grimaud A, May K J, Stoerzinger K A, Chen T J, Mansour A N and Shao-Horn Y 2013 Structural changes of cobalt-based perovskites upon water oxidation investigated by EXAFS *J. Phys. Chem. C* **117** 8628–35
- [20] May K J, Carlton C E, Stoerzinger K A, Risch M, Suntivich J, Lee Y-L, Grimaud A and Shao-Horn Y 2012 Influence of oxygen evolution during water oxidation on the surface of perovskite oxide catalysts *J. Phys. Chem. Lett.* **3** 3264–70
- [21] Speck F D, Santori P G, Jaouen F and Cherevko S 2019 Mechanisms of manganese oxide electrocatalysts degradation during oxygen reduction and oxygen evolution reactions *J. Phys. Chem. C* **123** 25267–77
- [22] Liu Y, Liang X, Gu L, Zhang Y, Li G D, Zou X and Chen J S 2018 Corrosion engineering towards efficient oxygen evolution electrodes with stable catalytic activity for over 6000 hours *Nat. Commun.* **9** 2609
- [23] Lee J, Kim I and Park S 2019 Boosting stability and activity of oxygen evolution catalyst in acidic medium: bimetallic Ir–Fe oxides on reduced graphene oxide prepared through ultrasonic spray pyrolysis *ChemCatChem* **11** 2615–23
- [24] Eßmann V, Barwe S, Masa J and Schuhmann W 2016 Bipolar electrochemistry for concurrently evaluating the stability of anode and cathode electrocatalysts and the overall cell performance during long-term water electrolysis *Anal. Chem.* **88** 8835–40
- [25] Huynh M, Shi C, Billinge S J L and Nocera D G 2015 Nature of activated manganese oxide for oxygen evolution *J. Am. Chem. Soc.* **137** 14887–904
- [26] Zhao S, Yu H, Maric R, Danilovic N, Capuano C B, Ayers K E and Mustain W E 2015 Calculating the electrochemically active surface area of iridium oxide in operating proton exchange membrane electrolyzers *J. Electrochem. Soc.* **162** F1292–8
- [27] Xiao Q, Zhang Y, Guo X, Jing L, Yang Z, Xue Y, Yan Y M and Sun K 2014 A high-performance electrocatalyst for oxygen evolution reactions based on electrochemical post-treatment of ultrathin carbon layer coated cobalt nanoparticles *Chem. Commun.* **50** 13019–22
- [28] Oh H S, Nong H N, Reier T, Bergmann A, Gliech M, Ferreira De Araujo J, Willinger E, Schlögl R, Teschner D and Strasser P 2016' Electrochemical catalyst-support effects and their stabilizing role for IrO_x nanoparticle catalysts during the oxygen evolution reaction *J. Am. Chem. Soc.* **138** 12552–63
- [29] Song F, Schenk K and Hu X 2016 A nanoporous oxygen evolution catalyst synthesized by selective electrochemical etching of perovskite hydroxide CoSn(OH)₆ nanocubes *Energy Environ. Sci.* **9** 473–7
- [30] Song F and Hu X 2014 Ultrathin cobalt-manganese layered double hydroxide is an efficient oxygen evolution catalyst *J. Am. Chem. Soc.* **136** 16481–4
- [31] Villalobos J *et al* 2019 Structural and functional role of anions in electrochemical water oxidation probed by arsenate incorporation into cobalt-oxide materials *Phys. Chem. Chem. Phys.* **21** 12485–93
- [32] Frydendal R, Paoli E A, Knudsen B P, Wickman B, Malacrida P, Stephens I E L and Chorkendorff I 2014 Benchmarking the stability of oxygen evolution reaction catalysts: the importance of monitoring mass losses *ChemElectroChem* **1** 2075–81
- [33] Geiger S *et al* 2018 The stability number as a metric for electrocatalyst stability benchmarking *Nat. Catal.* **1** 508–15
- [34] Baumung M, Schönewald F, Erichsen T, Volkert C A and Risch M 2019 Influence of particle size on the apparent electrocatalytic activity of LiMn₂O₄ for oxygen evolution *Sustain. Energy Fuels* **3** 2218–26
- [35] Gorlin Y, Lassalle-Kaiser B, Benck J D, Gul S, Webb S M, Yachandra V K, Yano J and Jaramillo T F 2013 In situ X-ray absorption spectroscopy investigation of a bifunctional manganese oxide catalyst with high activity for electrochemical water oxidation and oxygen reduction *J. Am. Chem. Soc.* **135** 8525–34
- [36] Walter C, Menezes P W, Loos S, Dau H and Driess M 2018 Facile formation of nanostructured manganese oxide films as high-performance catalysts for the oxygen evolution reaction *ChemSusChem* **11** 2554–61
- [37] Yang Y *et al* 2019 In situ x-ray absorption spectroscopy of a synergistic Co–Mn oxide catalyst for the oxygen reduction reaction *J. Am. Chem. Soc.* **141** 1463–6
- [38] Risch M, Stoerzinger K A, Han B, Regier T Z, Peak D, Sayed S Y, Wei C, Xu Z J and Shao-Horn Y 2017 Redox processes of manganese oxide in catalyzing oxygen evolution and reduction: an in situ soft x-ray absorption spectroscopy study *J. Phys. Chem. C* **121** 17682–92
- [39] Tesch M F *et al* 2019 Evolution of oxygen–metal electron transfer and metal electronic states during manganese oxide catalyzed water oxidation revealed with in situ soft x-ray spectroscopy *Angew. Chemie* **131** 3464–70

- [40] Xi L, Schwanke C, Xiao J, Abdi F F, Zaharieva I and Lange K M 2017 In situ L-edge XAS study of a manganese oxide water oxidation catalyst *J. Phys. Chem. C* **121** 12003–9
- [41] Seitz L C, Hersbach T J P, Nordlund D and Jaramillo T F 2015 Enhancement effect of noble metals on manganese oxide for the oxygen evolution reaction *J. Phys. Chem. Lett.* **6** 4178–83
- [42] Lian S, Browne M P, Domínguez C, Stamatini S N, Nolan H, Duesberg G S, Lyons M E G, Fonda E and Colavita P E 2017 Template-free synthesis of mesoporous manganese oxides with catalytic activity in the oxygen evolution reaction *Sustain. Energy Fuels* **1** 780–8
- [43] Gorlin Y, Chung C-J, Benck J D, Nordlund D, Seitz L, Weng T-C, Sokaras D, Clemens B M and Jaramillo T F 2014 Understanding interactions between manganese oxide and gold that lead to enhanced activity for electrocatalytic water oxidation *J. Am. Chem. Soc.* **136** 4920–6
- [44] Takashima T, Hashimoto K and Nakamura R 2012 Mechanisms of pH-dependent activity for water oxidation to molecular oxygen by MnO₂ electrocatalysts *J. Am. Chem. Soc.* **134** 1519–27
- [45] Ooka H, Takashima T, Yamaguchi A, Hayashi T and Nakamura R 2017 Element strategy of oxygen evolution electrocatalysis based on: in situ spectroelectrochemistry *Chem. Commun.* **53** 7149–61
- [46] Rabe M, Toparli C, Chen Y H, Kasian O, Mayrhofer K J J and Erbe A 2019 Alkaline manganese electrochemistry studied by: in situ and operando spectroscopic methods-metal dissolution, oxide formation and oxygen evolution *Phys. Chem. Chem. Phys.* **21** 10457–69
- [47] Suntivich J *et al* 2011 A perovskite oxide optimized for oxygen evolution catalysis from molecular orbital principles *Science* **334** 1383–5
- [48] Köhler L, Szabadics L, Jooss C and Risch M 2019 Peroxide yield of the (001) La_{0.6}Sr_{0.4}MnO₃ surface as a bifunctional electrocatalyst for the oxygen reduction reaction and oxygen evolution reaction in alkaline media *Batter. Supercaps* **2** 364–72
- [49] Aziz E F, Xiao J, Golnak R and Tesch M 2016 LiXEDrom: high energy resolution RIXS station dedicated to Liquid Investigation at BESSY II *J. Large-scale Res. Facil. JLSRF* **2** A80
- [50] Risch M, Stoerzinger K A, Regier T Z, Peak D, Sayed S Y and Shao-Horn Y 2015 Reversibility of ferri-/ferrocyanide redox during operando soft x-ray spectroscopy *J. Phys. Chem. C* **119** 18903–10
- [51] Többsen D M and Zander S 2016 KMC-2: an X-ray beamline with dedicated diffraction and XAS endstations at BESSY II *J. Large-scale Res. Facil. JLSRF* **2** A49
- [52] Erko A, Packe I, Gudat W, Abrosimov N and Firsov A 2001 A crystal monochromator based on graded SiGe crystals *Nucl. Instrum. Methods Phys. Res.* **467–468** 623–6
- [53] Ankudinov A and Ravel B 1998 Real-space multiple-scattering calculation and interpretation of x-ray-absorption near-edge structure *Phys. Rev. B* **58** 7565–76
- [54] Fontana C 1926 Struttura dell'ossido manganoso *Gazz. Chim. Ital.* **56** 396–7
- [55] Koza J A, Schroen I P, Willmering M M and Switzer J A 2014 Electrochemical synthesis and nonvolatile resistance switching of Mn₃O₄ thin films *Chem. Mater.* **26** 4425–32
- [56] Guo X, Wu F, Hao G, Peng S, Wang N, Li Q, Hu Y and Jiang W 2019 Activating hierarchically hortensia-like CoAl layered double hydroxides by alkaline etching and anion modulation strategies for the efficient oxygen evolution reaction *Dalt. Trans.* **48** 5214–21
- [57] Wang X, Tong R, Wang Y, Tao H, Zhang Z and Wang H 2016 Surface roughening of nickel cobalt phosphide nanowire arrays/Ni foam for enhanced hydrogen evolution activity *ACS Appl. Mater. Interfaces* **8** 34270–9
- [58] Jiang T, Ansar S A, Yan X, Chen C, Fan X, Razmjooei F, Reisser R, Montavon G and Liao H 2019 In situ electrochemical activation of a codoped heterogeneous system as a highly efficient catalyst for the oxygen evolution reaction in alkaline water Electrolysis *ACS Appl. Energy Mater.* **2** 8809–17
- [59] Wei C, Rao R R, Peng J, Huang B, Stephens I E L, Risch M, Xu Z J and Shao-Horn Y 2019 Recommended practices and benchmark activity for hydrogen and oxygen electrocatalysis in water splitting and fuel cells *Adv. Mater.* **31** 1806296
- [60] McCrory C C L, Jung S, Peters J C and Jaramillo T F 2013 Benchmarking heterogeneous electrocatalysts for the oxygen evolution reaction *J. Am. Chem. Soc.* **135** 16977–87
- [61] Doyle R L, Godwin I J, Brandon M P and Lyons M E 2013 Redox and electrochemical water splitting catalytic properties of hydrated metal oxide modified electrodes *Phys. Chem. Chem. Phys.* **15** 13737–83
- [62] El-Sayed H A, Weiß A, Olbrich L F, Putro G P and Gasteiger H A 2019 OER catalyst stability investigation using RDE technique: a stability measure or an artifact? *J. Electrochem. Soc.* **166** F458–64
- [63] Scholz J, Risch M, Stoerzinger K A, Wartner G, Shao-Horn Y and Jooss C 2016 Rotating ring-disk electrode study of oxygen evolution at a perovskite surface: correlating activity to manganese concentration *J. Phys. Chem. C* **120** 27746–56 [64] Fletcher S 2008 Tafel slopes from first principles *J. Solid State Electrochem.* **13** 537–49
- [65] Bockris J O 1956 Kinetics of activation controlled consecutive electrochemical reactions: anodic evolution of oxygen *J. Chem. Phys.* **24** 817
- [66] Jaklevic J, Kirby J A, Klein M P, Robertson A S, Brown G S and Eisenberger P 1977 Fluorescence detection of EXAFS: sensitivity enhancement for dilute species and thin films *Solid State Commun.* **23** 679–82
- [67] Koningsberger D C, Mojet B L, van Dorssen G E and Ramaker D E 2000 XAFS spectroscopy: fundamental principles and data analysis *Top. Catal.* **10** 143–55
- [68] Calvin S 2013 *XAFS for Everyone* (Boca Raton, FL: CRC Press)
- [69] Iyer A, Del-Pilar J, King'ondo C K, Kissel E, Garces H F, Huang H, El-Sawy A M, Dutta P K and Suib, S L 2012 Water oxidation catalysis using amorphous manganese oxides, octahedral molecular sieves (OMS-2), and octahedral layered (OL-1) manganese oxide structures *J. Phys. Chem. C* **116** 6474–83
- [70] Abrashev M V, Chervnev P, Kubella P, Mohammadi M R, Pasquini C, Dau H and Zaharieva I 2019 Origin of the heat-induced improvement of catalytic activity and stability of MnO_x electrocatalysts for water oxidation *J. Mater. Chem. A* **7** 17022–36
- [71] Ruosi A, Raisch C, Verna A, Werner R, Davidson B A, Fujii J, Kleiner R and Koelle D 2014 Electron sampling depth and saturation effects in perovskite films investigated by soft x-ray absorption spectroscopy *Phys. Rev. B* **90** 125120

- [72] Maruthapandian V, Pandiarajan T, Saraswathy V and Muralidharan S 2016 Oxygen evolution catalytic behaviour of Ni doped Mn_3O_4 in alkaline medium *RSC Adv.* **6** 48995–9002
- [73] Guo C X, Chen S and Lu X 2014 Ethylenediamine-mediated synthesis of Mn_3O_4 nano-octahedrons and their performance as electrocatalysts for the oxygen evolution reaction *Nanoscale* **6** 10896–901
- [74] Rani B J, Ravi G, Yuvakkumar R, Hong S I, Velauthapillai D, Thambidurai M, Dang C and Saravanakumar B 2020 Neutral and alkaline chemical environment dependent synthesis of Mn_3O_4 for oxygen evolution reaction (OER) *Mater. Chem. Phys.* **247** 122864
- [75] Frey C E *et al* 2017 Evaporated manganese films as a starting point for the preparation of thin-layer MnO : X water-oxidation anodes *Sustain. Energy Fuels* **1** 1162–70
- [76] Fekete M, Hocking R K, Chang S L Y, Italiano C, Patti A F, Arena F and Spiccia L 2013 Highly active screen-printed electrocatalysts for water oxidation based on β -manganese oxide *Energy Environ. Sci.* **6** 2222–32
- [77] Messaoudi B, Joiret S, Keddam M and Takenouti H 2001 Anodic behaviour of manganese in alkaline medium *Electrochim. Acta* **46** 2487–98
- [78] Su H-Y, Gorlin Y, Man I C, Calle-Vallejo F, Nørskov J K, Jaramillo T F and Rossmeisl J 2012 Identifying active surface phases for metal oxide electrocatalysts: a study of manganese oxide bi-functional catalysts for oxygen reduction and water oxidation catalysis *Phys. Chem. Chem. Phys.* **14** 14010–22
- [79] Huynh M, Bediako D K and Nocera D G 2014 A functionally stable manganese oxide oxygen evolution catalyst in acid *J. Am. Chem. Soc.* **136** 6002–10
- [80] Wei C, Feng Z, Scherer G G, Barber J, Shao-Horn Y and Xu Z J 2017 Cations in octahedral sites: a descriptor for oxygen electrocatalysis on transition-metal spinels *Adv. Mater.* **29** 1521–4095
- [81] Chan Z M, Kitchaev D A, Weker J N, Schnedermann C, Lim K, Ceder G, Tumas W, Toney M F and Nocera D G 2018 Electrochemical trapping of metastable Mn^{3+} ions for activation of MnO_2 oxygen evolution catalysts *Proc. Natl Acad. Sci. USA* **115** E5261–8
- [82] Surendranath Y, Lutterman D A, Liu Y and Nocera D G 2012 Nucleation, growth, and repair of a cobalt-based oxygen evolving catalyst *J. Am. Chem. Soc.* **134** 6326–36
- [83] Khan M, Suljoti E, Singh A, Bonke S A, Brandenburg T, Atak K, Golnak R, Spiccia L and Aziz E F 2014 Electronic structural insights into efficient MnO_x catalysts *J. Mater. Chem. A* **2** 18199–203
- [84] Raabe S, Mierwaldt D, Ciston J, Uijtewaal M, Stein H, Hoffmann J, Zhu Y, Blöchl P and Jooss C 2012 In situ electrochemical electron microscopy study of oxygen evolution activity of doped manganite perovskites *Adv. Funct. Mater.* **22** 3378–88
- [85] Kölbach M, Fiechter S, van de Krol R and Bogdanoff P 2017 Evaluation of electrodeposited α - Mn_2O_3 as a catalyst for the oxygen evolution reaction *Catal. Today* **290** 2–9

Supplementary material

Reversible and irreversible processes during cyclic voltammetry of an electrodeposited manganese oxide as catalyst for the oxygen evolution reaction

Javier Villalobos¹, Ronny Golnak², Lifei Xi¹, Götz Schuck³ and Marcel Risch^{1,4,*}

¹ *Nachwuchsgruppe Gestaltung des Sauerstoffentwicklungsmechanismus, Helmholtz-Zentrum Berlin für Materialien und Energie GmbH, Hahn-Meitner Platz 1, 14109 Berlin, Germany*

² *Department of Highly Sensitive X-ray Spectroscopy, Helmholtz-Zentrum Berlin für Materialien und Energie, Albert-Einstein-Straße 15, 12489 Berlin, Germany*

³ *Department of Structure and Dynamics of Energy Materials, Helmholtz-Zentrum Berlin für Materialien und Energie, Hahn-Meitner Platz 1, 14109 Berlin, Germany*

⁴ *Institut für Materialphysik, Georg-August-Universität Göttingen, Friedrich-Hund-Platz 1, 37077 Göttingen, Germany*

Corresponding author

* marcel.risch@helmholtz-berlin.de

11 pages, 3 supplementary tables, 16 supplementary figures

Table S1. General protocol for electrochemical data collection on an RRDE station with samples on glassy carbon disks. All potentials are reported vs. RHE (pH 13).

Step	Conditions
1. Cleaning	Clean and polish electrodes, cells and any other tool properly.
2. Calibration of reference electrodes	OCV against commercial RHE electrode
3. Argon purge at OCV	At least 30 minutes
4.a. Ring EIS	Frequency: 1 MHz – 1 Hz. Points/decade: 10 OCV and take note of Ru
4.b. Disk EIS	Frequency: 1 MHz – 1 Hz. Points/decade: 10 OCV and take note of Ru
5. Disk CV: ECSA*	Hold 10 s at 1.0 V. Potential window: 0.95 V – 1.05 V. Scan rates: 50, 100, 150, 200, 250, 300, 350, 400, 450, 500 mV s ⁻¹ . Cycles: 3. Rotation: 0 rpm. Purge: Blanket. No dynamic iR compensation.
6.a. Ring conditioning	Hold ring potential for 1800 s at 0.40 V.
6.b. Ring: CA (O₂ detection)	Hold ring potential at 0.40 V.
6.c. Disk CV: OER	Potential window: 1.40 V - 1.80 V Scan rate: 100 mV/s Step size: 2 mV Cycles: 100 Rotation: 1600 rpm Purge: yes No dynamic iR compensation.
7. Disk CV: ECSA*	Hold 10 s at 1.0 V. Potential window: 0.95 V – 1.05 V. Scan rates: 50, 100, 150, 200, 250, 300, 350, 400, 450, 500 mV s ⁻¹ . Cycles: 3. Rotation: 0 rpm. Purge: Blanket. No dynamic iR compensation.
8. Disk OCV	1800 s
9.a. Disk EIS	Frequency: 1 MHz – 1 Hz. OCV and take note of Ru
9.b. Ring EIS	Frequency: 1 MHz – 1 Hz. OCV and take note of Ru
10.a. Ring conditioning	Hold ring potential for 1800 s at 0.40 V.
10.b. Ring: CA (O₂ detection)	Hold ring potential at 0.40 V.
11. Disk CV: OER	Potential window: 1.40 V - 1.80 V

	Scan rate: 100 mV/s Step size: 2 mV Cycles: 10 Rotation: 1600 rpm Purge: yes No dynamic iR compensation.
--	-------------------------------------------------------------------------------------------------------------------------

* not used due to inappropriate data for analysis.

Table S2. General protocol for electrochemical data collection with samples on graphite foil. All potentials are reported vs. RHE (pH 13).

1. Cleaning	Clean and polish electrodes, cells and any other tool properly.
2. Calibration of reference electrodes	OCV against commercial RHE electrode
3. Argon purge at OCV	At least 30 minutes
4. Foil CV: OER	Potential window: 1.40 V - 1.80 V Scan rate: 100 mV/s Step size: 2 mV Cycles: 100 Rotation: 1600 rpm Purge: yes No dynamic iR compensation
5. Sample rinsing	Soaked in deionized water for 5 minutes.

Table S3. Summary of the fit parameters from three sets of data used for Tafel slope calculation and their average. One example of the graphs involved in the calculation is shown in Figure S11. The average of the three values for each cycle and each sample is used to generate Figure 3b. SD represents the standard deviation of the three measurements.

Cycle	Slope \pm error (R ²)			Average \pm SD
	Sample A	Sample B	Sample C	
2	170 \pm 1 (0.999)	160 \pm 1 (0.999)	230 \pm 1 (0.999)	186 \pm 48
3	168 \pm 1 (0.999)	151 \pm 1 (0.999)	224 \pm 1 (0.999)	181 \pm 46
5	165 \pm 1 (0.999)	141 \pm 1 (0.999)	212 \pm 1 (0.999)	172 \pm 37
10	162 \pm 1 (0.999)	128 \pm 1 (0.999)	189 \pm 1 (0.999)	159 \pm 30
20	159 \pm 1 (0.999)	118 \pm 1 (0.999)	162 \pm 1 (0.999)	146 \pm 25
50	147 \pm 1 (0.999)	108 \pm 1 (0.999)	126 \pm 1 (0.999)	127 \pm 20
100	135 \pm 1 (0.999)	102 \pm 1 (0.998)	106 \pm 1 (0.999)	114 \pm 18
2aOCV*	165 \pm 1 (0.999)	133 \pm 1 (0.999)	179 \pm 1 (0.999)	159 \pm 23
10aOCV*	149 \pm 1 (0.999)	107 \pm 1 (0.999)	137 \pm 1 (0.999)	131 \pm 22

* aOCV = after OCV break.

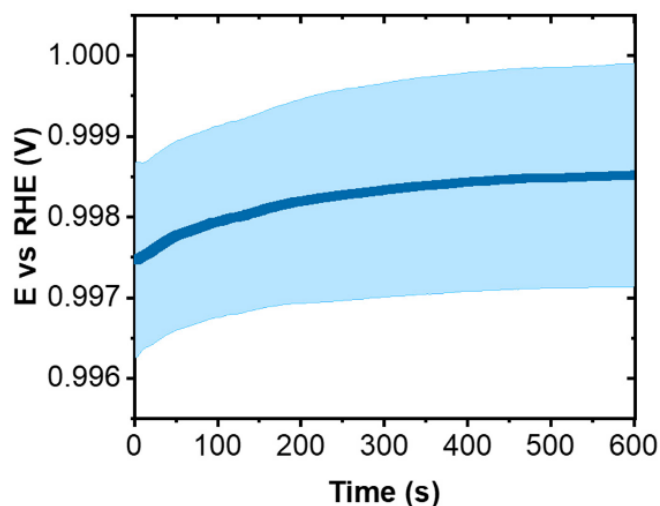


Figure S1. Calibration of reference electrode (SCE) vs. RHE. The blue line represents one single measurement and the light blue shade the error (standard deviation) of the measurements of the same two electrodes on three different days.

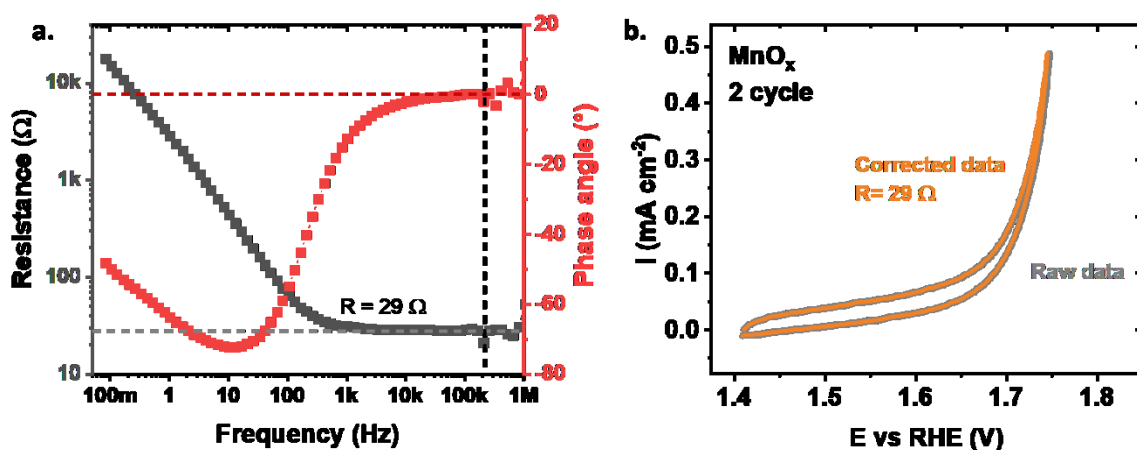


Figure S2. Example of data treatment of MnO_x after 2 cycles of catalysis: **a.** Electrochemical impedance spectrum (EIS) showing resistance (black) and phase angle (red) as function of frequency. Dashed lines represent the resistance value where the phase angle approaches zero. **b.** CV of cycle 2 with the correction of the raw data (gray) by a resistance value = 29Ω , and the resulting corrected CV (orange).

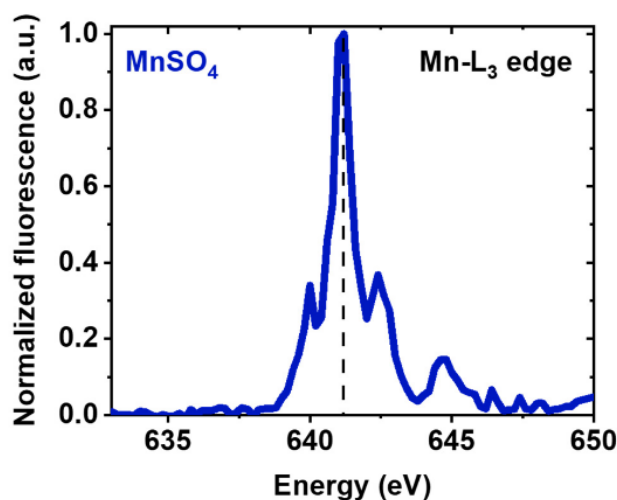


Figure S3. Mn-L₃ edge spectrum of MnSO₄, used as a reference for energy calibration. The dashed line was calibrated to 641 eV.

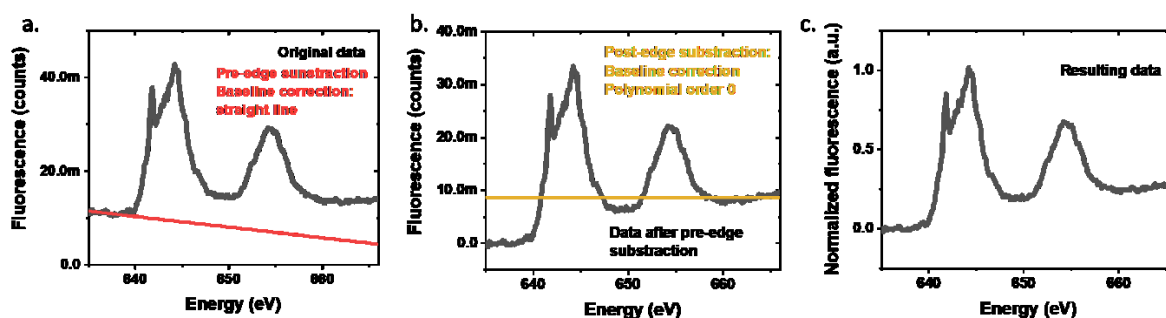


Figure S4. Spectra of a representative normalization for soft XAS of Mn-L₃ edge: **a.** Raw data (black) and baseline (red) for fitting before the edge (fit between 632 and 638 eV), **b.** Data after pre-edge subtraction (black) and baseline for fitting after the edge (yellow; fit between 660 and 667 eV), **c.** Final normalized spectrum.

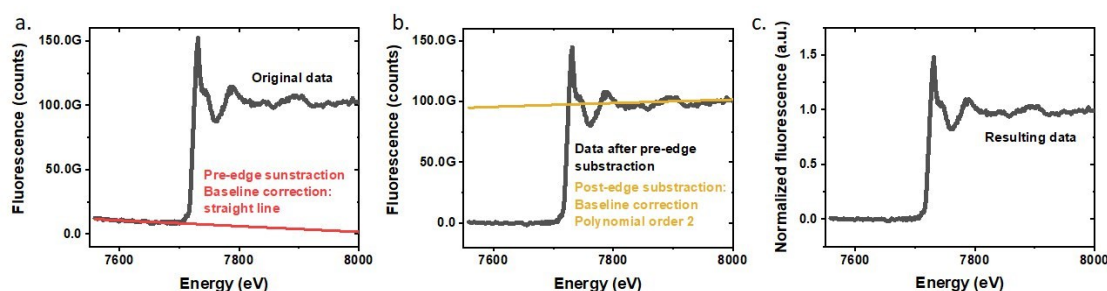


Figure S5. Spectra of a representative normalization for hard XAS of Mn-K edge (zoom on near edge region): **a.** Raw data (black) and baseline (red) for fitting before the edge (fit between 7560 and 7695 eV), **b.** Data after pre-edge subtraction (black) and fitted polynomial for division after the edge (yellow; fit between 7960 and 8255 eV) on a wider energy range as the shown spectrum, **c.** Final normalized spectrum.

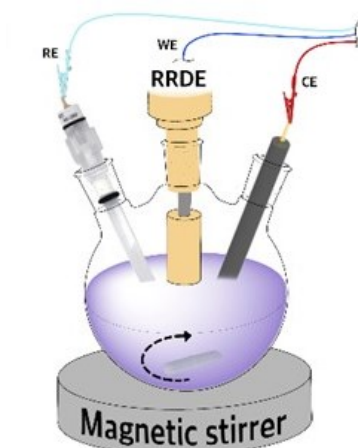


Figure S6. Scheme of the 3-electrode cell and RDE used for the electrodeposition of the films on glassy carbon.

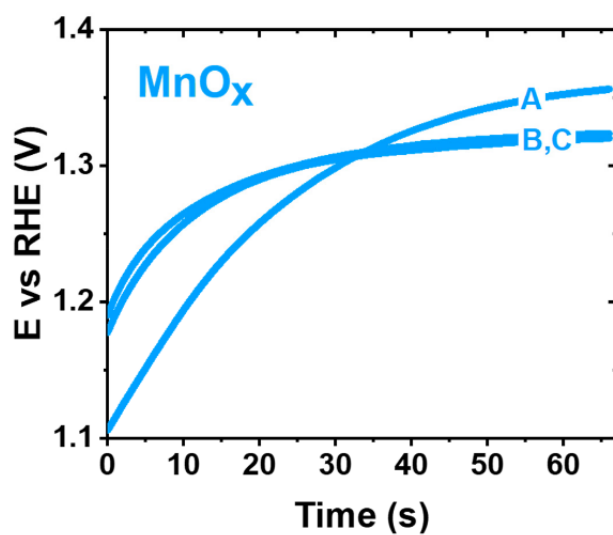


Figure S7. Chronopotentiometry during electrodeposition of MnO_x samples A, B and C on graphite foil to be characterized by XAS.

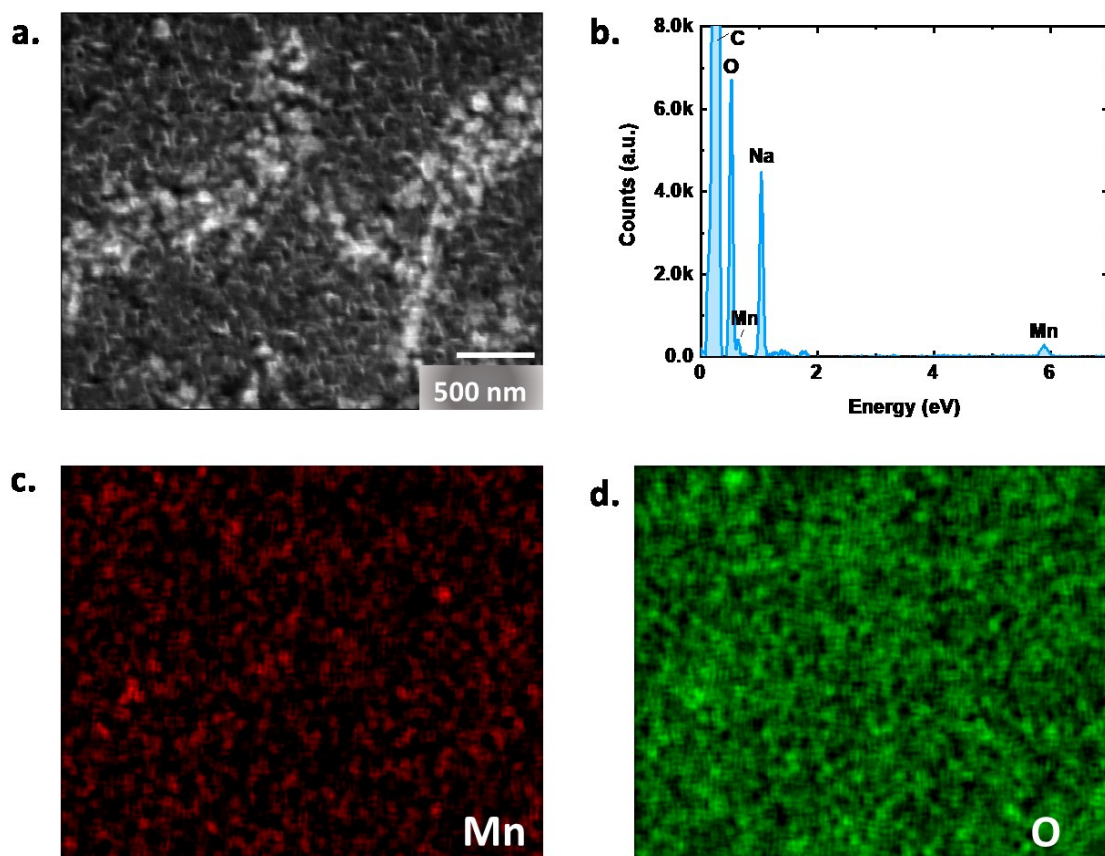


Figure S8. SEM-EDX analysis of pristine MnO_x films on glassy carbon. a. Gray contrast image, b. EDX spectrum. Elemental mapping by EDX of c. Manganese and d. Oxygen.

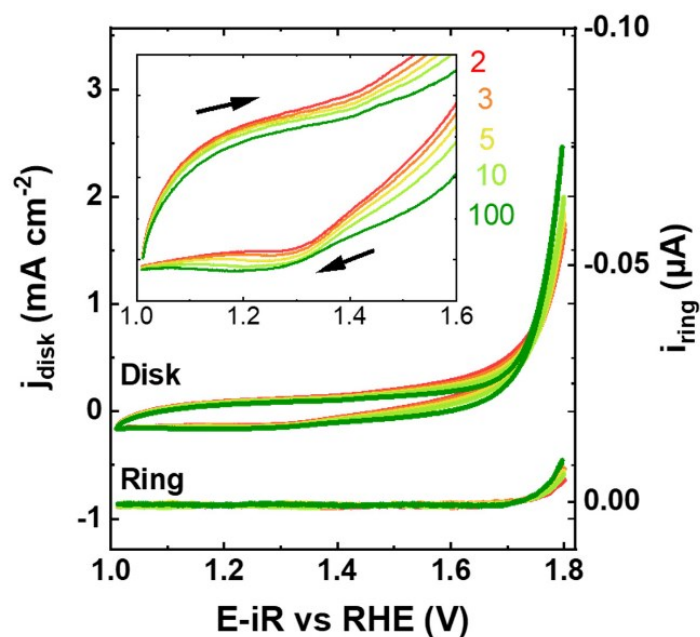


Figure S9. CV performed on a MnO_x-covered disk and step potential of 0.4 V vs. RHE at the ring. The was performed with a scan rate of 100 mV s⁻¹ in 0.1 M NaOH with rotation: 1600 rpm. This sample was measured with lower voltage boundary as samples shown in Fig. 2a. The

inset shows a zoom of the region of interest due to the presence of redox peaks. The arrows indicate the direction of the scan.

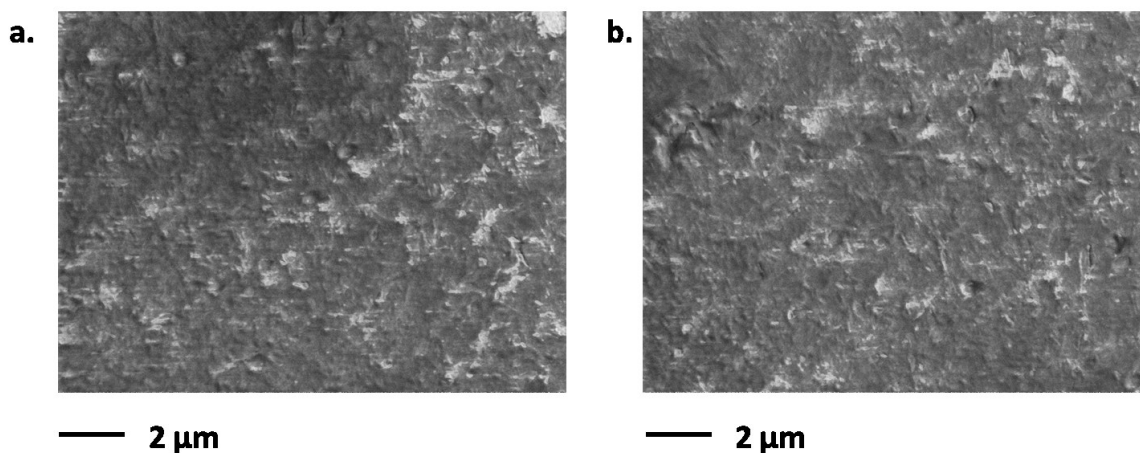


Figure S10. SEM images of: **a.** Pristine MnO_x and **b.** MnO_x after 100 cycles of OER catalysis. These measurements correspond to sample A.

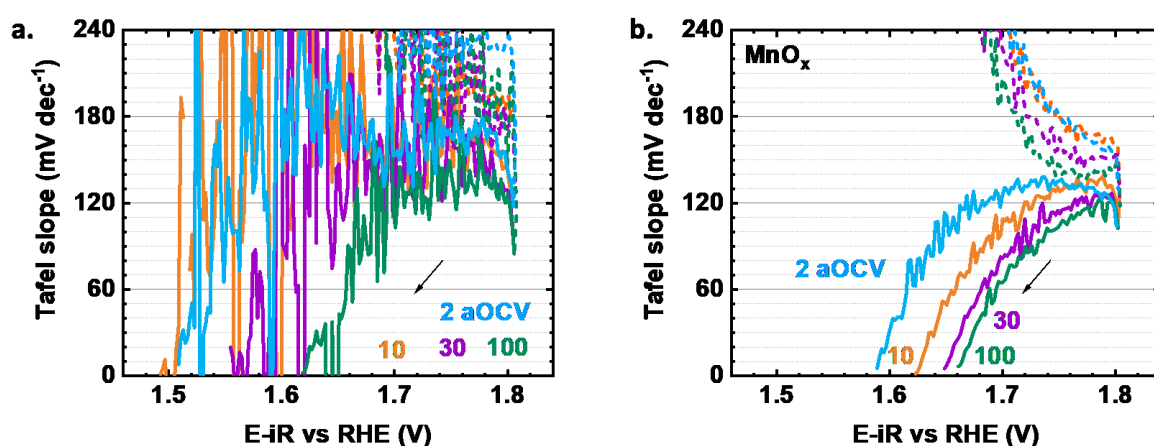


Figure S11. Instantaneous Tafel slope as function of potential of additional MnO_x films: **a.** Sample A and **b.** Sample B. Before OCV, cycles 10, 50 and 100 are shown, and after OCP cycle 2 is shown (2aOCV). All Tafel slope values were calculated from CVs with a scan rate of 100 mV s^{-1} in 0.1 M NaOH rotated at 1600 rpm . iR correction was done in post-processing. Arrows shows the direction of the CV.

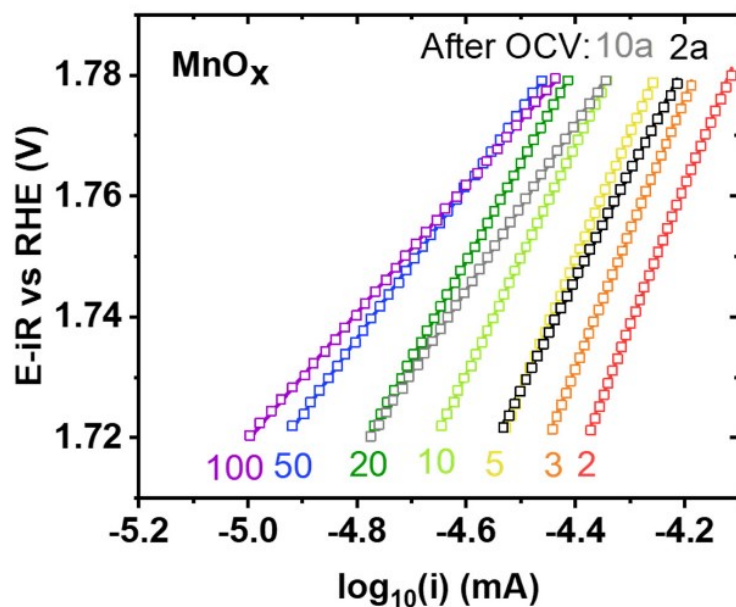


Figure S12. Representative graphs of Tafel slope calculation for selected cycles (2, 3, 5, 10, 20, 50, 100, 2 after OCV and 10 after OCV). Tafel plots of MnO_x . The measurements were performed in 0.1 M NaOH pH 13. Scan rate 100 mV s^{-1} . iR compensation was performed during post-processing. The lines represent the linear fit (denoted E-iR) of E-iR as function of $\log_{10}(i)$, the slope represents the Tafel slope. All fit parameters are summarized in Table S3.

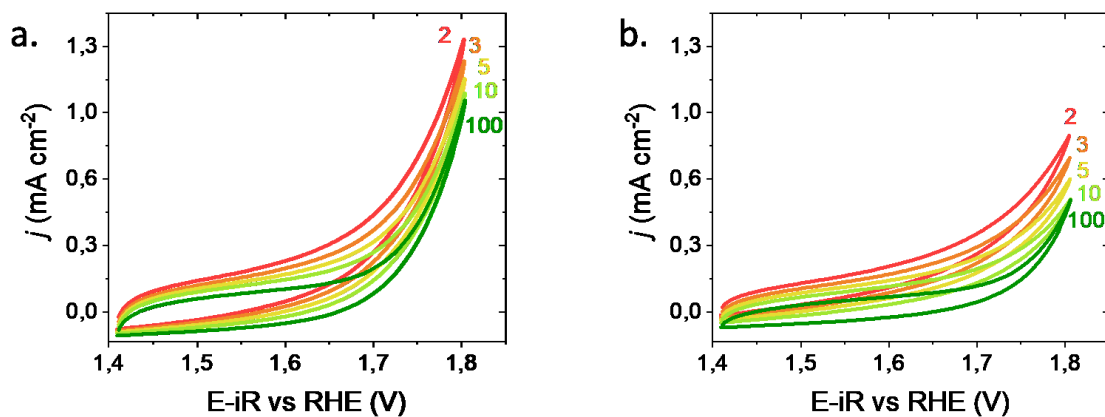


Figure S13. Series of CV of additional MnO_x films: **a.** Sample B and **b.** Sample C, performed at the disk. CV with a scan rate of 100 mV s^{-1} in 0.1 M NaOH rotated at 1600 rpm .

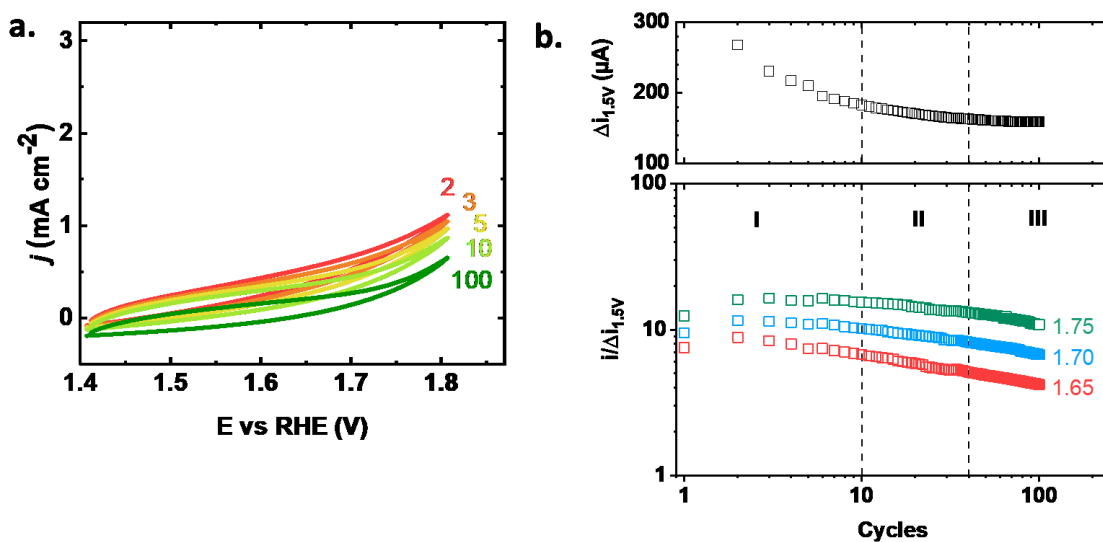


Figure S14. **a.** Series of CV of MnO_x performed at the samples on graphite foil. CV with 100 mV s^{-1} in 0.1 M NaOH . **b.** Average current ratios $i/\Delta i_{1.5\text{V}}$ as function of cycles at selected potentials of MnO_x . The data was evaluated during the first 100 cycles (open squares). The dashed lines delimit three different regions, labeled as: I, II and III.

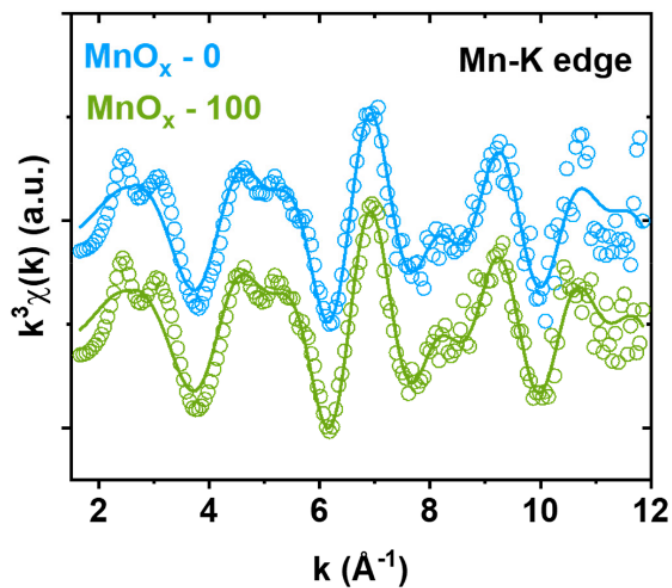


Figure S15. k^3 -weighted EXAFS spectra of pristine MnO_x ($\text{MnO}_x - 0$) and after 100 cycles ($\text{MnO}_x - 100$) recorded at the Mn-K edge. The solid lines represent the respective EXAFS simulations. The symbols represent the measurement.

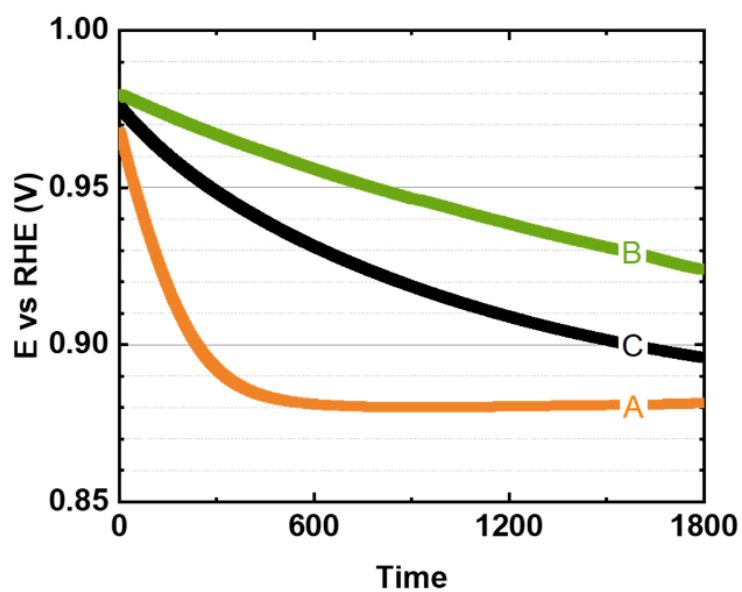


Figure S16. Open-circuit voltage profile during 30 minutes after 100 cycles of catalysis for three samples of MnO_x .

Chapter 5. Stabilization of a Mn-Co oxide during oxygen evolution in alkaline media

www.chemelectrochem.org

Stabilization of a Mn Co Oxide During Oxygen Evolution in Alkaline Media

Javier Villalobos,^[a] Dulce M. Morales,^[a] Denis Antipin,^[a] Götz Schuck,^[b] Ronny Golnak,^[c] Jie Xiao,^[c] and Marcel Risch^{*[a]}

Improving the stability of electrocatalysts for the oxygen evolution reaction (OER) through materials design has received less attention than improving their catalytic activity. We explored the effects of Mn addition to a cobalt oxide for stabilizing the catalyst by comparing single phase CoO_x and $(\text{Co}_{0.7}\text{Mn}_{0.3})\text{O}_x$ films electrodeposited in alkaline solution. The obtained disordered films were classified as layered oxides using X-ray absorption spectroscopy (XAS). The CoO_x films showed a constant decrease in the catalytic activity during cycling, confirmed by oxygen detection, while that

of $(\text{Co}_{0.7}\text{Mn}_{0.3})\text{O}_x$ remained constant within error as measured by electrochemical metrics. These trends were rationalized based on XAS analysis of the metal oxidation states, which were $\text{Co}^{2.7+}$ and $\text{Mn}^{3.7+}$ in the bulk and similar near the surface of $(\text{Co}_{0.7}\text{Mn}_{0.3})\text{O}_x$, before and after cycling. Thus, Mn in $(\text{Co}_{0.7}\text{Mn}_{0.3})\text{O}_x$ successfully stabilized the bulk catalyst material and its surface activity during OER cycling. The development of stabilization approaches is essential to extend the durability of OER catalysts.

Introduction

The use of fluctuating renewable sources, such as sunlight and wind, limits renewable energy production due to the lack of efficient energy storage systems. A promising solution is chemical energy storage using hydrogen obtained by water splitting.^[1,2] The most daunting challenges in the efficient use of water splitting are finding highly active electrocatalysts to overcome the slow kinetics of the oxygen evolution reaction (OER), which simultaneously exhibit sufficient stability under the harsh operating conditions.^[3–5] In the last decades, most of the research in this field has been focused on developing new electrocatalysts or improving the catalytic properties of the already known electrocatalysts in terms of catalytic activity, which has been the primary parameter of interest.^[6] Nevertheless, stability should not be considered a parameter of secondary importance since novel long-term stable catalysts are urgently needed for technical applications.

Alkaline electrolyzers are a mature technology for low temperature electrolysis with a target stack lifetime of 25 years.^[7]


Many amorphous transition-metal oxides (ATMO) are thermodynamically stable in alkaline electrolytes and show high catalytic activity.^[8–11] In academic research, ATMO based on earth-abundant metals own many advantages over the benchmark Ir- or Ru-based oxides, such as high catalytic activity, high stability and low-cost.^[12–14] We define stability herein as the absence of catalyst corrosion,^[15] erosion^[16,17] or blockage of active sites (e.g., by oxygen bubbles),^[18–24] for which a first indication is a lack of change in activity over time, e.g., measured by cyclic voltammetry.^[25–27] Yet, the discussion of stability requires additional measurements to determine dissolved cations,^[28–30] as well as changes in the catalyst composition,^[20,31] morphology^[32–34] and structure.^[35,36]

Co-based ATMO have attracted particular attention due to their high catalytic activity. However, pure Co oxides suffer from insufficient electrical conductivity^[37,38] and tend to corrode over time.^[39] The introduction of a second transition metal into the Co-based oxides alters the electronic structure and potentially also modifies the atomic rearrangement, affecting catalysis and corrosion resistance when a new phase is formed.^[40–43] Introducing Mn as a second metal has enhanced stability of perovskite-like oxides^[44] and electrodeposited mixed metal oxides,^[45] which has been attributed to separation of the structural framework from the catalytically active site(s).^[45] The activity was also enhanced by adding Mn in some reports, e.g., the introduction of 25 % of Mn into the Co_3O_4 spinel structure showed an overpotential decrease from 368 mV to 345 mV (at a current density, j , of 10 mA cm^{-2}).^[40] Menezes and collaborators^[42] compared the current stability of the spinels CoMn_2O_4 and Co_2MnO_4 . The current of both catalysts remained mostly constant after 30000 s, yet Co_2MnO_4 (containing more Co than Mn) showed a higher catalytic current. The role of Mn in layered Co oxide has been attributed to the modulation of the electronic properties, resulting in a more efficient charge-transfer.^[46] Recently, the stability of the spinel-type Co_3O_4 was enhanced in acid media by the partial substitution of the octahedral Co sites by octahedral Mn sites.^[47] The improvement in stability was assigned to a modulation of the metal-oxygen binding energies ($E_{\text{Mn-O}} > E_{\text{Co-O}}$), which agrees with thermodynamic studies.^[48] Furthermore, Sugawara et al.^[49] proposed a higher metal-metal coordination in layered, tunnel and spinel oxides as beneficial for activity and stability in CoMn oxides. In summary, there is no clear consensus on the possible roles of Mn in the Co oxide structures in the current state-of-

[a] J. Villalobos, Dr. D. M. Morales, D. Antipin, Dr. M. Risch
Nachwuchsgruppe Gestaltung des Sauerstoffentwicklungsmechanismus
Helmholtz-Zentrum Berlin für Materialien und Energie GmbH Hahn-Meitner Platz 1,
Berlin 14109, Germany
E-mail: marcel.risch@helmholtz-berlin.de
Homepage: https://www.helmholtz-berlin.de/forschung/oe/ce/oxygenevolution/index_en.html

[b] Dr. G. Schuck
Abteilung Struktur und Dynamik von Energiematerialien
Helmholtz-Zentrum Berlin für Materialien und Energie GmbH
Hahn-Meitner Platz 1, Berlin 14109, Germany

[c] Dr. R. Golnak, Dr. J. Xiao
Department of Highly Sensitive X-ray Spectroscopy
Helmholtz-Zentrum Berlin für Materialien und Energie GmbH Albert-Einstein-Straße
15, Berlin 12489, Germany

 Supporting information for this article is available on the WWW under
<https://doi.org/10.1002/celec.202200482>

© 2022 The Authors. ChemElectroChem published by Wiley-VCH GmbH. This is an open access article under the terms of the Creative Commons Attribution License, which permits use, distribution and reproduction in any medium, provided the original work is properly cited.

the-art research so that the extent to which the addition of Mn will beneficially affect activity, stability or both cannot be predicted *a priori*.

In this study, we extended our previously reported alkaline electrodeposition method^[50] to Na-containing single phase CoO_x and $(\text{Co}_{0.7}\text{Mn}_{0.3})\text{O}_x$ films without long-range order to study the effect of Mn in $(\text{Co}_{0.7}\text{Mn}_{0.3})\text{O}_x$ on stability. During cyclic voltammetry and open-circuit conditions in 0.1 M NaOH, we did not observe a significant change in the current of $(\text{Co}_{0.7}\text{Mn}_{0.3})\text{O}_x$, whereas CoO_x showed a decrease in the catalytic current. The post-mortem samples were analyzed by XAS to rationalize the observed electrochemical changes. We conclude that Mn in $(\text{Co}_{0.7}\text{Mn}_{0.3})\text{O}_x$ increases the stability of the films, both structurally and catalytically.

Results and discussion

CoO_x and $(\text{Co}_{0.7}\text{Mn}_{0.3})\text{O}_x$ films were deposited on glassy carbon (GC) rods following a previously reported protocol from our group for the electrodeposition of MnO_x films in alkaline pH.^[50] Like Mn and other metals in water-based solutions, Co may spontaneously deposit as oxides or hydroxides in alkaline media. Thus, tartrate ions are included in the electrodeposition electrolyte as a complexing agent to stabilize the metal ions within the electrodeposition procedure. Using the same ions (Na^+ , OH^-) in the electrolyte for both the electrodeposition and the catalytic investigation prevents the plausible anionic exchange between the catalytic material and the electrolyte during OER.^[51]

The galvanostatic electrodeposition of the films was carried out in a three-electrode cell using a commercial (unrotated) RDE holder (Figure 1a). A constant current of 0.15 mA cm^{-2} was applied until a charge density of 40 mC cm^{-2} was reached. CoO_x reached a minimum steady-state potential of 1.45 V vs. RHE after about 20 s, whereas $(\text{Co}_{0.7}\text{Mn}_{0.3})\text{O}_x$ reached 1.91 V vs. RHE after the same time. The different potentials suggest the formation of different materials.

Since the glassy carbon (GC) rods used as substrates have a small surface area, the films were also deposited on larger graphite foil (GF) following the same protocol for further XAS and energy-dispersive X-ray spectroscopy (EDX) characterization. In both cases a steady current was reached after several seconds, yet the absolute potentials differ between both substrates (Figure S1), likely because the electrodeposition potential also depends on the substrate's properties, e.g., electrical conductivity and morphology. The steady-state was reached with a potential shift of about 0.4 V for $(\text{Co}_{0.7}\text{Mn}_{0.3})\text{O}_x$ and 0.1 V for CoO_x to higher potential on GC relative to GF. Electrochemical experiments on both substrates were performed to exclude that these electrodeposition potential variations affect the catalytic properties of the films. These results are discussed below. The films were characterized by scanning electronic microscopy (SEM) to check the coverage and homogeneity of the film on the substrate. The SEM images (Figure S2) showed a full coverage of the film over the GC surface. Moreover, EDX was used to map the homogeneous distribution of the two metals on the film deposited graphite foil (Figure 1b). The average ratio of Co/Mn in $(\text{Co}_{0.7}\text{Mn}_{0.3})\text{O}_x$ was 2.45 ± 0.06 , which we estimated as an average of the composition observed in different regions of three samples. The Co/Mn ratio indicates that out of the total metal sites (Co+Mn), approximately $70 \pm 5\%$ correspond to Co and $30 \pm 5\%$ to Mn. Moreover, the EDX spectrum showed high content of carbon (from the carbon-based substrate), oxygen (from the substrate and the film), and sodium (coming from the electrolyte). Iron could be a possible (unwanted) dopant affecting the catalysis.^[41,52–54] It may be introduced by the alkaline electrolyte during deposition but no significant amount of Fe was detected by EDX (Inset of Figure 1c). Yet, we cannot exclude minor concentration (mass fraction $<0.1\%$)^[55,56] and it is unknown if such small concentrations would affect the activity of Co oxides.^[57]

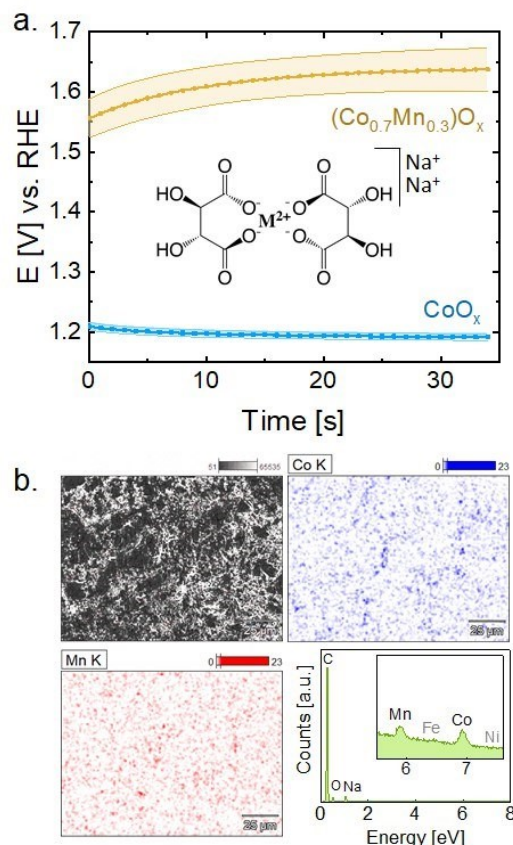


Figure 1. a. Electrodeposition chronoamperometry of CoO_x and $(\text{Co}_{0.7}\text{Mn}_{0.3})\text{O}_x$ films on glassy carbon in NaOH 0.1 M until a charge of 40 mC cm^{-2} . The inset shows the coordination complex of divalent metal (M^{2+}) due to tartrate ions. b. EDX map of the $(\text{Co}_{0.7}\text{Mn}_{0.3})\text{O}_x$ film: SEM image (top left), Co map (top right), Mn map (bottom left), and EDX spectrum (bottom right). Dataset in ref.^[58]

No substantial morphology differences were observed between the pristine CoO_x and $(\text{Co}_{0.7}\text{Mn}_{0.3})\text{O}_x$ films (Figure S2). Additionally, no significant morphological changes were observed in comparison with the previously reported MnO_x .^[50] In summary, the protocol of electrodeposition in alkaline pH was successfully extended to the deposition of Na-containing CoO_x and $(\text{Co}_{0.7}\text{Mn}_{0.3})\text{O}_x$ films without long-range order.

By electrochemical impedance spectroscopy (EIS), the uncompensated resistance (R_u) of the pristine films was collected and the results showed a $R_u = 95 \pm 7 \Omega$ in the CoO_x film and $R_u = 40 \pm 11 \Omega$ in the $(\text{Co}_{0.7}\text{Mn}_{0.3})\text{O}_x$ film (Figure S3). We attribute the difference in R_u to a difference in bulk resistance of the films and conclude that Mn addition lowered the resistance. The catalytic stability of the films during OER catalysis was evaluated by cyclic voltammetry (CV) in a three-electrode cell in a rotating-ring disk electrode station (RRDE), comprising the CoO_x - and $(\text{Co}_{0.7}\text{Mn}_{0.3})\text{O}_x$ -covered GC rod as the disk electrode and a Pt ring as the ring electrode (protocols are shown in Table S1 for GC and Table S2 for GF). The CV series of CoO_x and $(\text{Co}_{0.7}\text{Mn}_{0.3})\text{O}_x$ (Figure 2a, 2b, S4) were collected in 0.1 M NaOH with a scan rate of 100 mV s^{-1} for a total of 100 cycles. Similar scan rates and number of cycles are typical conditions for film stabilization or activation during OER.^[51,59–63] Meanwhile, the Pt ring was set at a constant potential of 0.4 V vs. RHE for oxygen detection by reduction.^[30] Since the exponential increase in the ring current density due to reduction of oxygen ($j_{\text{ring},\text{O}_2}$) matches that observed at the disk electrode (j_{disk}), the latter can be associated with oxygen evolution. At the same time, a rough estimation of the OER onset potential can be determined, which we defined at the potential where the ring current reaches $0.15 \mu\text{A cm}^{-2}$ during the second cycle. For CoO_x , the OER onset is around $1.64 \pm 0.02 \text{ V}$ vs. RHE, whereas for $(\text{Co}_{0.7}\text{Mn}_{0.3})\text{O}_x$ is $1.66 \pm 0.01 \text{ V}$, a negligible difference within error. The overpotential of the electrode (η_{10})

was calculated at a specific current density per geometric area, $j=10 \text{ mA cm}^{-2}$, which is chosen based on the current drawn by a solar-to-fuel device with a 10 % of efficiency under one sun illumination.^[64] It is important to note that η_{10} is a helpful metric to compare electrodes but it cannot be used to compare the intrinsic properties of different materials,^[64,65] unless microstructure and morphology do not vary as is the case in our study (see above). In CoO_x , η_{10} was $466 \pm 15 \text{ mV}$ after 2 cycles, and it increased to $520 \pm 19 \text{ mV}$ after 100 cycles. In $(\text{Co}_{0.7}\text{Mn}_{0.3})\text{O}_x$, η_{10} was $510 \pm 30 \text{ mV}$ after the first 2 cycles and $500 \pm 27 \text{ mV}$ after 100 cycles, i.e., it remained constant within error. Electrodes with similar composition (Co, Mn- and Co-based oxide), but possibly different microstructure and morphology, showed η_{10} in a range of 320–430 mV in alkaline pH (13–14),^[66–70] where η_{10} tended to increase under OER conditions, which agrees qualitatively with the observations herein. Although the introduction of a second transition metal into the Co oxide structure has reduced the overpotential in some cases,^[40,71–73] while it was increased in other cases.^[74]

Catalytic trends can also be followed using the maximum current density (j_{max} , at an ohmic drop-corrected potential ($E-iR_u$) of approximately 1.73 V vs. RHE) over cycling. In the case of CoO_x , the disk j_{max} decreases over cycling; about $-33 \pm 15 \%$ of the initial current is lost after 100 cycles. This effect is also observed at the ring current detecting O_2 , where the current drops about $-35 \pm 14 \%$ compared to the initial value, indicating that the drop in j_{max} is (mainly) due to deactivation of the catalyst film during cyclic voltammetry. In contrast, j_{max} of the $(\text{Co}_{0.7}\text{Mn}_{0.3})\text{O}_x$ disk remained mostly stable (with slight increase) over 100 cycles compared to the initial value, about $+10 \pm 1 \%$ at the disk and $+11 \pm 4 \%$ at the ring, indicating a stabilization of the catalytic current during cycling voltammetry, namely, a higher amount of oxygen is produced and detected at the disk and ring electrode, respectively. The CV series were also collected with a wider potential range to confirm that a possible incomplete reduction does not affect the j_{max} trends during cycling (Figure S5).

The CV experiment was extended after the 100 cycles with 30 minutes at open circuit potential (OCP) and 10 additional cycles in the same potential range. The goal of introducing an OCP break between the two series of CV is to identify if the catalytic current suffers changes after the OCP period, therefore distinguishing reversible and irreversible changes in the catalyst.^[50,75] The current density at selected potentials was plotted as a function of number of cycles for a more detailed analysis of the trends (Figure 3). Note that both x and y axis are presented in a logarithmic scale. The capacitance was corrected by normalizing the average between the anodic and cathodic scans by the difference between the cathodic and anodic current at $E-iR_u=1.5 \text{ V vs. RHE}$, $\Delta i_{1.5V}$, (Figure 3a,c).^[65] This represents a rough approximation of the capacitance, which is more commonly estimated by a systematic experiment that involves recording CVs at several scan rates.^[76] Yet, it allows tracking changes in the surface area with cycling. The current trend was analyzed at three different potential values, which were selected based on the estimation of the oxygen evolution onset: no OER (1.55 V vs. RHE), onset of OER (1.64 V for CoO_x and 1.66 V vs. RHE for $(\text{Co}_{0.7}\text{Mn}_{0.3})\text{O}_x$), and OER (1.70 V vs. RHE). The normalized current, $i/\Delta i_{1.5V}$, follows different exponents (slopes in the logarithmic plot) depending on the cycle number, the selected potential, and whether the cycles were recorded before or after the OCP break. Thus, a negative exponent represents a current decrease, an exponent close to zero represents stable current, and a positive exponent represents a current increase with cycling. Since the exponent depends on the cycle number, the 100 cycles before the OCP break were split into three regions, 1 (1–10th cycle), 2 (11–50th cycle) and 3 (51–100th) for analysis.

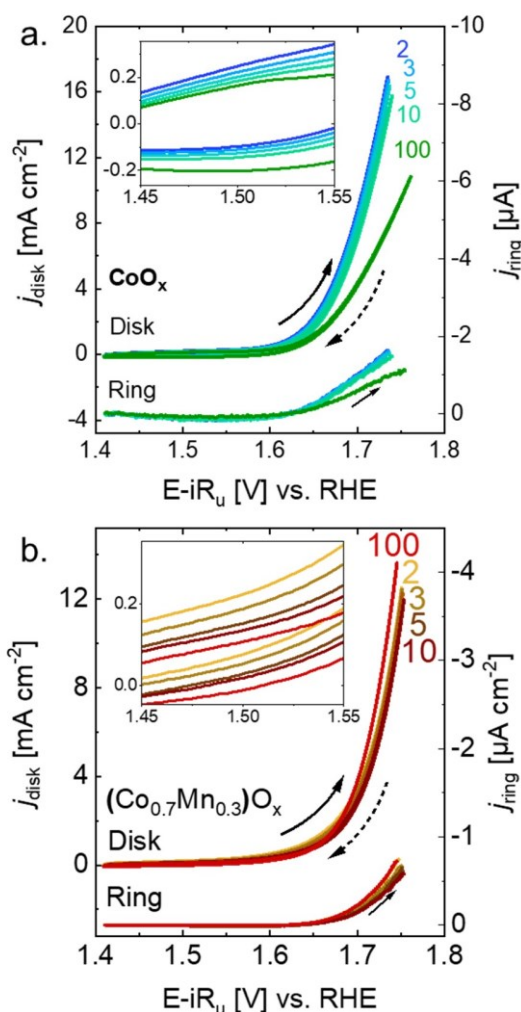


Figure 2. Series of CV performed on: a. CoO_x -covered disk and b. $(\text{Co}_{0.7}\text{Mn}_{0.3})\text{O}_x$ -covered disk. The data was collected with a scan rate of 100 mV s^{-1} in 0.1 M NaOH with an electrode rotation 1600 rpm and a constant potential of 0.4 V vs. RHE at the Pt ring to detect oxygen. Dataset in ref.^[58]

The current trends of CoO_x show a constant decrease during the first 100 cycles at each of the selected potentials (Figure 3a). After the OCP break, the current partially recovers at both $i_{1.55}/\Delta i_{1.5V}$ and $i_{1.64}/\Delta i_{1.5V}$, which can be observed by the position of the solid squares (after OCP) below the open squares (before OCP) in Figure 3a. Only at $i_{1.70}/\Delta i_{1.5V}$, the current fully recovers after the OCP break (Figure 3a). This recovery was also observed in the oxygen ring current, $j_{\text{ring}, \text{O}_2}$ (Figure S6). The decay exponents did not strongly vary among the three different regions (Table S3). Since the OER catalytic current is the major current component at $i_{1.70}/\Delta i_{1.5V}$, a current trend recovery could be observed. Whereas, at $i_{1.64}/\Delta i_{1.5V}$ and $i_{1.55}/\Delta i_{1.5V}$, there might be a significant current contribution from irreversible processes, e.g., Co redox changes, which cannot be recovered after the OCP break. The current trends of $(\text{Co}_{0.7}\text{Mn}_{0.3})\text{O}_x$ show a clear difference in the exponent, depending on the selected potential. At the nonOER potential, $i_{1.55}/\Delta i_{1.5V}$ decreases over cycling in all three regions. Whereas, at the OER onset, $i_{1.66}/\Delta i_{1.5V}$ showed a negative exponent in region 1 and 2 and became positive in region 3. For $i_{1.70}/\Delta i_{1.5V}$, the exponent changed from a positive value close to zero in region 1 and kept increasing towards more positive values in region 2 and 3, indicating the stabilization of the current (with a slight activation) at this potential (as also observed with the ring, $j_{\text{ring}, \text{O}_2}$, and disk j_{max} in Figure 2b). The exponent values are summarized in Table S3.

The trends during continuous potential cycling of the films on GF were also plotted (Figure S7) and showed trends similar to those observed on GC. Thereby, we confirmed that the variations in the electrodeposition potential due to different substrates did not significantly affect the current trends during cycling.

The Tafel slope ($b = \partial \log i / \partial E$) indicates the scaling of kinetic currents with applied potential where a desirable low value leads to a large increase in current can be achieved with a small increment in overpotential (i.e., far from equilibrium). Its values can also be rationalized based on mechanistic considerations such as the rate-limiting step and the populations of surface intermediates.^[77,78] For instance, a value of 60 mV dec⁻¹ is associated with a chemical rate-limiting step with an electrochemical pre-equilibrium. A value of 120 mV dec⁻¹ is related to an electrochemical rate-limiting step, and a value much greater than 120 mV dec⁻¹ is due to chemical limiting step or poor material conductivity.^[79]

The Tafel plots were analyzed for both materials, CoO_x and (Co_{0.7}Mn_{0.3})O_x, at the OER potential range (1.70–1.76 V vs. RHE). From the plots, Tafel slopes were determined and plotted as a function of the number of cycles (Figure 4). A representative calculation is shown in Figure S8 with averaged parameters shown in Table S4. The Tafel slope as function of potential was also plotted (Figure S9). Considering that a scan rate of 100 mV s⁻¹ may be too fast to establish a complete chemical equilibrium, the produced intermediates can be shifted towards the oxidized sites during the cathodic scans (since high potentials are applied) if an electrochemical step is part of the OER mechanism. Thus, only the anodic scans are used to estimate the Tafel slopes. The Tafel slope of CoO_x was around 135 ± 10 mV dec⁻¹ in the initial 10 cycles and it increased insignificantly to 158 ± 25 mV dec⁻¹ at the 100th cycle. Yet, the slope went down to 133 ± 11 mV s⁻¹ after the OCP break. The Tafel slope of (Co_{0.7}Mn_{0.3})O_x was mostly constant during 100 cycles and 10 cycles after OCP break, with a value of 89 ± 2 mV s⁻¹. Typical Tafel slope values for layered Co oxides are about 60 mV dec⁻¹,^[34,51,80,81] whereas layered Mn oxides show values between 60 mV dec⁻¹ and 180 mV dec⁻¹.^[50,82–84] Tafel slope values between 60 and 120 mV dec⁻¹ are not predicted by common kinetic modeling. However, variations in the material's symmetry coefficient (β) would lead to different Tafel slope values,^[78,85] as well as non-catalytic side reactions such as metal redox independent of catalysis,^[77] and changes in coverage and/or electrical conductivity during the potential scan.^[86]

The upper limit of the CV series is clearly anodic enough to produce permanganate ions by an irreversible process, e.g., by the reaction $\text{Mn}^{4+}\text{O}_2 + 4\text{OH}^- \rightarrow \text{Mn}^{7+}\text{O}_4^- + 2\text{H}_2\text{O} + 3\text{e}^-$ ($E^0 = 1.36$ V vs RHE at pH 13).^[87] The production of unwanted permanganate is one of the key processes leading to corrosion of Mn oxides.^[30,77,88] The ring of an RRDE has been used as method to detect permanganate for the discussion of the stability of Mn-based films^[89,90] and particles.^[30,77] We used a potential of 1.2 V vs. RHE applied at a Pt ring^[30] to detect permanganate on a (Co_{0.7}Mn_{0.3})O_x film for comparison with the previously reported MnO_x film (Figure S10).^[50]

On MnO_x, the ring current due to Mn dissolution, $j_{\text{ring,Mn}}$, was up to 2 μA (0.1 % of disk current) during the first few cycles and decreased to 0.7 μA after 100 cycles, which was concomitant with a decrease of the disk current. On (Co_{0.7}Mn_{0.3})O_x, $j_{\text{ring,Mn}}$ was up to 1 μA (0.01 % of disk current) and remained constant with during 100 cycles, which also corresponded to the lack of changes in the disk current. Our reference electrode was placed far from the two working electrodes, which mitigates the contributions of electric cross talk on the ring current.^[91] We conclude that Mn loss in the form of permanganate is a key factor reducing the observed disk currents.

In summary, CoO_x films slightly deactivated during 100 cycles, yet the current fully recovered at the catalytic potential (1.70 V vs. RHE) after a 30-minute OCP break, indicating reversible changes likely due to coverage changes, for instance, unreacted intermediates.^[75] The Tafel slope remained larger than 120 mV dec⁻¹ and increased over cycling, suggesting a change in the coverage over time. In contrast, the current at OER potentials and the Tafel slope values of (Co_{0.7}Mn_{0.3})O_x were stable with cycling. The contribution of the currents due to Mn dissolution were much reduced in (Co_{0.7}Mn_{0.3})O_x (0.01 %) as compared to MnO_x (0.1 %). CoO_x and (Co_{0.7}Mn_{0.3})O_x were studied under the same conditions, yet they show different catalytic properties and current trends with cycling, due to the presence of Mn. Both metals, Mn and Co, are well known as OER catalysts, therefore it is likely the Mn (as well as Co) plays an important role in the catalytic process. The OER activity of Co and Mn has been reported for bimetallic oxides.^[40,42,46,49] Thus, the study of the structural positions of both

metals is necessary for a better understanding of the changes observed over cycling.

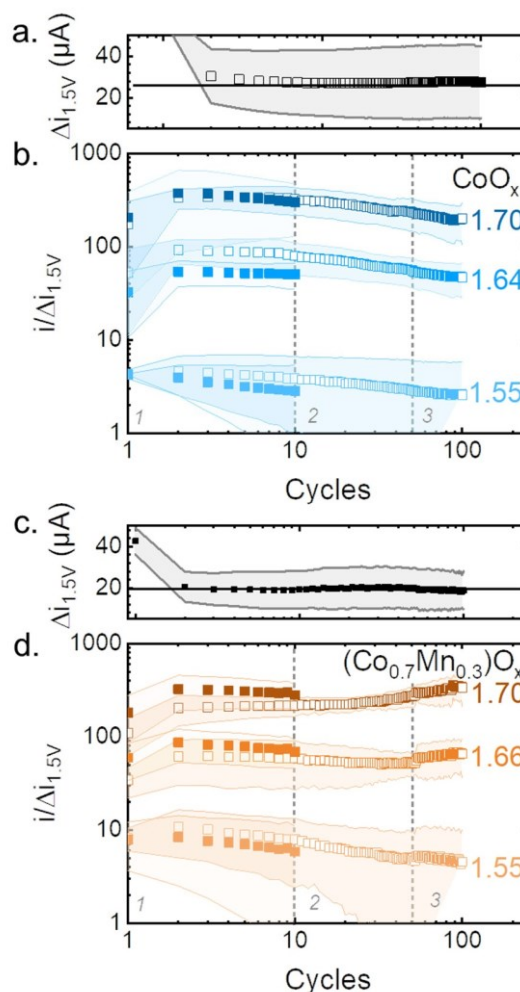


Figure 3. Average $\Delta I_{1.5V}$ of all samples as function of cycles for the first 100 cycles for a. CoO_x and c. (Co_{0.7}Mn_{0.3})O_x. Average current ratio $i/I_{1.5V}$ of all samples as function of cycling at selected potentials for b. CoO_x and d. (Co_{0.7}Mn_{0.3})O_x. The data was extracted from the first 100 cycles (open squares) and from 10 cycles recorded after 30 min of OCP break (solid squares). The light-colored areas represent the standard deviation of three samples. The dashed lines separate three regions: 1, 2 and 3. Dataset in ref.^[58]

XAS experiments were performed to investigate irreversible structural changes in the catalyst due to cyclic voltammetry. The absence of crystallinity in the films requires XAS experiments to analyze possible structural changes, which is not possible by diffraction-based techniques. The Co-K and Mn-K edge were used to study the bulk of the material since the radiation deeply penetrates the catalyst. Using XANES (X-ray absorption near edge structure), changes in the averaged oxidation state were identified and using the EXAFS (extended X-ray absorption fine structure), changes in the local structure were tracked. The escape depth (3x attenuation length) of photons at the Co-K α and Mn-K α lines is about 15 μm at the Co-K edge and 30 μm at the Mn-K edge in layered oxides,^[92] which is much smaller than the expected film thickness $\ll 1 \mu\text{m}$, making it a bulk method. The FT (Fourier transform) of EXAFS spectra collected on CoO_x and (Co_{0.7}Mn_{0.3})O_x showed typical features of layered hydroxides (Figure 5a, 5b) in both edges, Co-K and Mn-K. Two prominent peaks were identified: a M-O peak of around 1.87 Å, and a M-M peak of around 2.81 Å, where M is either Mn or Co. The phase functions were simulated using

several reasonable structural models, such as spinels (Mn_3O_4 , Co_3O_4), birnessite ($\text{MnOOH} \cdot x\text{H}_2\text{O}$), heterogenite (CoO_2H), and $\text{Co}(\text{OH})_2$ (Figure S11). The choice of the structural model had only minor effects on the Rf factor, fit parameters and error (Table 1, 2, S5, S6 and S7). The absence of an FT peak corresponding to M-M distances of 3.2–3.4 Å rules out a spinel structure so that heterogenite and birnessite were selected as representative layered oxides. Three relevant parameters were obtained from the simulations: N , which is related to the number of neighboring atoms around the absorber atom, R , related to the averaged interatomic distance between the absorber atom and the scatterer, and σ (Debye-Waller factor), associated with the distance distribution in a disordered material. The simulation parameters are summarized in Table 1 and Table 2, and the corresponding k-space spectra are shown in Figure S12. Note that that reduced distance is shorter than the precise distance obtained by EXAFS simulations by about 0.3 Å. The FT of EXAFS spectra did not change strongly due to cycling. Minor changes were observed in the $(\text{Co}_{0.7}\text{Mn}_{0.3})\text{O}_x$ spectra before and after cycling, nevertheless, these changes are not prominent, thus not conclusive.

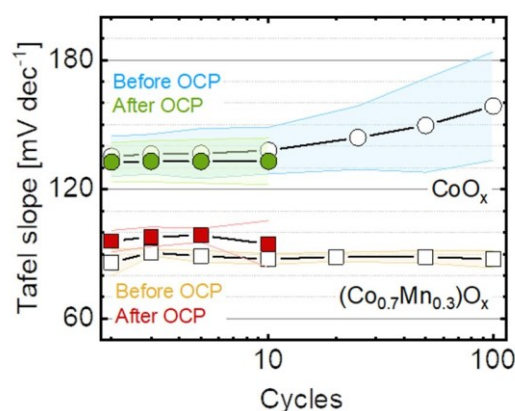


Figure 4. Averaged Tafel slope as function of cycle number before (open symbols) and after (solid symbols) a 30-minute break at OCP. The light-colored areas represent the standard deviation of three samples. The Tafel slopes were calculated in the potential range between 1.70 V and 1.76 V vs. RHE. Dataset in ref.^[58]

The two prominent peaks were simulated in the Co-K edge: the metal-oxygen distance at 1.87 Å, which is a typical distance for octahedral Co^{3+}O_6 cations,^[93] and the metal-metal distance around 2.81 Å, associated with metal-metal di- μ -oxo bridge.^[51,94] No clear peaks are observed at a higher reduced distance, suggesting a lack of long-range order in the films. On the other hand, the same peaks were observed in the Mn-K edge, with similar interatomic distances. The peak at 1.87 Å suggests the presence of octahedral $\text{Mn}^{3+/4+}\text{O}_6$ cations^[95,96] and Mn-Mn di- μ -oxo bridge^[97] is confirmed by the peak positioned at 2.81 Å. Moreover, an extra Mn-O distance of about 2.30 Å was included in the simulations, improving the fit significantly. This structural motif has been associated with $\text{Mn}^{3+}\text{-O}$ with a JahnTeller elongation or $\text{Mn}^{2+}\text{-O}$.^[98] A distance around 2.3 Å has been typically observed in Mn^{2+}O in spinel-type oxides.^[99] As in the CoK edge, no clear peaks of additional M-M scatters were observed at higher reduced distance.

EXAFS of the Mn-K and Co-K edge indicated that the pristine films were electrodeposited as a layered hydroxide and did not suffer significant changes in the local structure due to cycling. The Mn-M and Co-M distance in $(\text{Co}_{0.7}\text{Mn}_{0.3})\text{O}_x$ are identical within 2σ fit error and their values are closer to the Co-Co distance in CoO_x (Table 2) as compared to the Mn-Mn distance in electrodeposited MnO_x (2.86 Å).^[50] Taking together, it suggests that Mn and Co are in the same phase in $(\text{Co}_{0.7}\text{Mn}_{0.3})\text{O}_x$ with bond distances akin to CoO_x so that Mn is forced into a bonding environment typical for Co oxides. The M-O and M-M distances are typical for disordered layered oxides^[51,59,80] relating to heterogenite.^[100] Moreover, a mixed Co,Mn-containing phase agrees with the well distributed Mn and Co content on the surface found by EDX (Figure 1b). Yet, the presence of other minor Mn- or Co-phases cannot

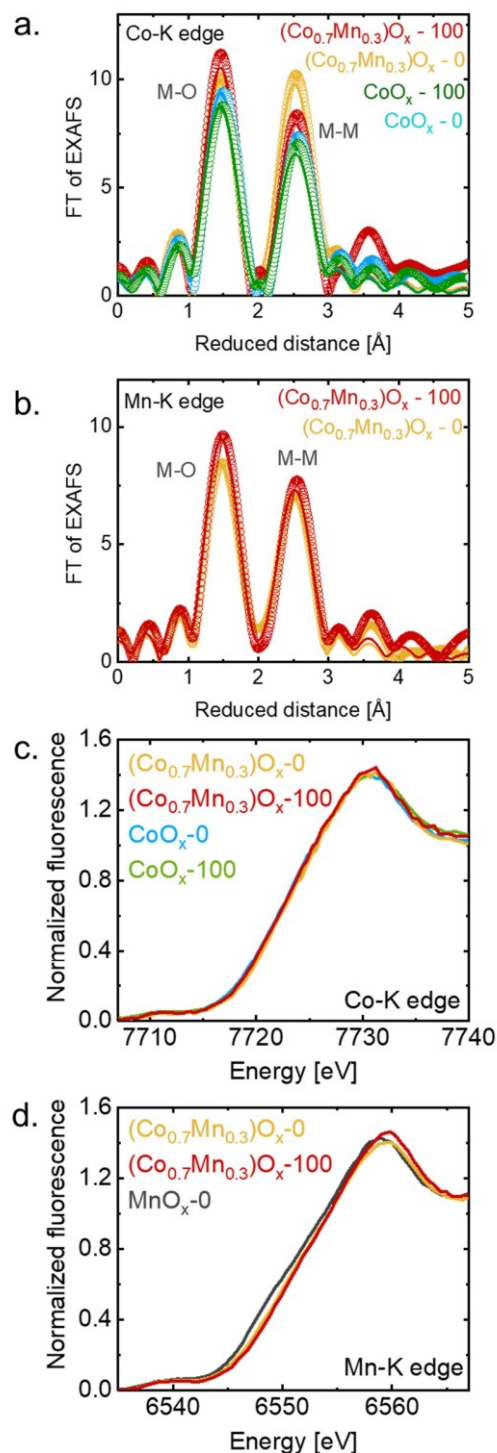


Figure 5. FT of EXAFS spectra of: a. Co-K edge and b. Mn-K edge, collected on pristine CoO_x and $(\text{Co}_{0.7}\text{Mn}_{0.3})\text{O}_x$, and after 100 cycles. The open symbols represent the experimental spectra and the solid lines represent the simulations. The reduced distance is shorter than the precise distance obtained by EXAFS simulations by about 0.3 Å. c. XANES spectra of Co-K edge and d. Mn-K edge. The Mn-K edge collected on MnO_x (black line) from a previous report was added for comparison.^[50] Dataset in ref.^[58]

be rigorously discarded. Finally, the Fe-K edge was not observed in Mn-K edge spectrum of $(\text{Co}_{0.7}\text{Mn}_{0.3})\text{O}_x$ after 100 cycles (Figure S14). We expect less than the detection limit of about 50 ppm Fe^[101] in the cycled film. The

increase in activity with Fe appears to be linear up to the optimal composition^[41,54] which spreads much in the range from about 3 to 70%.^[57] The lowest optimal Fe content is 2.8% Fe (2.8 10⁴ ppm).^[57] In summary, major Fe incorporation could not be detected by EDX nor XAS, and it is unknown if small concentrations of Fe (< 0.1% fraction mass)^[55,56] would significantly affect the activity of Co oxides.

The Co-K and Mn-K edge XANES spectra were used to analyze the nominal metal oxidation state by the calibration of the edge energy with references (Figure S13 and Table S8); Co²⁺O, Co^{2.6+}₃O₄ and LiCo³⁺O₂ were the references for Co-K edge, and Mn²⁺O, Mn^{2.6+}₃O₄, Mn³⁺₂O₃ and Mn⁴⁺O₂ for Mn-K edge. The average bulk Co oxidation state was between 2.7+ and 2.8+ in all the samples, indicating that any redox changes that may have occurred to Co due to potential cycling did not influence the chemical state of the bulk.

In the case of Mn-K edge in the (Co_{0.7}Mn_{0.3})O_x films, the averaged bulk Mn oxidation state was 3.7+ and did not change after cycling. However, the white line and edge were shifted by 1 eV in comparison to previously studied MnO_x films, resulting in a averaged Mn oxidation state of (Co_{0.7}Mn_{0.3})O_x 0.2 higher than MnO_x films (black line in Figure 5d).^[50] In summary, the Co oxidation state of Co_{0.7}Mn_{0.3}O_x was identical to that in CoO_x and the Mn oxidation state was slightly higher as compared to MnO_x.

The metal-K edges previously discussed can identify bulk material changes, but they might neglect changes occurring only at the near-surface region. As catalysis is a surface process, the films were also analyzed using the total electron yield (TEY) of the Co-L₂ and Mn-L₃ edges, whose electron escape depth is of a few nm (2.6±0.3 nm for a similar oxide at the Mn-L edge).^[102] If we assume that our deposited Co-containing films are related to heterogenite (a=b= 2.86 Å, c= 8.81 Å)^[100] as supported by EXAFS analysis, then the escape depth corresponds to 3 to 9 probed unit cells, which we consider sufficient to qualitatively resolve changes of the top unit cell where oxygen is catalyzed but insufficient to state the oxidation state of the active sites on the surface. The Co-L₃ spectrum of the pristine CoO_x showed clear features of the Co²⁺ references (highlighted in blue in Figure 6a), indicating the dominant Co²⁺ content, which differed from the Co-K edge spectrum. Yet, after 100 cycles the spectrum changed drastically, and the Co²⁺ features were no longer strongly pronounced. Instead, only one prominent peak was observed, which closely resembles the spectrum of the Co³⁺ reference, LiCoO₂ (highlighted in orange in Figure 6a), yet there was additional spectral intensity between 777 eV and 780 eV, which suggests that some Co²⁺ remained in the near surface region. A Co oxidation state slightly smaller than 3+ agrees with the bulk oxidation state of 2.7+ (Table S8).

The apparent increase in the Co oxidation state with cycling can be attributed either to the oxidation of Co²⁺ sites to Co³⁺ sites or dissolution of Co²⁺ sites. A potential around 1.42 V vs. RHE likely corresponds to Co oxidation.^[59,80] The CV of CoO_x (inset in Figure 2a) shows a weak redox peak at around 1.5 V vs. RHE, which can be assigned to the oxidation of a small number of Co²⁺ sites. However, the oxidation of Co²⁺ into Co³⁺ sites should increase the catalytic activity,^[59,80] which was not observed. Therefore, we find it more plausible that the catalytically less relevant Co²⁺ ions were lost from the near surface region since they are well soluble in aqueous solutions.^[104] These ions could come either from minor Co²⁺ phases or from the Co²⁺-rich electrodeposition electrolyte. The latter is less likely as the samples were soaked in DI water to remove the electrodeposition electrolyte. CoO_x is not stable at pH 7 at OCP and the formation of Co²⁺-containing phases is thus expected due to the cleaning procedure.^[105]

In contrast to CoO_x, the Co-L₃ edge spectra of (Co_{0.7}Mn_{0.3})O_x did not significantly change after 100 cycles and resemble the Co³⁺ reference (LiCoO₂) with minor intensity due to Co²⁺. Again, the oxidation state slightly below 3+ of the near surface region agrees with the bulk value of 2.7+ (Table S8). We conclude that the Co oxidation state of the relevant ions in the near surface region was comparable to that in the bulk.

Table 1. EXAFS absorber-scatter averaged distance (R), neighbouring atoms number (N) and Debye-Waller factor (σ) as determined by simulation of the k³-weighted EXAFS spectra at the Co-K edge for pristine CoO_x (CoO_x-0), CoO_x after 100 cycles (CoO_x-100), pristine (Co_{0.7}Mn_{0.3})O_x ((Co_{0.7}Mn_{0.3})O_x-0) and (Co_{0.7}Mn_{0.3})O_x after 100 cycles ((Co_{0.7}Mn_{0.3})O_x-100). Shells were simulated using phase functions from a structural model created based on CoO₂H.^[100] The error of the last digit is shown in parentheses.

Sample	Parameter	Co-O1	Co-M _[b]	R – factor
CoO _x -0	N	5.7(7)	3.2(6)	4.00 %
	R (Å)	1.88(1)	2.81(1)	
	σ (Å)	0.05 _[a]	0.05 _[a]	
CoO _x -100	N	5.3(5)	3.0(4)	3.06 %
	R (Å)	1.87(1)	2.81(1)	
	σ (Å)	0.05 _[a]	0.05 _[a]	
(Co _{0.7} Mn _{0.3})O _x -0	N	6.0(8)	4.6(6)	1.47 %
	R (Å)	1.87(1)	2.79(1)	
	σ (Å)	0.05 _[a]	0.05 _[a]	
(Co _{0.7} Mn _{0.3})O _x -100	N	6 _[a]	3.5(6)	3.18 %
	R (Å)	1.87(1)	2.79(1)	
	σ (Å)	0.05 _[a]	0.05 _[a]	

[a] indicates fixed values (not simulated). [b] M indicates Mn or Co.

Table 2. EXAFS absorber-scatter averaged distance (R), neighboring atoms number (N) and Debye-Waller factor (σ) as determined by simulation of the k³-weighted EXAFS spectra at the Mn-K edge for pristine MnO_x (MnO_x-0), MnO_x after 100 cycles (MnO_x-100), pristine (Co_{0.7}Mn_{0.3})O_x ((Co_{0.7}Mn_{0.3})O_x-0) and (Co_{0.7}Mn_{0.3})O_x after 100 cycles ((Co_{0.7}Mn_{0.3})O_x-100). Shells were simulated using phase functions from a structural model created based on MnO₂·nH₂O.^[103] The error of the last digit is shown in parentheses.

Sample	Parameter	Mn-O1	Mn-O2	Mn-M _[b]	R – factor
MnO _x -0 _[c]	N	5 _[a]	1 _[a]	4.2(2)	0.60 %
	R (Å)	1.87(1)	2.31(6)	2.86(1)	
	σ (Å)	0.05 _[a]	0.05 _[a]	0.05 _[a]	
MnO _x -100 _[c]	N	5 _[a]	1 _[a]	4.2(2)	1.09 %
	R (Å)	1.88(1)	2.30(5)	2.86(1)	
	σ (Å)	0.05 _[a]	0.05 _[a]	0.05 _[a]	
(Co _{0.7} Mn _{0.3})O _x -0	N	5.1(5)	1 _[a]	3.4(4)	0.79 %
	R (Å)	1.87(1)	2.36(1)	2.82(1)	
	σ (Å)	0.05 _[a]	0.05 _[a]	0.05 _[a]	
(Co _{0.7} Mn _{0.3})O _x -100	N	5 _[a]	1 _[a]	3.7(5)	2.44 %
	R (Å)	1.87(1)	2.31(8)	2.83(1)	
	σ (Å)	0.05 _[a]	0.05 _[a]	0.05 _[a]	

[a] indicates fixed values (not simulated). [b] M indicates Mn or Co. [c] data from reference.^[50]

The Mn-L₂ edge of (Co_{0.7}Mn_{0.3})O_x showed two prominent peaks (highlighted in green in Figure 6b) that resemble the MnO₂ (and partially Mn₂O₃) reference and no evident changes are observed due to cycling. The near-surface region exhibits an oxidation state between 3+ and 4+, which agrees with Mn-K edge measurements, where an oxidation state of the bulk of the material was estimated to be 3.7+. In comparison to the previously reported MnO_x films, the averaged Mn oxidation state of 3.5+ was 0.2 lower as compared to the herein studied (Co_{0.7}Mn_{0.3})O_x films (Table S8), yet in both cases the averaged bulk Mn oxidation state remained unaffected after 100 cycles. On the other hand, the near-surface region of the previously reported MnO_x suffered an oxidation towards Mn⁴⁺,^[50] which affected the catalytic activity by decreasing the current over cycling. The Mn oxidation was identified as an irreversible change; therefore, the catalytic current did not fully recover after the OCP break. Such effect is not observed on the (Co_{0.7}Mn_{0.3})O_x films since the near-surface region (as well as the bulk) remained unaffected also at the MnL₃ edge. These observations indicate that Mn was stabilized in a slightly higher oxidation state (3.7+) by the presence of Co in (Co_{0.7}Mn_{0.3})O_x with concomitant stable activity.

In summary, using the Co-K and Mn-K edge the electrodeposited Co-based films were characterized as layered hydroxides. The local structure of the investigated films was similar to that of heterogenite^[100] but EXAFS cannot resolve the interlayer distance to unambiguously assign a phase and the electrodeposited films were too disordered to confirm the heterogenite phase by XRD. Nonetheless, our EXAFS analysis supported the formation of a new mixed oxide phase, (Co_{0.7}Mn_{0.3})O_x, upon co-deposition of Mn and Co. Microstructure and morphology were comparable among (Co_{0.7}Mn_{0.3})O_x and the end members of the materials system, CoO_x and MnO_x. A comparable surface roughness is further supported by identical differential currents at 1.5 V vs RHE within error of the three phases (Table S9). Yet, the electronic properties in the pristine films differed among these phases in terms of oxidation state and conductivity. Catalysis is a surface process so that one should thrive for an atomistic description of the topmost atoms. Our soft XAS analysis of the near surface region was qualitatively in agreement with the bulk analysis of the films in our post-mortem study. The bulk thermochemistry and surface adsorption energetics depend similarly on the number of outer electrons, which has been shown in a theoretical study.^[106] This enables us to correlate our near surface and bulk insights into the electronic structure with the electrocatalysis of the OER.

The current density of (Co_{0.7}Mn_{0.3})O_x did not change significantly during 100 cycles between 1.4 V and 1.75 V vs RHE, which is in contrast to the catalytic trends of both end members, CoO_x and MnO_x.^[50] Furthermore, Mn dissolution was drastically reduced in (Co_{0.7}Mn_{0.3})O_x as compared to MnO_x. We address the most likely explanations of the beneficial effects of Mn and Co in (Co_{0.7}Mn_{0.3})O_x based on electronic structure.

Even though Co oxides are considered promising OER catalysts, they do not exhibit sufficiently high electrical conductivity,^[107–109] which is a desirable feature in OER catalysts^[110–112] as it benefits the rate of electron transport through the material.^[111] The introduction of Mn⁴⁺ into the predominantly Co³⁺ host oxide of (Co_{0.7}Mn_{0.3})O_x introduces holes as charge carriers for conduction, while (high spin) Mn³⁺ (0.645 Å) has a significantly larger ionic radius as compared to (low spin) Co³⁺ (0.545 Å),^[113] which causes local distortions that can increase charge mobility, e.g., via hopping.^[114,115] Therefore, adding Mn to Co oxides may improve their bulk conductivity as also reported elsewhere for various crystal structures.^[43,116–121]

Electronic descriptors such as the oxidation state have proven very valuable in rationalizing electrocatalytic trends even though they are predominantly based on bulk electronic properties in experimental studies.^[122–124] In (Co_{0.7}Mn_{0.3})O_x, Co remained in a bulk oxidation state close to 3+ being optimal for the OER,^[59,125] while Mn in (Co_{0.7}Mn_{0.3})O_x was in bulk oxidation state 3.7+ independent of potential cycling. Mn oxides with both octahedral Mn³⁺ and Mn⁴⁺ sites have been found as optimal for the OER.^[88,126–134] Mn³⁺ is believed to be the active state, where small amounts of Mn⁴⁺ are beneficial but the predominance of Mn⁴⁺ over Mn³⁺ has a negative impact by making the material less active or inactive.^[30,128] The most active catalysts in literature usually have average Mn oxidation states between 3.5+ and 3.7+. The near surface of MnO_x oxidizes beyond this optimal range with voltage cycling and we previously argued that Mn oxidation is the main irreversible cause of activity loss.^[50] Thus, both Co and Mn ions retain a near optimal Mn and Co oxidation state for OER catalysis on (Co_{0.7}Mn_{0.3})O_x.

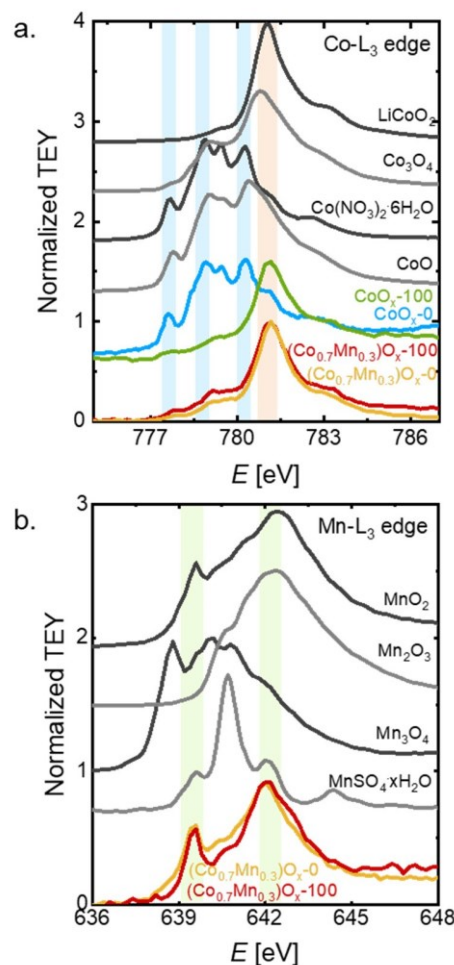


Figure 6. a. XAS spectra of: a. Co-L₃ edge and b. Mn-L₃ edge, collected on pristine CoO_x and (Co_{0.7}Mn_{0.3})O_x, and after 100 cycles. The light-colored regions are added to help assign the relevant peaks in Co-L₃ edge (orange highlights CoO_x-100, (Co,Mn)O_x-0 and (Co,Mn)O_x-100 peaks; blue highlights CoO_x-0 peaks, and green highlights (Co,Mn)O_x-0 and (Co,Mn)O_x-100 peaks). MnO₂, Mn₂O₃, Mn₃O₄, Mn(SO₄)_xH₂O, CoO, Co(NO₃)₂·6H₂O, Co₃O₄ and LiCoO₂ were used as references. Dataset in ref.^[58]

While some Mn oxides were proposed to be sufficiently stable,^[89,135,136] other Mn oxides, to which the layered oxides usually belong, suffer from insufficient stability.^[50,137–139] The lack in stability is often inferred from electrochemical data alone, this was found to be insufficient.^[18,19,137] The dissolution of Mn ions from the catalyst material is a common cause of low stability.^[89,140–142] In comparison to the single MnO_x, the presence of Co sites in (Co_{0.7}Mn_{0.3})O_x hindered the dissolution of Mn sites, where the oxidation of Mn⁴⁺ to Mn⁷⁺O₄[−] in the solid was within the used voltage range. The lower dissolution rate likely avoids the irreversible current drop reported for MnO_x.^[50] Moreover, the introduction of Mn as a second metallic site in the Co oxide structure may generate more optimal binding between the metal site and the oxygen atoms, M-O. This effect was recently reported for a crystalline CoMn oxide in acid media.^[47] Density functional theory (DFT) calculation showed that the electronic interaction between the 2p orbital in the oxygen atom and the 3d orbitals in the metal are located in lower energy for the mixed CoMn oxide than the single Co oxide, which results in overall more stable bond in the mixed oxide^[47] with optimized bulk oxidation states, which are expected to also provide favorable binding of surface Mn and Co with OH[−] in the electrolyte.

Conclusion

Na-containing layered CoO_x and $(\text{Co}_{0.7}\text{Mn}_{0.3})\text{O}_x$ films were electrodeposited in 0.1 M NaOH solution, using a complexing agent for the stabilization of the ions. The co-deposition of Mn and Co ions produced single phase $(\text{Co}_{0.7}\text{Mn}_{0.3})\text{O}_x$, whose OER onset during the 2nd cycle and overpotential at 10 mA/cm² after 100 cycles were identical to CoO_x within error. Moreover, the Tafel slope of $(\text{Co}_{0.7}\text{Mn}_{0.3})\text{O}_x$ was constantly 89 ± 2 mV s⁻¹ during 100 cycles, while that of CoO_x tended to increase indicating that CoO_x may not efficiently support high currents for long durations.

Additionally, Mn dissolution in $(\text{Co}_{0.7}\text{Mn}_{0.3})\text{O}_x$ was significantly reduced as compared to MnO_x . Often, there is a trade-off between catalytic activity and stability.^[6] While we showed that 30 % Mn in layered CoO_x only had a minor effect on activity, it stabilized the structural integrity and activity during potential cycling under OER conditions.

As expected from the electrocatalytic trends, no changes were identified by XAS in $(\text{Co}_{0.7}\text{Mn}_{0.3})\text{O}_x$. We discussed the correlation between bulk and surface properties and concluded that the absence of changes in bulk and near surface oxidation state can explain the electrocatalytic trends of activity and stability at the surface. Overall, our study identifies Mn as a suitable addition to Co oxides with beneficial effects on the electric conductivity, metal oxidation states and binding energies that resulted in a promising electrocatalyst with high durability, while sacrificing little activity. Further microscopic and macroscopic insights into the origin of stabilization are essential for the future knowledge-guided design of durable electrocatalysts for electrolyzers.

Experimental Section

Materials

$\text{Co}(\text{NO}_3)_2 \cdot 6\text{H}_2\text{O}$ (≥ 99.99 %), Co_3O_4 (99.99), CoO (99.99 %), LiCoO_2 (>99.8 %), $\text{Mn}(\text{NO}_3)_2 \cdot 4\text{H}_2\text{O}$ (≥ 99.99 %), $\text{Mn}(\text{SO}_4)_2 \cdot x\text{H}_2\text{O}$ (99.99), MnO_2 (≥ 99 %), Mn_3O_4 (≥ 97 %), Mn_2O_3 (≥ 99.9 %), L-(+)-Tartaric acid (≥ 99.5 %) and (2 M and 0.1 M) NaOH solutions were ordered from Sigma-Aldrich. Graphite foil (≥ 99.8) with a thickness of 0.254 mm ordered from VWR. All reactants were used as received, without any further treatment. Solutions were prepared with deionized water (>18 M Ω cm).

Films electrodeposition

CoO_x films: 0.6 mmol of $\text{Co}(\text{NO}_3)_2 \cdot 6\text{H}_2\text{O}$ and 6 mmol of L-(+)-tartaric acid were dissolved in a small volume of deionized water (approx. 1 mL). 120 mL of Ar-purged 2 M NaOH solution were added slowly to the previous solution while stirring, changing from colorless to beige.

$(\text{Co}_{0.7}\text{Mn}_{0.3})\text{O}_x$ films: were prepared with a similar procedure to CoO_x using a mixture of 0.6 mmol of $\text{Co}(\text{NO}_3)_2 \cdot 6\text{H}_2\text{O}$ and 0.6 mmol of $\text{Mn}(\text{NO}_3)_2 \cdot 4\text{H}_2\text{O}$ as precursor solution. All other parameters remained the same.

The electrodeposition of the films was performed in a three-electrode cell made from a three-neck round-bottom flask and using a Gamry Reference 600+ potentiostat. The distance between the necks and thus the electrodes was kept lower than 1 cm. The working electrodes were either a glassy carbon disk (4 mm diameter; HTW Sigradur G) in a rotating disk electrode (RDE) or graphite paper (Alfa Aesar). The unrotated RDE was mounted onto a commercial rotator (ALS RRDE-3A Ver 2.0). We used a saturated calomel reference electrode (SCE; ALS RE-2BP) and a graphite rod (redox.me, HP-III, High Pure Graphite) as the counter electrode. The galvanostatic deposition was performed at 150 $\mu\text{A cm}^{-2}$ until a charge density of 40 mC cm⁻² was reached.

Electrochemical measurements

The detailed protocol for electrocatalytic investigations is documented in Table S1 for glassy carbon electrodes and in Table S2 for graphite foil. The measurements on glassy carbon electrodes were carried out using two Gamry Reference 600+ potentiostats connected as a bipotentiostat in a single compartment three-electrode electrochemical cell made of polymethyl pentene (ALS) filled with about 60 mL solution of 0.1 M NaOH. A commercial rotator (ALS RRDE3-A Ver 2.0) was used with commercial

rotating ring-disk electrodes (RRDE) with exchangeable disks of 4 mm diameter and a Pt ring with inner ring diameter of 5 mm and outer diameter of 7 mm. The graphite foil was clamped in the same cell as the RRDE. A coiled platinum wire was used as a counter electrode and a SCE (ALS RE-2BP) as a reference electrode, which was calibrated daily against a commercial reversible hydrogen electrode (RHE; Gaskatel HydroFlex). The electrochemical experiments were performed at constant controlled temperature of 25.0 °C. The ring was set to detect oxygen at 0.4 V vs. RHE as calibrated previously.^[30] Before any experiment, the electrolyte was purged with Ar for at least 30 minutes. The ohmic drop (also called iR_u drop) was corrected during post-processing by subtraction of iR_u from the measured potentials, where i and R_u are the measured current and uncompensated resistance, respectively. All potentials are given relative to the reversible hydrogen electrode (RHE). The Tafel slope was also calculated with a fitting of potential as function of the logarithm of the current, using the cathodic halfcycle of the cyclic voltammetry of iR_u -corrected data in the range between 1.71 and 1.76 V vs. RHE. The electrodes were swept at 100 mV s⁻¹ and rotated at 1600 rpm. The Tafel slope was obtained by linear regression of the iR_u -corrected potential ($E-iR_u$) against $\log_{10}(i)$. The error represents the standard deviation of three independently prepared electrodes.

Scanning electron microscopy (SEM) and energy dispersive X-ray spectroscopy (EDX)

The morphology of the samples was studied using a Zeiss LEO Gemini 1530 scanning electron microscope, with an acceleration voltage of 3 keV in high vacuum (approximately 10^{-9} bar) and using a secondary electron inLens detector. Images were taken in several regions of the sample to get representative data. EDX measurements were performed using a Thermo Fischer detector with an acceleration voltage of 12 keV.

X-ray absorption spectroscopy (XAS)

All XAS data were collected at an averaged nominal ring current of 300 mA in top-up and multi-bunch mode at the BESSY II synchrotron operated by Helmholtz-Zentrum Berlin. Soft XAS measurements at the Mn-L edges were conducted using the LiXEDrom experimental station at the UE56/2 PGM-2 or U492 PGM-1 beamline.^[143] Reference samples were measured as finely dispersed powders attached to carbon tape and electrodeposited samples were measured on graphite foil (Alfa Aesar). All samples were measured at room temperature and in total electron yield (TEY) mode and with horizontally linear polarization of the beam. The TEY measurements were carried out by collecting the drain current from the sample. The sample holder was connected to an ammeter (Keithley 6514). In order to avoid radiation damage, the incoming photon flux was adjusted to get a TEY current from the sample of around 10 pA. In addition, the sample was kept as thin as possible. XAS spectra for each sample were collected at a few locations to ensure representativity of the data and further minimize radiation damage and local heating. The energy axis was calibrated using a Mn-L edge spectrum of MnSO_4 as a standard where the maximum of the L_3 -edge was calibrated to 641 eV. This reference was calibrated against molecular oxygen as described elsewhere.^[144,145] All spectra were normalized by the subtraction of a straight line obtained by fitting the data before the L_3 edge and division by a polynomial function obtained by fitting the data after the L_3 edge.

Hard XAS measurements were performed at the KMC-2 or KMC3 beamlines.^[146,147] Co-K and Mn-K edge references were collected at KMC-3. Samples at Co-K edge and Mn-K edge as well as a few references were collected at KMC-2. Two references spectra were compared to confirm the correct energy calibration. At KMC-3, spectra were recorded in fluorescence mode using a 13-element silicon drift detector (SDD) from RaySpec. The used monochromator was a double-crystal Si (111), and the polarization of the beam was horizontal. Reference samples were prepared by dispersing a thin and homogeneous layer of the ground powder on Kapton tape. After removing the excess material, the tape was sealed, and the excess of Kapton was folded several times to get 1 cm \times 1 cm windows. The energy was calibrated using a Co metal foil (fitted reference energy of 7709 eV in the first derivative spectrum) with an accuracy ± 0.1 eV. Up to three scans of each sample were collected to $k = 14$ Å⁻¹.

At KMC-2, the general used setup was organized as it follows: I_0 ionization chamber, sample, I_1 ionization chamber or FY detector, energy reference and

I₂ ionization chamber. The used double monochromator consisted of two Ge-graded Si(111) crystal substrates^[148] and the polarization of the beam was linear horizontal. Reference samples were prepared by dispersing a thin and homogenous layer of the powder on Kapton tape, after removing excess of powder, the tape was folded several times to get 2 cm x 1 cm windows. Reference samples were measured in transmission mode between two ion chambers detector at room temperature. Electrodeposited samples were measured on graphite foil in fluorescence mode with a Bruker X-Flash 6/60 detector. Energy calibration of the X-ray near edge structure (XANES) was made with the corresponding metal foil, setting the inflection point for Mn at 6539 eV. All spectra were normalized by the subtraction of a straight line obtained by fitting the data before the K edge and division by a polynomial function obtained by fitting the data after the K edge. The Fourier transform (FT) of the extended X-ray absorption fine structure (EXAFS) was calculated between 40 and 440 eV (3.2 to 10.7 Å⁻¹) above the K edge (E₀ = 6539 eV for Mn and E₀ = 7709 eV for Co). A cosine window covering 10 % on the left side and 10 % on the right side of the EXAFS spectra was used to suppress the side lobes in the FTs.

EXAFS simulations were performed using the software SimXLite. After calculation of the phase functions with the FEFF8-Lite^[149] program (version 8.5.3, self-consistent field option activated). Atomic coordinates of the FEFF input files were generated from various structures of Mn- and Co-based oxide (Figure S13, Tables 1, 2, S5, S6 and S7),^[95,150,151] The EXAFS phase functions did not depend strongly on the details of the used model. An amplitude reduction factor (S₀²) of 0.7 was used. The EXAFS simulations were optimized by the minimization of the error sum obtained by summation of the squared deviations between measured and simulated values (least-squares fit). The errors were estimated using a useful R-space range of 4.2 Å and Fourier filters of 1 (left) and 3 (right).^[152] The fit was performed using the Levenberg–Marquardt method with numerical derivatives. The authors do not declare a conflict of interest.

The data that support the findings of this study are openly available on Figshare at DOI 10.6084/m9.figshare.18415520.

Acknowledgements

The authors thank Dr. Max Baumung, Joaquín Morales-Santelices and Sepideh Madadkhani for helping in data collection. Frederik Stender is acknowledged for writing the electrochemistry analysis script and Dr. Petko Chernev for permission to use his software SimXLite. Dr. Michael Haumann and Dr. Ivo Zizak are thanked for support at the beamline station. We thank Helmholtz-Zentrum Berlin (HZB) for the allocation of synchrotron radiation beamtime and acknowledge the HZB CoreLab CCMS (Correlative Microscopy and Spectroscopy) for training and advising in SEM. The XAS experiments were financially supported by funds allocated to Prof. Holger Dau (Freie Univ. Berlin) by the Bundesministerium für Bildung und Forschung (BMBF, 05K19KE1, OPERANDO-XAS) and by the Deutsche Forschungsgemeinschaft (DFG, German Research Foundation) under Germany's Excellence Strategy—EXC 2008—390540038—UniSysCat. This project has received funding from the European Research Council (ERC) under the European Union's Horizon 2020 research and innovation programme under grant agreement No 804092.

Keywords: catalyst stability • bimetallic oxides • catalyst activation • oxygen evolution reaction • Co-based oxides

References

- [1] D. G. Nocera, *Acc. Chem. Res.* **2017**, *50*, 616–619.
- [2] M. Risch, *Nat. Energy* **2021**, *6*, 576–577.
- [3] H. Dau, I. Zaharieva, *Acc. Chem. Res.* **2009**, *42*, 1861–1870.
- [4] T. Faunce, S. Styring, M. R. Wasielewski, G. W. Brudvig, A. W. Rutherford, J. Messinger, A. F. Lee, C. L. Hill, H. Degroot, M. Fontecave, D. R. MacFarlane, B. Hankamer, D. G. Nocera, D. M. Tiede, H. Dau, W. Hillier, L. Wang, R. Amal, *Energy Environ. Sci.* **2013**, *6*, 1074–1076.
- [5] Z. P. Ifkovits, J. M. Evans, M. C. Meier, K. M. Papadantonakis, N. S. Lewis, *Energy Environ. Sci.* **2021**, *14*, 4740–4759.
- [6] J. Masa, C. Andronesco, W. Schuhmann, *Angew. Chemie - Int. Ed.* **2020**, *59*, 15298–15312.
- [7] M. Carmo, D. Fritz, J. Mergel, D. Stolten, *Int. J. Hydrogen Energy* **2013**, *38*, 4901–4934.
- [8] M. S. Burke, L. J. Enman, A. S. Batchellor, S. Zou, S. W. Boettcher, *Chem. Mater.* **2015**, *27*, 7549–7558.
- [9] J. Yang, M. J. Jang, X. Zeng, Y. S. Park, J. Lee, S. M. Choi, Y. Yin, *Electrochem. commun.* **2021**, *131*, 107118. [10] M. Gong, H. Dai, *Nano Res.* **2015**, *8*, 23–39.
- [11] F. Song, L. Bai, A. Moysiadou, S. Lee, C. Hu, L. Liardet, X. Hu, *J. Am. Chem. Soc.* **2018**, *140*, 7748–7759.
- [12] L. Zhang, Q. Fan, K. Li, S. Zhang, X. Ma, *Sustain. Energy Fuels* **2020**, *4*, 5417–5432.
- [13] A. Moysiadou, X. Hu, *J. Mater. Chem. A* **2019**, *7*, 25865–25877.
- [14] D. Zhou, P. Li, W. Xu, S. Jawaid, J. Mohammed-Ibrahim, W. Liu, Y. Kuang, X. Sun, *ChemNanoMat* **2020**, *6*, 336–355.
- [15] Y. Liu, X. Liang, L. Gu, Y. Zhang, G. D. Li, X. Zou, J. S. Chen, *Nat. Commun.* **2018**, *9*, 1–10.
- [16] Q. Shi, C. Zhu, D. Du, Y. Lin, *Chem. Soc. Rev.* **2019**, *48*, 3181–3192.
- [17] B. Mayerhöfer, F. D. Speck, M. Hegelheimer, M. Bierling, D. Abbas, D. McLaughlin, S. Cherevko, S. Thiele, R. Peach, *Int. J. Hydrogen Energy* **2022**, *47*, 4304–4314.
- [18] S. Geiger, O. Kasian, M. Ledendecker, E. Pizzutillo, A. M. Mingers, W. T. Fu, O. Diaz-Morales, Z. Li, T. Oellers, L. Fruchter, A. Ludwig, K. J. J. Mayrhofer, M. T. M. Koper, S. Cherevko, *Nat. Catal.* **2018**, *1*, 508–515.
- [19] S. Geiger, O. Kasian, A. M. Mingers, S. S. Nicley, K. Haenen, K. J. J. Mayrhofer, S. Cherevko, *ChemSusChem* **2017**, *10*, 4140–4143.
- [20] M. Baumung, L. Kollenbach, L. Xi, M. Risch, *ChemPhysChem* **2019**, *20*, 1–9.
- [21] M. Risch, A. Grimaud, K. J. May, K. A. Stoerzinger, T. J. Chen, A. N. Mansour, Y. Shao-Horn, *J. Phys. Chem. C* **2013**, *117*, 8628–8635.
- [22] K. J. May, C. E. Carlton, K. A. Stoerzinger, M. Risch, J. Suntivich, Y.-L. Lee, A. Grimaud, Y. Shao-Horn, *J. Phys. Chem. Lett.* **2012**, *3*, 3264–3270.
- [23] F. D. Speck, P. G. Santori, F. Jaouen, S. Cherevko, *J. Phys. Chem. C* **2019**, *123*, 25267–25277.
- [24] A. R. Zeradjanin, A. A. Topalov, Q. Van Overmeere, S. Cherevko, X. Chen, E. Ventosa, W. Schuhmann, K. J. J. Mayrhofer, *RSC Adv.* **2014**, *4*, 9579–9587.
- [25] M. Huynh, C. Shi, S. J. L. Billinge, D. G. Nocera, *J. Am. Chem. Soc.* **2015**, *137*, 14887–14904.
- [26] S. Zhao, H. Yu, R. Maric, N. Danilovic, C. B. Capuano, K. E. Ayers, W. E. Mustain, *J. Electrochem. Soc.* **2015**, *162*, F1292–F1298.
- [27] Q. Xiao, Y. Zhang, X. Guo, L. Jing, Z. Yang, Y. Xue, Y. M. Yan, K. Sun, *Chem. Commun.* **2014**, *50*, 13019–13022.
- [28] I. Spanos, A. A. Auer, S. Neugebauer, X. Deng, H. Tüysüz, R. Schlögl, *ACS Catal.* **2017**, *7*, 3768–3778.
- [29] S. Polani, K. E. Macarthur, M. Klingenhof, X. Wang, P. Paciok, L. Pan, Q. Feng, A. Kormányos, S. Cherevko, M. Heggen, P. Strasser, *ACS Catal.* **2021**, *11*, 11407–11415.
- [30] M. Baumung, F. Schönewald, T. Erichsen, C. A. Volkert, M. Risch, *Sustain. Energy Fuels* **2019**, *3*, 2218–2226.
- [31] J. Wang, S. J. Kim, J. Liu, Y. Gao, S. Choi, J. Han, H. Shin, S. Jo, J. Kim, F. Ciucci, H. Kim, Q. Li, W. Yang, X. Long, S. Yang, S. P. Cho, K. H. Chae, M. G. Kim, H. Kim, J. Lim, *Nat. Catal.* **2021**, *4*, 212–222.
- [32] D. Chinnadurai, R. Rajendiran, O. L. Li, K. Prabakar, *Appl. Catal. B Environ.* **2021**, *292*, DOI 10.1016/j.apcatb.2021.120202.
- [33] C. L. I. Flores, M. D. L. Balela, *J. Solid State Electrochem.* **2020**, *24*, 891–904.
- [34] A. Bergmann, E. Martinez-Moreno, D. Teschner, P. Chernev, M. Gliech, J. F. De Araújo, T. Reier, H. Dau, P. Strasser, *Nat. Commun.* **2015**, *6*, 8625.
- [35] J. Wang, L. Han, B. Huang, Q. Shao, H. L. Xin, X. Huang, *Nat. Commun.* **2019**, *10*, 1–11.
- [36] M. Görlin, M. Gliech, J. F. De Araújo, S. Dresch, A. Bergmann, P. Strasser, *Catal. Today* **2016**, *262*, 65–73.
- [37] H. Jin, J. Wang, D. Su, Z. Wei, Z. Pang, Y. Wang, *J. Am.*

- Chem. Soc.* **2015**, *137*, 2688–2694.
- [38] X. Li, Y. Sun, Q. Wu, H. Liu, W. Gu, X. Wang, Z. Cheng, Z. Fu, Y. Lu, *J. Am. Chem. Soc.* **2019**, *141*, 3121–3128.
- [39] M. R. Mohammadi, S. Loos, P. Chernev, C. Pasquini, I. Zaharieva, D. González-Flores, P. Kubella, K. Klingan, R. D. L. Smith, H. Dau, *ACS Catal.* **2020**, *10*, 7990–7999.
- [40] K. Lankauf, K. Cysewska, J. Karczewski, A. Mielewczyk-Gryn, K. Górnicka, G. Cempura, M. Chen, P. Jasiński, S. Molin, *Int. J. Hydrogen Energy* **2020**, *45*, 14867–14879.
- [41] M. S. Burke, M. G. Kast, L. Trotochaud, A. M. Smith, S. W. Boettcher, *J. Am. Chem. Soc.* **2015**, *137*, 3638–3648.
- [42] P. W. Menezes, A. Indra, N. R. Sahraie, A. Bergmann, P. Strasser, M. Driess, *ChemSusChem* **2015**, *8*, 164–167.
- [43] H. Y. Wang, Y. Y. Hsu, R. Chen, T. S. Chan, H. M. Chen, B. Liu, *Adv. Energy Mater.* **2015**, *5*, 1–8.
- [44] N. I. Kim, Y. J. Sa, T. S. Yoo, S. R. Choi, R. A. Afzal, T. Choi, Y. S. Seo, K. S. Lee, J. Y. Hwang, W. S. Choi, S. H. Joo, J. Y. Park, *Sci. Adv.* **2018**, *4*, eaap9360.
- [45] M. Huynh, T. Ozel, C. Liu, E. C. Lau, D. G. Nocera, *Chem. Sci.* **2017**, *8*, 4779–4794.
- [46] Z. Wang, Y. Hu, W. Liu, L. Xu, M. Guan, Y. Zhao, J. Bao, H. Li, *Chem. - A Eur. J.* **2020**, *26*, 9382–9388.
- [47] A. Li, S. Kong, C. Guo, H. Ooka, K. Adachi, D. Hashizume, Q. Jiang, H. Han, J. Xiao, R. Nakamura, *Nat. Catal.* **2022**, *5*, DOI 10.1038/s41929-021-00732-9.
- [48] A. Navrotsky, O. J. Kleppa, *J. Inorg. Nucl. Chem.* **1967**, *29*, 2701–2714.
- [49] Y. Sugawara, H. Kobayashi, I. Honma, T. Yamaguchi, *ACS Omega* **2020**, *5*, 29388–29397.
- [50] J. Villalobos, R. Golnak, L. Xi, G. Schuck, M. Risch, *J. Phys. Energy* **2020**, *2*, 034009.
- [51] J. Villalobos, D. González-Flores, K. Klingan, P. Chernev, P. Kubella, R. Urcuyo, C. Pasquini, M. R. Mohammadi, R. D. L. Smith, M. L. Montero, H. Dau, *Phys. Chem. Chem. Phys.* **2019**, *21*, 12485–12493.
- [52] B. J. Kim, E. Fabbri, D. F. Abbott, X. Cheng, A. H. Clark, M. Nachtegaal, M. Borlaf, I. E. Castelli, T. Graule, T. J. Schmidt, *J. Am. Chem. Soc.* **2019**, *141*, 5231–5240.
- [53] W. Zhang, P. Anguita, J. Diez-Ramírez, C. Descorme, J. L. Valverde, A. Giroir-fendler, *Catalysts* **2020**, *10*, 865.
- [54] H. Jin, S. Mao, G. Zhan, F. Xu, X. Bao, Y. Wang, *J. Mater. Chem. A* **2017**, *5*, 1078–1084.
- [55] P. J. Statham, *J. Res. Natl. Inst. Stand. Technol.* **2002**, *107*, 531–546.
- [56] J. J. Friel, C. E. Lyman, *Microsc. Microanal.* **2006**, *12*, 2–25.
- [57] Z. Sun, A. Curto, J. Rodríguez-Fernández, Z. Wang, A. Parikh, J. Fester, M. Dong, A. Vojvodic, J. V. Lauritsen, *ACS Nano* **2021**, *15*, 18226–18236.
- [58] J. Villalobos, D. M. Morales, D. Antipin, G. Schuck, R. Golnak, J. Xiao, M. Risch, **2022**, DOI 10.6084/m9.figshare.18415520.
- [59] J. Villalobos, D. González-Flores, R. Urcuyo, M. L. Montero, G. Schuck, P. Beyer, M. Risch, *Adv. Energy Mater.* **2021**, *11*, 2101737.
- [60] D. González-Flores, I. Sánchez, I. Zaharieva, K. Klingan, J. Heidkamp, P. Chernev, P. W. Menezes, M. Driess, H. Dau, M. L. Montero, *Angew. Chemie - Int. Ed.* **2015**, *54*, 2472–2476.
- [61] X. Guo, F. Wu, G. Hao, S. Peng, N. Wang, Q. Li, Y. Hu, W. Jiang, *Dalt. Trans.* **2019**, *48*, 5214–5221.
- [62] X. Wang, R. Tong, Y. Wang, H. Tao, Z. Zhang, H. Wang, *ACS Appl. Mater. Interfaces* **2016**, *8*, 34270–34279.
- [63] T. Jiang, S. A. Ansar, X. Yan, C. Chen, X. Fan, F. Razmjooei, R. Reisser, G. Montavon, H. Liao, *ACS Appl. Energy Mater.* **2019**, *2*, 8809–8817.
- [64] C. C. L. McCrory, S. Jung, I. M. Ferrer, S. M. Chatman, J. C. Peters, T. F. Jaramillo, *J. Am. Chem. Soc.* **2015**, *137*, 4347–4357.
- [65] C. Wei, R. R. Rao, J. Peng, B. Huang, I. E. L. Stephens, M. Risch, Z. J. Xu, Y. Shao-Horn, *Adv. Mater.* **2019**, *31*, 1–24.
- [66] C. C. L. McCrory, S. Jung, J. C. Peters, T. F. Jaramillo, *J. Am. Chem. Soc.* **2013**, *135*, 16977–16987.
- [67] A. Grimaud, K. J. May, C. E. Carlton, Y. L. Lee, M. Risch, W. T. Hong, J. Zhou, Y. Shao-Horn, *Nat. Commun.* **2013**, *4*, 1–7.
- [68] S. W. Lee, C. Carlton, M. Risch, Y. Surendranath, S. Chen, S. Furutsuki, A. Yamada, D. G. Nocera, Y. Shao-Horn, *J. Am. Chem. Soc.* **2012**, *134*, 16959–16962.
- [69] M. Risch, K. A. Stoerzinger, S. Maruyama, W. T. Hong, I. Takeuchi, Y. Shao-Horn, *J. Am. Chem. Soc.* **2014**, *136*, 5229–5232.
- [70] M. S. Burke, S. Zou, L. J. Enman, J. E. Kellon, C. A. Gabor, E. Pledger, S. W. Boettcher, *J. Phys. Chem. Lett.* **2015**, *6*, 3737–3742.
- [71] Y. C. Zhang, C. Han, J. Gao, L. Pan, J. Wu, X. D. Zhu, J. J. Zou, *ACS Catal.* **2021**, *11*, 12485–12509.
- [72] Y. Hu, H. Chen, X. Zhang, W. Wen, Q. He, C. He, *J. Phys. Chem. C* **2019**, *123*, 22130–22138.
- [73] T. Priamushko, R. Guillet-Nicolas, M. Yu, M. Doyle, C. Weidenthaler, H. Tuýstüz, F. Kleitz, *ACS Appl. Energy Mater.* **2020**, *3*, 5597–5609.
- [74] I. Abidat, N. Bouchenafa-Saib, A. Habrioux, C. Comminges, C. Canaff, J. Rousseau, T. W. Napporn, D. Dambournet, O. Borkiewicz, K. B. Kokoh, *J. Mater. Chem. A* **2015**, *3*, 17433–17444.
- [75] H. A. El-Sayed, A. Weiß, L. F. Olbrich, G. P. Putro, H. A. Gasteiger, *J. Electrochem. Soc.* **2019**, *166*, F458–F464.
- [76] D. M. Morales, M. Risch, *JPhys Energy* **2021**, *3*, 034013.
- [77] L. Köhler, M. Ebrahimizadeh Abrishami, V. Roddatis, J. Geppert, M. Risch, *ChemSusChem* **2017**, *10*, 4479–4490.
- [78] D. Antipin, M. Risch, *ChemRxiv. Cambridge Cambridge Open Engag.* **2021**; This content is a Prepr. has not been peer-reviewed. **2021**, DOI 10.26434/chemrxiv-2021-hgbq6.
- [79] R. L. Doyle, I. J. Godwin, M. P. Brandon, M. E. Lyons, *Phys Chem Chem Phys* **2013**, *15*, 13737–13783.
- [80] M. Risch, F. Ringleb, M. Kohlhoff, P. Bogdanoff, P. Chernev, I. Zaharieva, H. Dau, *Energy Environ. Sci.* **2015**, *8*, 661–674.
- [81] Y. Surendranath, M. W. Kanan, D. G. Nocera, *J. Am. Chem. Soc.* **2010**, *132*, 16501–16509.
- [82] I. Zaharieva, P. Chernev, M. Risch, K. Klingan, M. Kohlhoff, A. Fischer, H. Dau, *Energy Environ. Sci.* **2012**, *5*, 7081–7089.
- [83] C. Walter, P. W. Menezes, S. Loos, H. Dau, M. Driess, *ChemSusChem* **2018**, *11*, 2554–2561.
- [84] A. Indra, P. W. Menezes, I. Zaharieva, E. Baktash, J. Pfrommer, M. Schwarze, H. Dau, M. Driess, *Angew. Chemie - Int. Ed.* **2013**, *52*, 13206–13210.
- [85] R. Guidelli, R. G. Compton, J. M. Feliu, E. Gileadi, J. Lipkowski, W. Schmickler, S. Trasatti, *Pure Appl. Chem.* **2014**, *86*, 245–258.
- [86] T. Shinagawa, A. T. Garcia-Esparza, K. Takanabe, *Sci. Rep.* **2015**, *5*, 1–21.
- [87] D. R. Lide, *CRC Handbook of Chemistry and Physics*, CRC Press, **2006**.
- [88] M. F. Tesch, S. A. Bonke, T. E. Jones, M. N. Shaker, J. Xiao, K. Skorupska, R. Mom, J. Melder, P. Kurz, A. KnopGerick, R. Schlögl, R. K. Hocking, A. N. Simonov, *Angew. Chemie* **2019**, *131*, 3464–3470.
- [89] A. Li, H. Ooka, N. Bonnet, T. Hayashi, Y. Sun, Q. Jiang, C. Li, H. Han, R. Nakamura, *Angew. Chemie - Int. Ed.* **2019**, *58*, 5054–5058.
- [90] J. Scholz, M. Risch, K. A. Stoerzinger, G. Wartner, Y. Shao-Horn, C. Jooss, *J. Phys. Chem. C* **2016**, *120*, 27746–27756.
- [91] S. Vesztergom, N. Barankai, P. Broekmann, H. Siegenthaler, *Electrochem. Comm.* **2016**, *68*, 54–58.
- [92] B. L. Henke, E. M. Gullikson, J. C. Davis, *At. Data Nucl. Data Tables* **1993**, *54*, 181–342.
- [93] M. Risch, K. Klingan, F. Ringleb, P. Chernev, I. Zaharieva, A. Fischer, H. Dau, *ChemSusChem* **2012**, *5*, 542–9.
- [94] M. Risch, V. Khare, I. Zaharieva, L. Gerencser, P. Chernev, H. Dau, *J. Am. Chem. Soc.* **2009**, *131*, 6936–6937. [95] C. Fontana, *Gazz. Chim. Ital.* **1926**, *56*, 396–397.
- [96] A. Iyer, J. Del-Pilar, C. K. King'andu, E. Kissel, H. F. Garces, H. Huang, A. M. El-Sawy, P. K. Dutta, S. L. Suib, *J. Phys. Chem. C* **2012**, *116*, 6474–6483.
- [97] M. V. Abrashev, P. Chernev, P. Kubella, M. R. Mohammadi, C. Pasquini, H. Dau, I. Zaharieva, *J. Mater. Chem. A* **2019**, *7*, 17022–17036.

- [98] A. Bergmann, I. Zaharieva, H. Dau, P. Strasser, *Energy Environ. Sci.* **2013**, *6*, 2745–2755.
- [99] Z. Geng, Y. Wang, J. Liu, G. Li, L. Li, K. Huang, L. Yuan, S. Feng, *ACS Appl. Mater. Interfaces* **2016**, *8*, 27825–27831.
- [100] M. Deliens, H. Goethals, *Mineral. Mag.* **1973**, *39*, 152–157. [101] J. E. Penner-Hahn, *Compr. Coord. Chem. II* **2003**, *2*, 159–186.
- [102] A. Ruosi, C. Raisch, A. Verna, R. Werner, B. A. Davidson, J. Fujii, R. Kleiner, D. Koelle, *Phys. Rev. B - Condens. Matter Mater. Phys.* **2014**, *90*, 1–8.
- [103] J. E. Post, D. R. Veblen, *Am. Mineral.* **1990**, *75*, 477–489.
- [104] M. W. Kanan, Y. Surendranath, D. G. Nocera, *Chem. Soc. Rev.* **2009**, *38*, 109–114.
- [105] L. F. Huang, J. M. Rondinelli, *npj Mater. Degrad.* **2019**, *3*, DOI 10.1038/s41529-019-0088-z.
- [106] F. Calle-Vallejo, O. Diaz-Morales, M. Kolb, M. T. M. Koper, *ACS Catal.* **2015**, *5*, 869–873.
- [107] L. Zhan, S. Wang, L. X. Ding, Z. Li, H. Wang, *J. Mater. Chem. A* **2015**, *3*, 19711–19717.
- [108] D. Lu, C. Yuan, M. Yu, Y. Yang, C. Wang, R. Guan, X. Bian, *ACS Omega* **2020**, *5*, 21488–21496.
- [109] V. Vashook, D. Franke, J. Zosel, L. Vasylechko, M. Schmidt, U. Guth, *J. Alloys Compd.* **2009**, *487*, 577–584. [110] L. Fan, E. L. Rautama, J. Lindén, J. Sainio, H. Jiang, O. Sorsa, N. Han, C. Flox, Y. Zhao, Y. Li, T. Kallio, *Nano Energy* **2022**, *93*, 106794.
- [111] Y. T. Kim, P. P. Lopes, S. A. Park, A. Y. Lee, J. Lim, H. Lee, S. Back, Y. Jung, N. Danilovic, V. Stamenkovic, J. Erlebacher, J. Snyder, N. M. Markovic, *Nat. Commun.* **2017**, *8*, 1–8.
- [112] J. Li, P. Liu, J. Mao, J. Yan, W. Song, *J. Mater. Chem. A* **2021**, *9*, 11248–11254.
- [113] R. D. Shannon, *Acta Crystallogr. Sect. A* **1976**, *32*, 751–767.
- [114] J. M. Honig, *J. Chem. Educ.* **1966**, *43*, 76–82.
- [115] C. Costentin, D. G. Nocera, *J. Phys. Chem. C* **2019**, *123*, 1966–1973.
- [116] M. K. Bates, Q. Jia, H. Doan, W. Liang, S. Mukerjee, *ACS Catal.* **2016**, *6*, 155–161.
- [117] L. Chen, H. F. Wang, C. Li, Q. Xu, *Chem. Sci.* **2020**, *11*, 5369–5403.
- [118] T. Ishihara, T. Yamada, H. Arikawa, H. Nishiguchi, Y. Takita, *Solid State Ionics* **2000**, *135*, 631–636.
- [119] Z. H. He, J. F. Gao, L. Bin Kong, *Ionics (Kiel)* **2020**, *26*, 1379–1388.
- [120] J. Xiao, S. Yang, *RSC Adv.* **2011**, *1*, 588–595.
- [121] K. Li, R. Zhang, R. Gao, Q. G. Shen, L. Pan, Y. Yao, K. Yu, X. Zhang, J. J. Zou, *Appl. Catal. B Environ.* **2019**, *244*, 536–545.
- [122] H. Wang, K. H. L. Zhang, J. P. Hofmann, V. A. de la Peña O'Shea, F. E. Oropeza, *J. Mater. Chem. A* **2021**, *9*, 19465–19488.
- [123] D. Antipin, M. Risch, *JPhys Energy* **2020**, *2*, DOI 10.1088/2515-7655/ab812f.
- [124] W. T. Hong, M. Risch, K. A. Stoerzinger, A. Grimaud, J. Suntivich, Y. Shao-Horn, *Energy Environ. Sci.* **2015**, *8*, 1404–1427.
- [125] J. Suntivich, K. J. May, H. A. Gasteiger, J. B. Goodenough, Y. Shao-horn, *Science* **2011**, *334*, 2010–2012.
- [126] J. Melder, P. Bogdanoff, I. Zaharieva, S. Fiechter, H. Dau, P. Kurz, *Z. Phys. Chem.* **2020**, *234*, 925–978.
- [127] S. Lian, M. P. Browne, C. Domínguez, S. N. Stamatini, H. Nolan, G. S. Duesberg, M. E. G. Lyons, E. Fonda, P. E. Colavita, *Sustain. Energy Fuels* **2017**, *1*, 780–788.
- [128] I. Zaharieva, D. González-Flores, B. Asfari, C. Pasquini, M. R. Mohammadi, K. Klingan, I. Zizak, S. Loos, P. Chernev, H. Dau, *Energy Environ. Sci.* **2016**, *9*, 2433–2443.
- [129] L. Xi, C. Schwanke, J. Xiao, F. F. Abdi, I. Zaharieva, K. M. Lange, *J. Phys. Chem. C* **2017**, *121*, 12003–12009.
- [130] A. Ramirez, P. Hillebrand, D. Stellmach, M. M. May, P. Bogdanoff, S. Fiechter, *J. Phys. Chem. C* **2014**, *118*, 14073–14081.
- [131] Y. Gorlin, T. F. Jaramillo, *J. Am. Chem. Soc.* **2010**, *132*, 13612–13614.
- [132] P. F. Smith, B. J. Deibert, S. Kaushik, G. Gardner, S. Hwang, H. Wang, J. F. Al-Sharab, E. Garfunkel, L. Fabris, J. Li, G. C. Dismukes, *ACS Catal.* **2016**, *6*, 2089–2099. [133] Z. M. Chan, D. A. Kitchaev, J. N. Weker, C. Schnedermann, K. Lim, G. Ceder, W. Tumas, M. F. Toney, D. G. Nocera, *Proc. Natl. Acad. Sci. U. S. A.* **2018**, *115*, E5261–E5268.
- [134] M. Khan, E. Suljoti, A. Singh, S. A. Bonke, T. Brandenburg, K. Atak, R. Golnak, L. Spiccia, E. F. Aziz, *J. Mater. Chem. A* **2014**, *2*, 18199–18203.
- [135] M. Huynh, D. K. Bediako, D. G. Nocera, *J. Am. Chem. Soc.* **2014**, *136*, 6002–6010.
- [136] Z. Zhou, X. Zheng, H. Huang, Y. Wu, S. Han, W. Cai, B. Lan, M. Sun, L. Yu, *CrystEngComm* **2022**, *24*, 2327–2335.
- [137] R. Frydendal, E. A. Paoli, B. P. Knudsen, B. Wickman, P. Malacrida, I. E. L. Stephens, I. Chorkendorff, *ChemElectroChem* **2014**, *1*, 2075–2081.
- [138] T. Takashima, K. Hashimoto, R. Nakamura, *J. Am. Chem. Soc.* **2012**, *134*, 1519–27.
- [139] H. Ooka, T. Takashima, A. Yamaguchi, T. Hayashi, R. Nakamura, *Chem. Commun.* **2017**, *53*, 7149–7161.
- [140] Q. Gao, C. Ranjan, Z. Pavlovic, R. Blume, R. Schlögl, *ACS Catal.* **2015**, *5*, 7265–7275.
- [141] K. Jin, H. Seo, T. Hayashi, M. Balamurugan, D. Jeong, Y. K. Go, J. S. Hong, K. H. Cho, H. Kakizaki, N. BonnetMercier, M. G. Kim, S. H. Kim, R. Nakamura, K. T. Nam, *J. Am. Chem. Soc.* **2017**, *139*, 2277–2285.
- [142] C. H. Kuo, W. Li, L. Pahalagedara, A. M. El-Sawy, D. Kriz, N. Genz, C. Guild, T. Ressler, S. L. Suib, J. He, *Angew. Chemie - Int. Ed.* **2015**, *54*, 2345–2350.
- [143] E. F. Aziz, J. Xiao, R. Golnak, M. Tesch, *J. large-scale Res. Facil.* **2016**, *2*, 1–4.
- [144] M. Risch, K. A. Stoerzinger, T. Z. Regier, D. Peak, S. Y. Sayed, Y. Shao-Horn, *J. Phys. Chem. C* **2015**, *119*, 18903–18910.
- [145] M. Risch, K. A. Stoerzinger, B. Han, T. Z. Regier, D. Peak, S. Y. Sayed, C. Wei, Z. Xu, Y. Shao-Horn, *J. Phys. Chem. C* **2017**, *121*, 17682–17692.
- [146] G. Schuck, I. Zisak, *J. large-scale Res. Facil.* **2020**, *6*, 139. [147] D. M. Többsen, S. Zander, *J. large-scale Res. Facil.* **2016**, *2*, 1–6.
- [148] A. Erko, I. Packe, W. Gudat, N. Abrosimov, A. Firsov, *Nucl. Instruments Methods Phys. Res. Sect. A Accel. Spectrometers, Detect. Assoc. Equip.* **2001**, *467–468*, 623–626.
- [149] A. Ankudinov, B. Ravel, *Phys. Rev. B - Condens. Matter Mater. Phys.* **1998**, *58*, 7565–7576.
- [150] R. G. Delaplane, J. A. Ibers, J. R. Ferraro, J. J. Rush, *J. Chem. Phys.* **1969**, *50*, 1920–1927.
- [151] R. W. G. Wyckoff, *Acta Crystallogr.* **1963**, *1*, 239–444.
- [152] M. Risch, K. Klingan, J. Heidkamp, D. Ehrenberg, P. Chernev, I. Zaharieva, H. Dau, *Chem. Commun.* **2011**, *47*, 1

Supplementary material

Stabilization of a Mn-Co oxide during oxygen evolution in alkaline media

Javier Villalobos,^[a] Dulce M. Morales,^[a] Denis Antipin,^[a] Götz Schuck,^[b] Ronny Golnak,^[c] Jie Xiao,^[c] Marcel Risch^{[a]*}

[a] Nachwuchsgruppe Gestaltung des Sauerstoffentwicklungsmechanismus
Helmholtz-Zentrum Berlin für Materialien und Energie GmbH
Hahn-Meitner Platz 1, Berlin 14109, Germany

[b] Abteilung Struktur und Dynamik von Energiematerialien
Helmholtz-Zentrum Berlin für Materialien und Energie GmbH
Hahn-Meitner Platz 1, Berlin 14109, Germany

[c] Department of Highly Sensitive X-ray Spectroscopy
Helmholtz-Zentrum Berlin für Materialien und Energie GmbH
Albert-Einstein-Straße 15, Berlin 12489, Germany

Corresponding author
marcel.risch@helmholtz-berlin.de

14 pages, 9 supplementary tables, 14 supplementary figures

Supporting Tables

Table S1. General protocol for electrochemical data collection on an RRDE station with samples on glassy carbon disks. All potentials are reported vs. RHE. Electrolyte was 0.1 M NaOH. Blanket indicates no purge.

Step	Conditions
1. Cleaning	Clean and polish electrodes, cells and any other tool properly.
2. Calibration of reference electrodes	OCP against commercial RHE electrode
3. Argon purge at OCP	At least 30 minutes
4.a. Ring EIS	Frequency: 1 MHz – 1 Hz. Points/decade: 10 OCP and take note of R_u
4.b. Disk EIS	Frequency: 1 MHz – 1 Hz. Points/decade: 10 OCP and take note of R_u
5. Disk CV: ECSA*	Hold 10 s at 1.0 V. Potential window: 0.95 V – 1.05 V. Scan rates: 50, 100, 150, 200, 250, 300, 350, 400, 450, 500 mV s ⁻¹ . Cycles: 3. Rotation: 0 rpm. Purge: Blanket. No dynamic iR_u compensation.
6.a. Ring conditioning	Hold ring potential for 1800 s at 0.40 V.
6.b. Ring: CA (O ₂ detection)	Hold ring potential at 0.40 V.
6.c. Disk CV: OER	Potential window: 1.40 V - 1.80 V Scan rate: 100 mV s ⁻¹ Step size: 2 mV Cycles: 100 Rotation: 1600 rpm Purge: yes No dynamic iR_u compensation.
7. Disk CV: ECSA*	Hold 10 s at 1.0 V. Potential window: 0.95 V – 1.05 V. Scan rates: 50, 100, 150, 200, 250, 300, 350, 400, 450, 500 mV s ⁻¹ . Cycles: 3. Rotation: 0 rpm. Purge: Blanket. No dynamic iR_u compensation.
8. Disk OCP	1800 s
9.a. Disk EIS	Frequency: 1 MHz – 1 Hz. OCP and take note of R_u
9.b. Ring EIS	Frequency: 1 MHz – 1 Hz. OCP and take note of R_u
10.a. Ring conditioning	Hold ring potential for 1800 s at 0.40 V.
10.b. Ring: CA (O ₂ detection)	Hold ring potential at 0.40 V.
11. Disk CV: OER	Potential window: 1.40 V - 1.80 V Scan rate: 100 mV s ⁻¹ Step size: 2 mV Cycles: 10 Rotation: 1600 rpm. Purge: yes No dynamic iR_u compensation.

* not used due to inappropriate data for analysis.

Table S2. General protocol for electrochemical data collection with samples on graphite foil. All potentials are reported vs. RHE. Electrolyte was 0.1 M NaOH.

1. Cleaning	Clean and polish electrodes, cells and any other tool properly.
2. Calibration of reference electrodes	OCP against commercial RHE electrode
3. Argon purge at OCP	At least 30 minutes
4. Foil CV: OER	Potential window: 1.40 V - 1.80 V Scan rate: 100 mV s ⁻¹ Step size: 2 mV Cycles: 100 Rotation: 1600 rpm Purge: yes No dynamic iR _u compensation
5. Sample rinsing	Soaked in deionized water for 5 minutes.

Table S3. Average exponent values of the current trends over cycling. The exponents were estimated from Figure 3 at each selected potential and each selected region.

Samples	Potential	Region's exponent			
		1	2	3	1 – OCP ^[a]
CoO _x	1.55	-1/25	-1/25	-1/25	-1/10
	1.64	-1/25	-1/25	-1/25	-1/30
	1.70	-1/25	-1/25	-1/25	-1/10
(Co _{0.7} Mn _{0.3})O _x	1.55	-1/7	-1/5	-1/15	-1/6
	1.66	-1/34	-1/17	1/4	-1/7
	1.70	1/16	1/9	1/5	-1/22

^[a] region 1 after the OCP break.

Table S4. Averaged Tafel slope values for CoO_x and (Co_{0.7}Mn_{0.3})O_x at selected cycles. The values are the average of three different samples and standard deviation is reported as error.

Cycle	CoO _x		(Co _{0.7} Mn _{0.3})O _x	
	Average [mV dec ⁻¹]	Error [mV dec ⁻¹]	Average [mV dec ⁻¹]	Error [mV dec ⁻¹]
2	135	9	86	6
3	136	9	91	1
5	136	12	89	3
10	138	11	88	2
20	144	15	89	2
50	149	27	89	3
100	158	25	88	4
2	132	9	96	5
3	133	9	98	4
5	133	10	99	3
10	133	11	95	11

Table S5. EXAFS absorber-scatter averaged distance (R), neighboring atoms number (N) and Debye-Waller factor (σ) as determined by simulation of the k^3 -weighted EXAFS spectra at the Mn-K edge for pristine MnO_x (MnO_x -0) and MnO_x after 100 cycles (MnO_x -100), pristine $(\text{Co}_{0.7}\text{Mn}_{0.3})\text{O}_x$ ($(\text{Co}_{0.7}\text{Mn}_{0.3})\text{O}_x$ -0) and $(\text{Co}_{0.7}\text{Mn}_{0.3})\text{O}_x$ after 100 cycles ($(\text{Co}_{0.7}\text{Mn}_{0.3})\text{O}_x$ -100). Shells were simulated using phase functions created from the interatomic distances of Mn_3O_4 (with Co replacing Mn when needed),^[1] The error of the last digit is shown in parentheses.

Sample	Parameter	Mn–O1	Mn–O2	Mn–M ^[b]	R – factor
MnO_x -0 ^[c]	N	5 ^[a]	1 ^[a]	2.5(5)	
	R (Å)	1.87(1)	2.31(7)	2.87(1)	1.42 %
	σ (Å)	0.05 ^[a]	0.05 ^[a]	0.05 ^[a]	
MnO_x -100 ^[c]	N	5 ^[a]	1 ^[a]	2.6(5)	
	R (Å)	1.88(1)	2.31(7)	2.86(1)	2.18 %
	σ (Å)	0.05 ^[a]	0.05 ^[a]	0.05 ^[a]	
$(\text{Co}_{0.7}\text{Mn}_{0.3})\text{O}_x$ -0	N	5 ^[a]	1 ^[a]	3.5(5)	
	R (Å)	1.87(1)	2.36(7)	2.82(1)	0.82 %
	σ (Å)	0.05 ^[a]	0.05 ^[a]	0.05 ^[a]	
$(\text{Co}_{0.7}\text{Mn}_{0.3})\text{O}_x$ -100	N	5 ^[a]	1 ^[a]	3.7(5)	
	R (Å)	1.87(1)	2.31(7)	2.83(1)	2.44 %
	σ (Å)	0.05 ^[a]	0.05 ^[a]	0.05 ^[a]	

[a] indicates fixed values (not simulated). [b] M indicates Mn or Co. [c] data was obtained from reference.^[2]

Table S6. EXAFS absorber-scatter averaged distance (R), neighboring atoms number (N) and Debye-Waller factor (σ) as determined by simulation of the k^3 -weighted EXAFS spectra at the Co-K edge for pristine CoO_x (CoO_x -0) and CoO_x after 100 cycles (CoO_x -100), pristine $(\text{Co}_{0.7}\text{Mn}_{0.3})\text{O}_x$ ($(\text{Co}_{0.7}\text{Mn}_{0.3})\text{O}_x$ -0) and $(\text{Co}_{0.7}\text{Mn}_{0.3})\text{O}_x$ after 100 cycles ($(\text{Co}_{0.7}\text{Mn}_{0.3})\text{O}_x$ -100). Shells were simulated using phase functions created from the interatomic distances of Co_3O_4 .^[3] The error of the last digit is shown in parentheses.

Sample	Parameter	Co–O1	Co–M ^[b]	R – factor
CoO_x -0	N	5.6(5)	3.3(4)	
	R (Å)	1.88(1)	2.82(1)	5.96 %
	σ (Å)	0.05 ^[a]	0.05 ^[a]	
CoO_x -100	N	5.3(5)	3.2(4)	
	R (Å)	1.88(1)	2.81(1)	3.93 %
	σ (Å)	0.05 ^[a]	0.05 ^[a]	
$(\text{Co}_{0.7}\text{Mn}_{0.3})\text{O}_x$ -0	N	6.3(5)	4.7(4)	
	R (Å)	1.87(1)	2.79(1)	2.49 %
	σ (Å)	0.05 ^[a]	0.05 ^[a]	
$(\text{Co}_{0.7}\text{Mn}_{0.3})\text{O}_x$ -100	N	6.9(5)	3.6(4)	
	R (Å)	1.87(1)	2.80(1)	4.13 %
	σ (Å)	0.05 ^[a]	0.05 ^[a]	

[a] indicates fixed values (not simulated). [b] M indicates Mn or Co.

Table S7. EXAFS absorber-scatter averaged distance (R), neighboring atoms number (N) and Debye-Waller factor (σ) as determined by simulation of the k^3 -weighted EXAFS spectra at the Co-K edge for pristine CoO_x (CoO_x -0) and CoO_x after 100 cycles (CoO_x -100), pristine $(\text{Co}_{0.7}\text{Mn}_{0.3})\text{O}_x$ ($(\text{Co}_{0.7}\text{Mn}_{0.3})\text{O}_x$ -0) and $(\text{Co}_{0.7}\text{Mn}_{0.3})\text{O}_x$ after 100 cycles ($(\text{Co}_{0.7}\text{Mn}_{0.3})\text{O}_x$ -100). Shells were simulated using phase functions created from the interatomic distances of $\text{Co}(\text{OH})_2$ (with Mn replacing Co when needed).^[4] The error of the last digit is shown in parentheses.

Sample	Parameter	Co–O1	Co–M ^[b]	R – factor
CoO_x -0	N	5.2(4)	3.3(3)	
	R (Å)	1.88(1)	2.83(1)	4.41 %
	σ (Å)	0.05 ^[a]	0.05 ^[a]	
CoO_x -100	N	5.0(4)	3.2(3)	
	R (Å)	1.88(1)	2.82(1)	2.43 %
	σ (Å)	0.05 ^[a]	0.05 ^[a]	
$(\text{Co}_{0.7}\text{Mn}_{0.3})\text{O}_x$ -0	N	5.9(6)	4.7(4)	
	R (Å)	1.87(1)	2.80(1)	1.25 %
	σ (Å)	0.05 ^[a]	0.05 ^[a]	
$(\text{Co}_{0.7}\text{Mn}_{0.3})\text{O}_x$ -100	N	6.4(6)	3.6(4)	
	R (Å)	1.87(1)	2.80(1)	3.47 %
	σ (Å)	0.05 ^[a]	0.05 ^[a]	

[a] indicates fixed values (not simulated). [b] M indicates Mn or Co.

Table S8. Co and Mn nominal oxidation state of pristine CoO_x and $(\text{Co}_{0.7}\text{Mn}_{0.3})\text{O}_x$, and after 100 cycles. The data was estimated using the metal K edges. The fit equation and graph are shown in Figure S13.

Sample	Pristine film	After 100 cycles
Co nominal oxidation state		
CoO_x	2.70	2.72
$(\text{Co}_{0.7}\text{Mn}_{0.3})\text{O}_x$	2.77	2.70
Mn nominal oxidation state		
$(\text{Co}_{0.7}\text{Mn}_{0.3})\text{O}_x$	3.71	3.67
MnO_x ^[a]	3.47	3.48

[a] obtained from reference.^[2]

Table S9. $\Delta i_{1.5V}$ obtained from the CV series collected on CoO_x -, $(\text{Co}_{0.7}\text{Mn}_{0.3})\text{O}_x$ -, and MnO_x -covered GC rods. CV were performed in 0.1 M NaOH Ar-purged solution

with a scan rate of 100 mV s⁻¹. Data from 2nd and 100th cycle is shown with is corresponding error, estimated from three samples.

	CoO _x		(Co _{0.7} Mn _{0.3})O _x		MnO _x ^[a]	
	$\Delta i_{1.5\text{ V}}$ [A]	Error [A]	$\Delta i_{1.5\text{ V}}$ [A]	Error [A]	$\Delta i_{1.5\text{ V}}$ [A]	Error [A]
2nd cycle	3.04468E-5	1.30904E-5	2.05627E-5	7.22939E-6	1.39052E-5	9.28102E-6
100th cycle	2.75242E-5	1.73901E-5	1.89229E-5	9.13858E-6	1.18643E-5	7.92817E-6

^[a]obtained from reference. ^[2]

Supporting Figures

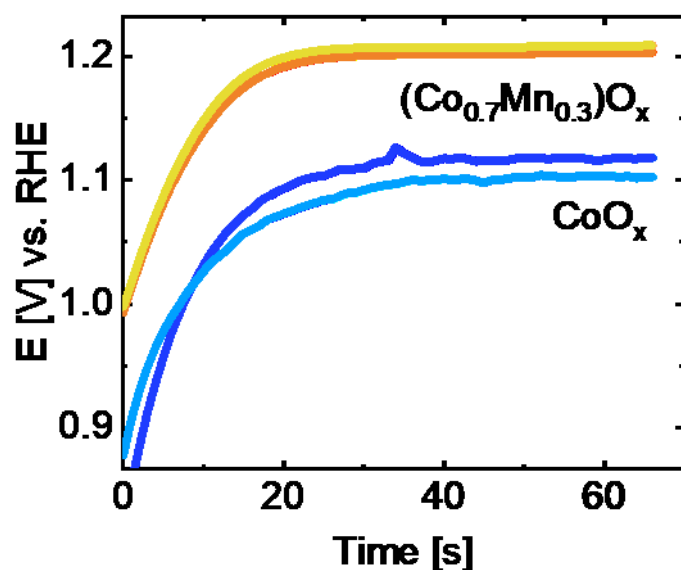


Figure S1. Chronopotentiometry during electrodeposition of CoO_x and $(\text{Co}_{0.7}\text{Mn}_{0.3})\text{O}_x$ films on graphite foil substrate. Curves are shown in duplicate, corresponding to two independent electrodepositions.

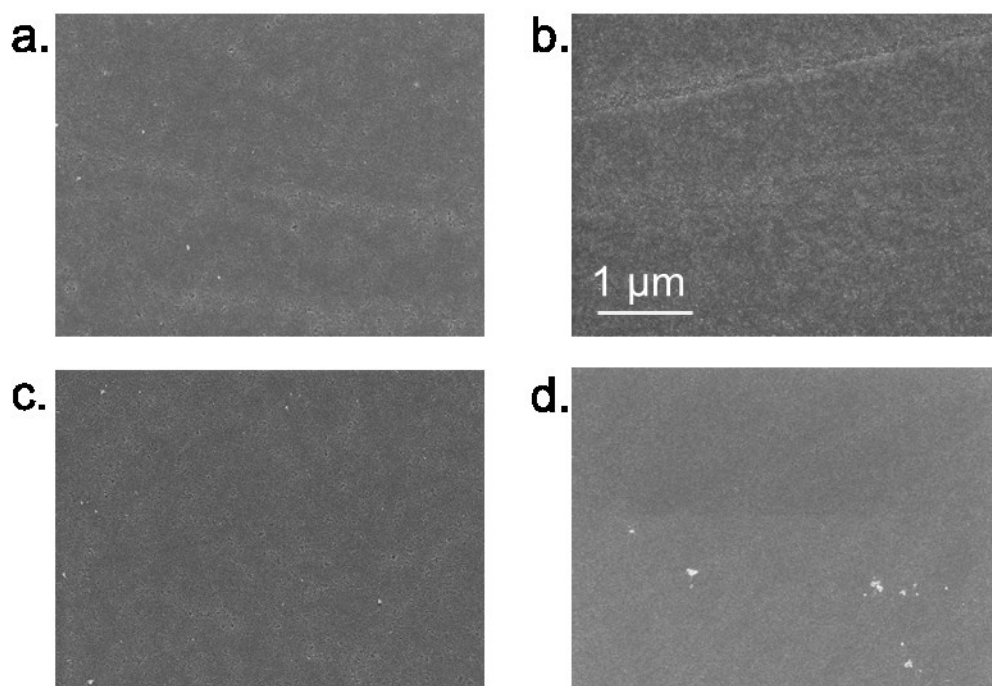


Figure S2. SEM images of: a. Pristine CoO_x , b. CoO_x after 100 cycles, c. Pristine $(\text{Co}_{0.7}\text{Mn}_{0.3})\text{O}_x$ and d. $(\text{Co}_{0.7}\text{Mn}_{0.3})\text{O}_x$ after 100 cycles.

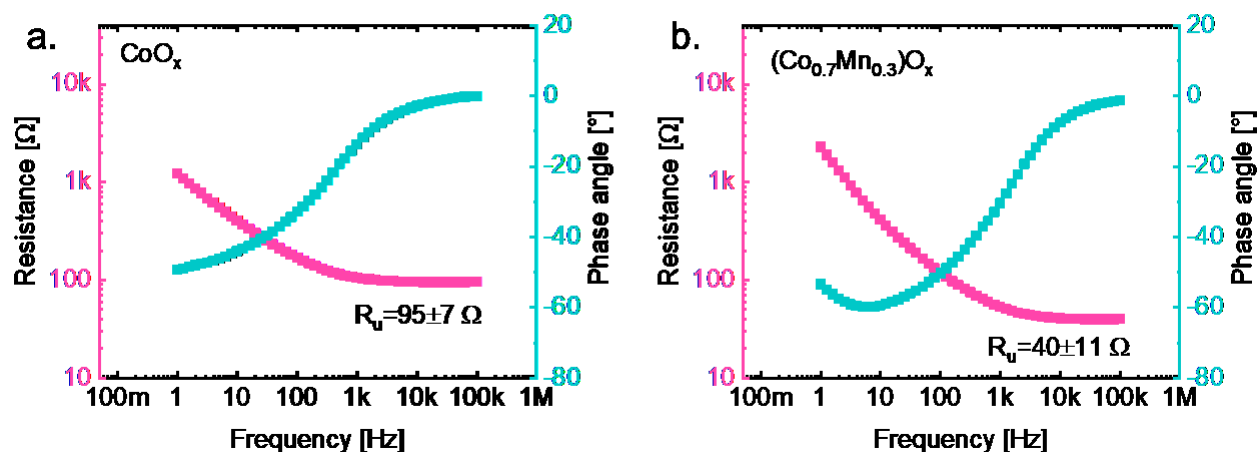


Figure S3. EIS spectra showing resistance (pink) and phase angle (turquoise) as a function of frequency collected on: a. CoO_x -covered glassy carbon rod and b. $(\text{Co}_{0.7}\text{Mn}_{0.3})\text{O}_x$ -covered glassy carbon rod. The data was collected before the experiment shown in Figure 2, in an Ar-purged 0.1 M NaOH electrolyte. R_u represents the uncompensated resistance with components $R_{\text{electrolyte}} + R_{\text{setup}} + R_{\text{film}}$. Using the same electrolyte and experimental setup, we expect that $R_{\text{electrolyte}} + R_{\text{setup}}$ have the same values for different electrodeposited films. Thus, the difference in R_u was attributed to the bulk resistance of the deposited films. The error represents the standard deviation of three measurements.

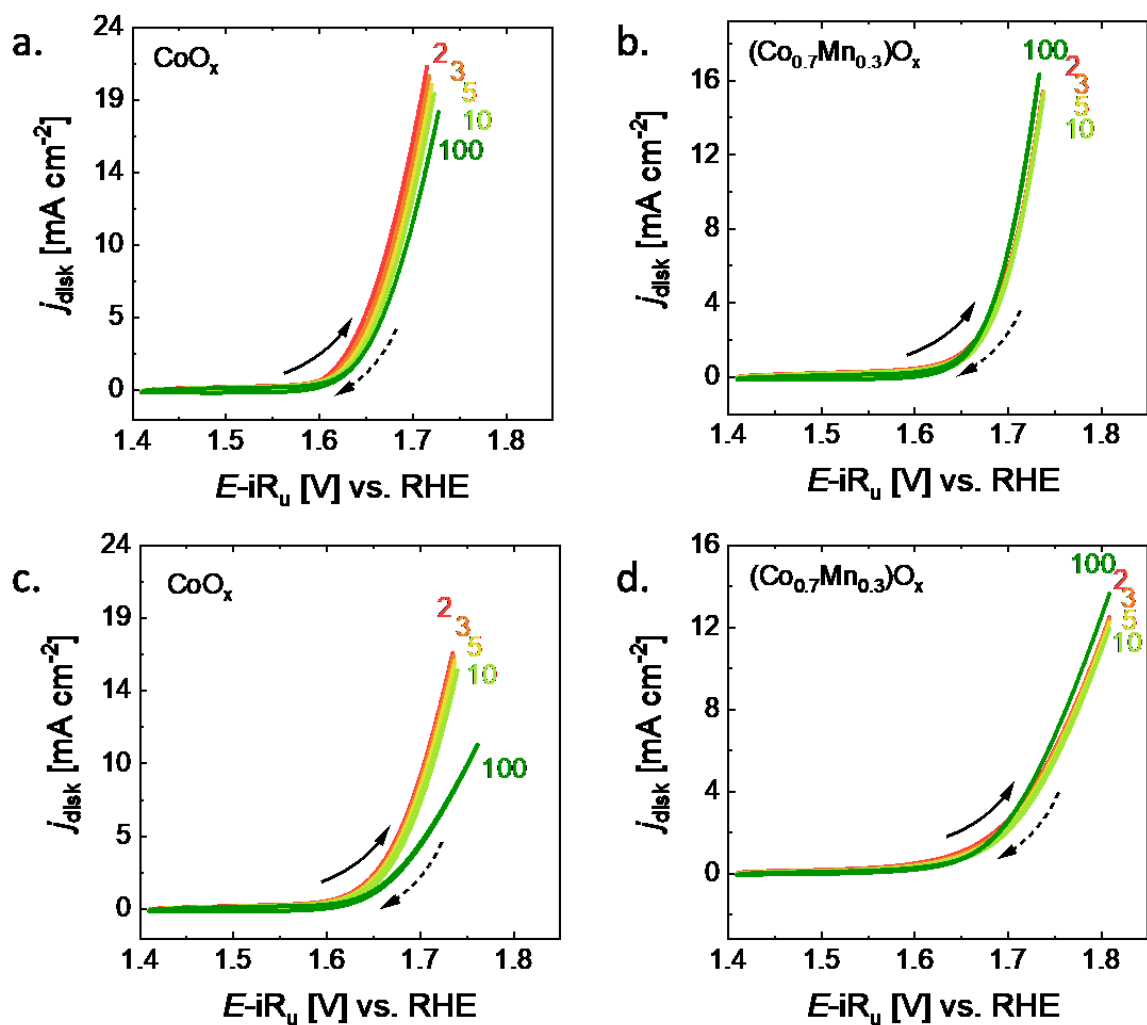


Figure S4. Additional CVs of CoO_x (a and c) and $(\text{Co}_{0.7}\text{Mn}_{0.3})\text{O}_x$ (b and d). These CVs were collected at the disk with a scan rate of 100 mV s^{-1} in $\text{NaOH } 0.1 \text{ M}$ with a rotation rate of 1600 rpm.

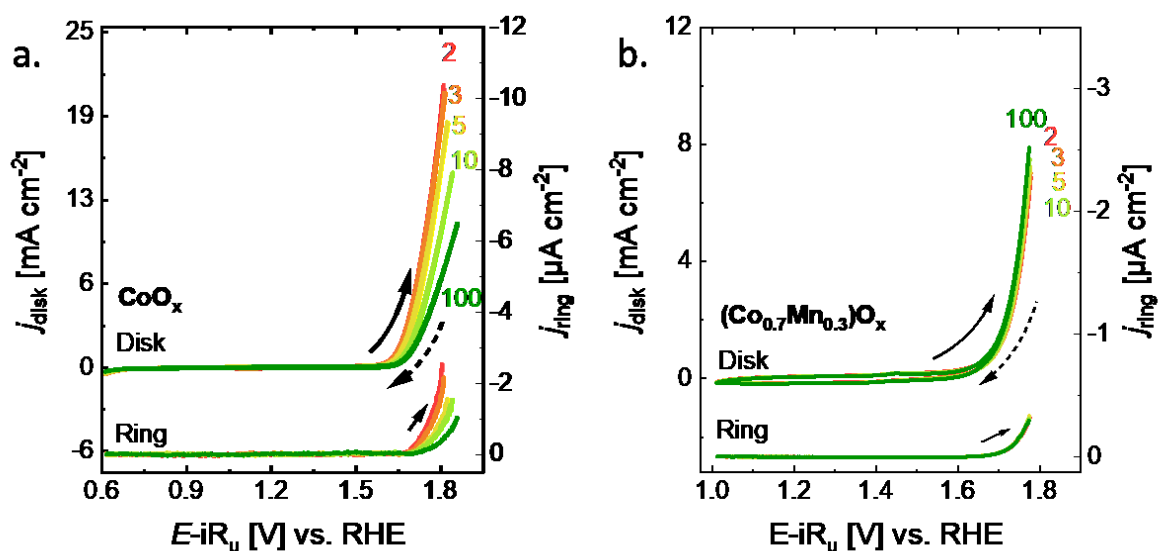


Figure S5. Series of CV performed on a: a. CoO_x -covered disk and b. $(\text{Co}_{0.7}\text{Mn}_{0.3})\text{O}_x$ -covered disk. A constant potential of 0.4 V vs. RHE was applied at the ring to detect O_2 .^[2] The CV was performed with a scan rate of 100 mV s^{-1} in 0.1 M NaOH with an electrode rotation of 1600 rpm. These samples were measured with lower potential boundary than samples shown in Figure 2. The arrows indicate the direction of the scan.

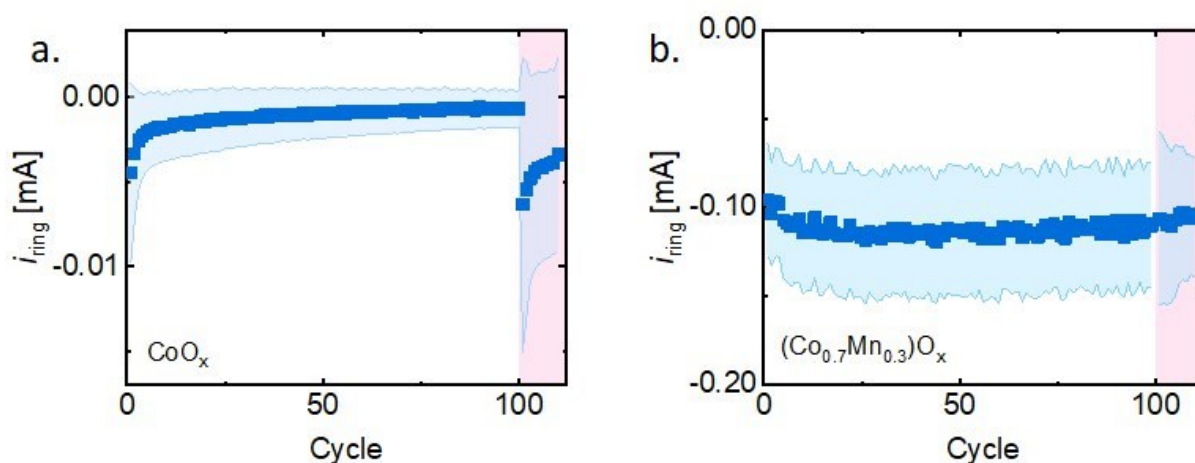


Figure S6. Average O_2 ring current trend as a function of cycling collected on: a. CoO_x and b. $(\text{Co}_{0.7}\text{Mn}_{0.3})\text{O}_x$ for $E-iR_u=1.70 \text{ V}$ vs. RHE. The blue light-colored area represents the error of three measurements. The pink background represents the 10 additional cycles collected after the OCP break.

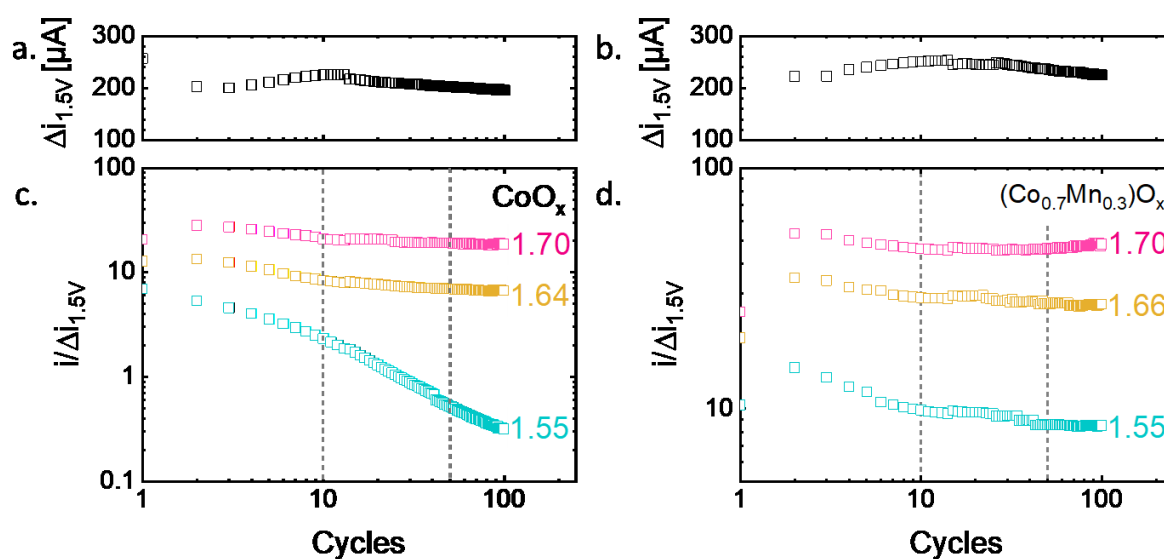


Figure S7. $\Delta i_{1.5\text{ V}}$ as function of cycles for the first 100 cycles for a. CoO_x and b. $(\text{Co}_{0.7}\text{Mn}_{0.3})\text{O}_x$ deposited on graphite foil. Current ratio $i/\Delta i_{1.5\text{ V}}$ as a function of cycling at selected potentials for c. CoO_x and d. $(\text{Co}_{0.7}\text{Mn}_{0.3})\text{O}_x$ deposited on graphite foil.

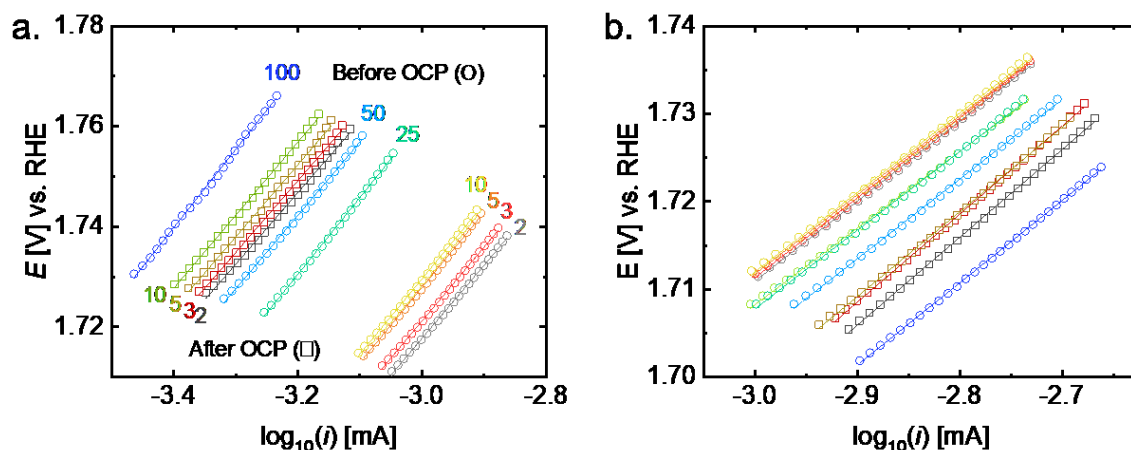


Figure S8. Tafel plots of CoO_x (a) and $(\text{Co}_{0.7}\text{Mn}_{0.3})\text{O}_x$ (b) films. Representative plot of Tafel slope calculation for selected cycles (before OCP: 2, 3, 5, 10, 25, 50, 100, and after OCP: 2, 3, 5, 10). The measurements were performed in 0.1 M NaOH. The data was collected with a scan rate 100 mV s^{-1} and the iR_u compensation was done during post-processing. The lines represent the linear fit of $E-iR_u$ as a function of $\log_{10}(i)$, the slope values represent the Tafel slope. Parameters are shown in Table S3.

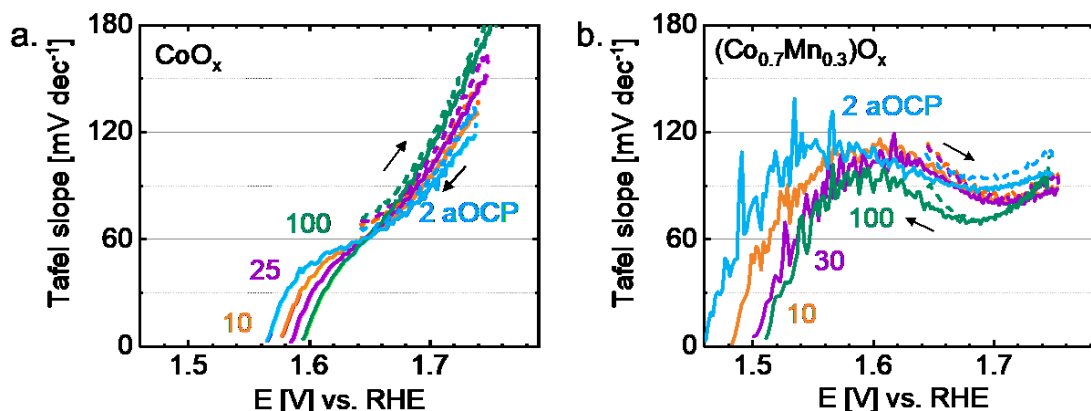


Figure S9. Instantaneous Tafel slope as a function of potential estimated for selected cycles (10th cycle, 25th cycle and 100th cycle before the OCP break and 2nd after the OCP break). The data was extracted from the anodic scans in the CVs shown in Figure 2. The instantaneous Tafel slope was calculated by the first derivative of the iR_u -corrected potential as function of the logarithm of the current density.

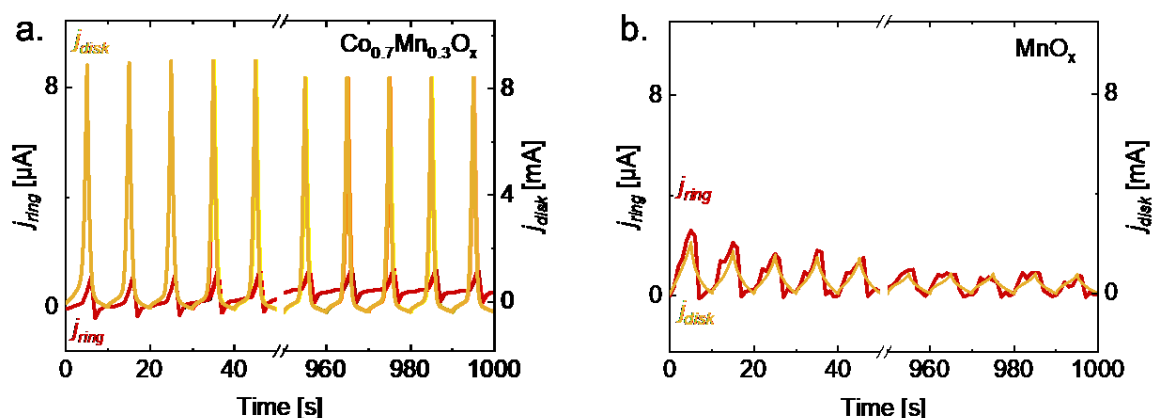


Figure S10. Detection of MnO_4^- at the ring of an RRDE. $j_{\text{ring, Mn}}$ and j_{disk} as a function of time collected on: a. $(\text{Co}_{0.7}\text{Mn}_{0.3})\text{O}_x$ -covered glassy carbon rod and MnO_x -covered glassy carbon rod. The data was collected using a CV experiment in the disk in a potential range of 1.4 – 1.8 V vs. RHE and a scan rate of 100 mV s^{-1} , while the ring was set to a CA experiment with a potential of 1.2 V vs. RHE.^[5] The electrolyte was Ar-purged 0.1 M NaOH. The rotation speed was set to 1600 rpm.

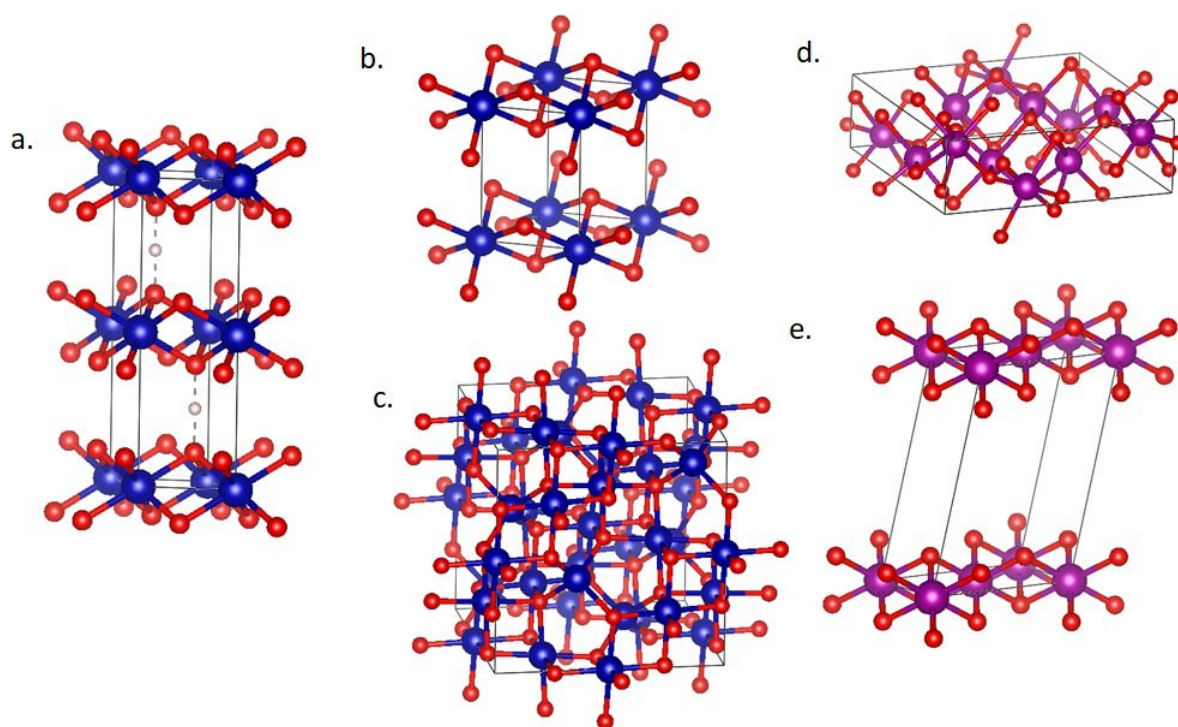


Figure S11. Structural models used for the estimation of reasonable phase functions for EXAFS simulations. a. CoO_2H ,^[6] b. $\text{Co}(\text{OH})_2$,^[4] c. Co_3O_4 ,^[3] d. Mn_3O_4 ,^[1]

e. $\text{MnO}_2 \cdot n\text{H}_2\text{O}$.^[7] Blue dots represent Co atoms, purple dots represent Mn atoms and red dots represent oxygen atoms.

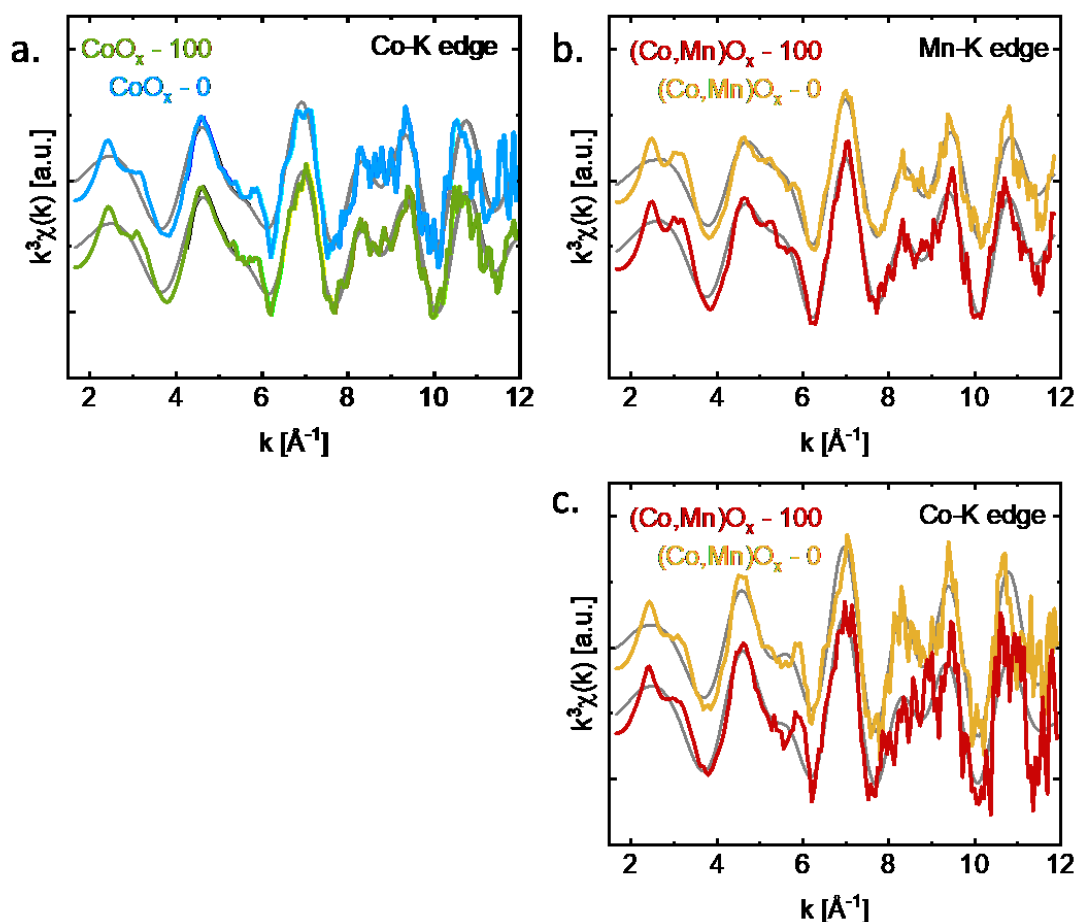


Figure S12. k^3 -weighted EXAFS spectra of pristine CoO_x and $(\text{Co}_{0.7}\text{Mn}_{0.3})\text{O}_x$, and after 100 cycles, recorded at the Mn-K edge and Co K-edge. The colored lines represent the measurements and the gray lines the respective EXAFS simulations.

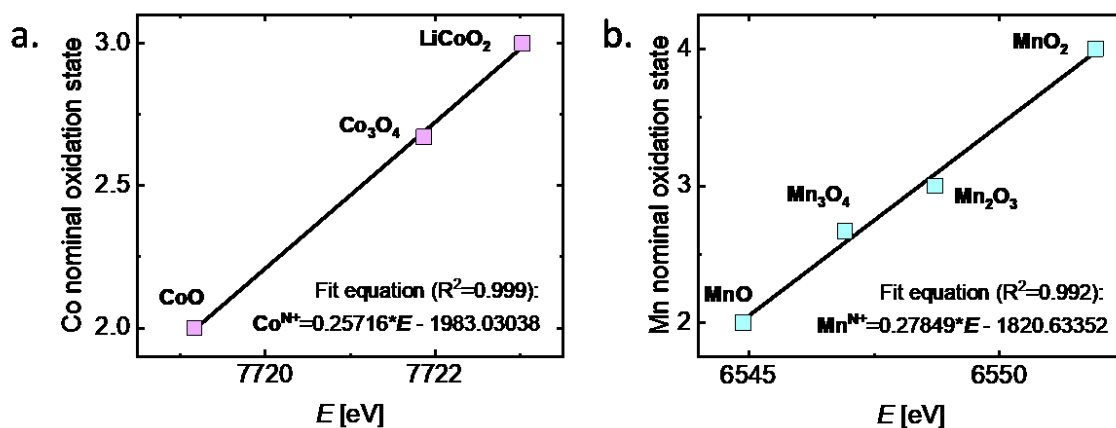


Figure S13. Nominal oxidation state of three Co-based references (a) and four Mn-based references (b) as a function of energy of the Co-K edge. The fit equation is

shown. CoO, Co₃O₄ and LiCoO₂ were used as Co references; and MnO, Mn₃O₄, Mn₂O₃ and MnO₂ were used as Mn references. The estimated oxidation states are shown in Table S5. The edge energy was estimated using the integral method ($\mu_1=1.00$, $\mu_2=0.15$).^[8]

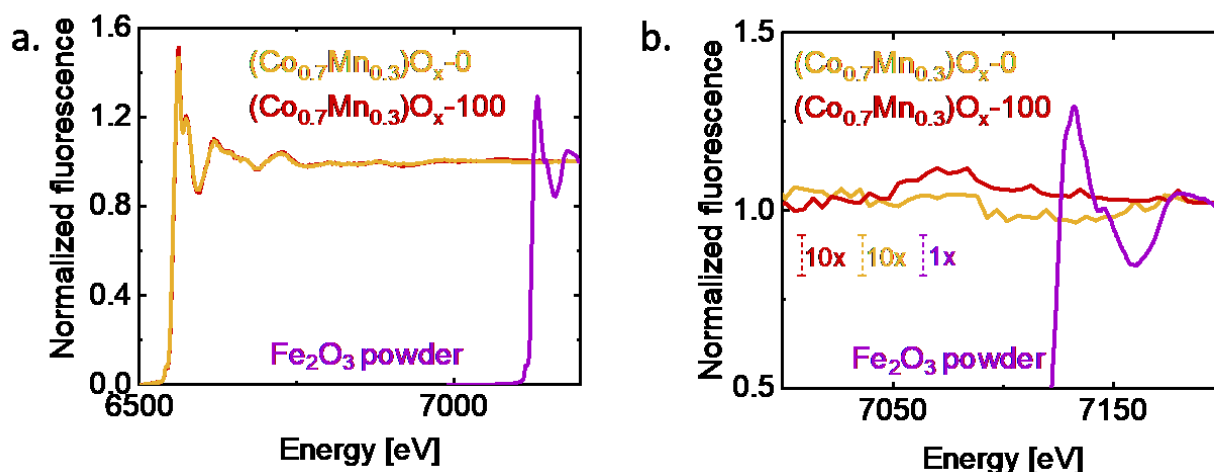


Figure S14. A. Mn-K edge spectra collected on pristine (Co_{0.7}Mn_{0.3})O_x ((Co_{0.7}Mn_{0.3})O_x-0) and after 100 cycles ((Co_{0.7}Mn_{0.3})O_x-100), and Fe-K edge spectrum collected on Fe₂O₃ powder, used as reference to show the energy and shape of Fe-K edge rise, b. Zoom-in of the spectra in the energy range where the Fe-K rises. The scale of the Mn-K edge spectra was enlarged by 10x (Fe-K edge spectrum remained as 1x) to facilitate the comparison.

References

1. C. R. Ross, D. C. Rubie and E. Paris, *Am. Mineral.*, 1990, **75**, 1249–1252.
2. J. Villalobos, R. Golnak, L. Xi, G. Schuck, M. Risch, *J. Phys. Energy* 2020, **2**, 034009.
3. X. Liu and C. T. Prewitt, *Phys. Chem. Miner.*, 1990, **17**, 168–172.
4. R. W. G. Wyckoff, *Acta Crystallogr.*, 1963, **1**, 239–444.
5. M. Baumung, F. Schönewald, T. Erichsen, C. A. Volkert, M. Risch, *Sustain. Energy Fuels*, 2019, **3**, 2218.
6. M. Deliens and H. Goethals, *Mineral. Mag.*, 1973, **39**, 152–157.
7. J. E. Post and D. R. Veblen, *Am. Mineral.*, 1990, **75**, 477–489.
8. H. Dau, P. Liebis and M. Haumann, *Anal. Bioanal. Chem.*, 2003, **376**, 562–583.

Chapter 6. Requirements for Beneficial Electrochemical Restructuring: A Model Study on a Cobalt Oxide in Selected Electrolytes

Requirements for Beneficial Electrochemical Restructuring: A Model Study on a Cobalt Oxide in Selected Electrolytes

Javier Villalobos, Diego González-Flores,* Roberto Urcuyo, Mavis L. Montero, Götz Schuck, Paul Beyer, and Marcel Risch*

The requirements for beneficial materials restructuring into a higher performance oxygen evolution reaction (OER) electrocatalyst are still a largely open question. Here erythrite ($\text{Co}_3(\text{AsO}_4)_2 \cdot 8\text{H}_2\text{O}$) is used as a Co-based OER electrocatalyst to evaluate its catalytic properties during in situ restructuring into an amorphous Co-based catalyst in four different electrolytes at pH 7. Using diffraction, microscopy, and spectroscopy, a strong effect in the restructuring behavior is observed depending of the anions in the electrolyte. Only carbonate electrolyte can activate the catalyst material, which is related to its slow restructuring process. While the catalyst turnover frequency (TOF) undesirably reduces by a factor of 28, the number of redox active sites continuously increases to a factor of 56, which results in an overall twofold increase in current of the restructuringd catalyst after 800 cycles. The activation is attributed to an adequate local order, a high Co oxidation state close to 3+, and a high number of redox-active Co ions. These three requirements for beneficial restructuring provide new insights into the rational design of high performance OER catalysts by electrochemical restructuring.

sunlight or wind. A promising solution is the storage of chemical energy by water splitting into hydrogen and oxygen.^[1,2] Complex kinetics make the oxygen evolution reaction (OER) one of the most considerable challenges for implementing water splitting as it requires high catalytic efficiency and stability under operating conditions.^[3]

For the use of carbon-based fuels as energy storage, near-neutral pH operating conditions are desirable to couple the anodic OER to the cathodic CO_2 reduction reaction since CO_2 enrichment of the electrolyte leads to pH values close to 7.^[4,5]


Amorphous transition-metal oxides have shown outstanding catalytic properties at neutral pH.^[6–8] Thanks to their unique atomic arrangement, these materials own structural flexibility and distinctively coordinated metal centers.^[9–11] Electrochemically, amorphous oxides can be obtained by electrodeposition^[12–14] or electrochemical restructuring^[9,15–19] of crystalline materials. The latter approach has improved catalytic activity compared to

Introduction

The widespread use of renewable energy requires efficient energy storage solutions due to the fluctuating energy production from renewable sources such as

J. Villalobos, M. Risch
Nachwuchsgruppe Gestaltung des Sauerstoffentwicklungsmechanismus
Helmholtz-Zentrum Berlin für Materialien und Energie GmbH
Hahn-Meitner Platz 1, Berlin 14109, Germany
E-mail: marcel.risch@helmholtz-berlin.de

D. González-Flores, R. Urcuyo, M. L. Montero
Centro de Investigación en Ciencia e Ingeniería de Materiales (CICIMA)
San José 11501 2060, Costa Rica
E-mail: diegoandres.gonzalez@ucr.ac.cr

 The ORCID identification number(s) for the author(s) of this article can be found under <https://doi.org/10.1002/aenm.202101737>.

© 2021 The Authors. Advanced Energy Materials published by Wiley-VCH GmbH. This is an open access article under the terms of the Creative Commons Attribution License, which permits use, distribution and reproduction in any medium, provided the original work is properly cited.

D. González-Flores, R. Urcuyo, M. L. Montero
Escuela de Química

Universidad de Costa Rica
San José 11501 2060, Costa Rica

D. González-Flores, R. Urcuyo
Centro de Electroquímica y Energía Química (CELEQ)
San José 11501 2060, Costa Rica

G. Schuck
Abteilung Struktur und Dynamik von Energiematerialien
Helmholtz-Zentrum Berlin für Materialien und Energie GmbH
Berlin 14109, Germany

P. Beyer
Fachbereich Physik
Freie Universität Berlin
Arnimallee 14, Berlin 14195, Germany

DOI: 10.1002/aenm.202101737

their crystalline variant in some cases,^[9,10,12,20] while this was not the case for other combinations of pristine materials and electrolytes.^[21,22] Wang et al.^[23] identified an optimal Co redox level for the activation of $\text{LiCoO}_{2-x}\text{Cl}_x$ by beneficial electrochemical restructuring in 1 M KOH. The requirements for beneficial electrochemical restructuring, particularly in neutral electrolytes, are still largely an open question.^[18,24]

Among a wide range of amorphous transition-metal oxides, Co-containing oxides own particular properties, such as selfhealing,^[25,26] semiconductivity,^[27–29] and the possibility of hosting higher oxidation states, such as Co(IV),^[8,30] which has been proposed as part of the active site.^[31] Electrodes of Co-based oxides present overpotentials of 400–490 mV at 10 mA $\text{cm}_{\text{geo}}^{-2}$ with turnover frequencies (TOF) as high as 0.21 O_2 $\text{Co}^{-1} \text{s}^{-1}$ for $\text{Co}(\text{PO}_3)_2$ nanoparticles^[32] and Tafel slopes of 60–80 mV dec^{-1} (for layered Co oxides and Co_3O_4) in near-neutral pH (Table S1, Supporting Information).^[31,33–35] The local structure of the Co oxide differs depending on the cations and anions present in the electrodeposition electrolyte; for instance, the local order of the final Co oxide decreases as a function of the electrolyte in the order $\text{CaCl}_2 > \text{KCl} > \text{LiOAc} > \text{KOAc} > \text{KPi}$.^[8] The numbers of Co–Co scattering interactions at 2.8^[36] and 5.6 Å^[8] were previously used to estimate the size of the ordered Co oxide fragments (also called clusters) by analysis of the extended X-ray absorption fine structure (EXAFS).^[36–38] Risch et al.^[36] identified an increase in current per Co with a number of Co–Co interactions at 2.8 Å for restructuringd perovskite oxides, which suggests an optimal cluster size containing nine Co atoms, when compared to an earlier study on electrodeposited Co oxide.^[8] Additionally, Kwon et al.^[39] reported larger interlayer spacing and cluster size by variation of the electrolyte anions during the electrodeposition of Co oxides as follows: borate (pH 9.2) > methyl phosphate (pH 8.0) > phosphate (pH 7.0). Thus, crystalline Co oxides are attractive starting materials for further enhancement by electrochemical restructuring into more active amorphous oxides.

In this study, we synthesized erythrite (Ery; $\text{Co}_3(\text{AsO}_4)_2 \cdot 8\text{H}_2\text{O}$) as a Co-based catalyst model to evaluate its catalytic properties during electrochemical restructuring into partially amorphous Co oxide in four different electrolytes at pH 7. The three electrolytes with clearly different restructuring behavior were chosen to track the conversion during cyclic voltammetry (CV) by diffraction, microscopy, and spectroscopy. We observed that the progress of the electrochemical restructuring with cycling strongly depended on the electrolyte anion. Only carbonate electrolyte activated the catalytic current over cycling due to a slow restructuring process. The final activated material showed an adequate cluster size, a high Co oxidation state, and high Co redox activity, which are essential features to enhance the catalytic activity. Hence, this work provides new insights into the

requirements of beneficial electrochemical restructuring of Co-based materials.

Results and Discussion

2.1. Electrochemical Restructuring of Ery in Selected Electrolytes

Erythrite was chosen as a model system to study the effect of electrochemical restructuring on catalytic activity in selected neutral electrolytes with different anions. Pristine Ery is a crystalline material, a part of a group of isostructural minerals called vivianites.^[40] We synthesized it by a thermal process at 65 °C, which assured crystal growth. Physical and chemical characterizations were carried out to confirm the formation of the Ery phase (Figure S1, Supporting Information). In the chemical structure of Ery,^[41,42] arsenate anions bind two positions of Co atoms: Co(1) on the hexacoordinated position and Co(2) bound via di- μ -oxo(arsenate)-bridge (Figure 1; various structures in Figure S2 of the Supporting Information). Ery^[43] and other isostructural materials^[12] have been previously used as catalysts for OER. We have observed their trend to lose long-range order (commonly called amorphization) after voltage cycling under OER conditions. This transformation, i.e., electrochemical restructuring, promoted layered cobalt oxide formation, which has significantly different interatomic distances as compared to Ery (Figure 1). For instance, the Co(2)–Co(2) distance changed from 3.1 Å in Ery to about 2.8 Å after restructuring (Figure 1).

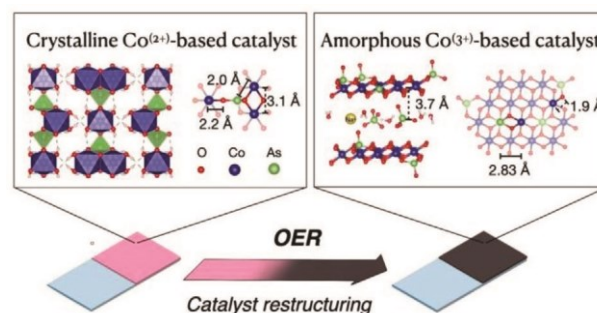


Figure 1. Diagram of the electrochemical restructuring of Ery. The crystalline Ery ($\text{Co}_3(\text{AsO}_4)_2 \cdot 8\text{H}_2\text{O}$) layers are joined by hydrogen bonds. Arsenate binding in Ery, Co–As, and Co–Co distances are shown. The amorphous layered Co oxide structure and distances of different binding modes from arsenate anions into the layer and at the border are shown. Ions and water molecules are present in the interlayer space at a distance of about 3.7 Å from the Co atoms of the layer (fragments).

Ery deposited on fluorine-doped tin oxide (FTO) glass showed clearly different trends during CV in four different electrolytes at pH 7 (electrochemical protocol in Table S2 of the Supporting Information). The used

anions were 0.1 m of borate, phosphate, carbonate, and arsenate, resulting in the restructured catalysts Ery-BO₃, Ery-PO₄, Ery-CO₃, and Ery-AsO₄, respectively (Figure 2; Figure S3, Supporting Information). We used a high number of cycles (here 800 cycles), a high upper potential limit (2.1 V vs reversible hydrogen electrode (RHE)), and a high sweep speed (100 mV s⁻¹) as typical for stability, restructuring, or activation studies.^[14,44–47] The maximum current density, j_{max} (at 2.1 V vs RHE), was comparable among all different electrolytes during the first cycles, i.e., it is mainly that of the as-synthesized Ery. Yet, j_{max} continuously increased in carbonate electrolyte, whereas, in phosphate and borate electrolytes, it rose during the first 200–300 cycles, after which it started decreasing. The current density after the OER onset remained mostly unaffected in arsenate electrolyte, indicating an equilibrium between the structural arsenate anions in Ery and the electrolyte. While there are minor shifts in the CV curves in Figure 2d, e.g., 20 mV between the 2nd and 800th cycles at 2 mA cm⁻², these are smaller than the potential shifts of around 30 mV at 2 mA cm⁻² for repeated experiments (Figure S3, Supporting Information). Thus, we conclude the absence of significant catalytic changes on Ery-AsO₄. All trends mentioned above were reproducible in three trials (Figure S4, Supporting Information).

In addition to catalytic changes, increased broad redox peaks were observed with cycling, which had previously been associated with the number of redox-active metal ions^[8,13] and in crystalline materials with the electrochemical restructuring to an amorphous material.^[9,12,36,43] The redox-active metal ions can be quantified by integrating the reductive currents in the CV resulting in an electroredox charge (ERC). In Co-based catalysts, the ERC correlates with the redox activity of Co during the catalytic reaction assuming a single electron transfer, as detailed elsewhere.^[8,12,13] ERC trends over cycling were estimated in different electrolytes (Figure S5, Supporting Information). The initial Ery phase had an ERC of 0.1 mC (Ery-BO₃, Ery-AsO₄) or 0.3 mC (Ery-PO₄, Ery-CO₃) during the second cycle. Ery-BO₃ reached a steady state at cycle 300 (ERC = 11.4 mC, 54× increase), whereas Ery-PO₄ and Ery-CO₃ increased constantly over 800 cycles and did not reach a steady state; the final ERC values are 15.5 mC (57× increase) and 16.0 mC (56× increase), respectively. Similar to the activity trends, the changes for Ery-AsO₄ were small (ERC = 3.3 mC, 25× increase, after 800 cycles).

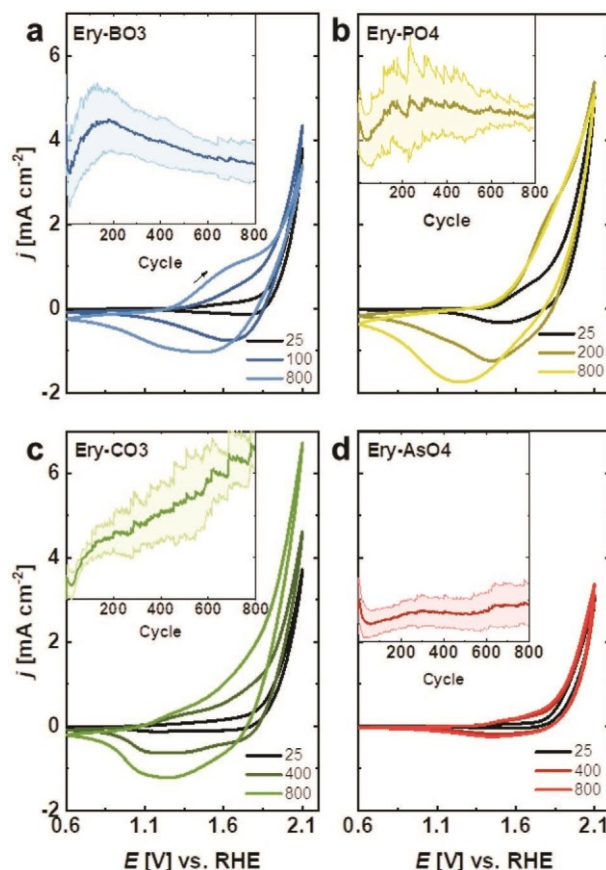


Figure 2. Series of CV performed on an Erythrite-deposited FTO glass in different electrolytes at pH 7 and a concentration of 0.1 m: a) borate, b) phosphate, c) carbonate, and d) arsenate. 800 cycles were performed with a sweep speed of 100 mV s⁻¹ and 85% *iR* compensation, of which the 25th, 400th, and 800th cycles are shown. The arrows indicate the scan direction. The insets show the j_{max} trends (at $E = 2.1$ V vs RHE) as a function of cycling. The light-colored areas represent the standard deviation of three different samples. The FTO substrates were coated with an equivalent mass of Ery (0.4 mg) on a 1 cm² area. Dataset in ref. [48].

The potential of the maximum of the reductive (i.e., cathodic) peak significantly differed depending on the electrolyte. The initial peak potentials were around 1.45 V versus RHE in the four electrolytes, i.e., that of pristine Ery. They changed to 1.42 V versus RHE in Ery-PO₄, 1.65 V versus RHE in Ery-BO₃, and 1.34 V versus RHE in Ery-CO₃ after 800 cycles (Figure S6, Supporting Information). Risch et al.^[31] reported similar redox peak positions for CoCat (abbreviation for Co-catalyst, electrodeposited in phosphate buffer, KPi, pH 7). They assigned the midpoint potential between the anodic and cathodic redox peaks at 1.42 V versus RHE to the Co²⁺/Co³⁺ transition and at 1.63 V versus RHE to the Co³⁺/Co⁴⁺ transition. The latter is not clearly resolved in our CV series (Figure 2). Similar peak positions were reported by Villalobos et al.,^[43] who also showed that the use of arsenate electrolyte for the electrodeposition of CoCat (instead of KPi) resulted in a shift of 0.1 V in the peak position of the Co²⁺/Co³⁺ transition to lower potential, whereas the Co³⁺/Co⁴⁺ remained unaffected.

Therefore, the position of the waves in the CV depends on the electrolyte used for restructuring, which means that the energy level of the Co redox can be tuned simply by the selection of the electrolyte anion similarly to the approach of Wang et al.^[23] who tune the cation of the catalyst material.

Three indicators were used to monitor the electrochemical restructuring during cycling in the three electrolytes with the most pronounced change, namely borate, phosphate, and carbonate. The indicators were I) estimation of the number of redox-active metal ions by the quantification of ERC, II) loss of the Ery phase from the initial material by X-ray diffraction (XRD) using the normalized (020) reflection of Ery (Figure S7, Supporting Information), and (III) anion exchange tracked as loss of arsenate from Ery ($\text{Co}_3(\text{AsO}_4)_2 \cdot 8\text{H}_2\text{O}$) by energy-dispersive X-ray spectroscopy (EDX; Figure S8, Supporting Information). The arsenic content was normalized by the cobalt content to ensure that the changes are not due to material loss. The loss of arsenate anions was also tracked by the signal of the As-O bond^[49] at 780 cm^{-1} in Fourier transform infrared (FTIR) spectroscopy (Figure S9, Supporting Information), corroborating the EDX results. These tracking experiments were based on the methods and properties most commonly used to understand the electrochemical restructuring process.^[10,12,15,43,50] How the changes of metal redox, loss of crystallinity, and anionic exchange relate to each other has been an important open question for understanding the mechanism of electrochemical restructuring. In this regard, these three indicators were compared as a function of cycling in borate, carbonate, and phosphate electrolytes to identify trends and correlations (Figure 3). They were complemented by j_{max} as an indicator of activity as extracted from the CVs in Figure 2 and Figure S4 (Supporting Information).

In Ery- BO_3 (Figure 3a), a plateau was reached by cycle 300 in all indicators, where the material has lost most of Ery's arsenate anions ($\text{As/Co} \approx 20\%$), the ERC reached a value of only 7 mC, and it did not show extended long-range order anymore, i.e., the normalized (020) reflection is $<1\%$ of its initial value. Thus, 300 cycles in borate electrolyte were sufficient to conclude the electrochemical restructuring. Scanning electron microscopy (SEM) images taken at selected cycles showed a constant homogeneous coverage of the substrate for all cycles (Figure S10, Supporting Information). However, the initial needle-like morphology melted with cycling, which was most pronounced after 300 cycles (Figure S10e, Supporting Information). Interestingly, the activity measured by j_{max} reached its maximum at cycle 180 before the restructuring was completed and then started to decrease, indicating the additional relevance of further materials changes, such as the morphology, for catalytic activity. In summary, all restructuring indicators were correlated for Ery- BO_3 .

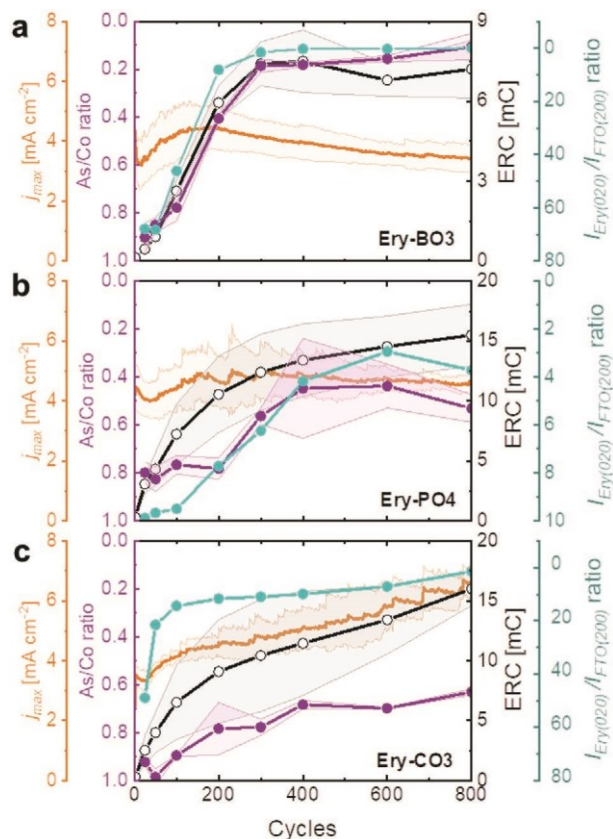


Figure 3. The three restructuring indicators As/Co ratio, $I_{\text{Ery}(020)}/I_{\text{FTO}(200)}$, and ERC as a function of cycling in a) borate (Ery- BO_3), b) phosphate (Ery- PO_4), and c) carbonate electrolyte (Ery- CO_3). The light-colored area represents the standard deviation of three independent measurements. The As/Co ratio was obtained from EDX analysis (Figure S8, Supporting Information). The j_{max} was extracted from CV. The ERC was obtained by the area integration of the cathodic current in the CV. The $I_{\text{Ery}(020)}/I_{\text{FTO}(200)}$ ratio was obtained by integration of the Ery(020) peak and its subsequent normalization by the integral of the FTO(200) peak. Dataset in ref. [48].

In Ery- PO_4 (Figure 3b), the ERC trend differed from the other two indicators of the As/Co ratio and the reduction of the normalized Ery(020) reflection. These two indicators shared the same trend and mainly increase during the first 400 cycles. (Note that their axes are plotted with the lowest value on top to better compare them to the ERC) Less than 50% of the arsenate was lost in Ery- PO_4 , and the material still showed sizable long-range order after 800 cycles, meaning that the processes follow different kinetics in phosphate electrolytes as compared to borate electrolytes. Furthermore, the increase in redox activity (i.e., ERC) does not solely depend on restructuring the material. The ERC increased continuously over 800 cycles and reached a final value of 15.5 mC; an ERC increase has commonly been related to the generation of more active sites.^[8,12,13] SEM images showed full coverage again at all cycles and a needle-like morphology but the images had no clear trend with cycling (Figure S11, Supporting Information). The activity indicator, j_{max} , did not change remarkably over cycling, yet a broad maximum of the average j_{max} was found around cycle 300, again before the

restructuring was completed. In summary, for Ery-PO₄, the partial loss of the Ery crystalline structure correlates with the loss of As during restructuring, whereas the ERC increased continuously and independently of the two other indicators.

In Ery-CO₃, the ERC also continuously increased, whereas the As/Co ratio and the Ery crystallinity mainly decreased during the first 200 cycles and then remained nearly constant.

On this plateau, less than 50% of the arsenate was lost. After 200 cycles, the crystallinity drops significantly from $I_{\text{Ery}(020)}/I_{\text{FTO}(200)} = 48.9$ to $I_{\text{Ery}(020)}/I_{\text{FTO}(200)} = 11.7$ and decreases further until 800 cycles ($I_{\text{Ery}(020)}/I_{\text{FTO}(200)} = 1.4$, i.e., 3% of the initial value; Figure S7b, Supporting Information). In contrast, the ERC increased continuously with cycling and reached a value of 16 mC (the highest among the three electrolytes). Interestingly, the activity indicator j_{max} decreased during the first 25 cycles, yet it increased continuously from cycle 25 up to cycle 800, indicating an evident twofold increase of the current density during restructuring of Ery-CO₃. In summary, none of the restructuring indicators correlated for Ery-CO₃, yet the electrochemical current increased monotonously.

Taken together, the data in Figure 3 showed that the electrolyte anions affected the evolution of restructuring on Ery with cycling and clearly influenced how the different dynamic processes, e.g., loss of Ery crystallinity, anionic exchange, and increase of redox active Co (i.e., ERC), correlate with each other. Previous reports have shown the relation between the electrolyte pH^[51] or the cation stoichiometry^[23] with the efficiency of restructuring. Here, the lack of correlation between the ERC and the other restructuring indicators for some electrolytes suggests further change in the resulting local and electronic structures as additional factors.

We used X-ray absorption spectroscopy (XAS) to understand the changes in local structure during cycling in different electrolytes as it does not require crystallinity and has high chemical sensitivity. The Co-*K* edge was used to analyze the Co oxidation state and local structure after a selected number of cycles. The nominal Co oxidation state was estimated by calibration with three Co references in different oxidation states (Figure S12 and Table S3, Supporting Information). The spectrum of the X-ray absorption near edge structure (XANES) of pristine Ery had a Co oxidation state of 2+ (Figure 4a). For Ery-BO₃, the catalyst material showed a shift in the X-ray edge position to higher energy, indicating oxidation to 2.3+ at 100 cycles and 2.8+ at 800 cycles. Similar continuous oxidation was observed for Ery-CO₃ from 2+ to 2.4+ at 100 cycles and 2.8+ at 800 cycles. Moreover, for Ery-CO₃ after 100 cycles, the Co edge looks different from Ery or layered LiCoO₂, suggesting an intermediate structure between the initial and final restructuringd materials. The Co atoms of Ery-PO₄ oxidized to 2.4+ at cycle 100, which remained unchanged until cycle 800. A doublet peak in the white

line (i.e., their maximum) of the XANES spectra suggested a combination of two different phases, Ery and another Co oxide,^[43] to be identified below. It was observed in all spectra for Ery-PO₄. In Ery-BO₃, the doublet peak in the white line was observed only in cycle 100 but not in cycle 800, indicating a single-phase material in agreement with the vanished Ery (020) reflection in XRD. In Ery-CO₃, the other Co oxide contributed negligibly at cycle 100, and the doublet peak in the white line was observed only after 800 cycles, also in agreement with partial loss of the Ery structure in XRD.

The FT of the EXAFS at the Co-*K* edge was used to study the local structure of the electrochemically restructuringd Ery after a selected number of cycles in borate, electrolyte, and carbonate electrolytes (Figure 4b). The FT of pristine Ery has a prominent peak at 2.1 Å (Co-O) and a weaker one at 3.1 Å (Co-Co).^[43]

The spectrum of Ery-PO₄ showed EXAFS peaks similar to pristine Ery after 100 and 800 cycles having the above Co-O and Co-Co distances typical of Ery.^[43] Additionally, distances at 1.9 Å (Co-O) and 2.85 Å (Co-Co) were visible; these are distinct signals of layered Co oxides such as LiCoO₂ that is also shown in Figure 4b for reference. The lack of change in the spectra was expected based on the XANES analysis above. The presence of Ery and a layered Co oxide corroborates our interpretation of the doublet peak in the white line.

The spectrum of Ery-BO₃ after 100 cycles also showed the peaks of Ery and the layered Co oxide. After cycle 800, the spectrum only showed the prominent peaks of a Co oxide, such as 1.9 Å (Co-O) and 2.8 Å (Co-Co), indicating complete electrochemical restructuring. Interestingly, the distance at 3.7 Å (Co-O, Figure 1) significantly decreases its amplitude. This signal has been previously associated with the distance between Co atoms into the oxide layer and oxygen atoms, either from water molecules or electrolyte ions, in the interlayer.^[8,37,38] A reduction of this signal amplitude may reflect a decrease in the long-range order of the layered Co oxide.

In Ery-CO₃, the nearly complete electrochemical restructuring from Ery into a layered Co oxide was apparent. After 100 cycles, the interatomic distance at 2.1 Å (Co-O) evidenced the presence of Ery; no distances associated with layered Co oxides were observed. Nonetheless, after cycle 800, the spectrum showed the interatomic distances at 1.9 Å (Co-O) and 2.85 Å (Co-Co) of the Co oxide, and signals of the Ery structure were not clearly observed, which do not exclude minor contributions from the Ery structure as found by XRD and suggested by the XANES.

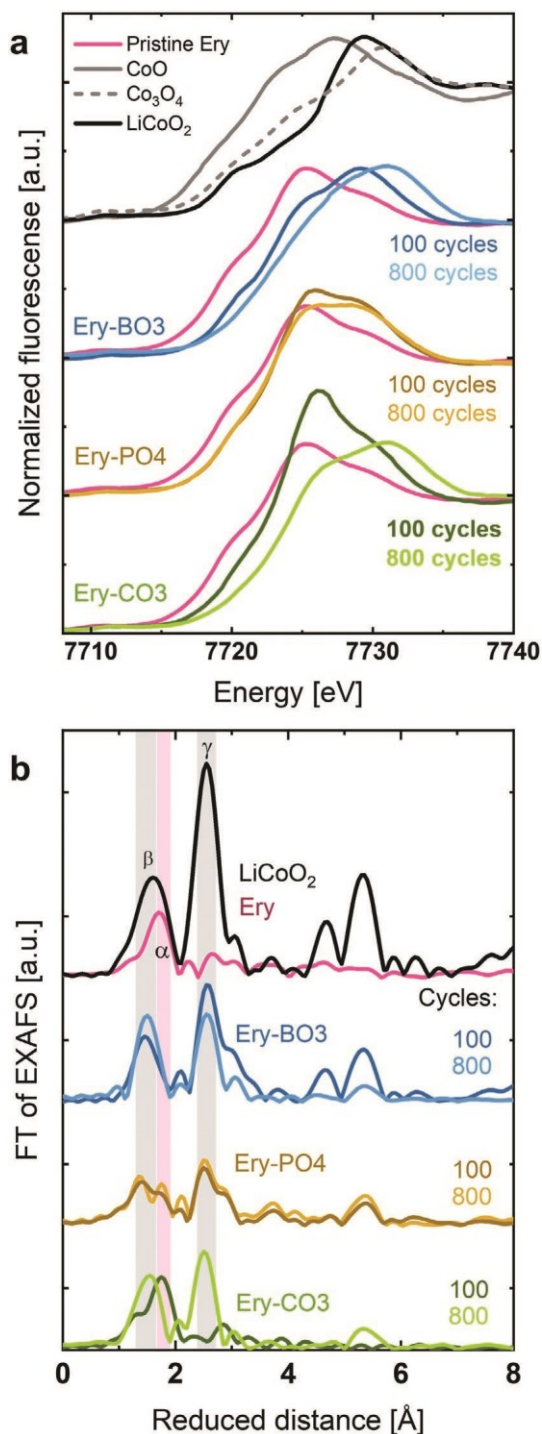


Figure 4. a) XANES spectra of Co-K edge collected on Ery after selected cycles in 0.1 m electrolytes of borate, phosphate, and carbonate at pH 7. The Co-K edge spectra of Co⁽²⁺⁾O, Co₃^(2.7+)O₄, and LiCo⁽³⁺⁾O₂ were added as references, b) Fourier transform of the EXAFS of the Co-K edge collected on Ery after selected cycles in 0.1 m electrolytes of borate, phosphate, and carbonate at pH 7. The light-colored gray areas highlight the interatomic distances related to layered Co oxides (peaks β and γ), whereas the light-colored pink areas show the distance of 2.1 Å typical for Ery (Co-O, peak α). The reduced distance is about 0.3 Å shorter than the precise distance obtained by EXAFS simulations (Figures S13–S15 and Table S4, Supporting Information). The spectra in all panels were offset on the y-axis to group them. Dataset in ref. [48].

Since the layered Co oxide formed to various degrees in all electrolytes, we will take a closer look at its properties to rationalize the differences in activity among the restructuringd Ery catalysts. Amorphous Co oxides are organized in layers of several hexa-oxo-coordinated Co atoms; the number of Co atoms determines the extent of the layer fragment or cluster.^[37,39,52] The cluster size of amorphous Co oxide has been used previously to understand activity trends on electrodeposited and restructuringd Co oxides.^[8,36,38] The cluster size of the Co oxide is effectively monitored by the ratio of the Co-Co peak height to the Co-O peak height (cobalt peak ratio, CPR) in the FT of EXAFS. A large CPR indicates a large cluster or ultimately a crystalline solid such as LiCoO₂ in Figure 4b, but its exact value depends on the *k*-weighting applied to the EXAFS data and parameters of the FT, which were identical for our analysis. Using highly crystalline LiCoO₂ as a reference, the upper limit of the CPR in our analysis is estimated as 2.1. In the limit of an isolated octahedron, the CPR would be zero.

We plotted the activity indicator, j_{\max} , as a function of the CPR (Figure 5a) to further investigate the nature of the layered Co oxide formed by restructuring Ery. For each individual dataset, j_{\max} increased with the CPR. This explained the activity decrease with cycling for Ery-PO₄ and Ery-BO₃ where CPR and activity were maximal after 400 and 100 cycles. However, the exact value of the CPR does not result in the same activity for electrochemical restructuring in different electrolytes, which suggested that another parameter also strongly affected activity.

The role of a high Co oxidation state (3+ and even 4+) has been widely reported as essential for oxygen evolution in neutral electrolytes.^[13,31,53–57] Thus, we plotted the restructuringd Ery catalysts as a function of the average Co oxidation state (Figure 5b) at a fixed CPR of 1.3. The plot was further enriched with the ERC at each point to discuss the number of potentially active sites provided by the ERC as well as the efficiency of a single active site, likely given by its Co oxidation state.

In Figure 5b, after 100 cycles in phosphate, the Co oxidation of Ery-PO₄ is also 2.4+, yet the ERC is only 7.2 mC, resulting in a lower catalytic current density (4.4 mA cm⁻²) due to comparably fewer (redox) active sites as compared to Ery-PO₄ after 800 cycles. After 25 cycles in borate, the ERC (1.3 mC) and Co oxidation state (2.3+) of Ery-BO₃ are the lowest among the samples, associated with the lowest current density (3.5 mA cm⁻²). In particular, the comparison of Ery-PO₄ at different cycles and fixed CPR clearly highlighted the importance of the number of redox active sites for high current.

For Ery-CO₃, Co atoms have the highest oxidation state (2.8+), the highest ERC (16.0 mC), which results in the highest current density (6.6 mA cm⁻²). After 800 cycles on Ery-PO₄, the ERC is almost as high as that of Ery-CO₃ (15.5 mC), yet the oxidation state is only 2.4+, resulting in a significantly lower catalytic current density (4.6 mA cm⁻²). Even though the redox activity is very similar and

the Co oxide clusters have an appropriate size (a CPR of 1.3), a high Co oxidation state is required additionally to increase the catalytic current.^[55,56,58] Therefore, we conclude that the more oxidized active sites in Ery-CO₃ are more efficient as compared to Ery-PO₄.

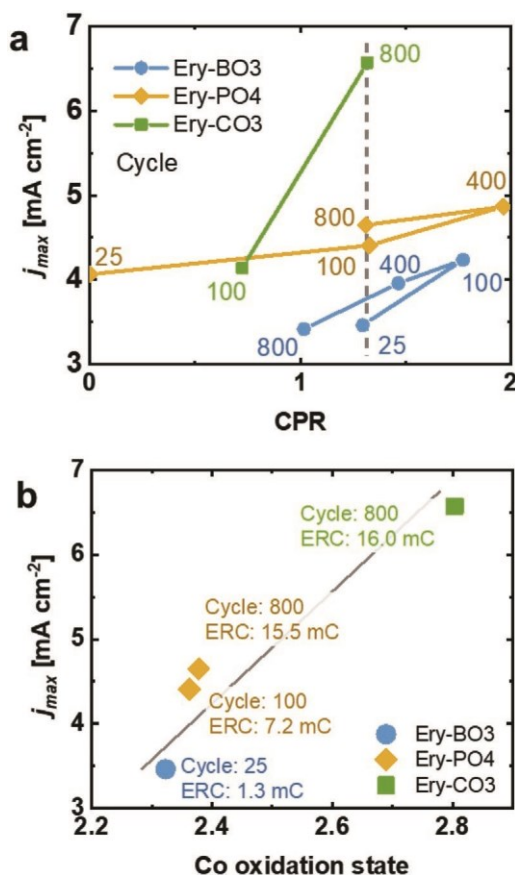


Figure 5. a) The activity indicator, j_{max} , as a function of the CPR obtained from the Fourier transform of the EXAFS of Ery in borate, phosphate, and carbonate after a selected number of cycles (shown in the graph). The solid lines connect the dots in chronological order (based on cycling). b) The activity indicator j_{max} (at 2.1 V vs RHE) as a function of the average Co oxidation state of Ery in borate (25 cycles), phosphate (100 and 800 cycles), and carbonate (800 cycles) at a CPR of 1.3. Dataset in ref. [48].

The efficiency of the active sites was quantified by the normalization of j_{max} by ERC, which corresponds to four times the TOF of O₂ per Co active site due to the four electrons transferred in the reaction **Figure 6**.^[8,12,13] Note that ERC was used in the calculation (full detail in Table S5 in the Supporting Information), which is an estimation of the number Co atoms with oxidation state changes; therefore, it also counts subsurface Co atoms that were oxidized and not involved in the catalytic reaction. Thus, the TOF is underestimated. The initial TOF of Ery was clearly higher than that of the restructuringd catalysts, as discussed in detail for a related structure,^[12] suggesting that crystallinity benefits the efficiency of an active site. For Ery-PO₄, the TOF decreased continuously, whereas it reached a steady value after 200–300 cycles for Ery-BO₃ and Ery-

CO₃. The TOF of Ery-CO₃ after 800 cycles (1.3×10^{-2} O₂ Co⁻¹ s⁻¹ at 0.3 V overpotential; Figure S16 and Table S1, Supporting Information) was slightly higher than that of other Co oxides at the same overpotential, even those measured in alkaline media, where the activity is usually higher.^[59,60] Moreover, its TOF was in the range of amorphous electrodeposited Co oxide,^[61] supporting that a similar surface is produced by restructuring Ery and electrodepositing Co oxide. Tafel slopes of Ery-CO₃ were evaluated before and after activation in carbonate electrolyte (Figure S17, Supporting Information) to examine if the current changes were due to different mechanisms.^[62] Yet, the Tafel slopes remain unaffected after activation, suggesting an unchanged mechanism. However, the Tafel slope values of Ery-CO₃ were higher (145 mV decade⁻¹) as compared to Ery-PO₄ (72 mV decade⁻¹), which were evaluated under the same conditions previously,^[43] indicating an electrolyte-dependent mechanism. Therefore, the increase of j_{max} for Ery-CO₃ was most likely due to an increase in the number of active sites in the restructuringd catalyst with cycling rather than an increase in the efficiency of the active sites (Figure 6).

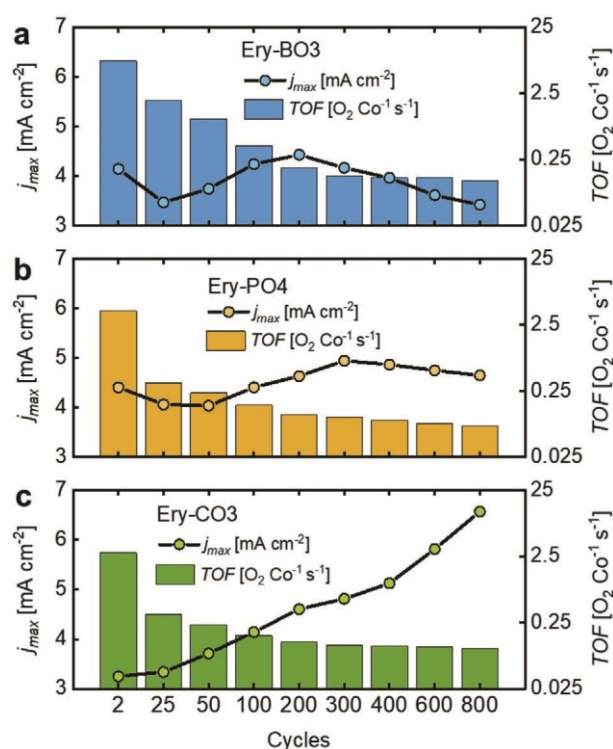


Figure 6. Relationship between the current density, j_{max} , (left y-axis, symbols) and TOF per redox-active site (right y-axis, bars) as a function of cycling in a) borate electrolyte, b) phosphate electrolyte, and c) carbonate electrolyte. j_{max} was evaluated at 2.1 V versus RHE. The TOF was estimated by the normalization of j_{max} by ERC and the four transferred electrons. Dataset in ref. [48].

Summary and Conclusion

Ery was used to identify the requirements for catalyst activation by electrochemical restructuring, for which we defined the indicators of the redox active Co (ERC), loss of Ery crystal structure, and anion exchange. All investigated electrolytes led to electrochemical restructuring to an amorphous layered cobalt (hydr)oxide to various degrees as demonstrated by XRD and EXAFS analyses. In Ery-BO₃, all three restructuring indicators correlated with cycling. In Ery-PO₄, only two indicators correlated: the loss of the Ery structure and arsenate, while the ERC increased monotonously. In the most interesting case of Ery-CO₃, none of the indicators correlated over 800 cycles. This indicated that the evolution of the restructuring processes with cycling, both structural and compositional, differed strongly in the selected electrolytes. Furthermore, the ERC increased by a factor of around 55 for Ery-BO₃, Ery-PO₄, and Ery-CO₃, which suggests an equal increase in the number of active sites on these restructuringd materials. Yet, its continuous increase resulted in the desired increase in activity only for Ery-CO₃. This highlights that the restructuring and activation are two separate processes, where activation has further requirements.

For activation, a large cluster size (i.e., high CPR) and high Co valence of the restructuringd surface (hydr)oxide were beneficial. An adequate cluster size has been reported to play an essential role in the mesostructure arrangement, which, together with intercalated electrolyte anions, impacts the electrical conductivity properties of the material.^[27,29] We hypothesize that a larger cluster size also aids in keeping anions in the amorphous structure where they act a proton buffers,^[13,63] so that larger clusters can support higher currents. Finally, we found that the current increased with the Co oxidation state at a fixed cluster size where an average oxidation state of 2.8 produced the highest activity. This is a typical oxidation state of a layered double hydroxide^[31,61,64] and close to ex situ measurements of electrodeposited Co oxide.^[37,38]

In summary, our work highlights the role of the electrolyte for electrochemical restructuring, where we found surprisingly different behavior of the restructuringd Ery. We expect that the simple method of anion exchange can be utilized in a wide range of catalyst materials, e.g., (oxy)phosphates,^[12,13] fluorides,^[65] oxychlorides,^[23] multimetallic oxyhydroxides,^[18,24,66,67] and perovskites,^[36] to control catalyst activation by restructuring with an optimal trinity of local order, transition metal valence, and high number of active sites.

Experimental Section

Materials: CoSO₄·7H₂O (Merck, 99,5%), Na₂HAsO₄·7H₂O (Merck, 99,5%), Nafion117 5% in ethanol (Sigma-Aldrich), FTO Pilkinton NSG TEC T15, K₂HPO₄ (Riedel-De Haën, 98%), KH₂PO₄ (Merck, >99,5%), H₃BO₃ (Sigma-Aldrich >99,5%), HCl (Merk, 32%), NaHCO₃ (Merk, 99,5%), isopropanol (Labquimar, 99,9%), MilliQ water (>18 MΩ cm), and CaCl₂ (Merk, PA).

Synthesis of Ery: About 400 mL of 7×10^{-3} m Na₂HAsO₄·7H₂O solution was added dropwise to 800 mL of 5×10^{-3} m CoSO₄ solution at 65 °C. The reddish solution of Co turned pink after several drops, and a precipitate started forming. The final suspension was stirred and heated (at 65 °C) for 72 h. The obtained solid was washed five times with deionized water and dried at room temperature and vacuum using CaCl₂ as a desiccant. The resulting product was denoted as "Ery" herein.

Electrode Preparation: About 5.00 mg of Ery was added to 1000 µL of isopropanol, and then the suspension was sonicated for 2 h to get a higher dispersion. About 80 µL of this suspension was slowly dropcoated on a 1 cm × 1 cm FTO glass surface. Once the isopropanol evaporated, 15 µL of 0.25% Nafion was drop-coated three times on the electrode's surface, waiting for 5 min between each addition. **Electrolyte Preparation:** All electrolytes were prepared at pH 7 (measured with a Daigger 5500 pH Meter) and 0.1 m concentration. For phosphate electrolyte, 0.1 m K₂HPO₄ and 0.1 m KH₂PO₄ solutions were prepared and mixed in an adequate ratio to adjust to pH 7. For borate electrolyte, 0.1 m B₄Na₂O₇ solution was prepared, and 0.1 m HCl solution was added dropwise to adjust to pH 7. For carbonate electrolyte, 0.1 m NaHCO₃ solution was prepared, and 0.1 m HCl solution was added dropwise to adjust to pH 7. For arsenate electrolyte, 0.1 m Na₂HAsO₄·7H₂O solution was prepared, and 0.1 m HCl solution was added dropwise to adjust to pH 7.

Electrochemical Measurements: The experiments were carried out on FTO glass electrodes as the working electrode in a single-compartment three-electrode electrochemical cell made of glass and filled with about 50 mL solution of the electrolyte. A high surface Pt mesh counter electrode and an Ag/AgCl (KCl saturated) reference electrode (separation of about 1 cm) were used. The electrochemical experiments were performed at room temperature using a potentiostat (SP-300, Biologic Science Instruments) controlled by the EC-Lab v11.01 software package. The typical electrolyte resistance (including the electrode) was about 65 Ω; *iR* compensation at 85% was dynamically applied. The solution remained unstirred during the experiments. All potentials were calculated and converted with respect to the RHE.

X-Ray Diffraction: Diffractograms were collected using a Bruker D8 Göbel-Mirror for grazing incidence in PT006 and an energy-dispersive Sol-X detector. Cu-Anode (Kα1+2) was used as source of X-ray. Data were collected in the range of $2\theta = 10^\circ - 70^\circ$ with increments of 0.02° and an equivalent time of 10 s per step. The measurements were carried out at the X-ray Core Lab at Helmholtz-Zentrum Berlin (HZB). The (020) reflection of Ery ($2\theta = 13^\circ$) normalized by the (200) reflection of FTO ($2\theta = 38^\circ$) was used as an indicator of the crystalline Ery phase.

Scanning Electron Microscopy and Energy-Dispersive X-Ray Spectroscopy: Sample morphology was determined using a low vacuum scanning electron microscope, Hitachi S-3700N, with an acceleration voltage of 10 keV and detecting secondary electrons. EDX measurements were performed using an energy-dispersive X-ray analysis probe, Oxford, and a Hitachi S-570 with an Aspe model Sirius 10/7.5 EDS. Normalization by the amount of Co guarantees that changes in As are due not to the dissolution of the material itself.

X-Ray Absorption Spectroscopy: Hard XAS spectra at Co-K edge were collected at the KMC-3 beamline^[68] at Helmholtz-Zentrum Berlin. Spectra were recorded in fluorescence mode using a 13 element silicon drift detector (SDD) from RaySpec. The used monochromator was a double-crystal Si (111), and the polarization of the beam was horizontal. Reference samples were prepared by dispersing a thin and homogeneous layer of the ground powder on Kapton tape. After removing the excess material, the tape was sealed, and the excess of Kapton was folded several times to get 1 cm × 1 cm windows. The energy was calibrated using a Co metal foil (fitted reference energy of 7709 eV in the first derivative

spectrum) with an accuracy ± 0.1 eV. Up to three scans of each sample were collected to $k = 14 \text{ \AA}^{-1}$.

All spectra were normalized by subtracting a straight line obtained by fitting the data before the K edge and division by a polynomial function obtained by fitting the data after the K edge, as illustrated elsewhere.^[14] The FT of the EXAFS was calculated between 15 and 800 eV above the Co- K edge ($E_0 = 7709$ eV). A cosine window covering 10% on the left side and 10% on the right side of the EXAFS spectra was used to suppress the side lobes in the FTs. Weighing of the intensity by k^3 was chosen to emphasize the heavier scatterers, i.e., Co, and thereby which samples had extended local order and which lacked it.

EXAFS simulations were performed using the software SimXLite. After calculating the phase functions with the FEFF8-Lite^[69] program (version 8.5.3, self-consistent field option activated), atomic coordinates of the FEFF input files were generated from the structure of Ery and other several reasonable structural models (Figure S1, Supporting Information); the EXAFS phase functions did not depend strongly on the details of the used model. An amplitude reduction factor (S_0^2) of 0.85 was used, which is typical for Co oxides.^[43] The data range used in the simulation was 34–747 eV (3.0–14.0 \AA^{-1}) above the Co- K edge ($E_0 = 7709$ eV). The EXAFS simulations were optimized by minimizing the error sum obtained by summation of the squared deviations between measured and simulated values (least-squares fit). The fit was performed using the Levenberg–Marquardt method with numerical derivatives.

Supporting Information

Supporting Information is available from the Wiley Online Library or from the author.

Acknowledgements

The authors thank Dr. Dulce Morales, Denis Antipin, and Joaquin Morales for helping in XAS data collection, and David Sánchez and Gabriela Fernández for helping in electrochemical measurements. The authors acknowledge Dr. Michael Haumann and Dr. Ivo Zizak for the support at the beamline; Dr. Katharina Klingan and Prof. Holger Dau for fruitful discussion; and Dr. Petko Chernev for permission to use his software SimXLite. The authors also thank Helmholtz–Zentrum Berlin (HZB) for the allocation of synchrotron radiation beamtime at BESSY, KMC-3. The XAS experiments were financially supported by funds allocated to Prof. Holger Dau (Freie Univ. Berlin) by the Bundesministerium für Bildung und Forschung (BMBF, 05K19KE1, OPERANDO-XAS) and by the Deutsche Forschungsgemeinschaft (DFG, German Research Foundation) under Germany's Excellence Strategy—EXC 2008—390540038—UniSysCat. The authors again thank HZB X-ray CoreLab for training and advising in XRD. This project received funding from Posgrado en Química and Vicerrectoría de Investigación (UCR), CONICIT-MICIT (Costa Rica), and the European Research Council (ERC) under the European Union's Horizon 2020 Research and Innovation Programme under grant agreement No. 804092.

Open access funding enabled and organized by Projekt DEAL.

Conflict of Interest

The authors declare no conflict of interest.

Data Availability Statement

The data that support the findings of this study are openly available in Figshare at <http://doi.org/10.6084/m9.figshare.14717997>.

Keywords

catalyst activation, Co-based electrocatalysts, electrochemical reconstruction, electrolyte, oxygen evolution reaction

Received: June 4, 2021

Revised: July 15, 2021

Published online: August 7, 2021

- [1] D. G. Nocera, *Acc. Chem. Res.* **2017**, *50*, 616.
- [2] M. Risch, *Nat. Energy* **2021**, *6*, 576.
- [3] S. Chu, A. Majumdar, *Nature* **2012**, *488*, 294.
- [4] C. W. Li, J. Ciston, M. W. Kanan, *Nature* **2014**, *508*, 504.
- [5] C. Liu, B. C. Colón, M. Ziesack, P. A. Silver, D. G. Nocera, *Science* **2016**, *352*, 602.
- [6] R. D. L. Smith, C. Pasquini, S. Loos, P. Chernev, K. Klingan, P. Kubella, M. R. Mohammadi, D. Gonzalez-Flores, H. Dau, *Nat. Commun.* **2017**, *8*, 2022.
- [7] J. Liu, Y. Ji, J. Nai, X. Niu, Y. Luo, L. Guo, S. Yang, *Energy Environ. Sci.* **2018**, *11*, 1736.
- [8] M. Risch, K. Klingan, F. Ringleb, P. Chernev, I. Zaharieva, A. Fischer, H. Dau, *ChemSusChem* **2012**, *5*, 542.
- [9] W. Cai, R. Chen, H. Yang, H. B. Tao, H. Y. Wang, J. Gao, W. Liu, S. Liu, S. F. Hung, B. Liu, *Nano Lett.* **2020**, *20*, 4278.
- [10] A. Indra, P. W. Menezes, N. R. Sahraie, A. Bergmann, C. Das, M. Tallarida, D. Schmeißer, P. Strasser, M. Driess, *J. Am. Chem. Soc.* **2014**, *136*, 17530.
- [11] J. Li, C. A. Triana, W. Wan, D. P. Adiyeri Saseendran, Y. Zhao, S. E. Balaghi, S. Heidari, G. R. Patzke, *Chem. Soc. Rev.* **2021**, *50*, 2444.
- [12] D. González-Flores, I. Sánchez, I. Zaharieva, K. Klingan, J. Heidkamp, P. Chernev, P. W. Menezes, M. Driess, H. Dau, M. L. Montero, *Angew. Chem., Int. Ed.* **2015**, *54*, 2472.
- [13] K. Klingan, F. Ringleb, I. Zaharieva, J. Heidkamp, P. Chernev, D. Gonzalez-Flores, M. Risch, A. Fischer, H. Dau, *ChemSusChem* **2014**, *7*, 1301.
- [14] J. Villalobos, R. Golnak, L. Xi, G. Schuck, M. Risch, *JPhys Energy* **2020**, *2*, 034009.
- [15] A. Bergmann, E. Martinez-Moreno, D. Teschner, P. Chernev, M. Gliech, J. F. De Araújo, T. Reier, H. Dau, P. Strasser, *Nat. Commun.* **2015**, *6*, 8625.
- [16] Y. Shi, Y. Yu, Y. Liang, Y. Du, B. Zhang, *Angew. Chem., Int. Ed.* **2019**, *58*, 3769.
- [17] H. Jiang, Q. He, X. Li, X. Su, Y. Zhang, S. Chen, S. Zhang, G. Zhang, J. Jiang, Y. Luo, P. M. Ajayan, L. Song, *Adv. Mater.* **2019**, *31*, 1805127.
- [18] A. Sivanantham, P. Ganesan, A. Vinu, S. Shanmugam, *ACS Catal.* **2020**, *10*, 463.
- [19] E. Fabbri, M. Nachtegaal, T. Binninger, X. Cheng, B. J. Kim, J. Durst, F. Bozza, T. Graule, R. Schaublin, L. Wiles, M. Pertoso, N. Danilovic, K. E. Ayers, T. J. Schmidt, *Nat. Mater.* **2017**, *16*, 925.
- [20] E. Tsuji, A. Imanishi, K. I. Fukui, Y. Nakato, *Electrochim. Acta* **2011**, *56*, 2009.
- [21] X. Zhao, X. Chen, Y. Wang, P. Song, Y. Zhang, *Sustainable Energy Fuels* **2020**, *4*, 4733.
- [22] X. Bao, Y. Li, J. Wang, Q. Zhong, *ChemCatChem* **2020**, *12*, 6259.
- [23] J. Wang, S. J. Kim, J. Liu, Y. Gao, S. Choi, J. Han, H. Shin, S. Jo, J. Kim, F. Ciucci, H. Kim, Q. Li, W. Yang, X. Long, S. Yang, S. P. Cho, K. H. Chae, M. G. Kim, H. Kim, J. Lim, *Nat. Catal.* **2021**, *4*, 212.
- [24] H. Jiang, Q. He, Y. Zhang, L. Song, *Acc. Chem. Res.* **2018**, *51*, 2968.
- [25] C. Costentin, D. G. Nocera, *Proc. Natl. Acad. Sci. USA* **2017**, *114*, 13380.

- [26] D. A. Lutterman, Y. Surendranath, D. G. Nocera, *J. Am. Chem. Soc.* **2009**, *131*, 3838.
- [27] C. Costentin, T. R. Porter, J. M. Savéant, *J. Am. Chem. Soc.* **2016**, *138*, 5615.
- [28] G. Kwon, H. Jang, J. S. Lee, A. Mane, D. J. Mandia, S. R. Soltan, L. M. Utschig, A. B. F. Martinson, D. M. Tiede, H. Kim, J. Kim, *J. Am. Chem. Soc.* **2018**, *140*, 10710.
- [29] C. Costentin, T. R. Porter, J. M. Savéant, *ACS Appl. Mater. Interfaces* **2019**, *11*, 28769.
- [30] P. W. Menezes, A. Indra, N. R. Sahraie, A. Bergmann, P. Strasser, M. Driess, *ChemSusChem* **2015**, *8*, 164.
- [31] M. Risch, F. Ringleb, M. Kohlhoff, P. Bogdanoff, P. Chernev, I. Zaharieva, H. Dau, *Energy Environ. Sci.* **2015**, *8*, 661.
- [32] H. S. Ahn, T. D. Tilley, *Adv. Funct. Mater.* **2013**, *23*, 227.
- [33] Y. Surendranath, M. W. Kanan, D. G. Nocera, *J. Am. Chem. Soc.* **2010**, *132*, 16501.
- [34] L. Ma, S. F. Hung, L. Zhang, W. Cai, H. Bin Yang, H. M. Chen, B. Liu, *Ind. Eng. Chem. Res.* **2018**, *57*, 1441.
- [35] R. D. L. Smith, M. S. Prévot, R. D. Fagan, S. Trudel, C. P. Berlinguette, *J. Am. Chem. Soc.* **2013**, *135*, 11580.
- [36] M. Risch, A. Grimaud, K. J. May, K. A. Stoerzinger, T. J. Chen, A. N. Mansour, Y. Shao-Horn, *J. Phys. Chem. C* **2013**, *117*, 8628.
- [37] M. Risch, V. Khare, I. Zaharleva, L. Gerencser, P. Chernev, H. Dau, *J. Am. Chem. Soc.* **2009**, *131*, 6936.
- [38] M. W. Kanan, J. Yano, Y. Surendranath, M. Dinc'a, V. K. Yachandra, D. G. Nocera, *J. Am. Chem. Soc.* **2010**, *132*, 13692.
- [39] G. Kwon, O. Kokhan, A. Han, K. W. Chapman, P. J. Chupas, P. Du, D. M. Tiede, *Acta Crystallogr., Sect. B: Struct. Sci., Cryst. Eng. Mater.* **2015**, *71*, 713.
- [40] H. Mori, T. Ito, *Acta Crystallogr.* **1950**, *3*, 1.
- [41] M. Wildner, G. Giester, C. L. Lengauer, C. A. Mccammon, *Eur. J. Mineral.* **1996**, *8*, 187.
- [42] R. L. Frost, J. T. Klopogge, W. N. Martens, *J. Raman Spectrosc.* **2004**, *35*, 28.
- [43] J. Villalobos, D. González-Flores, K. Klingan, P. Chernev, P. Kubella, R. Urcuyo, C. Pasquini, M. R. Mohammadi, R. D. L. Smith, M. L. Montero, H. Dau, *Phys. Chem. Chem. Phys.* **2019**, *21*, 12485.
- [44] X. Guo, F. Wu, G. Hao, S. Peng, N. Wang, Q. Li, Y. Hu, W. Jiang, *Dalton Trans.* **2019**, *48*, 5214.
- [45] X. Wang, R. Tong, Y. Wang, H. Tao, Z. Zhang, H. Wang, *ACS Appl. Mater. Interfaces* **2016**, *8*, 34270.
- [46] T. Jiang, S. A. Ansar, X. Yan, C. Chen, X. Fan, F. Razmjooei, R. Reisser, G. Montavon, H. Liao, *ACS Appl. Energy Mater.* **2019**, *2*, 8809.
- [47] F. Song, X. Hu, *J. Am. Chem. Soc.* **2014**, *136*, 16481.
- [48] J. Villalobos, D. Gonzalez-Flores, R. Urcuyo, M. L. Montero, G. Schuck, P. Beyer, M. Risch, **2021**, <https://doi.org/10.6084/m9.figshare.14717997>.
- [49] Y. Furutani, H. Kandori, *Biochim. Biophys. Acta, Bioenerg.* **2014**, *1837*, 598.
- [50] P. Baláz, M. Baláz, O. Shpotyuk, P. Demchenko, M. Vlček, M. Shopka, J. Briančin, Z. Bujňakova, Y. Shpotyuk, B. Selepová, L. Balážova, *J. Mater. Sci.* **2017**, *52*, 1747.
- [51] S. W. Lee, C. Carlton, M. Risch, Y. Surendranath, S. Chen, S. Furutsuki, A. Yamada, D. G. Nocera, Y. Shao-Horn, *J. Am. Chem. Soc.* **2012**, *134*, 16959.
- [52] M. W. Kanan, D. G. Nocera, *Science* **2008**, *321*, 1072.
- [53] D. K. Bediako, Y. Surendranath, D. G. Nocera, *J. Am. Chem. Soc.* **2013**, *135*, 3662.
- [54] A. Grimaud, K. J. May, C. E. Carlton, Y. L. Lee, M. Risch, W. T. Hong, J. Zhou, Y. Shao-Horn, *Nat. Commun.* **2013**, *4*, 2439.
- [55] J. Suntivich, K. J. May, H. A. Gasteiger, J. B. Goodenough, Y. Shao-horn, F. Calle-vallejo, A. D. Oscar, M. J. Kolb, M. T. M. Koper, J. Suntivich, K. J. May, H. A. Gasteiger, J. B. Goodenough, Y. Shao-horn, *Science* **2011**, *334*, 2010.
- [56] D. Friebe, M. Bajdich, B. S. Yeo, M. W. Louie, D. J. Miller, H. Sanchez Casalongue, F. Mbuga, T. C. Weng, D. Nordlund, D. Sokaras, R. Alonso-Mori, A. T. Bell, A. Nilsson, *Phys. Chem. Chem. Phys.* **2013**, *15*, 17460.
- [57] C. E. Beall, E. Fabbri, T. J. Schmidt, *ACS Catal.* **2021**, *11*, 3094.
- [58] J. Zhou, L. Zhang, Y. C. Huang, C. L. Dong, H. J. Lin, C. Te Chen, L. H. Tjeng, Z. Hu, *Nat. Commun.* **2020**, *11*, 1984.
- [59] B. Han, M. Risch, Y. L. Lee, C. Ling, H. Jia, Y. Shao-Horn, *Phys. Chem. Chem. Phys.* **2015**, *17*, 22576.
- [60] M. Görlin, M. Gliech, J. F. De Araújo, S. Dresch, A. Bergmann, P. Strasser, *Catal. Today* **2016**, *262*, 65.
- [61] W. T. Hong, M. Risch, K. A. Stoerzinger, A. Grimaud, J. Suntivich, Y. Shao-Horn, *Energy Environ. Sci.* **2015**, *8*, 1404.
- [62] L. Köhler, M. E. Abrishami, V. Roddatis, J. Geppert, M. Risch, *ChemSusChem* **2017**, *10*, 4479.
- [63] D. K. Bediako, C. Costentin, E. C. Jones, D. G. Nocera, J. M. Savéant, *J. Am. Chem. Soc.* **2013**, *135*, 10492.
- [64] M. S. Burke, L. J. Enman, A. S. Batchellor, S. Zou, S. W. Boettcher, *Chem. Mater.* **2015**, *27*, 7549.
- [65] Q. Xu, H. Jiang, X. Duan, Z. Jiang, Y. Hu, S. W. Boettcher, W. Zhang, S. Guo, C. Li, *Nano Lett.* **2021**, *21*, 492.
- [66] M. B. Stevens, L. J. Enman, A. S. Batchellor, M. R. Cosby, A. E. Vise, C. D. M. Trang, S. W. Boettcher, *Chem. Mater.* **2017**, *29*, 120.
- [67] J. T. Mefford, A. R. Akbashev, M. Kang, C. L. Bentley, W. E. Gent, H. D. Deng, D. H. Alsem, Y. Yu, N. J. Salmon, D. A. Shapiro, P. R. Unwin, W. C. Chueh, *Nature* **2021**, *593*, 67.
- [68] G. Schuck, I. Zisak, *J. large-scale Res. Facil.* **2020**, *6*, 139.
- [69] A. Ankudinov, B. Ravel, *Phys. Rev. B: Condens. Matter Mater. Phys.* **1998**, *58*, 7565.

Supporting Information

Requirements for beneficial electrochemical restructuring: A model study on a cobalt oxide in selected electrolytes

Javier Villalobos, Diego González-Flores, Roberto Urcuyo, Mavis L. Montero, Götz Schuck, Paul Beyer, Marcel Risch**

Methods

Fourier transform infrared spectroscopy (FTIR)

Spectra were collected on the electrodes containing the material after a selected number of cycles in a Perkin Elmer Frontier FTIR-ATR mode using a diamond crystal. Measurements were performed using 64 scans between 600 and 4000 cm⁻¹.

Raman spectroscopy

Spectra were acquired on a WITec Alpha 300R Raman microprobe system, with 750 nm excitation at a power of 20 mW and an integration time of 2 s with 20 accumulations. Measurements were replicated on three different areas of samples.

Average Co oxidation state estimation

The Co edge energy was estimated from XANES spectra using the integral method,^[1] which is accomplished by using a step integral function with the following equation: $E^{edge} = E_1 + \frac{1}{\mu_2 - \mu_1} \int_{E_1}^{E_2} \mu_2 - \tilde{\mu}(E) dE$, where E represents the energy, $\mu_1=0.15$ and $\mu_2=1.00$. μ_1 was set above 0 to exclude pre-edges from the analysis. Dau et al.^[1] showed that the edge energy, E^{edge} obtained by this method scales more linearly with the oxidation state of references as compared to defining the edge as 0.5 normalized intensity or as the first inflection point. The edge energies of three Co references (CoO, Co₃O₄, LiCoO₂) were used to build a calibration curve, in which the Co samples were subsequently interpolated.

Figures

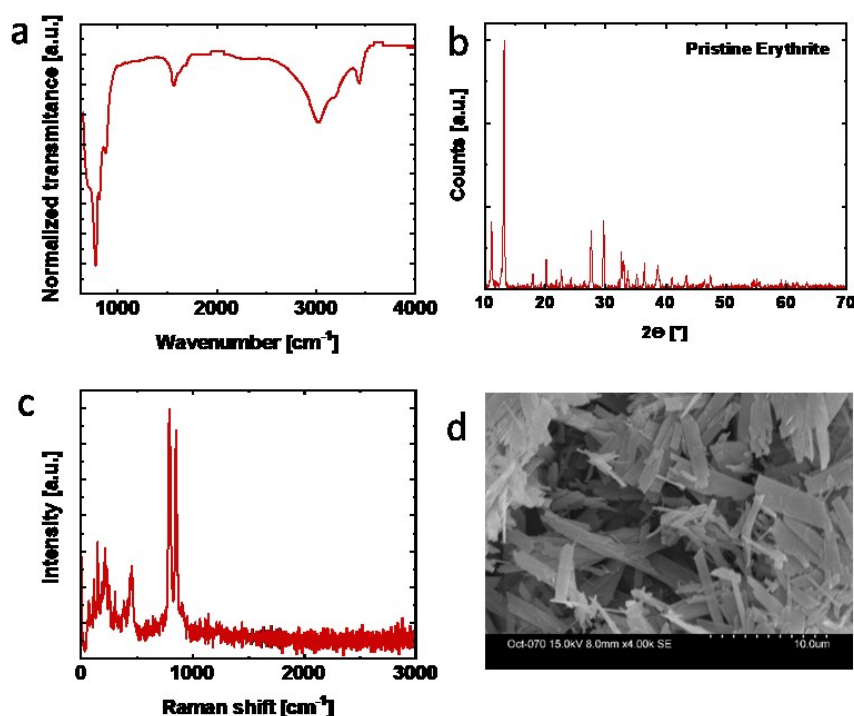


Figure S1. Characterization of Ery: a. ATR-FTIR spectrum, b. Powder X-ray diffractogram of Ery. The peak around 13 ° confirms the presence of the vivianite face, c. Raman spectrum, d. SEM images of some crystals. Dataset in ref.^[2]

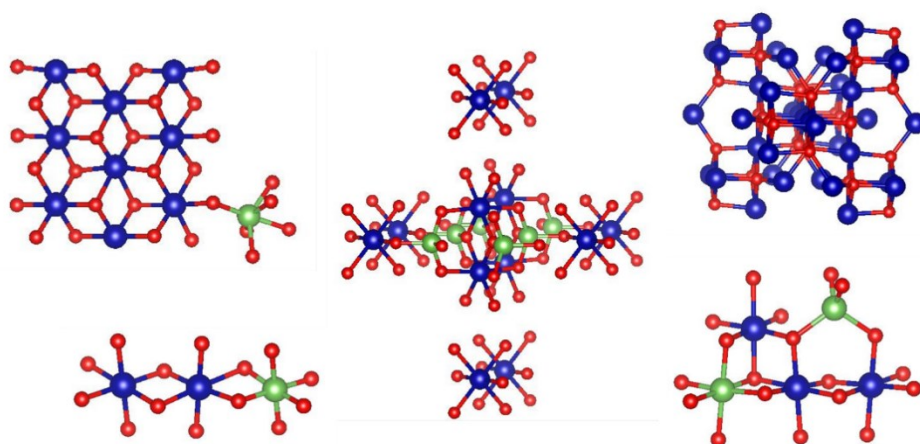


Figure S2. Structural models for the estimation of reasonable phase functions for EXAFS simulations. Blue dots represent Co atoms, red dots oxygen atoms, and green dots arsenic atoms.

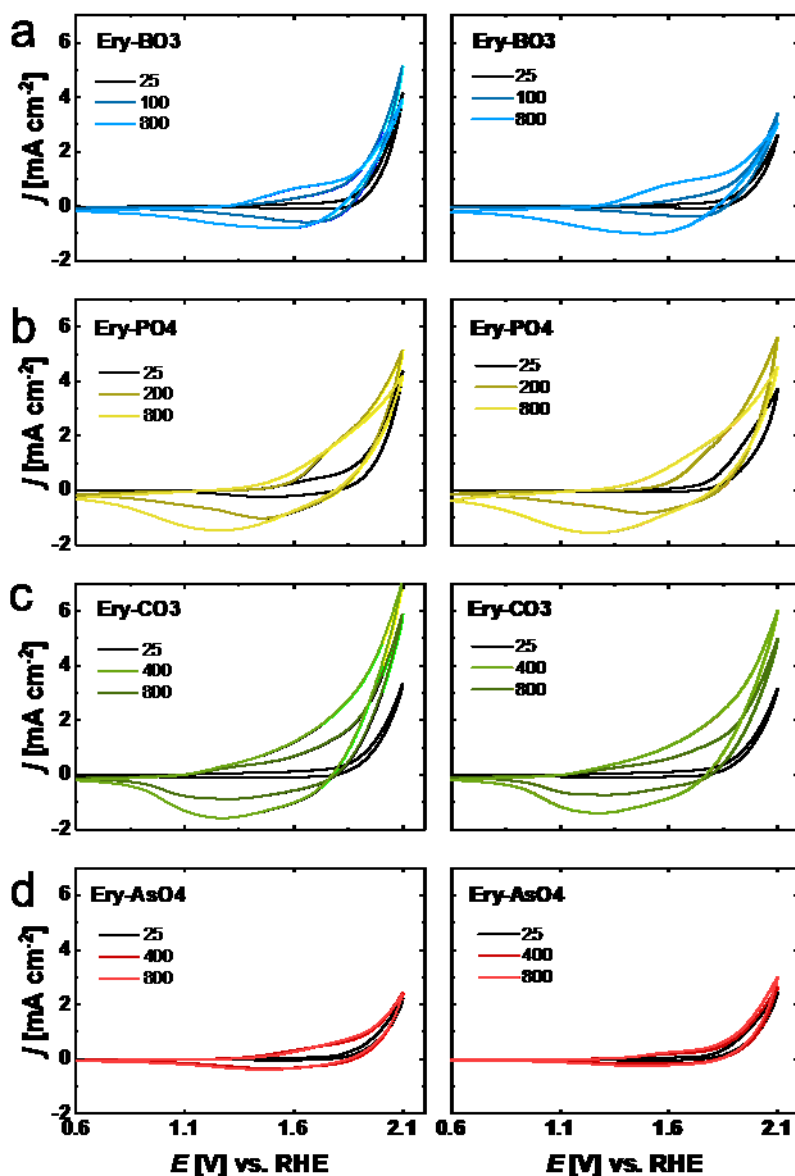


Figure S3. Series of CV performed on an Erythrite-deposited FTO glass (sample set b and c) in different electrolytes at pH 7 and a concentration of 0.1 M: **a.** borate, **b.** phosphate, **c.** carbonate and **d.** arsenate. 800 cycles were performed with a sweep speed of 100 mV s⁻¹ and 85 % iR compensation. Potential is represented as E vs. RHE. The cycle number is indicated in each CV series. Dataset in ref.^[2]

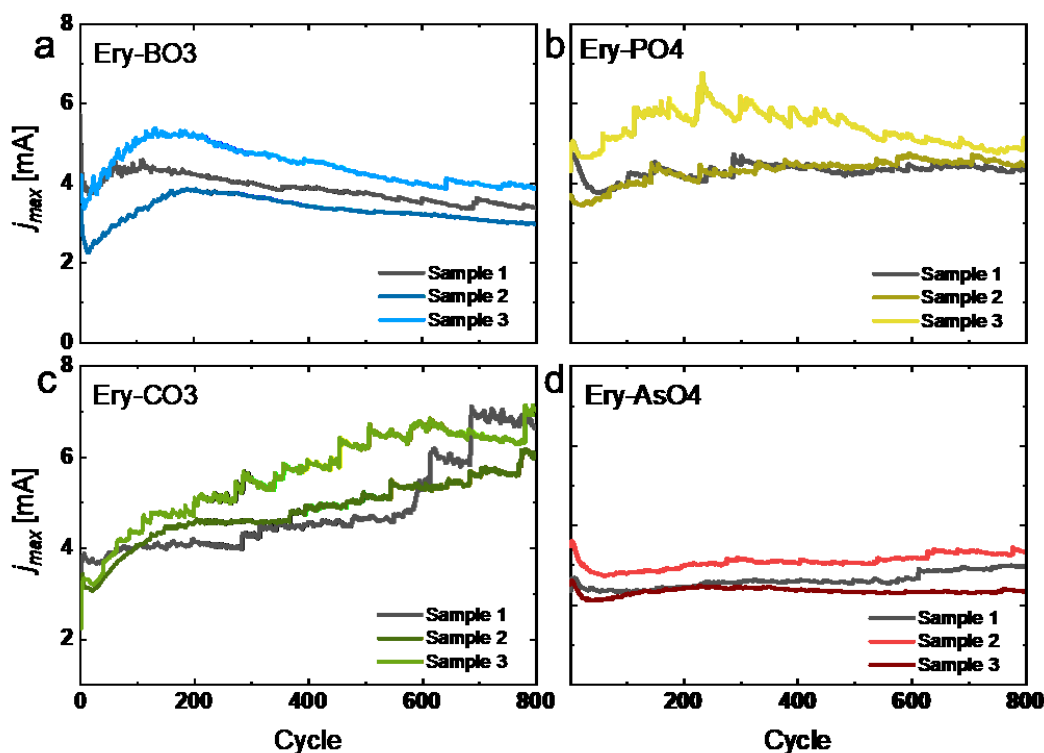


Figure S4. Maximum current (j_{max}) as a function of cycling of Ery-deposited FTO in: **a.** borate, **b.** phosphate, **c.** carbonate and **d.** arsenate electrolytes. All electrolytes at pH 7 and 0.1 M concentration. The three lines represent three different samples. j_{max} were obtained at $E=2.1$ V vs. RHE. Dataset in ref. [2]

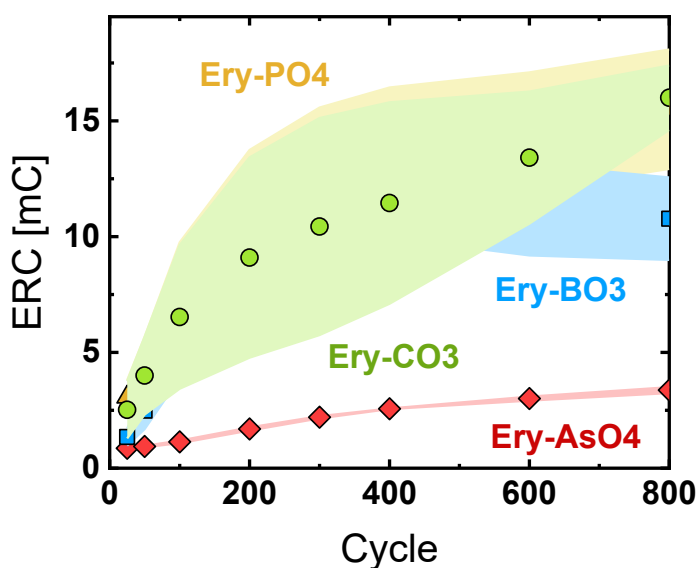


Figure S5. ERC as a function of cycling of Ery-deposited FTO in borate (blue squares), phosphate (yellow triangles), carbonate (green circles) and arsenate (red diamonds) electrolytes. All electrolytes at pH 7 and 0.1 M concentration. The light-colored area represents

the standard deviation of three values. ERC values were estimated by the integration of the reductive currents. Dataset in ref. [2]

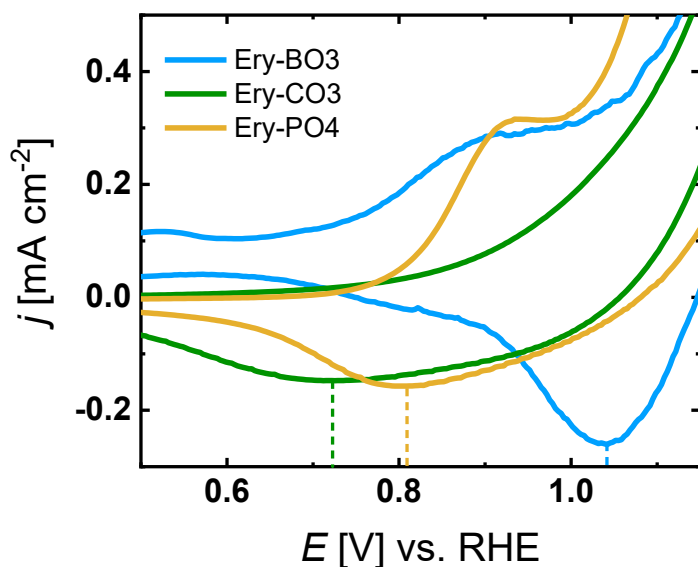


Figure S6. Series of CV performed on Ery-BO3, Ery-PO4 and Ery-CO3 after 800 cycles with a scan rate of 5 mV s^{-1} to identify the position of the oxidative redox peaks. Dataset in ref. [2]

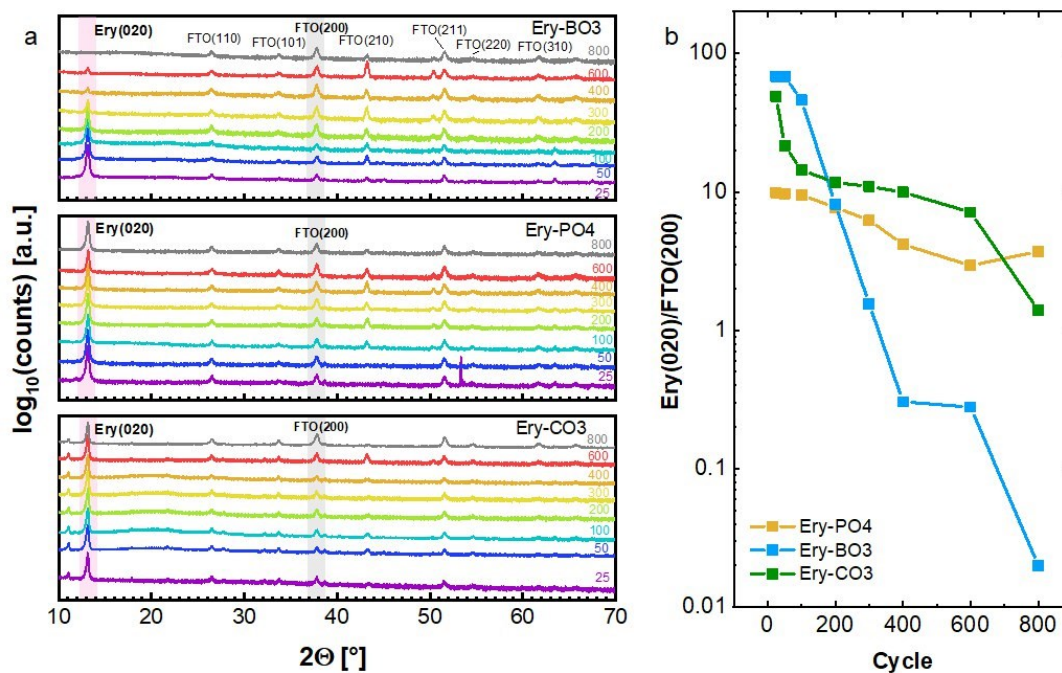


Figure S7. a. XRD patterns of Ery-deposited FTO glass after a selected number of cycles in pH 7 0.1 M borate, phosphate and carbonate electrolyte (top to bottom). The pink light-colored area highlights the peak corresponding to Ery(020) and the gray light-colored area highlights

the peak corresponding to FTO(200). All other peaks in the diffractogram are assigned to FTO.
b. Ratio of the integrals under the Ery (020) and FTO (200) peaks. Dataset in ref. [2]

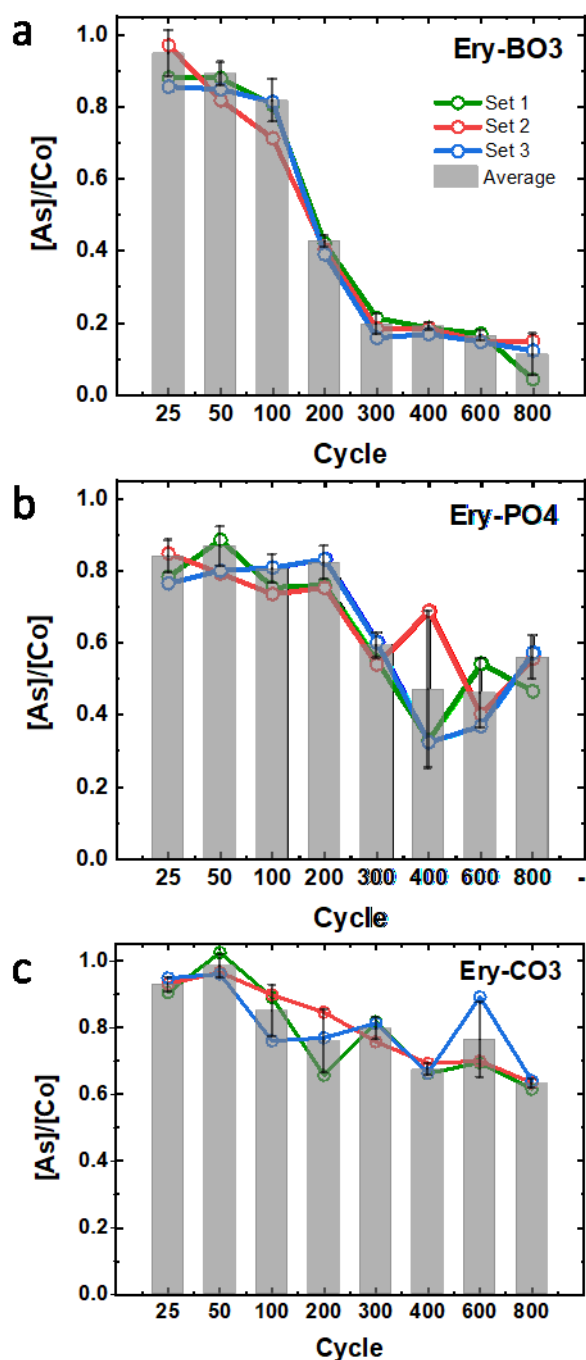


Figure S8. As/Co ratio by EDX as a function of cycling of Ery-deposited FTO glass in: **a.** borate, **b.** phosphate and **c.** carbonate electrolyte. Three set of samples sets are represented with lines and the average is represented with bars (including standard deviation). Dataset in ref. [2]

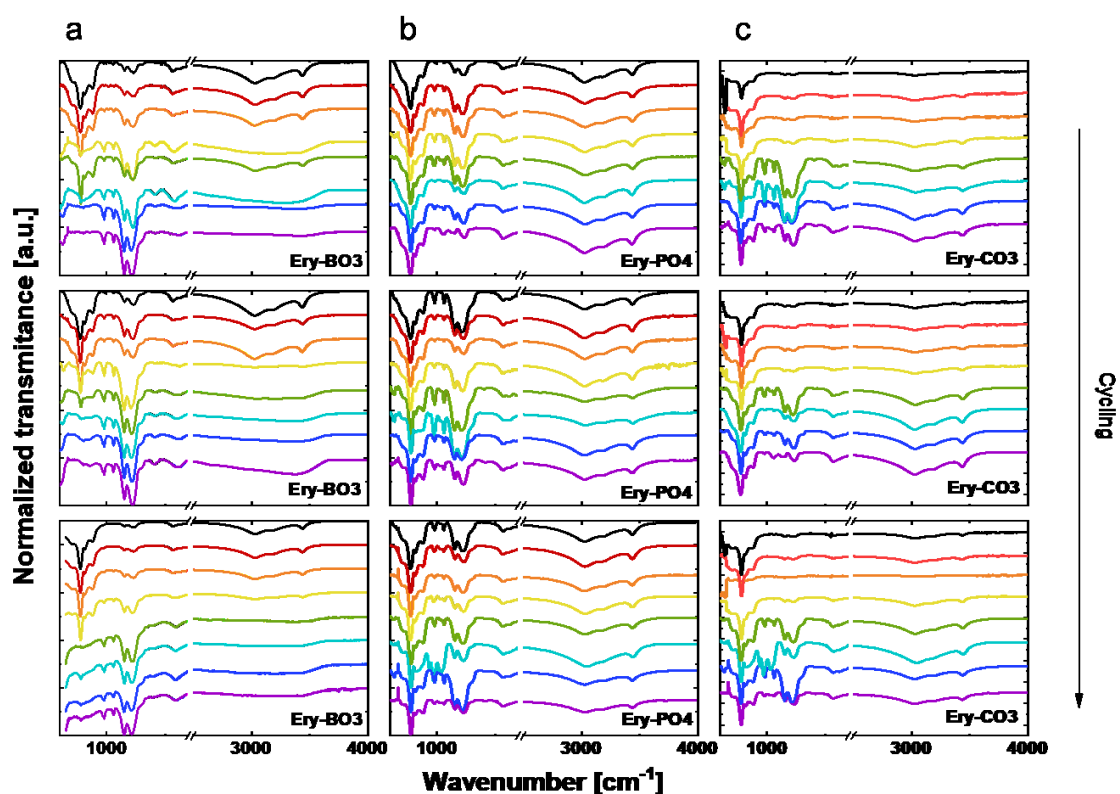


Figure S9. ATR-FTIR spectra of Ery-deposited FTO glass after a selected number of cycles (25, 50, 100, 200, 300, 400, 600, 800; descending) in pH 7 0.1 M: **a.** borate, **b.** phosphate and **c.** carbonate electrolytes. The loss of arsenate anions is tracked by the decrease of the 780 cm⁻¹ signal. Dataset in ref. [2]

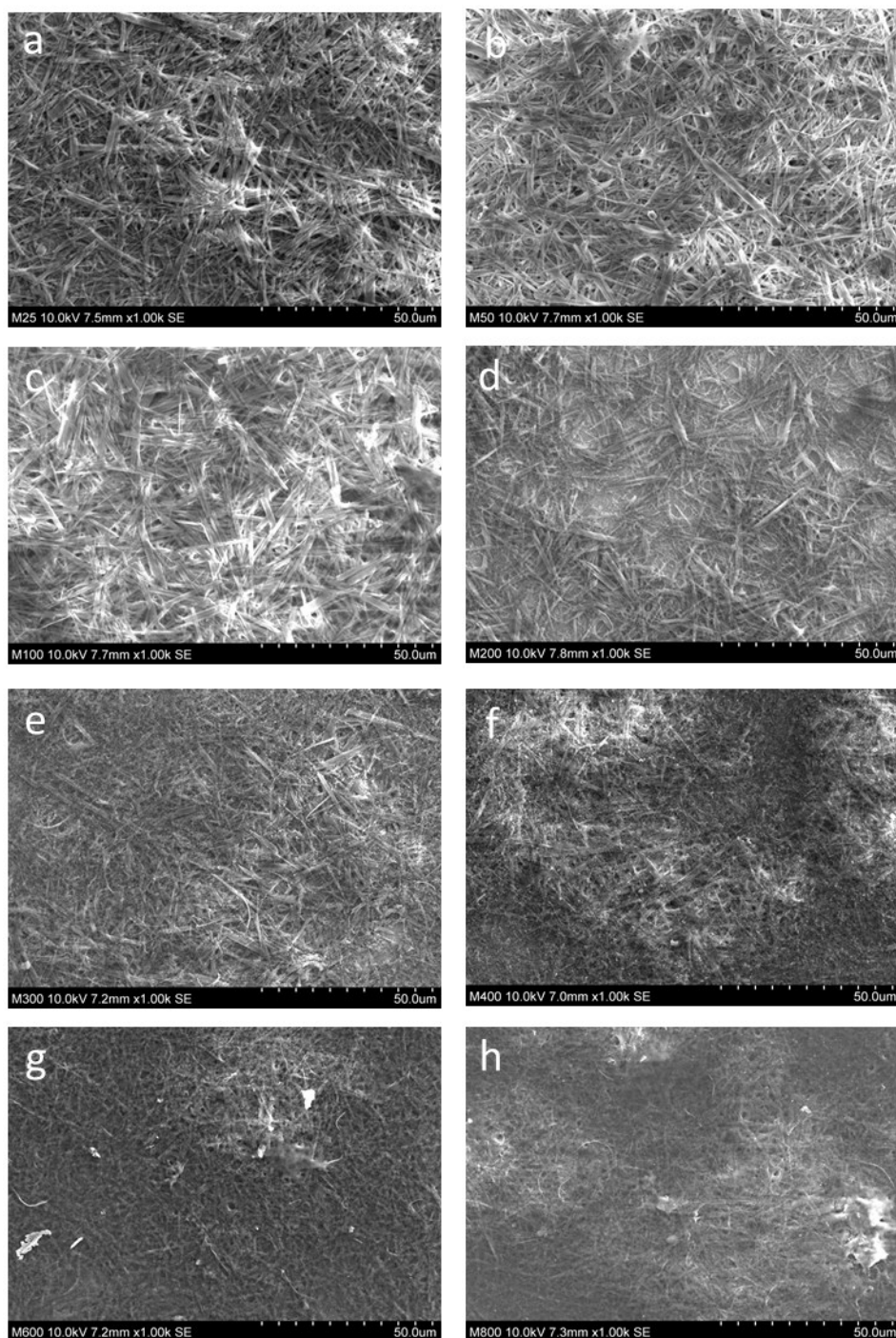


Figure S10. SEM images of Ery-deposited FTO glass in 0.1 M pH 7 borate electrolyte after a selected number of cycles: a. 25, b. 50, c. 100, d. 200, e. 300, f. 400, g. 600 and h. 800.

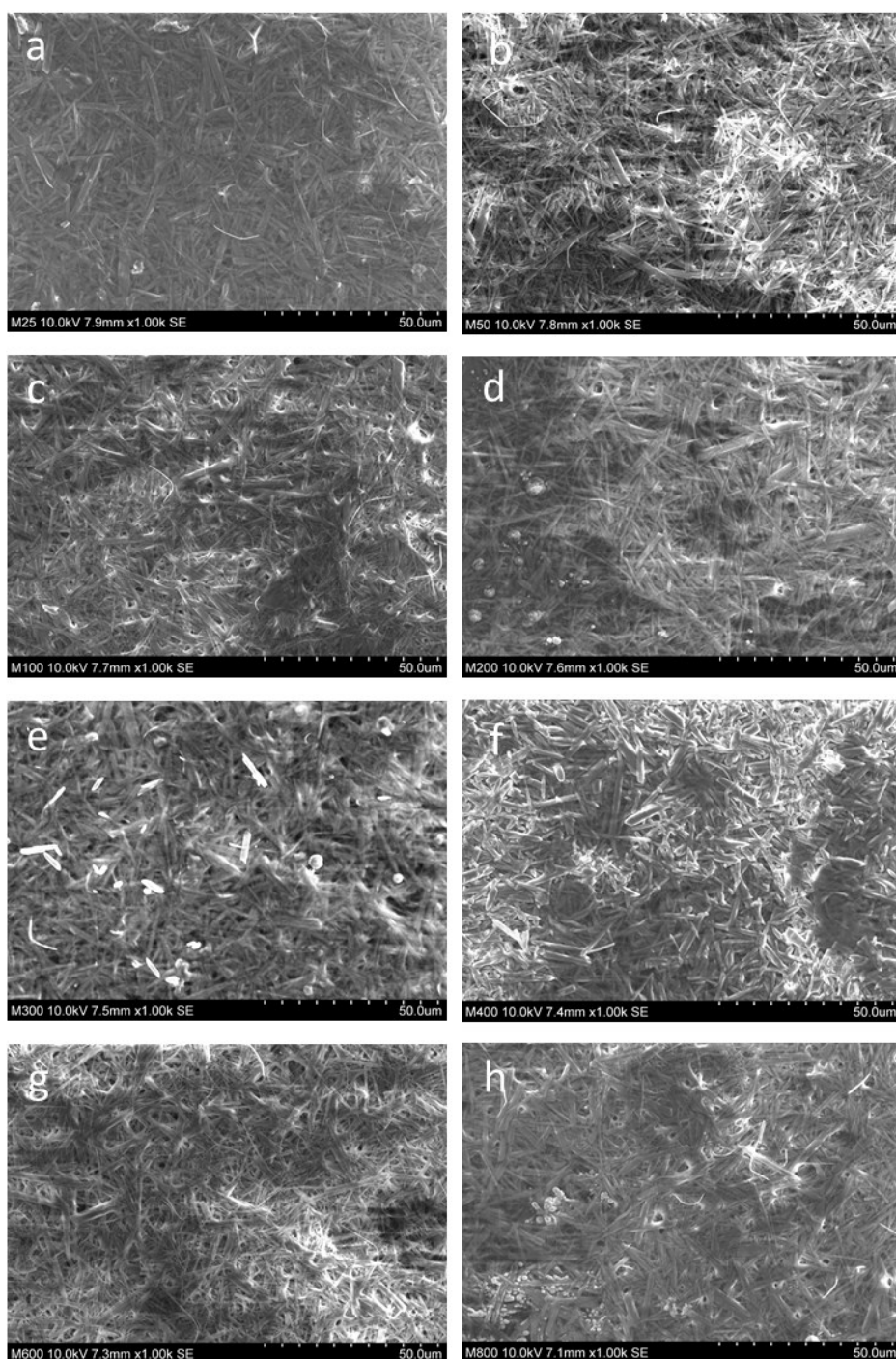


Figure S11. SEM images of Ery-deposited FTO glass in 0.1 M pH 7 phosphate electrolyte after a selected number of cycles: a. 25, b. 50, c. 100, d. 200, e. 300, f. 400, g. 600 and h. 800.

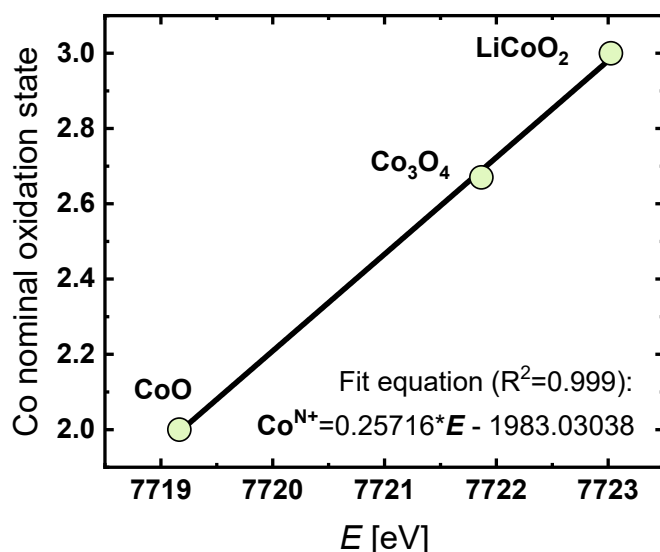


Figure S12. Nominal Co oxidation state of references as a function of the energy of the Co-K edge denoted by E . The fit equation is shown in the graph. $\text{Co}^{(+2)}\text{O}$, $\text{Co}^{(+2.67)}_3\text{O}_4$ and $\text{LiCo}^{(+3)}\text{O}_2$ were used as references. The calculated nominal oxidation state for each sample is shown in **Table S3**. The energy of the edge was estimated by the integral method. ^[1] Dataset in ref. ^[2]

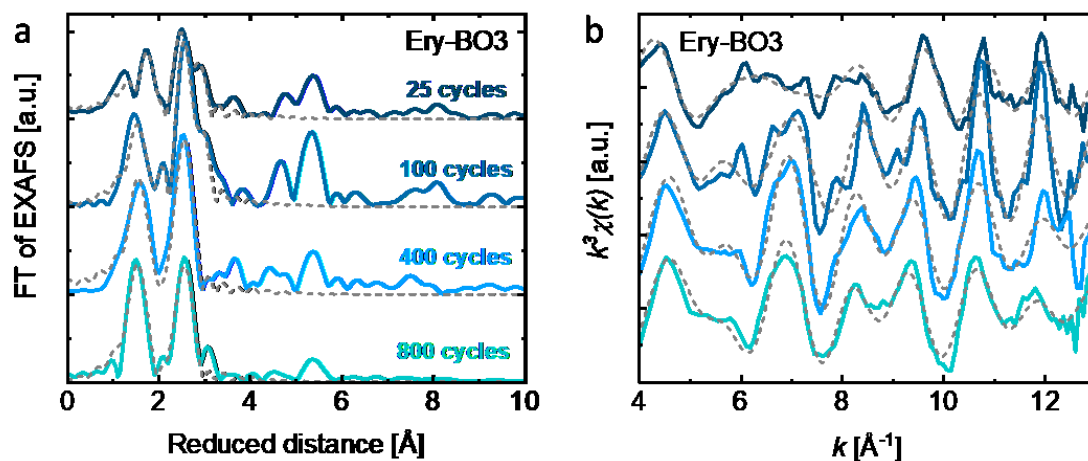


Figure S13. a. Fourier-transformed EXAFS spectra of the Co K-edge collected on Ery-BO3 after a selected number of cycles. The corresponding dashed lines are results from EXAFS simulations (see **Table S4** for parameters). The reduced distance is by about 0.3 Å shorter than the precise distance obtained by EXAFS simulations. **b.** k^3 -weighted EXAFS spectra of Ery-BO3 after a selected number of cycles recorded at the Co-K edge. The solid lines represent the measurements. The dashed lines represent the respective EXAFS simulations. Dataset in ref. ^[2]

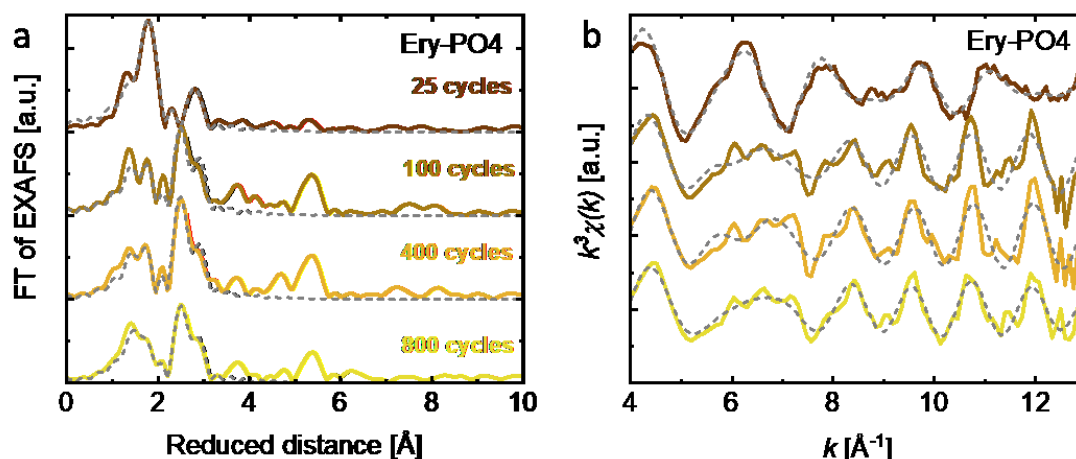


Figure S14. **a.** Fourier-transformed EXAFS spectra of the Co K-edge collected on Ery-PO4 after a selected number of cycles. The corresponding dashed lines are results from EXAFS simulations (see **Table S4** for parameters). The reduced distance is by about 0.3 Å shorter than the precise distance obtained by EXAFS simulations. **b.** k^3 -weighted EXAFS spectra of Ery-PO4 after a selected number of cycles recorded at the Co-K edge. The solid lines represent the measurements. The dashed lines represent the respective EXAFS simulations. Dataset in ref. [2]

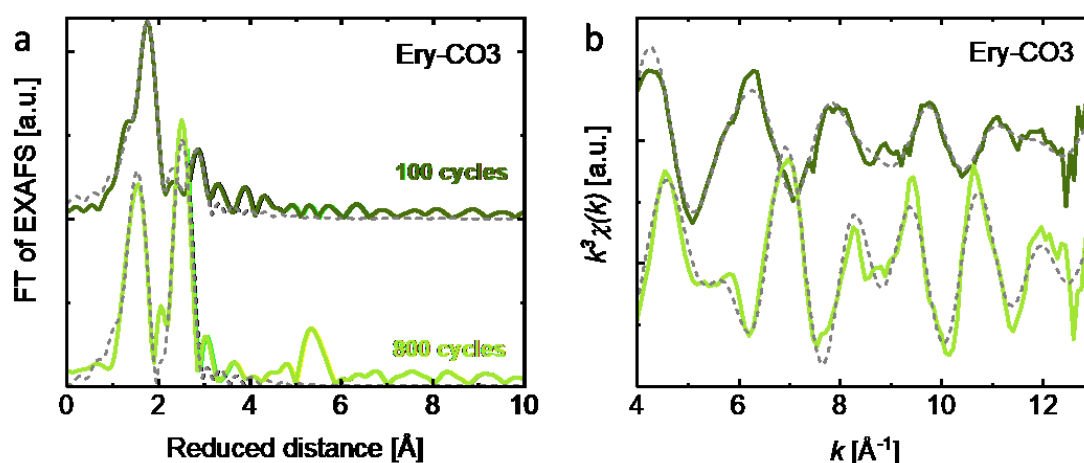


Figure S15. **a.** Fourier-transform EXAFS spectra of the Co K-edge collected on Ery-CO3 after a selected number of cycles. The corresponding dashed lines are results from EXAFS simulations (see **Table S4** for parameters). The reduced distance is by about 0.3 Å shorter than the precise distance obtained by EXAFS simulations. **b.** k^3 -weighted EXAFS spectra of Ery-CO3 after a selected number of cycles recorded at the Co-K edge. The solid lines represent the measurements. The dashed lines represent the respective EXAFS simulations. Dataset in ref. [2]

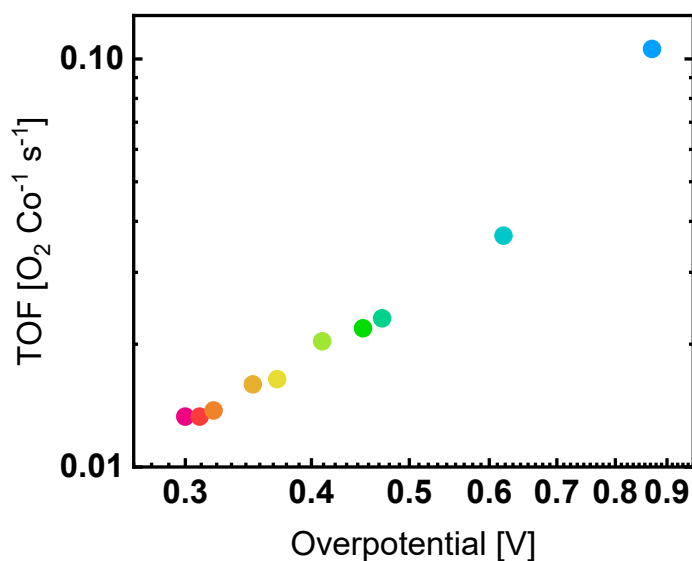


Figure S16. Turnover frequency (TOF) as a function of the overpotential of Ery-CO3 after 800 cycles. The values are estimated from the current density and ERC. The line was added to guide the eye. Dataset in ref. [2]

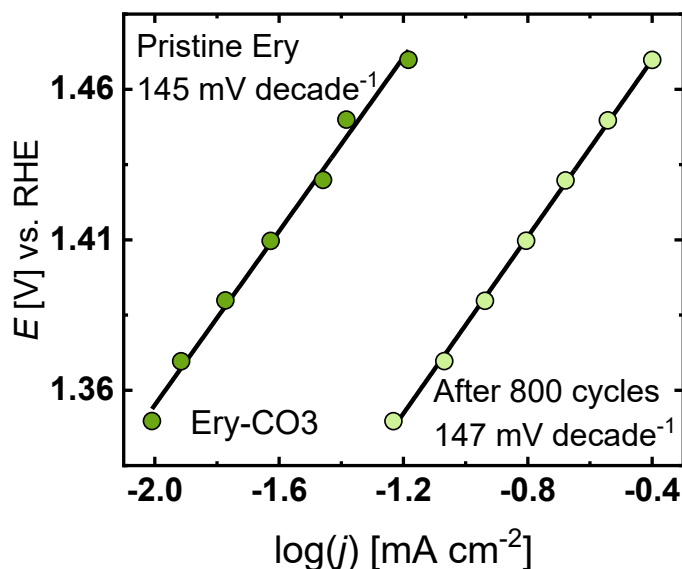


Figure S17. Tafel slope before and after restructuring Ery in carbonate pH 7 and 0.1 M concentration. The lines represent the linear fit of $E-iR$ as function of $\log(i)$, the slope represents the Tafel slope. Tafel plots were collected with 50 mV steps, each potential was applied for 5 min. No iR compensation was applied. The potential was iR -corrected after the measurements. Dataset in ref. [2]

Tables

Table S1. Catalytic properties of common Co-based OER catalysts and the Mn₄Ca oxygen evolution cluster in photosystem II for various electrolyte conditions and catalyst loadings.

Active material	Conditions	Loading	pH	Over-potential (mV)*	TOF (O ₂ Co ⁻¹ s ⁻¹)	Method	Ref.
Ery-CO ₃ , after 800 cycles	Carbonate electrolyte 0.1 M	0.4 mg cm ⁻²	7	300	1.3x10 ⁻²	ERC ^a	This work
				310	1.3x10 ⁻²	ERC ^a	
				320	1.4x10 ⁻²	ERC ^a	
				350	1.6x10 ⁻²	ERC ^a	
				370	1.6x10 ⁻²	ERC ^a	
				400	1.7x10 ⁻²	ERC ^a	
				410	1.7x10 ⁻²	ERC ^a	
				440	2.0x10 ⁻²	ERC ^a	
				450	2.2 x10 ⁻²	ERC ^a	
				470	2.3 x10 ⁻²	ERC ^a	
				620	3.7 x10 ⁻²	ERC ^a	
				870	1.1 x10 ⁻¹	ERC ^a	
Reconstructed Pakhomovskiyite	KPi 0.1 M	3.0 mg cm ⁻²	7	620	≈0.1	ERC ^a	[3]
Co-Pi	KPi 0.1 M	24 mC cm ⁻²	7	410	2.6x10 ⁻³	TC ^c	[4]
Co(PO ₃) ₂ nanoparticles	KPi 0.1 M	1 mg cm ⁻²	6.4	440	0.10-0.21	CS ^b	[5]
Co ₃ O ₄	KPi 0.2 M	50 μg cm ⁻²	7	400-490	0.07-0.004	TC ^c	[6]
Co ₃ O ₄	KOH 0.1 M	0.25 mg cm ⁻²	13	320	≈2x10 ⁻³	CS ^b	[7]
LaCoO ₃	KOH 0.1 M	0.25 mg cm ⁻²	13	370	2.5x10 ⁻²	CS ^b	[7]
Co-Pi	KOH 0.1 M	24 mC cm ⁻²	13	370	1x10 ⁻³ -0.3	CS ^b	[8]
Ba _{0.5} Sr _{0.5} Co _{0.8} Fe _{0.2} O _{3-δ}	KOH 0.1 M	0.25 mg cm ⁻²	13	470	4x10 ⁻³ -0.3	CS ^b	[9]
PrBaCo ₂ O _{5+δ}	KOH 0.1 M	0.25 mg cm ⁻²	13	370	≈2	CS ^b	[7]
CoO _x H _y	KOH 1 M	12 μg cm ⁻²	14	350	6x10 ⁻³	CS ^b	[10]
LiMn ₂ O ₄	NaOH 1 M	0.40 mg cm ⁻²	14	450	0.07	CS ^b	[11]
NiFeO _x	Borate electrolyte 0.1 M	20 μg cm ⁻²	9.2	400	0.32	ERC ^a	[12]
NiFeO _x	KPi 0.1 M	20 μg cm ⁻²	7	400	0.01	ERC ^a	[13]

Mn ₄ Ca oxygen evolution cluster in photosystem II	Membranes particles in lumen	N.A.	≈5.5	300	≈100	R ^d	[13,14]
---------------------------------------------------------------------	------------------------------------	------	------	-----	------	----------------	---------

* at 10 mA/cm_{geo}²; ^a TOF = $i/ERC/4$; ^b TOF = $i/\rho_{\text{surface}}/4$ (surface atoms from crystal structure);
^c TOF = $i/q_T/4$ (total electrodeposited charge); ^d TOF = reciprocal of total duration for one catalytic turnover.

Table S2. General electrochemical protocol for data collection.

Step	Conditions
1. Cleaning	FTO substrates were washed with soap to remove any grease on the surface and then, sonicated in isopropanol for 30 minutes to remove the soap and any dust. Lastly, they were sonicated for 30 minutes in deionized water. The substrates were dried at room conditions. The glass cells were cleaned in a diluted solution of HNO ₃ and then in deionized water.
2. Reference electrode calibration	The Ag/AgCl 3 M KCl reference electrode was calibrated against another Ag/AgCl 3 M KCl, which is only used with such purpose.
3. Dynamic iR compensation	Potential: 0.4 V vs. Ag/AgCl 3 M KCl Frequency: 10 KHz Amplitude: 10 mV Waiting time between measurements: 0.1 s Average from 4 measurements 85 % of compensation Current range: 10 mA Bandwith 7 fast
4. Cyclic voltammetry	Potential window: 0 V – 1.5 V vs. Ag/AgCl 3 M KCl. Scan rate: 100 mV s ⁻¹ Cycles: 25-800 iR dynamic compensation Measured current over the last 50 % of the step duration Recorded current averaged over 10 voltage steps Current range: 10 mA Bandwith 7 fast
5. Sample rinsing	After the electrochemical experiments the samples are soaked in deionized water during 5 minutes to remove the excess of electrolyte.

Table S3. Co nominal oxidation state of Ery in phosphate and borate electrolyte in selected cycles. The fit equation and graph are shown in Figure S12.

Electrolyte	Co nominal oxidation state in a selected cycle			
	25	100	400	800
Borate	2.3	2.6	2.8	2.8
Phosphate	2.3	2.4	2.4	2.4
Carbonate	-	2.4	-	2.8

Table S4. EXAFS absorber–backscatter distance (R) and coordination numbers (N) as determined by simulation of the k^3 -weighted EXAFS spectra at the cobalt K-edge for samples Ery-BO3, Ery-PO4 and Ery-CO3, after a selected number of cycles. The Debye-Waller factor (σ) was fixed at a value of $2\sigma^2=0.01$, as used previously for similar materials.^[15]

Sample	Co-O	Co-O	Co-O	Co-Co	Co-Co	R-factor
Ery-BO3, after 25 cycles						
R	1.836	2.0(1)	2.11(6)	2.81(1)	3.04(1)	10.5
N	1.4(6)	3(1)	3(2)	2.6(3)	2.3(3)	
Ery-BO3, after 100 cycles						
R	1.92(2)	2.25(2)	2.06(5)	2.85(1)	3.09(1)	11.3
N	3.3(7)	2.7(5)	2.0(6)	4.7(3)	3.3(3)	
Ery-BO3, after 400 cycles						
R	1.91(1)	-	-	2.82(1)	-	11.0
N	4.4(2)	-	-	4.0(2)	-	
Ery-BO3, after 800 cycles						
R	1.90(1)	-	-	2.83(1)	-	9.1
N	4.4(2)	-	-	4.0(2)	-	
Ery-PO4, after 25 cycles						
R	1.92(7)	2.10(2)	-	2.85(4)	3.03(1)	5.2
N	2(2)	2.11(1)	-	0.6(4)	1.9(4)	
Ery-PO4, after 100 cycles						
R	1.90(2)	2.07(2)	2.25(4)	2.84(1)	3.07(1)	15.8
N	2.0(4)	3.8(5)	1.6(6)	2.8(3)	2.4(3)	
Ery-PO4, after 400 cycles						
R	1.90(3)	2.06(2)	2.25(4)	2.83(1)	3.05(1)	10.6
N	1.7(4)	3.2(4)	1.3(5)	3.2(3)	2.5(3)	
Ery-PO4, after 800 cycles						
R	1.90(4)	2.04(6)	2.19(9)	2.83(1)	3.07(1)	6.5
N	1.9(8)	2.7(6)	1.2(8)	2.2(3)	1.7(3)	
Ery-CO3, after 100 cycles						
R	1.97(6)	2.12(2)	2.34(4)	2.87(3)	3.05(2)	5.9
N	1.5(6)	5.4(6)	1.2(8)	0.6(3)	1.3(4)	
Ery-CO3, after 800 cycles						
R	1.89(1)	-	-	2.81(1)	-	7.0
N	4.0(2)	-	-	3.3(2)	-	

The R-factor used Fourier filtered data between 1 and 3 Å using the formula $R_f = 100 \frac{\sum (m_i^{ff} - e_i^{ff})^2}{\sum (e_i^{ff})^2}$, where m^{ff} represents the Fourier-filtered model and e^{ff} represents the experimental k-weighted EXAFS curve.

Table S5. Calculation of the TOF ($\text{O}_2\text{Co}^{-1}\text{s}^{-1}$) for Ery-CO3 after a selected number of cycles, with the equation $TOF = \frac{i_{max}}{4 \cdot ERC}$. Where i_{max} is the current at 2.1 V vs. RHE, ERC is obtained by integrating the cathodic current area in the CV series in Figure 2 in the main text, and 4 is the number of electrons transferred in the catalytic reaction.

Cycle	ERC (mC)	i_{max} (mA)	TOF ($\text{O}_2\text{Co}^{-1}\text{s}^{-1}$)
2	0.28595	3.2528	2.84383
25	2.522	3.33759	0.33085
50	3.99967	3.71503	0.23221
100	6.53033	4.14362	0.15863
200	9.098	4.60828	0.12663
300	10.439	4.81378	0.11528
400	11.45233	5.126	0.1119
600	13.41333	5.81218	0.10833
800	16.0203	6.56905	0.10264

References

- [1] H. Dau, P. Liebisch, M. Haumann, *Anal. Bioanal. Chem.* **2003**, 376, 562.
- [2] J. Villalobos, D. Gonzalez-Flores, R. Urcuyo, M. L. Montero, G. Schuck, P. Beyer, M. Risch, "Requirements for beneficial electrochemical restructuring: A model study on a cobalt oxide in selected electrolytes," DOI 10.6084/m9.figshare.14717997, **2021**.
- [3] D. González-Flores, I. Sánchez, I. Zaharieva, K. Klingan, J. Heidkamp, P. Chernev, P. W. Menezes, M. Driess, H. Dau, M. L. Montero, *Angew. Chemie - Int. Ed.* **2015**, 54, 2472.
- [4] Y. Surendranath, M. W. Kanan, D. G. Nocera, *J. Am. Chem. Soc.* **2010**, 132, 16501.
- [5] H. S. Ahn, T. D. Tilley, *Adv. Funct. Mater.* **2013**, 23, 227.
- [6] L. Ma, S. F. Hung, L. Zhang, W. Cai, H. Bin Yang, H. M. Chen, B. Liu, *Ind. Eng. Chem. Res.* **2018**, 57, 1441.
- [7] A. Grimaud, K. J. May, C. E. Carlton, Y. L. Lee, M. Risch, W. T. Hong, J. Zhou, Y. Shao-Horn, *Nat. Commun.* **2013**, 4, 1.
- [8] S. W. Lee, C. Carlton, M. Risch, Y. Surendranath, S. Chen, S. Furutsuki, A. Yamada, D. G. Nocera, Y. Shao-Horn, *J. Am. Chem. Soc.* **2012**, 134, 16959.
- [9] M. Risch, K. A. Stoerzinger, S. Maruyama, W. T. Hong, I. Takeuchi, Y. Shao-Horn, *J. Am. Chem. Soc.* **2014**, 136, 5229.
- [10] M. S. Burke, S. Zou, L. J. Enman, J. E. Kellon, C. A. Gabor, E. Pledger, S. W. Boettcher, *J. Phys. Chem. Lett.* **2015**, 6, 3737.
- [11] L. Köhler, M. Ebrahimizeh Abrishami, V. Roddatis, J. Geppert, M. Risch, *ChemSusChem* **2017**, 10, 4479.
- [12] M. Görlin, M. Glieth, J. F. De Araújo, S. Dresch, A. Bergmann, P. Strasser, *Catal. Today* **2016**, 262, 65.
- [13] H. Dau, I. Zaharieva, *Acc. Chem. Res.* **2009**, 42, 1861.
- [14] H. Dau, C. Limberg, T. Reier, M. Risch, S. Roggan, P. Strasser, *ChemCatChem* **2010**, 2, 724.
- [15] J. Villalobos, D. González-Flores, K. Klingan, P. Chernev, P. Kubella, R. Urcuyo, C. Pasquini, M. R. Mohammadi, R. D. L. Smith, M. L. Montero, H. Dau, *Phys. Chem. Chem. Phys.* **2019**, 21, 12485.

Chapter 7: Conclusions and outlook

The central goal of this work has been using transition metal oxides, namely Mn- and Co-based, as a model to study the structural changes suffered after the oxygen evolution catalysis. Single Na-containing Mn- and Co-based oxides, and Na-containing mixed Mn,Co-based oxide were electrodeposited using a new method. The new electrodeposition method was developed in alkaline media (2 M NaOH) with the assistance of tartrate ions as complex ions for the stabilization of the metal ions (Mn^{2+} and/or Co^{2+}).

The single oxides, CoO_x and MnO_x , suffered a continuous current decrease (and a continuous Tafel slope increase) over cycling. Interestingly, in the case of CoO_x , the current fully recovered after a 30-minute break at open-circuit. In the case of MnO_x , the current recovered only partially after the OCP break, indicating that some changes can happen irreversibly. These irreversible changes might be related to dissolution of permanganate ions, MnO_4^- , which is a typical corrosion path and it was observed in the MnO_x films. The mixed Co,Mn oxide was proposed to increase the stabilization of the catalytic current. The obtained mixed oxide, $(\text{Co}_{0.7}\text{Mn}_{0.3})\text{O}_x$, owned a j_{max} much higher than MnO_x and slightly lower (only during the first cycles) than CoO_x . Even though both single oxides showed Tafel slope values higher than 120 mV dec^{-1} , the $(\text{Co}_{0.7}\text{Mn}_{0.3})\text{O}_x$ films own a Tafel slope of 90 mV dec^{-1} . A value that cannot be explained by kinetic calculations. As expected, no structural changes were observed in $(\text{Co}_{0.7}\text{Mn}_{0.3})\text{O}_x$ after catalysis. Various effects can be associated to the increase in stability, namely, the prevention of MnO_4^- ions dissolution, an increase in the conductivity of the material (in comparison with CoO_x), and an optimization of the metal oxygen (M-O) binding energy.

The previously-studied structural changes were beneficially used to improve catalytic properties of the materials. Ery (Erythrite: $\text{Co}_3(\text{AsO}_4)_2 \cdot 8\text{H}_2\text{O}$, a crystalline mineral) was synthesized and used as Co-based crystalline model to study the electrochemical restructuring during OER in four different electrolytes (with same pH and concentration). The restructuring was deconvoluted in three processes: amorphization, anionic exchange and redox Co activity change, which were tracked by XRD, EDX, and ERC, respectively. Even though the experimental conditions are similar, the rate of the three processes is completely different depending on the electrolyte's nature. For instance, the slowest processes were observed in carbonate electrolyte, where the amorphization took 800 cycles to complete and the ERC kept increasing the whole period. The different restructuring rates affected the final Co oxide structure, e.g., long-range order or cluster size. Interestingly, the current was only significantly

activated in carbonate electrolyte (around 100 % from the initial value), indicating that the electrochemical restructuring and the activation are two different processes, where the activation has further requirements. (I) adequate cluster size: larger clusters are more conductive and able to retain more anions, which act as proton acceptors. (II) High Co oxidation state: Co atoms tend to oxide due to OER, an oxidation state of 2.8+ showed the highest current. (III) High Co redox activity: it relates to the amount of cathodic (and anodic) current observable in a CV, a bigger area implies more accessible Co redox sites.

The role of the different Mn oxidations states for OER catalysis is still in debate, yet the results herein reported show a relation between the stability over cycling and the oxidation state of Mn. In the MnO_x and the $(\text{Co}_{0.7}\text{Mn}_{0.3})\text{O}_x$ films, Mn was present in an oxidation state between 3+ and 4+, yet the oxidation state was 0.2 higher in the mixed $(\text{Co}_{0.7}\text{Mn}_{0.3})\text{O}_x$ oxide, where the catalytic current was more stable in 0.1 M NaOH electrolyte; the partial oxidation of the near surface of MnO_x after 100 cycles was observed by XAS and associated with the irreversible current drop. This is an indication that a higher oxidation state, close to 4+, owns higher stability than lower oxidation state values. Nevertheless, the exclusive content of Mn^{4+} has been reported as non-active.

A similar effect was observed in the oxidation state of Co. In the CoO_x films, the near surface owned an oxidation state slightly lower than 3+, which oxidized in 0.1 M NaOH over cycling toward Co^{3+} . In the $(\text{Co}_{0.7}\text{Mn}_{0.3})\text{O}_x$, Co^{3+} was mostly observed and no changes were observed either in bulk or at the near surface. This behavior was also confirmed in near neutral pH by the electrochemical restructuring of Ery, where the Co^{2+} continuously oxidizes toward Co^{3+} during 800 cycles in different electrolytes. In this case and additionally, the catalytic activity was also related to a higher Co oxidation state, indicating that Co^{3+} is optimal for OER in disorder Co-based oxides.

Moreover, Co oxides were produced with two different methods (i) electrodeposition in alkaline media and (ii) electrochemical restructuring in near-neutral media. In case of the electrochemical restructuring, the final structural properties strongly depended on the nature of the electrolyte. For instance, the final Co oxidation state went from 2.4+ (in phosphate) to 2.8+ (in borate and carbonate), similar to the electrodeposited Co oxide, which was about 2.8+. The long-range order (or disorder) of the material can also vary depending on the production method or the electrolyte. The least disorder material was obtained by electrochemical restructuring in carbonate electrolyte, whereas the most disorder oxide was obtained by electrodeposition in NaOH, as it can be observed by the CPR in the EXAFS spectra. The CPR from EXAFS spectra is an indicator of the oxide cluster size and an adequate cluster size is

required to obtain OER-active Co oxides. Therefore, the conditions and the production method of the Co oxides strongly affect the catalytic properties for OER.

In summary, the identification of structural changes during deactivation was used to develop new strategies to increase the stability and enhance the current during electrochemical restructuring of OER electrocatalysts. The stability can be increased by preventing the dissolution of ions, increasing the material's conductivity and optimizing the M-O binding energy; whereas the activation during electrochemical restructuring can be enhanced by tuning an adequate cluster size, adjusting the metal oxidation state and increasing the redox activity. Promoting new strategies to extend the lifetime of OER electrocatalysts is fundamental for their future use in applications of energy storage. OER is the most promising process to supply electrons and protons, which are needed for hydrogen production, CO₂ reduction, nitrogen fixation, among others.

The results showed in this work are highly relevant to understand how the structural changes after catalysis can be used beneficially in increasing the current or the stability of the electrocatalysts. Moreover, they confirm that other processes, such as surface oxidation, ionic exchange and dissolution or amorphization, can simultaneously occur to the OER. Thus, the current observed in the electrochemical experiments might not exclusively be due to OER.

These results proved that the introduction of 30 % of MnO_x into the CoO_x can increase the stability of the CoO_x without affecting the catalytic activity significantly. Yet, a systematic study, varying the MnO_x content in CoO_x, is necessary to identify the optimal Mn:Co ratio for catalytic activity and stability. Moreover, since a stability increase due to Mn introduction has been reported for spinel-type Co oxides as well, it would be interesting to study other conditions and similar materials to understand the extend of this effect. For instance, the introduction of Fe oxide into the amorphous Co oxide.

More efforts are required to study the materials' structural changes not only after catalysis but also during the catalytic reaction. For this purpose, *operando* experiments are required, in which the structural changes can be tracked while the electrochemical experiments are performed and the products, e.g., oxygen, are detected. For instance, with an *in situ* setup, the effect of open-circuit conditions in the reactivation of the catalytic current of CoO_x and MnO_x could be studied in detailed. As well as the identification of reversible structural changes in the films during OER conditions.

Three requirements for a beneficial electrochemical restructuring were defined for Co-based oxides in near-neutral pH. However, the universality of these requirements is yet to be proved. Thus, it is relevant to investigate other broadly used OER catalysts, such as other transition-

metal oxides, multimetallic oxyhydroxides or perovskites, to define if they possess similar requirements for a beneficial electrochemical restructuring.